Development of Tunable Terahertz Quantum Cascade Wire Lasers

by

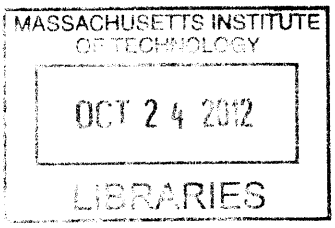

Qi Qin

Submitted to the Department of Electrical Engineering and Computer Science

in partial fulfillment of the requirements for the degree of

Doctor of Philosophy

at the

MASSACHUSETTS INSTITUTE OF TECHNOLOGY

September 2012

Author .....

Department of Electrical Engineering and Computer Science

August 31, 2012

Certified by .....

Qing Hu

Professor

Thesis Supervisor

Accepted by .....

Leslie A. Kolodziejski

Chairman, Department Committee on Graduate Students

Development of Tunable Terahertz Quantum Cascade Wire Lasers

by

Qi Qin

Submitted to the Department of Electrical Engineering and Computer Science on August 31, 2012, in partial fulfillment of the requirements for the degree of Doctor of Philosophy

Abstract

For a long time, terahertz (THz) radiation has been of great interest to scientific community because of its spectroscopic and imaging applications based on its unique properties, such as the capabilities to penetrate many materials which are opaque in other frequency range (e.g. packaging, plastics, paints and semiconductors), and spectroscopic signatures of many important materials.

In this thesis, a continuously tunable THz wire QC laser, which comprises a QC laser with deep sub-wavelength transverse dimensions, and a movable side object, termed as "plunger", is demonstrated. This deep sub-wavelength cross-section results in a large fraction of mode propagating outside of the laser core ($GaAs/Al_{0.15}Ga_{0.85}As$ material system). The frequency tuning is achieved by changing the transverse wave vector, using a plunger made by metal (metal plunger) or silicon (dielectric plunger). When nudged close to the wire laser core, the metal plunger can push modes to the opposite side of the

waveguide. Confined by a metal-metal waveguide, the mode is squeezed and the transverse wave vector is increased, resulting in a blue-shifted frequency. In contrast, a silicon plunger can suck the mode out due to its similar refractive index to GaAs/AlGaAs material system of laser core. Thus a decreased transverse wave vector results in a red-shifted frequency.

Although a tuning record of 138GHz (3.6%) was achieved, a discontinuous tuning resulted from a jittering movement of the plungers due to its friction with the guiding system. To solve this problem, an improved plunger based on micro-mechanical system (MEMS) was implemented. This MEMS plunger uses a two-stage folded-beam flexure to isolate the misaligned external actuation. The plunger is attached with the flexure which suspends above a silicon substrate to eliminate friction. Eventually, this MEMS flexure was actuated by a mechanical system which comprised a lever to de-amplify the displacement of a linear mechanical feedthrough. This MEMS plunger enabled a restorable and frictionless movement which led to a continuous tuning range of 330GHz (8.6%) centered at ~3.85 THz.

The challenges posted by the weak mode discrimination led to the development of comb-shape connectors which electrically connect the top metal of wire lasers and the side bonding pad. This design can significantly increase the mode discrimination by selectively guiding undesired mode into the lossy bonding pad. This robust design of single mode operation enables the initial lasing at a frequency far below the gain peak, which can potentially increase the tuning range significantly.

Thesis Supervisor: Qing Hu
Title: Professor

Acknowledgements

I would like to take this opportunity to thank many people who made this thesis possible.

First, it is difficult to overstate the importance of the guidance from my supervisor, Professor Qing Hu. His sound advice and inspiration helped me progress fast in the thesis work. I am also lucky enough to observe how he approaches and solves problems, which is very helpful for me to grow as a researcher.

I would like to thank many people who contribute to this thesis work. First, the excellent MBE growth from John Reno provided me good gain mediums to work on. My group-mates, Benjamin Williams and Sushil Kumar not only designed the best terahertz quantum-cascade lasers used in this thesis work, they also taught me valuable lab techniques. I am indebted to Alan Lee who always made him available to discuss the research and teach me how to fit into the new culture. I would like to thank many student colleagues for providing a stimulating and fun working environment: Hans Callebaut, Allen Hsu, Wilt Kao, David Burghoff, Ivan Chan, Ningren Han and Shengxi Huang. I would particularly like to thank Wilt Kao and David Burghoff for their help in experimental work and in electromagnetic simulation.

I am grateful to my thesis committee members, Professor Erich Ippen and Jeffery Lang, whose useful suggestions and comments are very important to push the project forward. I would like to thank Professor Martin L. Culpepper, Professor Carol Livermore and Dr. Hanqing Li who helped me on mechanical design. I am also obligated to Dr. Vicky Diadiuk and other MTL staff for their help on the fabrication.

This work would not have been possible without the love and support of my parents, although they are in the other side the earth. They are always protecting me from being lost especially in the hard time of my research and life. I would like to thank my friends, Wenzhe Ma and Yufei Ge, who are always supportive and happen to be in the same city with me from the college time.

I dedicate this work to my beloved mother and father

1 Introduction

1.1 Underdeveloped terahertz spectrum

Terahertz (THz) radiation lies between 300GHz (3×10^{11}Hz) to 10 THz (1×10^{13}Hz), corresponding to a sub-millimeter wavelength range between 1mm to 30um in wavelength. For many years, THz radiation has been the most underdeveloped frequency range in the electromagnetic spectrum. The underdeveloped status of this frequency range is due to a lack of high quality sources and limited applications which have been explored. First, the lack of an efficient, compact and high-power terahertz source with room temperature operation has deterred the extensive practical research on the material interaction with THz radiation. Thus until recently, the primary interest in THz spectrum has come from atmosphere and astronomy science communities. This lack of application has discouraged the further development of THz sources. The key to break this vicious cycle between lack of good sources and applications is to develop compact and high efficient THz source within working temperature range of a thermal electric (TE) cooler.

Although THz is adjacent with two well-accessible frequency bands, the microwave (<0.3 THz) and the infrared (>10 THz), it lacks convenient and efficient radiation sources to generate THz radiation for several reasons. First, the traditional technologies in the microwave range, such as transistors, Gunn oscillators, and Schottky-diode frequency multipliers, are hampered by the fact that the transit time of charge carriers is longer than the oscillation period of THz radiation. With the normal maximum operation frequency as hundreds of gigahertz, these devices can only generate micro watts of power at THz range which is far from enough for practical applications. Secondly, the solid state devices used in the infrared frequency band cannot be operated in THz frequency, due to the unavailable materials whose band gap is equal to THz energy quanta. This is further worsened by the fact that photon energy is smaller than the thermal energy at room temperature, which will be further discussed later.

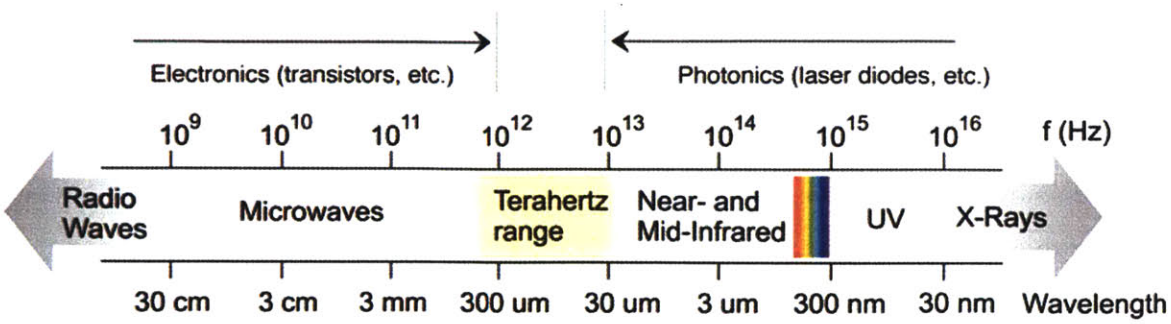

Figure 1.1.1 The electromagnetic spectrum, which shows the underdeveloped terahertz spectrum between the well-developed microwave and infrared ranges.

1.2 Application of THz radiation

Until recently, the primary interest in the terahertz spectrum has been from the astronomy and atmospheric science community [1]. However, terahertz radiation can potentially extends its applications into the fields of spectroscopy, astrophysics, biomedical research, microelectronics, agriculture, forensic science, and many other fields. It is worth specially mentioning that recently THz radiation has attracted medical community's attention in T-ray imaging because of its low interference and non-ionizing characteristics. These unique properties make THz radiation a powerful technique for safe and in vivo medical imaging.

Most of the applications of THz radiation stems from THz spectroscopy, which is essentially based on the fact that different molecule rotational and vibrational excitations have different characteristics of emission or absorption. Among these spectroscopic features is the strong water absorption in THz region. So in most THz spectroscopic application, a dry environment or water absorption window in spectrum is required. However, on the other hand, the strong wafer absorption also makes THz spectroscopy a good technique to measure water concentration [2]. Besides, some imaging applications, such as THz airport security imaging, are enabled by the fact that many plastics and cloth are transparent in THz region.

Here we briefly review several important THz applications which generally desire a compact, highly efficient, continuously tunable THz source. Being able to fast and

precisely sweep the desired frequency range, tunable THz source can be used to analyze spectroscopic information or probe the spatial information non-destructively. It is worth, for readers, paying attention to the advantages of using a compact and powerful THz tunable source in these applications. These advantages become the fundamental driving force of this thesis.

1.2.1 Astronomy

The universe is bathed in THz radiation from big bang, and most of it is unnoticed and undetected[3]. THz technologies enable study of interstellar dust cloud, planetary atmosphere monitoring, and observation of asteroids, moons and comet.

Studying the terahertz radiation background help astronomers to decode the evolving process during the universe formed. The observation of the spectral energy distributions in galaxies shows that approximately one-half of the total luminosity and 98% of the photons emitted since the Big Bang fall into the submillimeter and far-IR[4] region. Additionally, the interstellar dust spectra fall into the range from 1mm to 100um. Usually, analyzing this information requires high spectral resolution and large aperture for high angular resolution. Specifically, lower terahertz band detection needs heterodyne detector in which THz quantum cascade lasers are required. NASA's Far-IR/Submillimeter Roadmap Missions SAFIR and SPECS are the recent example to explore universe by analyzing rich information contained in THz spectral lines. Spectral lines in THz region contain particularly valuable information about the cooling, collapse, and chemistry of molecular cloud cores and protostars. [5]

The THz traces of atmospheric phenomena make THz spectroscopy a good technique to monitor several important global problems, such as ozone destruction and global warming. These traces are from thermal emission lines of stratospheric and upper tropospheric gases. Usually, the spectroscopic signatures of these gases fall into the range from 300GHz to 2500GHz which is revealed by heterodyne receivers[6]. The recent example of this kind application is the THz laser system carried by NASA EOS-Aura satellite launched in 2004. It can monitor ozone layer by measuring the concentration and

distribution of the hydroxyl radical (OH–(2.510 THz and 2.514 THz)) in the stratosphere, a critical component in the ozone cycle[7]. Furthermore, THz detesters are also used to disclose the evolution of the solar system by observing asteroid, moon and comet[8] [9]. It is also suggested to explore planets containing atmospheric conditions suitable for extraterrestrial life using submillimeter-wave remote detection and terahertz spectroscopy [10].

1.2.2 Biomedical applications

Biomedical applications of THz radiation are normally based on THz spectroscopic platforms or imaging systems. Compared to other techniques, THz radiation can penetrate many materials while experiencing low scattering compared to infrared radiation. Besides it is nonionizing and able to provide spectral "finger print" for a broad spectrum of materials from explosive to cancers[11]. A single cycle of THz radiation is ~ 1 ps, which makes it suitable to monitor dynamic biological systems with picosecond time scale.

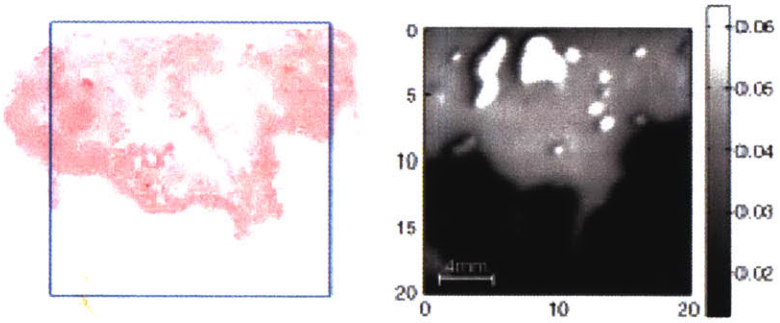

Figure 1.2.1 The demonstration of the correlation between a THz image (right) of a breast tumor and the corresponding histology section (left). The size and shape of the tumor in THz image match well with the histology section.

Figure 1.2.1 illustrates a biomedical application of THz imaging as a diagnostic tool. The imaging result shows that time domain imaging (TPI), which will be explained in detail later, can be a reliable technique to distinguish tumor, normal breast and even in *situ* disease (early stage cancer) in the experimental sample [12]. Actually, similar research can be traced back to the previous experiment done by Arnone et al. which showed contrast between muscle and fat in TPI[13]. Later TeraView also found a contrast

between healthy skins and basal cell carcinoma which commonly exists in skin cancer. These findings make TPI potentially a powerful non-ionizing diagnostic tool for the early detection of cancers.

Traditionally the sources used in time domain techniques for these applications have a small average power which is in microwatt range. Given the broad band over which this small power spreads, the average power over unit frequency range is even weaker, and limits the detection distance and speed. Additionally, resolution of the TDS technique is limited by the length of the delay stage which cannot be very long for practical applications. Furthermore, the bulky and expensive fs lasers used in TDS hamper the broad and portable applications of this technique. Thus a powerful, compact and continuous tunable THz source is highly desirable for biomedical applications.

1.2.3 Security applications

Similar with the biomedical applications, security applications of THz radiation are based on spectroscopic and imaging setup. These applications are based on the fact that many materials are semitransparent or transparent to terahertz radiation, such as typical clothing and package materials (Figure 1.2.2). Although these materials can be more transparent in microwave, THz radiation has a better resolution. This unique property makes THz radiation a powerful tool to disclose hidden objects which is demonstrated in Figure 1.2.2.

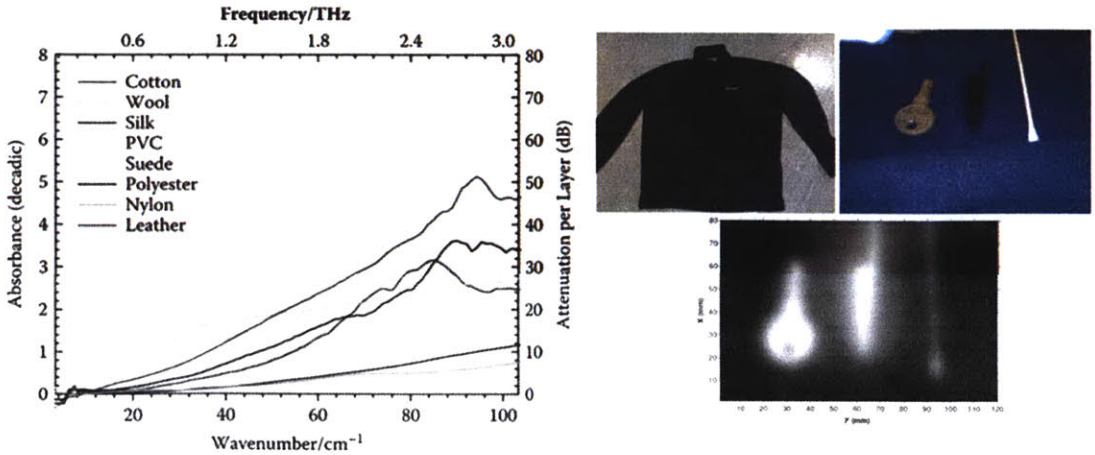

Figure 1.2.2 THz absorption spectra of several clothing materials (left) [14] and THz imaging through a typical jacket (right) [15]. The underneath objects were disclosed clearly.

Another example is illustrated in Figure 1.2.3. Letters of "MIT" written on a paper sealed in a paper envelope was disclosed by subtracting the background signal from the THz image [16]. In this demonstration, a 320 x 240 microbolometer focal-plane array was used to achieve a real time imaging with the illumination of a THz quantum cascade laser. In a measurement cycle, the THz QCL was first turned on to illuminate the envelope and frame 1 was recorded. Then the illumination was turned off and frame 2 was taken. Finally, the difference between frame 1 and 2 was displayed in order to remove the background signal. In the above example, the THz QCL was turned on and off to get the differential signal. Potentially, a continuous tunable THz source can be used in this situation to get much richer information by differentiate signals from multi frequencies.

Another important security application of THz radiation is to detect explosive material. Figure 1.2.4 plots the absorption spectra of two important explosive materials, both of which have clear spectral fingerprints in THz region. A setup to detect explosive materials behind a barrier was illustrated in part c of this Figure. In this setup, a distant mirror is used to reflect back the signal and the detected signal has pass through the sample and atmosphere twice. For safety purpose, this explosive detection requires remote sensing which needs a powerful and tunable THz source.

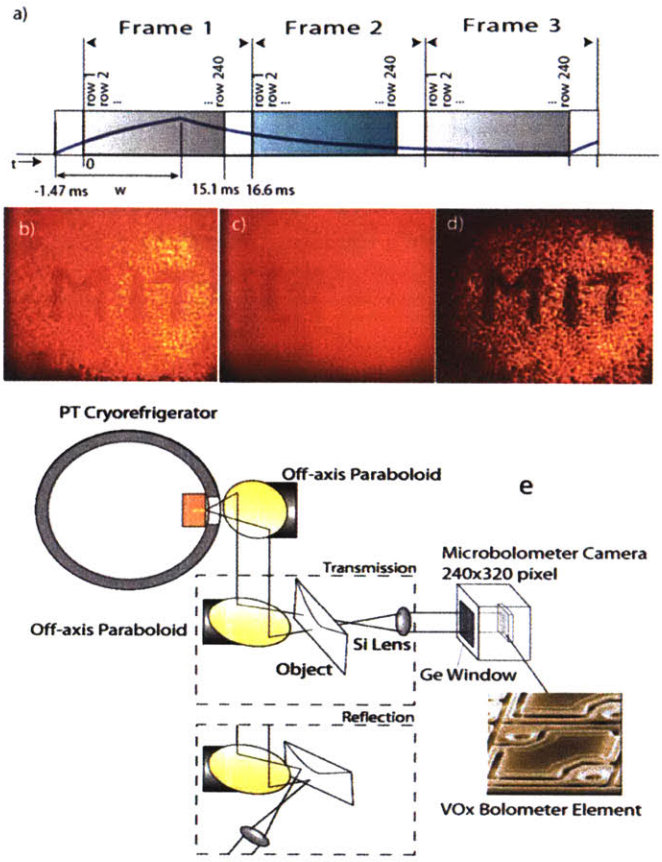

Figure 1.2.3 Part (a): solid trace shows signal/temperature time response to a QCL pulse, over a three frame differential sequence; a frame is composed of sequential row samples of the signal. A 1.47 ms delay exists between frames allowing the pulse to be started before the first row is acquired to allow heating. Part (b) corresponds to frame 1 with THz superimposed on infrared signal. Part (c) corresponds to frame 3: infrared signal with a small amount of residual THz signal. Part (d) corresponds to difference between frames 1 & 3, resulting in THz only signal; showing absorption of pencil inside an envelope. Part (e) illustrates the experimental setup [16].

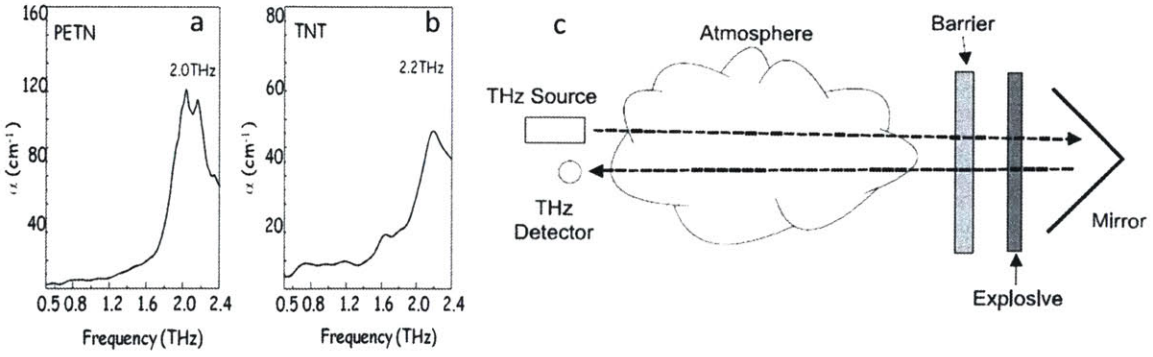

Figure 1.2.4 Part (a) and (b) show the absorption features of two important explosive materials PETN and TNT[17]. (c) Schematics of THz detection setup of explosives hidden behind a barrier material using a dual pass transmission geometry [18].

1.2.4 Industrial process

Additional to clothing materials, many other common materials that don't contain water or metals are relatively transparent in THz range. For instance, THz radiation can penetrate paper, dry wood, various paints, plastics and ceramic materials. This unique property makes THz radiation applicable in many industry processes. One of these applications is to characterize water content of newspaper print [19]. Another one is using THz radiation to detect small voids with the size and position information inside electric power cables[20]. High cost of THz system, however, hampers the further development of THz applications in industry processes.

1.2.5 Other applications

Besides the THz applications described above, there are several other interesting opportunities. For example, as a plasma fusion diagnostic tool, a narrow-band radiometer operating in THz frequency range can be used to measure the temperature of plasma core [21], and THz heterodyne imaging system was applied to separate fluctuated thermal electron noise [22]. In physics, THz spectroscopy is used to study molecule rotational transition, Rydberg transitions and excitons in solids. THz radiation was also applied to observe Anderson localization which is promising to develop random lasers. Additionally, THz communication was proposed because of its small antenna size and large bandwidth [23], and potentially data rates of tens of gigabits per second can be achieved [24]. THz radiation is further used to simulate radar system by scale down the object size [25][26].

1.3 THz generation and detection in time domain spectroscopy and imaging

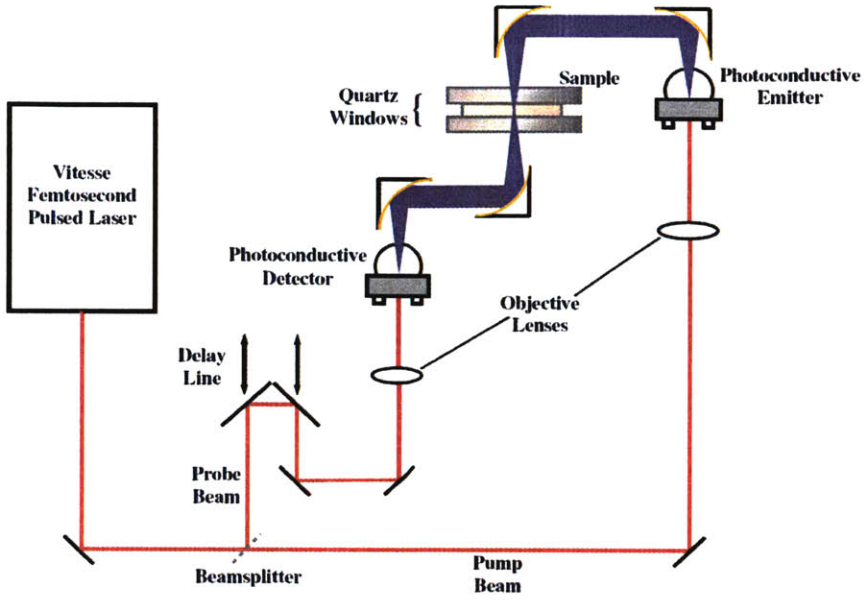

Figure 1.3.1. Schematic representation of a TPI spectra1000 [27]. A short pulse from femtosecond laser is split into a probe beam and pump beam by a beam splitter. Using a photoconductive emitter, the pump beam excites a THz wave which passes the sample. The transmission signal is detected by a photoconductive detector which uses a delayed probe beam as a reference.

THz time domain spectroscopy (TDS) and imaging are typical techniques used for THz biomedical applications. A commercially available system of this kind from TeraView is illustrated in Figure 1.3.1. In this TDS system, a Ti:Sapphire laser is used to generate a short pulse with ~ 100fs width and ~100MHz repetition rate. A portion of the beam is split and used as a reference in the detection stage. The other portion of the splitted pulse is focused by a lens and shined on a photoconductive emitter (Figure 1.3.2) which generates electron-hole pairs. These carrier pairs are accelerated by the large electrical field between the two electrodes. Then a THz pulse, typically from 0.1- 4THz, is radiated by the antenna from carrier relaxation. After this radiated THz pulse pass a sample sandwiched by quarts windows, a signal including the samples' spectroscopic information is sensed by a photoconductive detector which is gated by the reference signal inheriting from the original pulse mentioned earlier. This reference pulse is phase-shifted by a periodically varying delay line in order to create the time gate for a high signal to noise ratio (10000:1 at one THz) detection. The whole system is usually purged with nitrogen gas to reduce the water absorption due to its high sensitivity to the water vapor in the atmosphere. The detector and the emitter are assembled with hemispherical

lenses to efficiently collect or emit power. More detail of this kind of setup can be found in ref [28].

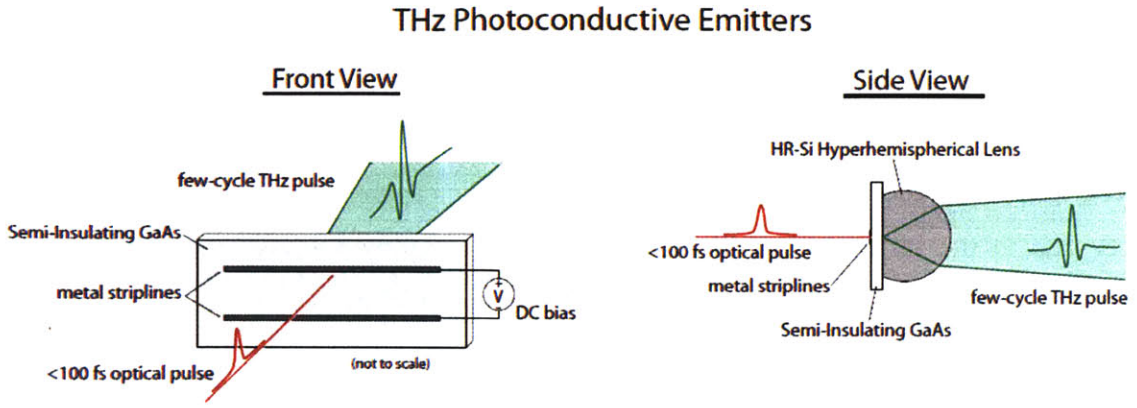

Figure 1.3.2 The schematics of THz photoconductive emitters[29]. The metal striplines on semi-insulating GaAs are biased to provide a large electric field. The current excited by fs optical pulse relax fast to generate THz pulses. The photoconductive detector has a similar structure.

It is worth discussing more about the THz detection technique used in this system. THz can be detected by a bolometer which is essentially a heat detector operating in cryogenic temperature. However, it is not suitable to THz TDS because it cannot measure the electrical field over time. Instead, photoconductive and electro-optical detection technique can be applied in TDS systems. As described earlier, a portion of the short pulse of infrared light from Ti:Sapphire laser is fed to the detector and arrives at the same time with the THz pulse from the generator. The electrical signal produced by the detector depends on the electrical field of the THz pulse at the time when detection infrared pulse arrives, which is varied by a delay line. This detection is coherent, and incoherent radiation does not come into play. Additionally, because of the narrow time window, the noise contribution is very small. Thus high signal-to-noise ratio, up to70dB, can be achieved with one minute averaging time.

In spite of the similar setup, there is a difference between photoconductive and electro-optical detection. In photoconductive detection, the antenna electrodes are biased by the electrical field of THz radiation. So the current, generated by THz electrical field, represents the strength of the THz pulse. In opto-electrical sampling, the polarization of the detection pulse is changed by a birefringent martial whose birefringent effect is

proportional to the electrical field of THz pulse. Finally, the changed polarization is measured by polarizers and photodiodes.

THz spectroscopy has broad applications in biomedical fields because THz range (0.1THz to 5THz) covers the vibrational modes of many biological and chemical molecules. For instance, THz TDS has demonstrated the capability to diagnosis the breast cancer due to the different optical property between healthy fibrous breast tissue and breast cancer [27]. Additionally, THz radiation can probe the different vibrations corresponding to collective molecule vibration and unfolding of molecule subdomain. Thus THz spectroscopy has the capability not only to differentiate the different materials, but also to explore the spatial structure of the molecules. For example, THz TDS instruments can detect different DNA structures by dielectric resonance (phonon absorption), and the twisting and deformation of the double-helix structure in DNA[30][31], enriching biologists' toolbox.

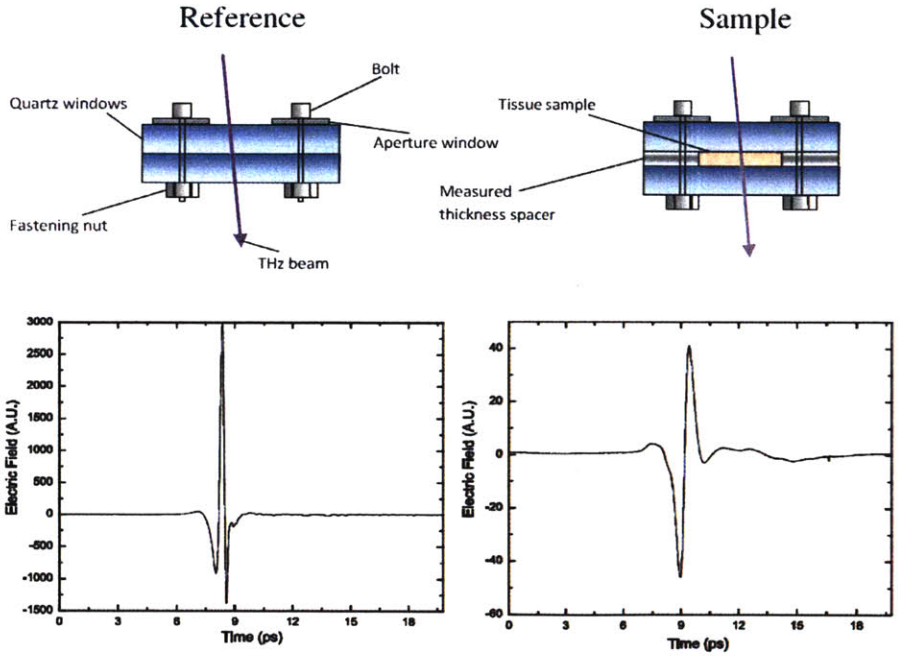

Figure 1.3.3 The upper figure is the illustration of the sample holder to measure the reference and sample pulse. The lower two plots are typical respective pulses [27].

THz pulse imaging (TPI) was first introduced by Hu and Nuss in 1995 [32]. The system is similar to TDS and full images are constructed by scanning beam over the objects. [32][33][34]. This technique is especially attractive for biomedical application because of

unique features of THz radiation. Compared to X-ray, in addition to its non-ionization feature mentioned earlier, THz radiation can provide a better contrast for soft tissue because of its sensitivity to polar materials, such as water. Besides, in TDS system the coherent detection measures both the phase and amplitude of temporal electrical field, which enables further extraction of the refractive index by Fourier transformation of the signal. Moreover, the spectroscopic information in THz region, such as rotational and vibrational transition of molecules, contributes to another dimension to distinguish different materials.

Due to the strong water absorption, TPI operating in reflective mode has more applications than transmission mode for biomedical samples. When a THz pulse is incident on a biological sample with various interfaces, a train of reflected pulses from different interfaces will be detected. According to the amplitude and the detection time recorded precisely, the information of internal dielectric profile can be extracted. This forms the foundation of THz 3D imaging for optically opaque material [35][36][37][38].

1.4 Quantum cascade lasers (QCLs)

The concept of quantum cascade laser was raised by R.F. Kazarinov and R.A. Suris [39] in 1971, and first demonstrated by Jerome Faist and Federico Capasso et al. in Bell Lab [40]. QCL is a semiconductor laser mainly covering mid- and far-infrared frequency range. Compared with the traditional interband semiconductor lasers, in which photons are generated through the recombination of electron-hole pairs in active region, QCL is a unipolar device in which laser emission is achieved through electron intersubband transition in cascaded repeated stacks of multiple quantum wells, termed "module", of a semiconductor heterostructure. Tens and even more than one hundred of these modules cascade sequentially and formed a quantum cascade laser. Thus the operation voltage of quantum cascade laser can be easily as high as ~10 volts due to a large number of modules.

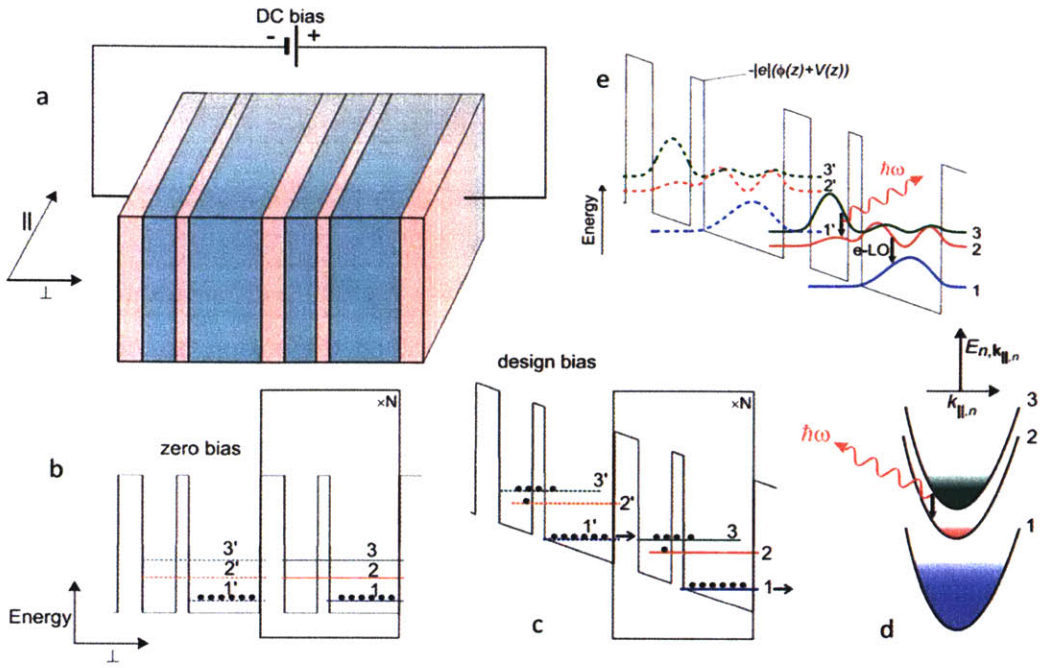

Figure 1.4.1 Illustration of the concept of the quantum cascade lasers. (a) Schematics of a module of QCLs. (b) Schematics of the conduction band diagram with zero bias. The energy levels are conceptualized as straight line for simple illustration. The black dots represent electrons in the quantum well structure. (c) The conduction band diagram at the design bias. Level 1 is aligned with level 3 under this bias. (d) The electron distribution in k space. The three bands correspond to the ones in part b and c. The population inversion is demonstrated in this figure. (e) A typical band diagram with simulated wavefunction illustrated.

Schematics of the physical structure and band diagram of QCL are illustrated in Figure 1.4.1. As shown in part a, the basic module of QCLs are composed of alternated barrier and well layers (AlGaAs/GaAs in the device used in this work). A typical thickness of a QCL's layer is in the order of a few nanometers. Thus the multiple quantum wells are usually grown by advanced growth techniques, such as molecular beam epitaxy (MBE) or metal organic chemical vapor deposition (MOCVD) to satisfy the requirement of precise thickness. The corresponding energy band diagram without a voltage bias is plot in part b of Figure 1.4.1, in which the basic three functional energy levels are shown. At thermal equilibrium, all electrons stay in state 1 which has the lowest energy. Under the design bias, the band is tilted along the direction of electrical field. State 1', called injector, is aligned with the state 3, which is the upper radiative lasing state. The population inversion is achieved between upper and lower radiative state (3 and 2 respectively) by designing a fast depopulation channel for state 2, as illustrated in part d. In each module a photon is generated when an electron transits from state 3 to 2. After

that, the electron drops to state 1 and is ready to be injected to the upper radiative level of the next module, which is the beginning of a new cycle. Thus the lasing frequency is determined by the energy difference between state 3 and 2 which can be engineered by the quantum well structure. Theoretically, for a QCL with many modules, one electron should be able to emit multi photons. This results in a greater-than-unity differential efficiency which is a key property of quantum cascade lasers. It is worth noticing that the energy space between different energy levels play more important role than the absolute energy. In the design of quantum cascade lasers, these energy differences between states can be precisely adjusted by engineering the thickness of quantum barriers or wells, and are directly related to the characteristics of the transport channels which determine the device performance. Due to the similarity between QCL's quantum level system and atomic states, the design concept of QCL is described as "designing of artificial atom", quoted from Professor Qing Hu. Compared to the natural atoms, the "atomic energy level" of QCLs can be artificially designed by carefully selecting the layer thickness.

The first QCL was designed based on GaInAs/AlInAs material system and operated at a wavelength of 4.2μm. It can only lase at cryogenic temperature in a pulsed mode. After sixteen years of development, quantum cascade laser has become the dominant mid-infrared laser source, due to a large performance improvement, and extended its spectrum coverage into terahertz range. The development history was reviewed by Capasso et al. [41] and Faist et al. [42]. The device structure of most mid-infrared QCLs has quantum well active region imbedded in a waveguide, and the laser resonator is mostly of DBR or DFB type. At liquid nitrogen temperature, it is easy to get multiple watt power from mid-infrared QCLs. Even at room temperature, more than one watts of power has been achieved with a CW operation [43][44]. Recently, device with >50% wall plug efficiency have been demonstrated [44][45] although only for cryogenic temperatures.

1.5 THz QCLs

Although mid-IR QCLs were first demonstrated in 1994 [46], THz QCL was not born until 2001. Breakthrough was first achieved by Köhler *et. al.* in 2001[47] based on a

chirped-superlattice design. Shortly after that, different designs of THz QCLs were demonstrated by Rochat *et. al.* [48], and Williams *et. al.* in 2002 [49]. It is worth noticing that the later design based on the resonant phonon depopulation scheme currently holds the record of the maximum operation temperature (199K) and highest CW power of 248mW [50] for THz QCLs. A similar design was used in the work of this thesis.

Although the basic design concepts of THz QCLs can find their counterparties in mid-IR QCLs, it is still very challenging to achieve THz radiation in QCLs even in cryogenic temperatures for two reasons. Firstly, the small energy difference (<20meV) between the upper and lower radiative states, corresponding to the THz photon energy, makes it difficult to selectively inject or depopulate the desired states. Secondly, due to the free carrier absorption which scales with square of wavelength (λ^2), low loss waveguides is difficult to design and implement for longer terahertz wavelengths, and one cannot use dielectric guiding due to the requirement of impractically thick cladding layers (~10's of microns).

Repeat 183 times	GaAs	undoped	76.3 A (27 ML)
	$Al_{0.15}Ga_{0.85}As$	undoped	22.6 A (8 ML)
	GaAs	undoped	73.5 A (26 ML)
	$Al_{0.15}Ga_{0.85}As$	undoped	39.6 A (14 ML)
	GaAs	1.9×10^{16} cm^{-3}	162.4 A (57.5 ML)
	$Al_{0.15}Ga_{0.85}As$	undoped	32.5 A (11.5 ML)
	GaAs	undoped	91.8 A (32.5 ML)
	$Al_{0.15}Ga_{0.85}As$	undoped	48.0 A (17 ML)

Figure 1.5.1 The schematics of quantum well stack of a design of FL183S. The doping level was listed in the second column. The thickness in terms of Armstrong and monolayer is illustrated in the third column. The module shown in the figure are repeated for 183 times in the real structure.

The schematics of quantum well stack of design FL183S, which is chosen to implement THz tunable wire QC lasers, are shown in Figure 1.5.1. $Al_{0.15}Ga_{0.85}As$ and GaAs are used as barrier and well materials, respectively. A delta doping is implemented in the thickest GaAs layer to minimize the free carrier absorption while providing enough electrons to generate photons. The total QCL active region is ~10 μm thick, consisting of 183 modules cascaded together.

The conduction band diagram of two modules at design bias, plot in Figure 1.5.2, illustrates the electron transport channel. Driven by an electrical field, electrons flow from the right to the left and the quantum states in the right module are marked with apostrophe. First, the electrons were injected into the upper radiative state 5 from a doublet injector composing state 1' and 2' through a thick injector barrier indicated in Figure 1.5.2. However, electrons can be undesirably injected to the lower radiative state 4, resulting in a non-unity injection efficiency η (<1). Compared with ideal situation with unity injection rate, this inefficient injection requires longer upper state life time in order to achieve population inversion in sub threshold region[51], which is described by equation

$$n_5 - n_4 = \frac{J}{et}\left[\eta\tau_5\left(1-\frac{\tau_4}{\tau_{54}}\right)-(1-\eta)\tau_4\right] \tag{1.5.1}$$

where n is population of the states, J is current density and e is electron charge, t is thickness of one module and τ is state lifetime. Above threshold, η is factored into the slope efficiency and decrease the value of this efficiency, demonstrated by the equation:

$$\frac{dL}{dI} = \frac{h\omega}{e} N_{mod} \frac{\alpha_m}{\alpha_m + \alpha_w}\left[\frac{\eta\tau_5\left(1-\frac{\tau_4}{\tau_{54}}\right)-(1-\eta)\tau_4}{\tau_4+\tau_5\left(1-\frac{\tau_4}{\tau_{54}}\right)}\right] \tag{1.5.2}$$

where L is optical power, I is current, N_{mod} is the number of modules, α_m is the mirror loss, α_w is the waveguide loss and τ represents lifetime of different states.

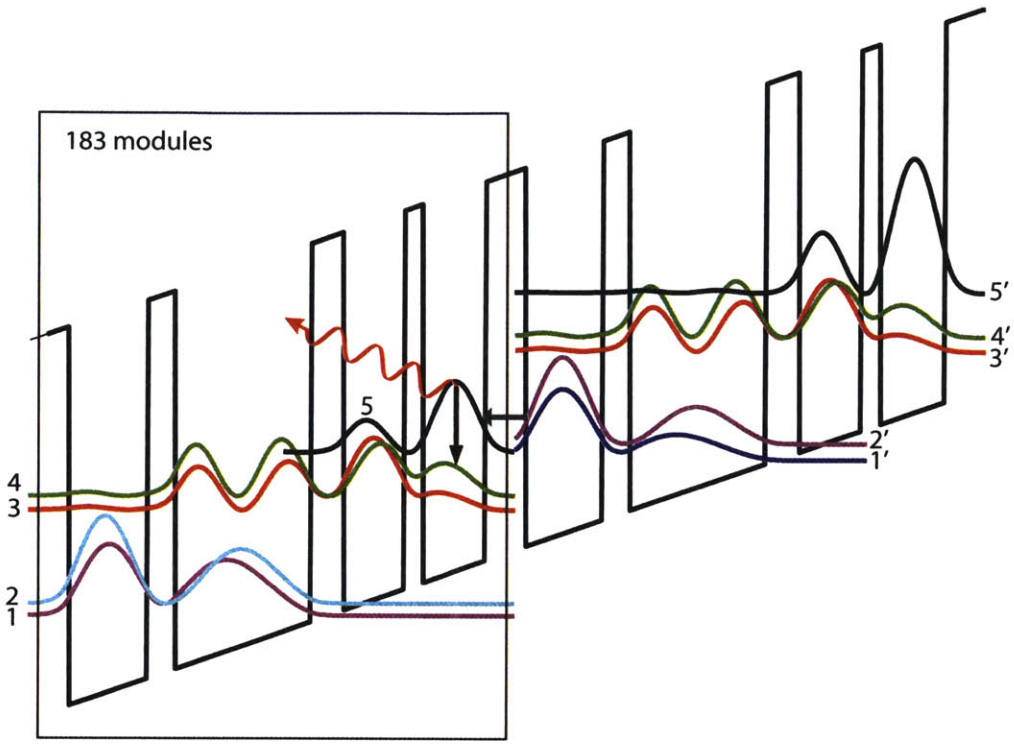

Figure 1.5.2 Schematics of the conduction band diagram of design FL183S. The basic module is repeated for 183 times. This graph included two modules in order to show the transport channel in which electrons flow from right to left direction. Apostrophe sign is used to differentiate the corresponding quantum states in the two repeated modules. An electron is injected into upper radiative state 5 from 1' through the injector barrier indicated by an arrow. Then the electron drops to state 4 by emitting a photon. Through a resonant tunneling, it transport to state 3 which is depopulated by a phonon-assisted depopulation scheme. After electron drops to state 2, it resonantly tunnels into state 1 where it is ready to be injected into the next module.

1.6 Traditional tunable THz source

As discussed in the section 1.2, tunable THz sources are highly desirable in most THz applications. Indeed, a THz tunable laser was described as "A wrench of wavelength"[52]. In spectroscopic applications, the importance of a tunable THz source lies in its capability to provide a convenient access to a broad spectrum at desired and precise wavelengths, which enables the collection of more spectroscopic information with a single device. For instance, using tunable THz narrow band source to scan the corresponding frequency range, the narrow spectroscopic features (~MHz) [53][54][55] of multiple gases and broad spectral features of different solids (>100 GHz) [56][57][58] can be extracted to identify the target contents. This frequency tunability is also a handy tool for THz

imaging application because the spectroscopic information can be converted to depth information as the case of swept source in optical coherence tomography[59][60].

Because of broad applications of THz tunable sources, a significant amount of research effort has been devoted into this field. In the RF side, Backward-Wave Oscillaor (BWO) [61] can provide up to tens of mW power of tunable narrow band THz radiation with up to 1.45 THz [62]. Due to the requirement of large magnetic field and a vacuum environment, however, the necessary equipment is bulky and expensive. In the optical domain, external cavity tunable quantum cascade lasers have been demonstrated although the performance is unsatisfactory for several reasons which will be discussed later. Additionally, non-linear generation and photo mixing are important techniques to generate tunable THz radiation. Before we dive into the topic of THz wire laser, it is necessary to briefly review the traditional tunable THz sources. The existing tunable QC lasers will be introduced in chapter three.

1.6.1 Tunable THz sources achieved based on the parametric method

Many research efforts have been carried out to generate tunable coherent THz radiation based on nonlinear parametric methods[63][64]. In the late 1960s and early 1970s, Pantell and Puthoff et al. achieved efficient and widely tunable THz generation [65][66][67] from the tunable light scattering by the long-wavelength side of the A_1-symmetry softest mode in $LiNbO_3$ [68].

Although other nonlinear materials, such as GaP et al., are also used, $LiNbO_3$ is used as an example to demonstrate this type of generation. Stimulated by the near infrared pump photon, a near-infrared Stokes photon (idler) is created at the difference frequency between the material vibrational mode and the pump photon. Meanwhile, the THz wave (signal) is generated by the parametric process due to the nonlinearity contributed from both electrons and material vibration which will be discussed in the next paragraph. The frequency tuning was enabled by changing the propagation direction. It is worth pointing out that due to $LiNbO_3$'s large absorption coefficient and large refractive index in THz, most generated THz photons are absorbed or trapped inside the crystal. These problems

were solved by introducing the monolithic grating coupler, the arrayed Si-prism coupler, doped crystals, and injection seeding [68], which resulted in much better performance.

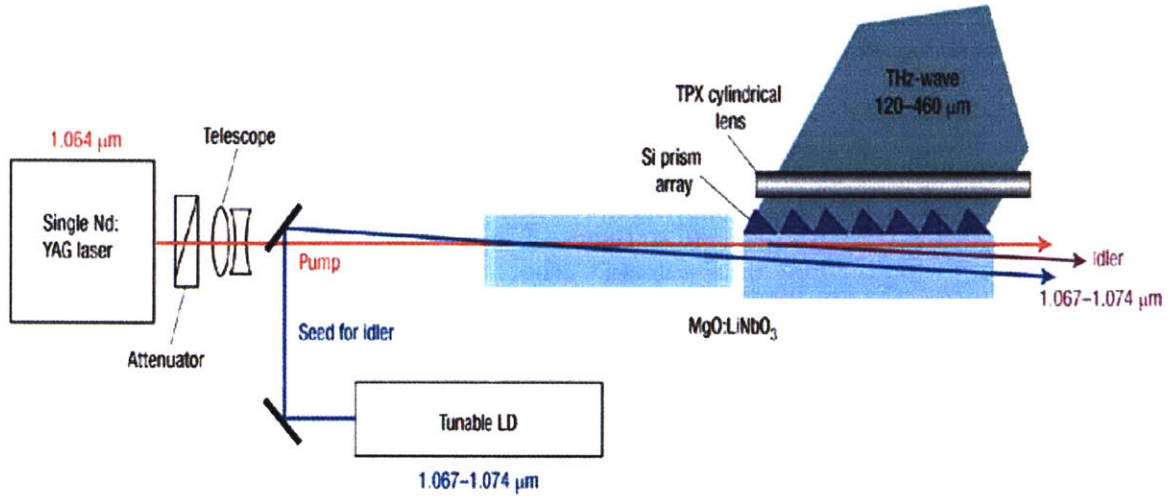

Figure 1.6.1 (IS-TPG). The pump laser was a single longitudinal mode Q-switched Nd:YAG laser (1.064 μm), and the seed for the idler was a c.w. Yb-fibre laser (1.070 μm) or tunable laser diode (1.067–1.074 μm). Generated THz waves in $LiNbO_3$ are coupled with a silicon prism array and emit into free space through a TPX (poly-methyl-1-pentene) cylindrical lens.

A typical injection-seeded THz–wave parametric generator (IS-TPG) is illustrated in Figure 1.6.1. First, photons with wavelength of 1.064μm are pumped into the crystal and interact with the lowest infrared- and Raman-active transverse optical phonon mode, termed A_1-symmetry modes, to form polaritons. At low frequencies, the polaritions behave like a photon, and a near-infrared idler photon (ω_i) are created parametrically from a near-infrared pump photon (ω_p) (energy is conserved in the process $\omega_p = \omega_T + \omega_i$ (p: pump; T: THz; i: idler)). The involved microscopic physical process is also very interesting. The pump photons excite the electronics dipole moment of the electron cloud outside of the atom nuclei, which is the origin of the second order nonlinear effect. Next, some of the energy absorbed by the electrons is transferred to the ions (nuclei) which begin to vibrate (phonons are generated). This leads to ionic dipole moment (stokes process) which is the origin of the third order nonlinear effect. Eventually, the electronic dipole moment is modulated by ionic vibration. Thus three photons, pump, stokes (idler), and THz (polariton), are involved into this parametric scattering process.

After THz wave is generated, a monolithic grating coupler, fabricated on the surface of $LiNbO_3$, is used to couple the THz radiation out, as shown in the Figure 1.6.1. Through this design, thousands of time higher efficiency, compared to the traditional method, was demonstrated. Finally, a seed for the idler is added into the system to enhance the power and narrow the line width. Through this configuration, a wide tunability from 0.7-2.4 THz was accomplished. The THz emission line width is less than 100MHz. The peak power produced by the system is as high as 1 watt, which is impressive. Furthermore, this system is capable to continuously tune frequency at high spectral resolution in 4 GHz segments.

Although this technique has demonstrated impressive power and large tuning range, it has several disadvantages for practical applications. First, its system is bulky and expensive. Secondly, to tune frequency, the incident angle of the pump beam has to be changed mechanically, so this mechanical process limits its tuning speed. Thirdly, the line width is limited by Fourier limitation and difficult to further narrowed, which might prevent it from the application requiring high spectral resolution.

1.6.2 Tunable THz sources based on the photomixing method

There are several ways to generate tunable THz radiation through optical mixing. For instance, THz radiation can be generated by difference mixing of the two laser beams of frequencies $\nu_+ = \nu_0 + \nu_{THz}/2$ and $\nu_- = \nu_0 - \nu_{THz}/2$ in a nonlinear material with a large second-order susceptibility. Termed as "optical rectification", this process requires NIR or IR power of several hundred W/cm^2 in order to generate a reasonable THz power. Usually only operation in a pulsed mode is achieved because CW operation requires phase matching over long distance. Additionally, there are several other limiting factors in high frequencies, such as transit time or lifetime roll-off, antenna-device RC rolloff, current screening and blocking, and heat dissipation [69]. To overcome these difficulties, various realizations, such as photoconductive and p-i-n diode based photomixers, are implemented.

CW or quasi-CW THz radiation is created by the THz-periodic generation of electrons and holes in semiconductors from absorption of two interfering laser beams of frequencies $\nu_+ = \nu_+ + \nu_{THz}/2$ and $\nu_- = \nu_- - \nu_{THz}/2$. The THz periodic carrier generation results in the intensity modulation from the interference of the two beating laser beams. There are two emission methods for this kind of generation, large area emitter (LAE) and antenna-based emitter (AE). For LAE, illustrated in part (a) of Figure 1.6.2, the THz emission is from the acceleration of the individual photo-generated carriers in a large area. Alternatively, in AE method, THz radiation is generated by the collective current in a very small area and collected by an antenna. In both cases, the tunability comes from the tuning of the original input frequencies. There are two basic concerns in designing antenna based emitters. First, the finite capacitance of the device is parallel to the radiation resistance of the antenna, yielding an "RC roll-off." The finite transport time of the photo-generated carriers creates a "transport-time roll-off." The best result so far has been achieved with the p-i-n–based "uni-travelingcarrier" (UTC) devices which have demonstrated 20mW at 100GHz [70] and 25 uW at 0.914Thz [71][72]. The other concern is that the antenna design should maximize the output power at the desired frequency by using a proper geometry.

Through much research efforts, the photomixing technique has achieved significant improvement. In the pulse mode, record power levels of 1.5 mW average power and conversion efficiencies as high as 2×10^{-3} have been obtained [73]. The THz linewidth basically depends on the linewidth of the lasers. Using commercial telecom lasers with linewidths of a few MHz, a HWHM linewidth of the THz signal of ~10 MHz was achieved [74]. Regarding the tunability, photomixers are easily continuously tunable over 1.0 THz, usually limited by the drive lasers (when using DFBs or similar laser diodes).

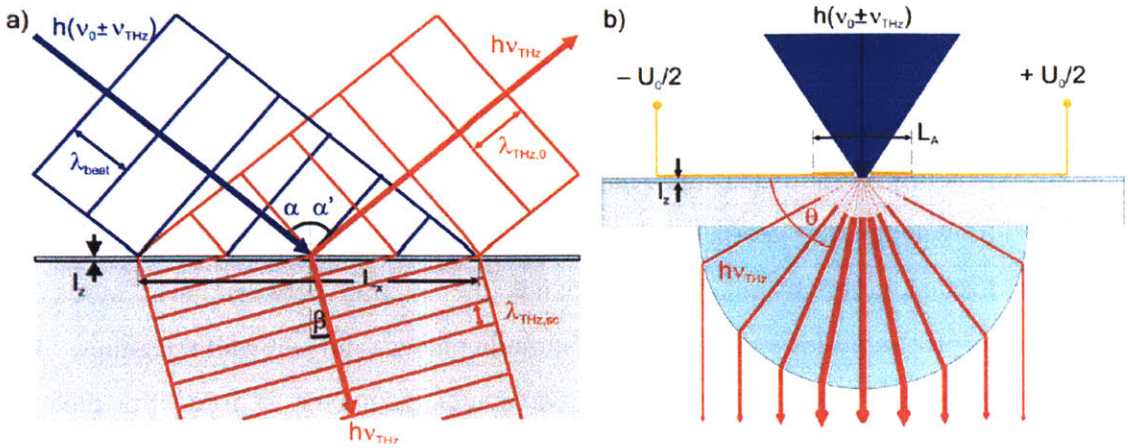

Figure 1.6.2 [69] Within a thin layer (thickness~Lz), the periodic change of free electron and hole concentration are from the beating between two collimated beams with frequencies ν+= ν_0+ ν_{THz}/2 and ν-= ν_0- ν_{THz}/2. Part a is the THz generation scheme with large area emission (LAE). The transverse dimensions of this LAE (L_x and L_y) are larger than the THz wavelength. According to Snell's law, the generated THz power is radiated into air partially and others are radiated into the semiconductor. Part b illustrates the THz generation with antenna emission method. With the two focused laser beams and an external bias U_0 between the electrodes of antenna with size L_A, the generated THz radiation is mostly fed into the semiconductor and collimated by a hyperhemispherical (silicon) lens.

1.7 Terahertz waveguide

It is challenging to design a low loss Terahertz waveguide by deploying traditional dielectric guiding due to the large free carrier absorption which is proportional to the square of the wavelength (~λ^2) and the required impractical cladding-layer thickness (>10μm). Furthermore, in the frequently used GaAs/AlGaAs material system, GaAs substrate provides no mode confinement since it has a higher refractive index than AlGaAs. So THz waveguide should use a novel mechanism or thin films to confine the THz mode, and can minimize the overlap between the THz optical mode and the doped region. The existing THz waveguides typically use different forms of Plasmon effect to achieve THz mode confinement.

Before the discussion of different types of THz waveguides, it is worth summarizing the important parameters describing THz waveguide in general. First, the lasing threshold g_{th}can be expressed as:

$$\Gamma g_{th} = \alpha_w + \alpha_m \tag{1.8.1}$$

where Γ is mode confinement, α_w and α_m are waveguide and mirror loss respectively. Generally speaking, Γ indicates the overlap between mode and gain medium which is related with waveguide geometry and confinement mechanism. The waveguide absorption loss is given by α_w which depends the overlap between THz mode and different absorptive sources e.g. doped layers, metal players and sidewall roughness. This α_w can be changed by designing specific waveguide geometry to force the mode to propagate in lossy region which will be discussed later. The other loss term is the mirror loss α_m due to the finite mirror reflectivies and can be written as:

$$\alpha_m = -\ln(R_1 R_2)/2L \tag{1.8.2}$$

where $R1$ and $R2$ are facet reflectivity, and L is cavity length. The mirror loss of a typical 2-mm-long Fabry-Perot ridge laser is ~6cm^{-1}. But this value can be sensitive to the waveguide geometry as described in ref [75].

The first THz QC laser[47] uses a semi-insulating surface plasmon (SISP) waveguide whose schematic structure is shown in Figure 1.7.1. In this design, a GaAs/AlGaA active region is sandwiched by a top metal layer and a highly doped GaAs thin layer in the bottom. The doping level of this GaAs thin layer is high enough to ensure that the plasma frequency is above lasing frequency, so that this n-doped layer has a negative dielectric constant in the frequency range below 5 THz. As illustrated in part b of Figure 1.7.1, a surface plasmon mode is attached to this n-doped layer and extends into the semi-insulating substrate significantly, resulting in a relatively low mode confinement (typically < 50%). As a result, this relatively large mode distribution enables a relatively low divergence beam patterns. Another result of this large mode is a low reflectivity (32%) at a cleaved facet, leading to a large output power, due to the relative small mode mismatch between the cavity mode and free space plan wave. The good beam pattern and high power of SISP waveguide make it a good THz source for imaging applications which require illuminations of multi-element direct detectors [76].

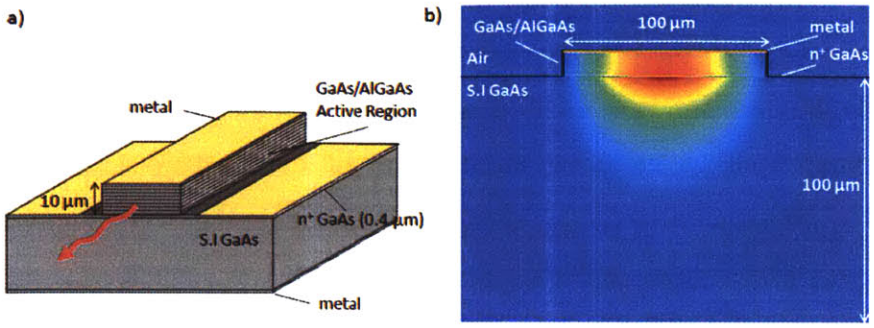

Figure 1.7.1 (from [1]) (a) Schematic structure of a THz semi-insulating surface Plasmon waveguide. A GaAs/AlGaAs active region is sandwiched by a top metal layer and a highly doped GaAs thin layer (400 nm, silicon doped at 3×10^{18} cm^{-3}) attached to semi-insulating GaAs substrate. (b) A typical mode of semi insulating surface plasmon waveguide. Mode confinement is provided by the top metal and the highly doped thin layer which has negative index. The thickness of the highly doped thin layer is optimized to achieve a better trade-off between mode confinement and mode loss.

On the other hand, the drawback of this kind of waveguide is obvious and mostly related with low mode confinement. As we can see from equation 1.6.1, the waveguide and mirror loss are "amplified" by a small confinement factor Γ. This essentially means that more gain is required to overcome the material loss because modes "see" less gain medium. Combined with gain degradation with increased operation temperature, this low mode confinement leads to limited maximum operating temperatures which is up to ~105K for pulse mode and ~40K for continuous wave (CW) mode [50].

In contrast to the SISP waveguide, a metal-metal (MM) waveguide, first introduced to THz QCL design by Professor Qing Hu's group [77] have a near unity confinement factor, Γ. This is mostly because of its mode confinement scheme achieved by two metal lays both on and under the gain medium (part (a) of Figure 1.7.2), which is similar to microstrip transmission line. Essentially, the mode of the MM waveguide is also a surface plasmon mode. Distinguished from the SISP modes, the extinction length of MM waveguide mode is very different in metal (~20-30nm for f>1THz) and gain medium (~1mm at 3THz). Thus, in 10um thick (compared to ~1mm extinction length in GaAs) gain medium, an almost uniform mode distribution along the vertical direction (part b of Figure 1.7.2) results in a mode confinement close to unity, which further leads to a low threshold gain. But the mode is highly confined in a deep subwavelength dimension in vertical direction, resulting in highly divergent beam patterns exceeding 180° [78], and a

high facet reflectivity of 70% to 90% due to a large impedance mismatch between guided and free space modes. In the case of wire lasers, this divergent beam pattern is further exacerbated by the deep subwavelength dimension in the transverse direction which will be discussed later. Thus typically the output power of a Fabry-Perot laser is below ~10 mW limited by this large reflectivity. Additionally, avoiding the overlap between cavity modes and highly doped layer, the waveguide loss of MM waveguide was measured as ~16cm^{-1}[79] and smaller compared to SISP waveguide. Combined with large mode confinement, the smaller mirror and waveguide loss result in a higher maximum operating temperatures of 199 K in pulsed operation [77]. It is worth pointing out that the value of facet reflectivity is a function of wavelength and waveguide geometry [75], which is every important for the discussion of wire laser in the later chapters.

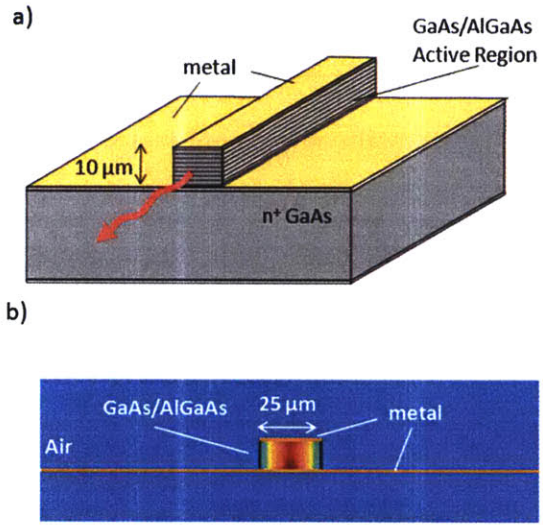

Figure 1.7.2 (a) Schematics of metal-metal (MM) waveguide. A top and bottom metal layers enclose QCL active region based on GaAs/AlGaAs material system. The waveguide is attached on a n$^+$ GaAs substrate for convenient electric bias. (b) THz optical mode in MM waveguide. Near uniform mode along vertical direction results in unity optical confinement which is similar to microstrip transmission line.

It is more meaningful to put our discussion of THz waveguide into the context of this thesis topic, tunable THz QCLs. Ideally, tunable QCLs prefer single mode operation which requires a robust mode selection mechanism. The mode discrimination is achieved by differentiating the threshold gain among cavity modes. From equation 1.7.1, it can be seen that, there are three parameters, mode confinement factor, mirror and waveguide losses, which can be played to achieve more robust mode discrimination. In this thesis,

the discussion will be focused on engineering these three parameters to realize tunable THz QCLs. As to be discussed later, by narrowing down the waveguide width to deep subwavelength size, the mode confinements of different order of lateral modes are differentiated significantly. Additionally, the mode discrimination can be obtained by different mirror loss enabled by a first order DFB structure. Furthermore, the waveguide loss can be engineered by introducing side connectors to the waveguide which will be discussed in the later chapter.

2 Terahertz Wire QC Lasers

2.1 Introduction and the previous work

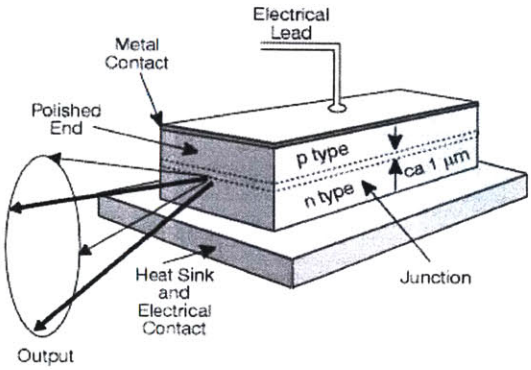

Figure 2.1.1 (From [80]) Schematics of a typical semiconductor diode laser.

Traditionally, a semiconductor laser is featured as a ridge structure illustrated in Figure 2.1.1. In the longitudinal direction, photons will be bounced back and forth between two polished ends and get amplified. Usually, the lateral size of lasers in telecom or visible frequency regions is larger than or at least comparable with the wavelength. So most of the lasing mode is confined in gain media and cladding material and does not see much external environment. Fig 2.1.2 (a) illustrates a typical mode profile in the cross-section of a QCL in mid-infrared range.

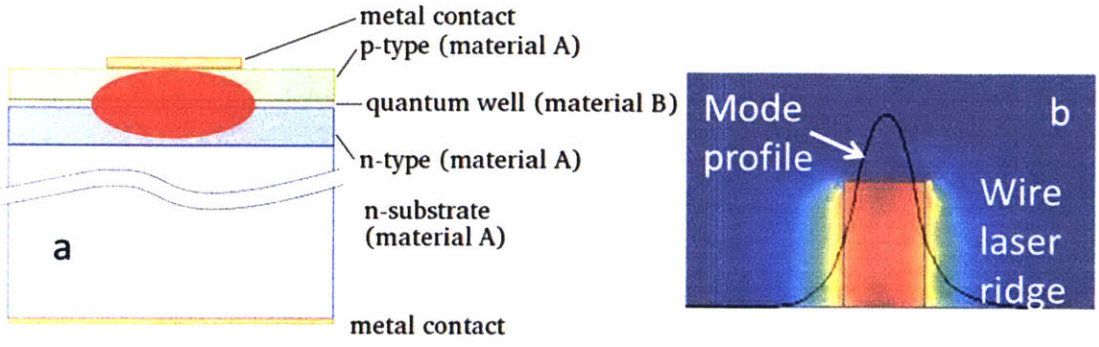

Figure 2.1.2 Schematic mode profile of a traditional semiconductor laser (part a [81]) and a typical wire laser (part b). In a traditional semiconductor laser, the mode is highly confined in the active region whose dimension is larger than the wavelength. In contrast, the waveguide width of a wire laser is much smaller than the lasing wavelength, which leads to a special mode which has a large portion of mode propagating outside the laser core.

A wire laser, which generally refers to miniaturized lasers with deep sub-wavelength dimensions in the lateral directions, was proposed in 1995 by J.P. Zhang [82] et al. to study the large enhancement of stimulated emission in a waveguide with very small optical volume. The driving force behind the development of wire lasers, or more generally nanowire lasers, is the mismatch between the silicon based microelectronic devices and the compound-semiconductor based optoelectronics. This size mismatch can be a critical problem if photonics need to be integrated with photonics [83]. After the first demonstration, this concept has been further developed in several researches of nanowire lasers or some other deep-subwavelength laser cavities[84][85][86][87][88]. The deep subwavelength cavity of wire lasers also enables a significant part of mode propagating outside of the waveguide, which is illustrated in Fig 2.1.2b. Usually, this leads to small mode confinement and is generally considered as a drawback since it can cause an increase of the lasing threshold. Another unique property of wire lasers is the very divergent (>40^{o}) far field beam pattern due to deed subwavelength apertures[83]. These researches were often taken in a telecom wavelength (~1.55μm) which requires nanofabrication techniques to demonstrate the wire laser concept (~100nm). This poses a fabrication challenge. In a contrast, a wire laser in THz region [88] can be a good choice to study the effect of subwavelength cavity because it only requires a deep subwavelength of ~10μm, which is easy to fabricate. The THz wire laser not only demonstrates the general properties of traditional wire lasers, but also has its unique features which will be discussed in this chapter.

Demonstrated in metal-metal waveguide, the most prominent feature of a THz wire laser is the distance its mode extends outside the laser core. These features originate from the wavelength of THz which spans from 30um to 300um, which enables an evanescent which vanishes at ~10um distance from the laser core. Additionally, the unique metal-metal waveguide of THZ QCLs allows a relatively strong mode confinement even in a deep sub-wavelength waveguide which ensures a reasonable lasing performance. Besides, THz wire laser has even larger beam divergence which can be modeled as the beam pattern of point sources in the two facets. At the same time, given the similarity between

the microstrip transmission line and MM waveguide, the analyzing methods deployed in THz region can be applied to study this THz wire laser intuitively.

In this chapter, we will discuss the different aspects of THz wire laser as well as several intuitive analyzing tools. Following the electromagnetic properties of the MM waveguide, the mode confinement, the facet reflectivity and the beam patter will be discussed.

2.2 Surface-Plasmon electromagnetic modes

Traditional wire lasers suffer from a poor mode confinement. A surface-plasmon polariton resonance was proposed to improve the mode confinement of nanowire lasers. As introduced in chapter one, THz QC lasers have two kinds of waveguides- surface plasmon semi insulating waveguide and metal-metal waveguide. It is desired to maintain the lasing performance while miniaturizing lateral size in designing a THz wire laser. THz wire lasers based on SISP waveguide can suffer from a poor confinement factor. Thus THz wire lasers use a metal-metal waveguide to achieve a double surface-plasmon mode which has a strong confinement.

Plasmon is collective oscillations of free electron gas density. Similar with quantization of electromagnetic wave and mechanical vibrations as photon and phonon, the plasmon is a quantum of plasma oscillation. Surface plasmon occurs and is confined at the interface between positive dielectric material and a negative one. Surface plasmon is involved in surface enhanced Raman Spectroscopy, explaining abnormal diffraction from metal grating and so on. Strongly interacting with external electromagnetic wave, it results in a polariton which is called surface plasmon polariton (SPP). Thus EM wave energy can propagate at the interface via the help of SPP. However, SPP modes are frequently referred as surface plasmon electromagnetic modes in literature.

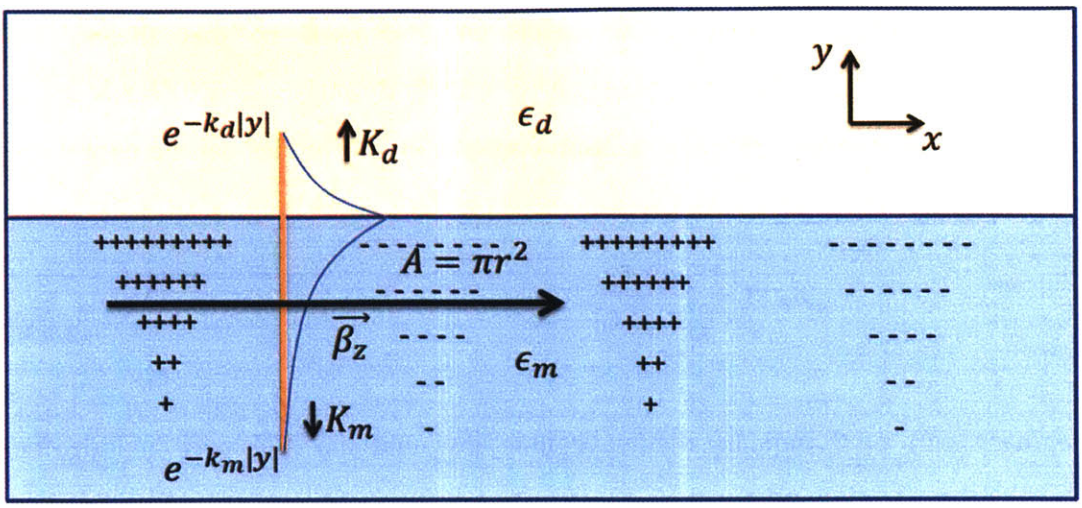

Figure 2.2.1 Illustration of a surface plasmon mode. The mode is bounded by the metal-dielectric interface. The positive and negative charges in metal are represented by + and – respectively. The propagation constant is represented by $\vec{\beta_z}$. The wavevectors in y direction are expressed by K_d (in dielectric material) and K_m (in metal).

As we described earlier, in order to have an SPP mode, one necessity is the positive and negative dielectric constant beside the interface. Starting from Drude model:

$$\varepsilon_r = \varepsilon_{core}\left(1 - \frac{\omega_p^2\tau^2}{1+\omega^2\tau^2} + i\frac{\omega_p^2\tau}{\omega(1+\omega^2\tau^2)}\right) \tag{2.2.1}$$

$$\omega_p = \sqrt{\frac{ne^2}{\varepsilon_0\varepsilon_{core}m^*}} \tag{2.2.2}$$

where, ε_{core} is the relative permittivity of the material excluding the contribution due to the free electrons, m^* is the electron effective mass, ε_0 is the permittivity of vacuum, n is the electron concentration in the conducting medium, e is the electronic charge, τ is the effective scattering time for the electrons, and ω is the frequency of the electromagnetic wave. ω_p is the plasma frequency in the material.

When $\omega > \omega_p$, the real part of ε_r is positive and the material appears as a dielectric one. When $\omega < \omega_p$, the real part of ε_r is negative and the material appears as a metal. As

examples of typical plasma frequency which will be used in this thesis, Au has $\omega_p \sim 2000THz \times 2\pi$, highly doped GaAs (n$\sim 5 \times 10^{18} cm^3$) has $\omega_p \sim 20THz \times 2\pi$. Solving the Maxwell equation, the propagation constant of TM modes can be expressed as

$$\beta_z = \frac{\omega}{c}\sqrt{\frac{\varepsilon_m \varepsilon_d}{\varepsilon_m + \varepsilon_d}} \tag{2.2.3}$$

The imaginary part of β_z indicate the waveguide loss and the real part include the information of the effective index.

The wave vector in evanescent direction is expressed as:

$$K_d^2 = \beta_z^2 - \frac{\omega^2}{c^2}\varepsilon_d \tag{2.2.4}$$

$$K_m^2 = \beta_z^2 - \frac{\omega^2}{c^2}\varepsilon_m \tag{2.2.5}$$

The real part of K_m and K_d represent the extinct lengths in metal and dielectric material respectively. It is worth to pointing the relation $\frac{K_d}{K_m} = -\frac{\varepsilon_d}{\varepsilon_m}$. Thus K_d is much smaller than K_m since ε_m is typically much larger than ε_d in a typical metal/semiconductor interface in THz region. For Au/GaAs interface, in THz region, the skin depth is in the order ~100-200 Angstroms in Au and ~1000μm in GaAs.

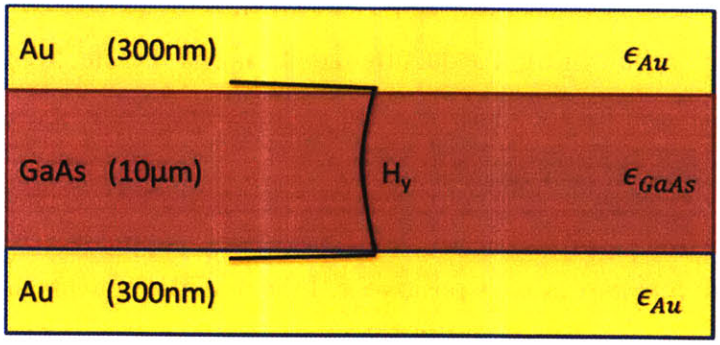

Figure 2.2.2 Schematics of the mode in a metal-metal waveguide. This mode is almost uniform in GaAs.

In a MM waveguide with subwavelength dimension, an active gain medium is encapsulated between the top and bottom metal which is often Au in THz case. The thickness of gain medium is optimized to ~10 μm which is much smaller than the mode skin depth in GaAs (~1000μm), which indicates an almost uniform mode distribution in this distance range. Thus, the mode of a double metal waveguide, illustrated in Figure 2.2.2, demonstrates an almost uniform mode in vertical direction. The mode is the combination of the double surface plasmon modes and highly confined between the two metal plates. This mode is similar to TEM mode of a transmission line. When the width is narrowed down to deep sub wavelength, a significant amount of mode extends out of the laser core from the semiconductor/air interface and propagates outside. The property of TEM-like mode inspires the thought to borrow transmission line theory to understand the systems, which will be discussed later.

For a THz wire QC laser, there are two categories of losses in general: mirrer loss (α_m) and waveguide loss (α_w). In a MM waveguide, mirror loss, which will be discussed in detail later, is relatively lower compared to SISP waveguide. Total waveguide loss can be broken down to free carrier loss, metal loss and scattering loss. THz QC lasers are lightly doped unipolar device with electron concentration n~10^{16}cm^{-3}. Based on Drude model, the free carrier loss , α_{fc}, is roughly given by

$$\alpha_{fc} \propto \frac{\lambda^2}{\tau} \tag{2.2.6}$$

where λ is wavelength and τ is Drude scattering time. This expression can be used with caution because it overestimates the free carrier loss. The reason is that electrons are not free in the material growth direction because of the existence of quantum wells in QCLs. The metallic loss is due to the penetration of the mode in the metal layer at the two sides of the gain media. This metallic loss in general weighs less than free carrier loss, depending on the metallization quality. Based on Drude model, it can be derived from $Im(\beta_z)$, and is typically ~3-4 cm^{-1} in THz region for a MM waveguide comprising a

metal with a Drude scattering time of 50fs. The scattering loss originates from the sidewall roughness of the laser ridge. The overlap between the mode and sidewall roughness determines this scattering loss. The narrower the device is, the more overlap between the mode and the sidewall roughness, and hence more loss is introduced. This is systematically investigated in ref [89]. An analysis based on perturbation theory was applied to a rough symmetrical slab waveguide[90] and a closed form expression for this scattering loss due to sidewall roughness was developed by Tien [91] derived from Rayleigh criterion and Marcuse's theory[90] :

$$\alpha_{scatt}(\sigma_{rough},\lambda) = \left(\frac{4\pi\sigma_{rough}}{\lambda}\right)^2 \left[\frac{cos^3\theta}{2\sin\theta}\right]\left[t + \left(\frac{1}{p_1}\right) + \left(\frac{1}{p_2}\right)\right]^{-1} \quad \textbf{(2.2.7)}$$

Where α_{scatt} the scattering loss, σ_{rough} is the standard deviation of sidewall roughness, λ is the lasing wavelength, θ is the angle of ray propagating in the waveguide, t is the waveguide thickness, and $\frac{1}{p_{1,2}}$ are the penetration depth of modes into the cladding layers. Although this expression was originally developed for a slab waveguide, the general trend, $\alpha_{scatt}(\sigma_{rough},\lambda) \propto \left(\frac{4\pi\sigma_{rough}}{\lambda}\right)^2$, should be applicable to THz MM waveguides.

Though it is difficult to analytically quantify each of the three losses, the total waveguide loss of the MM waveguide was experimentally measured as ~18cm^{-1} for a Fabry-Perot THz QCL with 80μm width and 1.2mm length[79]. The actual waveguide loss for terahertz wire lasers is larger than this value, because of the larger overlap of the mode with sidewall roughness.

2.3 Mode confinement

One important feature of THz wire lasers with a MM waveguide is the relatively small mode confinement factor, which represents the optical overlap between the mode and the gain media. It can be a crucial factor to determine the lasing performance for a THz wire laser and is worth being carefully understood.

Traditionally, the mode confinement factor is defined as:

$$\Gamma_0 = \frac{\iint_{active} w_e dxdy}{\iint dxdy(w_e + w_m)/2} \tag{2.3.1}$$

where w_e and w_m are the stored electrical and magnetic energy of the field respectively. However, strictly speaking, this definition as the ratio of inside to outside power is only correct in the case of weak waveguiding in which $n_{eff} \sim n_{active}$[92][93].

The derivation of a correct confinement factor starts from a basic equation which describes the power amplification:

$$\frac{dI}{dz} = G_m \tag{2.3.2}$$

where G_m is the modal gain and I is the total power flux. The material gain G_0 is linked with modal gain by the confinement factor Γ through the expression:

$$G_m = \Gamma G_0 \tag{2.3.3}$$

Electrical field can be decomposed into a fast varying component $\bar{E}(x,y)$ in longitudinal direction, and a quasi-stationary filed $A(z)$ in transverse direction:

$$E = A(z)\bar{E}(x,y)e^{i\beta_z z - i\omega t} + c.c. \tag{2.3.4}$$

where β_z is the propagation constant in the longitudinal direction z and ω is the frequency. Then it can be shown that Γ can be expressed as:

$$\Gamma = \frac{v_{ph}}{v_{E,z}} \frac{\iint_{active} w_e dxdy}{\iint dxdy(w_e + w_m)/2} = \frac{v_{ph}}{v_{E,z}} \Gamma_0 \tag{2.3.5}$$

where $v_{ph} = c/n_b$ is the phase velocity and $\boldsymbol{v}_{E,z}$ is the energy velocity in the waveguide. Finally, the confinement factor can be further written as:

$$\Gamma = \frac{n_{eff}}{n_g}\Gamma_0 \tag{2.3.6}$$

where n_g is the background index of the gain medium and n_{eff} is the group index of the waveguide. The effective index n_{eff} can be derived by $n_{eff} = Re\{\beta_z\}c/\omega$ or $n_{eff} = c/(2\Delta\nu L_{cav})$, where c is the light speed, $\Delta\nu$ is the longitudinal mode spacing and L_{cav} is the cavity length.

In THz QCLs, a strong mode guiding is resulted from the natural property of surface plasmon mode in MM waveguide. Thus the corrected form of the confinement factor should be used. However, a further correction should be included becauseof the intersubband selection rule: only transitions with the electrical field polarized along the growth axis are permitted. Thus in the gain medium of quantum cascade laser, the mode confinement factor is defined as:

$$\Gamma = \frac{v_{ph}}{\boldsymbol{v}_{E,z}}\Gamma_0 = \frac{v_{ph}}{\boldsymbol{v}_{E,z}}\frac{\int_{active}|E_x|^2 dx}{\int_{-\infty}^{\infty}|E|^2 dx} \tag{2.3.7}$$

where E_x is the electrical field in the vertical direction to the plane of quantum well. This definition is a little bit different from the previous by replacing the w_e by the energy associated with the electrical field polarized along the growth axis.

Compared with traditional slab waveguides, the mode confinement of a THz wire QC laser is much higher because of its MM waveguides. The mode is highly confined in the vertical direction by the top and bottom metal of the MM waveguide. The mode penetration depth depends on the metal quality, as discussed in the previous sector. In the lateral direction, the mode is strongly bounded by both the metal/semiconductor interface and the index mismatch between the laser core (GaAs/AlGaAs, n~3.6) and the

environment. These two mechanisms lead to a large confinement factor, close to one. However, when the waveguide is narrowed down to a deep sub wavelength size of ~10um, the traditional mode confinement factor Γ_0 can decrease to below 80% at 2THz. Figure 2.3.1 illustrates that the confinement factor Γ_0 drops significantly when the device width is shrinking. Additionally, higher order lateral modes have poorer mode confinement factors and smaller effective index both of which lead to weaker modal gains indicated by equation 2.3.6. For a same lateral mode at a lower frequency, it has a lower effective index and poorer mode confinement fact while these values changes slowly over different frequencies. These properties are important to develop tunable terahertz wire lasers, since the confinement-factor differentiation is used to discriminate different lateral modes, which will be discussed in later chapters.

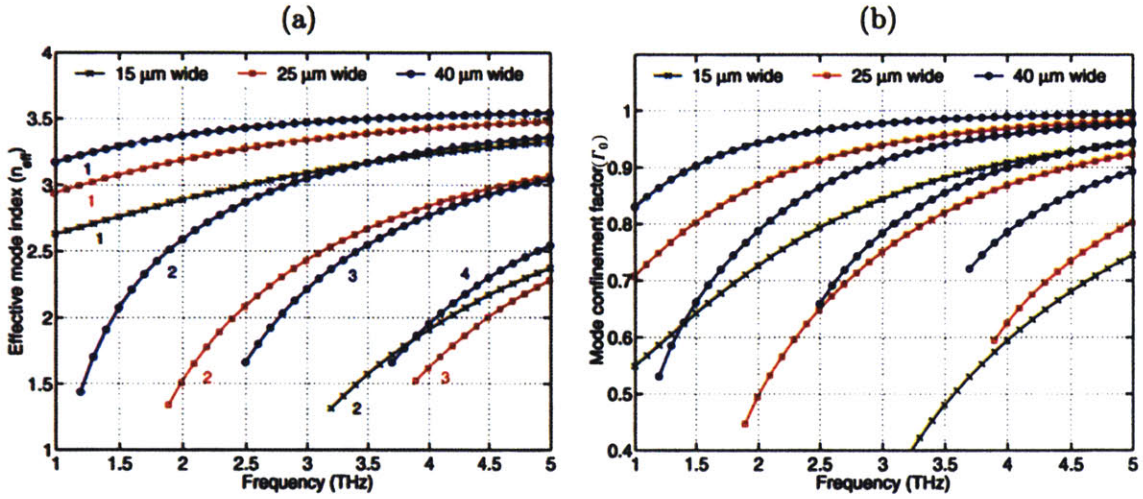

Figure 2.3.1 (from [94]) Effective mode index (n_{eff}) and traditional mode confinement factor (Γ_0) of Fabry-Perot MM waveguides with different widths. Using a finite-element mode solver, the calculation in a range of ν = 1 - 5 THz, was carried out for a waveguide with 10 μm thickness and open end sidewall. For a given waveguide width, both n_{eff} and Γ_0 for different lateral modes are demonstrated and the lower numbered curves (for both n_{eff} and Γ_0) correspond for progressively higher order lateral modes which is indicated by the numbers below the curves. For instance, n = 1 implies the fundamental mode. In the calculation, n_{GaAS} = 3.6 is assumed.

2.4 Facet Reflectivity

Understanding the facet reflectivity is crucial to design tunable THz QC wire lasers. The reasons are two folds. First, mirror loss due to the imperfect facet reflectivity can play an important role in discriminating different longitudinal modes to ensure a single mode operation. The mode discrimination mechanism will be discussed in detail in next chapter.

Secondly, understanding the facet reflectivity is helpful to interpret the emission characteristics of THz wire QC lasers, and then lead to further improvement. In the following discussion, since THz wire QC lasers have only been achieved in a MM waveguide, all the discussions are based on this design.

For THz wire QC lasers, the modes extend out of the laser core significantly because of its deep subwavelength waveguide. At the end facets, two factors contribute to a relatively high reflectivity compared to traditional slab waveguides. First, the traditional dielectric interface, GaAs/air interface in this case, partially provides the reflectivity. This reflectivity abides with Snell's law and can be expressed by Fresnel equation. The other contribution is the impedance mismatch between the strongly guided modes and free space modes. This reflectivity is further increased by the termination of the metal/semiconductor interface which the surface plasmon mode tightly binds to.

It is difficult to derive a closed form solution of facet-reflectivity due to these coupled reflective mechanisms. So a numerical simulation based on COMSOL3.0 was performed [75] while the results were understood intuitively. In this calculation, an approximated mode derived from a two dimensional simulation was used to excite the three dimensional cavity, which ends at two "cleaved" open facets. The calculated reflection from the open facet interferes with the excitation and form a standing wave, whose ratio is used to derive the facet reflectivity:

$$SWR = \frac{\langle E_1(x,y)|E(x,y)\rangle|_{max}}{\langle E_1(x,y)|E(x,y)\rangle|_{min}} = \frac{1+|r|}{1-|r|} \qquad \textbf{(2.4.1)}$$

Here E_1 is the y (growth axis direction) polarized electric field from the two dimensional simulation, and E is the value from the three dimensional simulation. The inner product in equation 2.4.1 is taken over the transverse plane at various locations along the propagation direction where the maximum and minimum values are observed.

The reflections resulted from different waveguide width is illustrated in Figure 2.4.1. From the top to the bottom, progressively, the reflectivity of f=3, 4 and 5 THz radiation ranges from ~90% down to ~60%. This high reflectivity corresponds to a mirror loss order of ~0.5-2cm^{-1} for a typical waveguide length of ~1mm. In general, when the waveguide width is fixed, lower frequency leads to a higher reflectivity, due to a stronger mode impedance mismatch and the aperture boundary effect. Additionally, the reflection is increased when the waveguide is narrowed. Specifically, in a wire laser case (deep subwavelength), the increasing rate of the reflectivity along the decreased waveguide width advances significantly. This is due to the increased mode impedance mismatch. The reflection can be as high as ~90% when the width is ~12um. This high reflectivity results in a low emission power of THz wire QC lasers. This high reflectivity also implies a weak mode selectivity because the difference of the radiation loss is small. Indeed, the small mirror loss, compared to the waveguide loss (10-20cm^{-1}), limit the upper bound of the mode differentiation. But the early effort to achieve a single mode operation relied on this the difference of the weak radiation loss, resulting in an unstable performance which will be explained in chapter 5.

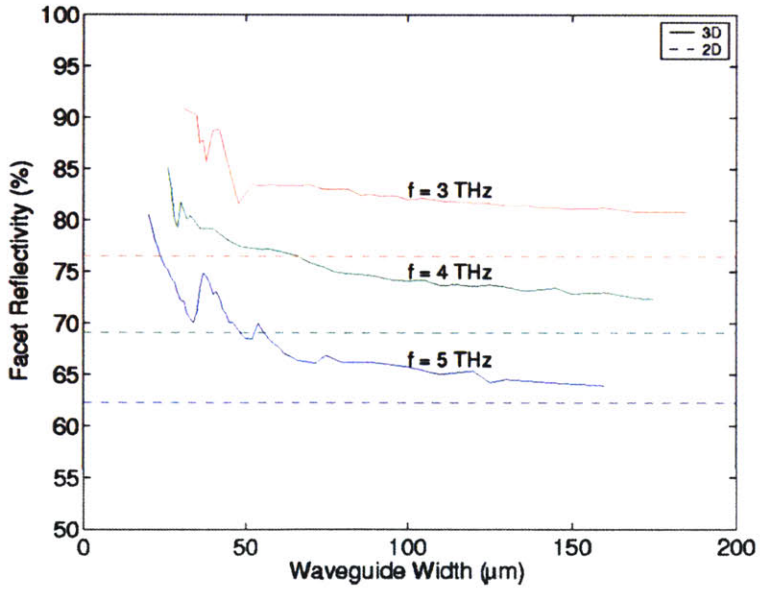

Figure 2.4.1 (from [95]) The facet reflectivity of THz QC lasers with different waveguide widths and lasing frequencies (f=3,4 and 5 THz). The solid lines represent the simulated result by a 3-D model while the dotted lines give the value of 2D simulation to show convergence.

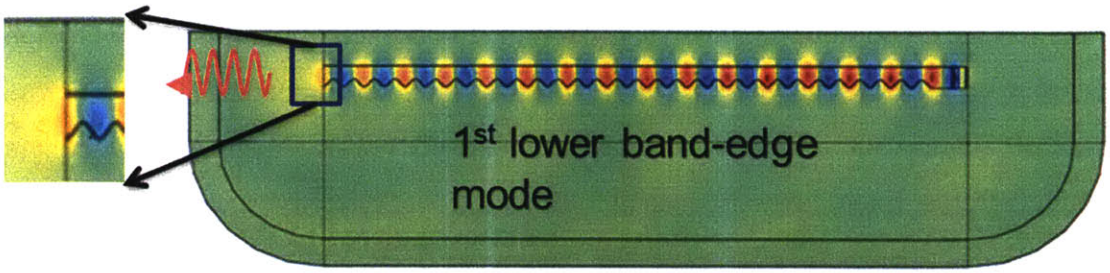

Figure 2.4.2 Mode distribution of a typical first order lateral mode. The wiggled arrow indicates the direction of THz radiation. The alternated blue and red colors represent positive and negative phase in a cycle of electromagnetic oscillation. Thus both colors indicate the maximum of the standing wave. The blowup of the mode distribution around the end facet clearly shows that the mode maximum of the standing wave is right on the facet.

It is worth noticing that an intuitive understanding of the mode behavior can play an important role in the design. The MM waveguide of the THz wire QC laser is essentially like a strip transmission line, and many analysis methodologies of microwave engineering can be applied to THz wire QC lasers. For instance, the end facets of MM waveguides are similar to an open circuit load because of the small radiation caused by the high reflectivity. So according to the standard transmission line theory, the maximum of the standing wave is roughly aligned with the end facet although a modest offset exists due to the weak radiation. Confirmed by the simulation shown in Figure 2.4.2, this property is crucial to enable a robust single mode operation. As an important design tool, it will be further discussed later.

2.5 Beam pattern

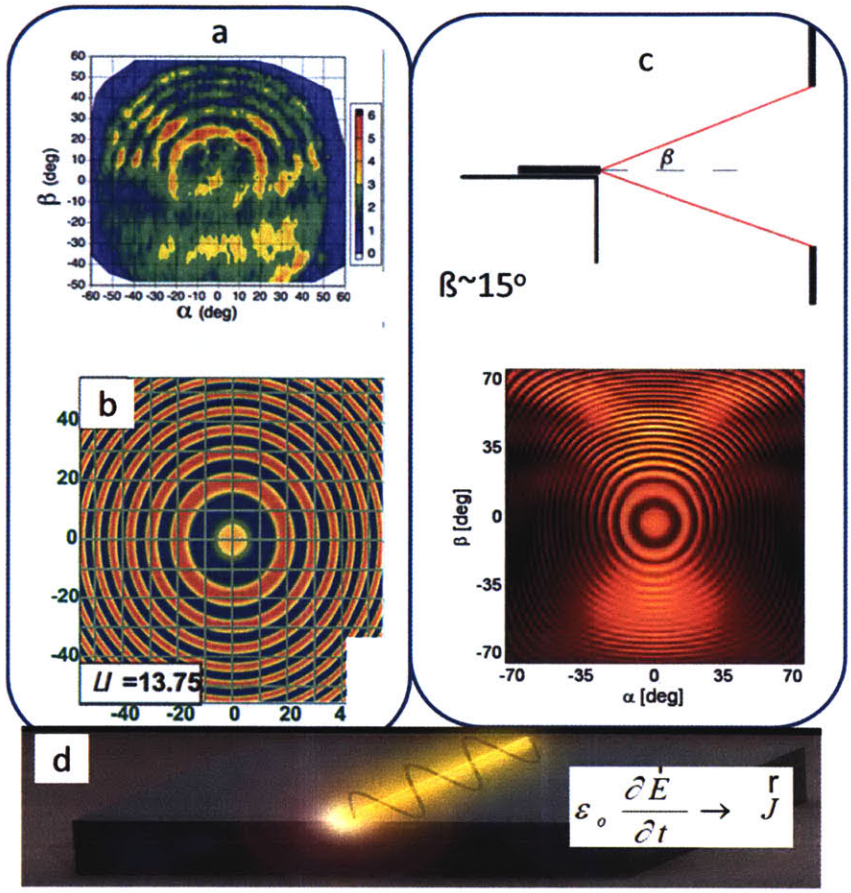

Figure 2.5.1 Illustration of the beam pattern of THz QC wire lasers. (a) The measured beam pattern [96] from a THz wire laser. (b) The simulated beam pattern based on the antenna model [88]. (c) The calculated beam pattern based on and the point source model[1], whose configuration is shown in the upper part. (d) The schematics of the wire laser and the mode attached to it.

The beam pattern of THz wire laser shows a strong interference pattern [96] which can be explained by both an antenna model [88] and a point source model which takes the facets as two point sources [1]. Actually, the concept of tunable THz wire lasers is inspired by the antenna model, which attributes the interference beam pattern to the emission from the mode attached to a wire laser and extended out of the solid core significantly. According to this model, the divergent far field beam pattern over 180° (Figure 2.5.1 a) is determined by the interference of the radiation from the longitudinal distribution of radiation, similar to a phase array. The other model, illustrated in part c of Figure 2.5.1, attributes the divergent beam pattern to the diffraction of the deep subwavelength radiation aperture and the strong aperture boundary effect. Then the deep subwavelength radiation apertures can be modeled as point sources which can interfere with each other,

resulting in an interference beam pattern. Compared with the antenna model, the point source model is simpler and was also verified by the experiments [1]. The theoretical calculations of the beam pattern, based on the antenna model and the point source model, are shown in part b and c of Figure 2.5.1. Compared with the experimental result, the two simulated patterns both reconstruct the basic interference features.

The divergent interference beam pattern has important implication for practical applications and the further development of THz QC wire lasers. Although the divergent beam pattern allows an easy optical alignment for the measurement during the preliminary developing stage, it does pose a technical difficulty for practical applications because of the low average power distributed in a unit solid angle. As discussed in the last sector, the radiation power is relatively low because of the high reflectivity. This inefficient radiation is further exacerbated by a difficult to collect the power resulted from divergent radiation exceeding 180^{o}. Consequently, although a large tuning range has been demonstrated in this thesis, the absolute emission power hasn't been successfully measured yet. Hence, an integrated power amplification and beam pattern shaping mechanism is desired in the future development, and will be further discussed in chapter five.

3 Tunable THz wire QCLs—First design

3.1 Previous tunable THz QCLs

THz QCL is actually an ideal candidate as a tunable THz source because its compactness, high power (>100mW), spectral purity and reliability. For practical applications, a broad band tunable THz QCL is desired. This broad band tuning range can be facilitated by the large gain bandwidth of up to 1THz in THz QCLs. Indeed, this broad gain bandwidth can be further extended by using multiple upper or lower radiative levels. Moreover, the interface roughness dephases the coherent lasing transition and further broadens the gain bandwidth. Besides, the cascading principle of THz QCLs allows the combination of the modules with different gain characteristics, e.g. design bias and gain peak. This enables the engineering of the gain band width [97] and even gain shape by designing each module separately. Traditional tuning mechanisms for semiconductor lasers include bias adjustment, cavity refractive index modulation enabled by carrier injection, temperature tuning and cavity length adjustment. In this section, different techniques to tune the lasing frequency of THz QCLs are reviewed.

3.1.1 Electrical tuning of THz QCLs

Electrical tuning of THz QCLs stems from the energy change of quantum states induced by the bias adjustment. In THz QCLs, electron transport relies heavily on resonant tunneling and phonon or photon assisted coupling. When the bias is changed, tunnel coupling and dipoles redistribute, causing the energy space among radiative states to change. Thereafter this shifts the lasing modes, as illustrated in ref. [97][98].

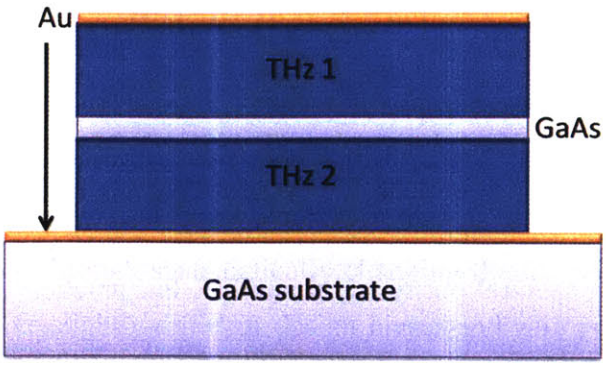

Figure 3.1.1 Schematics of a two-color terahertz quantum cascade laser with a metal-metal waveguide. A thin doped GaAs layer is incorporated in the structure to stabilize the voltage between each gain module.

Among the several electrical tuning schemes of THz QCLs is a frequency switching which has been demonstrated in different configurations. For instance, reversing the bias direction or changing bias voltage can enable different quantum-state alignment schemes which can achieve lasing condition [99][100][101]. Moreover, the sensitive dependence of the lasing frequency on the bias voltage [79] adds to the tunability of this technique. Another frequency switching was accomplished by cascading two different gain mediums heterogeneously [102] (Figure 3.1.1). In these designs, only two colors are achievable although each frequency can be varied slightly by changing temperature or voltage. So the limited spectral density restrains this technique in practical applications.

In another electrical tuning scheme, frequency tuning "in a step-wise manner from 3.07 to 3.40THz" [97] was demonstrated recently, thanks to a clever design borrowed from mid-IR QCLs [103]. Firstly, a heterogeneous gain media, comprising 23 different lasing sections, was designed through systematically changing the material growth parameters. All these modules have slightly different design biases and gain peaks. When the device bias increases progressively, different modules are proper aligned one by one and the gain maximum shifts to a higher frequency. Hence, a broadband gain spectrum results from these incrementally varied modules, and the frequency tuning is realized by changing the bias. Although impressive 330GHz tuning has been accomplished, the tuning actually arises from the mode hopping and exhibits a multimode form. As a comparison, the continuous tuning, in a homogeneous gain medium, can be realized by

Stark shift which is larger for a more diagonal lasing transition design and a relatively low ratio between the upper to lower state lifetime τ_{up}/τ_{lo} [104]. Actually, up to 240GHz tuning has been demonstrated by Stark shift, although the tuning is discontinuous in a multimode form.

3.1.2 Tuning distributed feedback THz QCLs by changing cavity parameters

Distributed feedback (DFB) is a common technique to make semiconductor lasers operate at a single frequency which can be varied by modulating cavity parameters. Often, a periodic grating, integrated into the cavity, is used to select the desired mode by manipulating the net gain (G_{net}=Gain-Loss). Similar with the periodic perturbation in the electronic system which results in an electronic band-gap, this periodic grating creates a photonic band gap around the Bragg frequency. The Bragg wavelength can be described as $\lambda_B=2n_{eff}\Lambda/n$, where n is an integer, Λ is the grating period and n_{eff} is the modal effective index. The lasing frequency is determined by the grating characteristics, such as modulation mechanism, amplitude and periodicity. The grating associated modulation should provide an enough feedback to ensure a single mode operation. Due to the permanent way to implement DFB grating, the grating parameters cannot be changed as a result of the rigid waveguide. So changing grating period is often not an option to tune the frequency of DFB QCLs. Alternatively, the frequency tuning can be accomplished by varying the heat sink temperature or varying injected carrier concentration. These tuning mechanisms can be explained by equation 3.1.1.

$$k_z^2 + k_\perp^2 = \omega^2 \mu_0 \varepsilon \tag{3.1.1}$$

Here k_z and $k_\perp$ stand for the longitudinal and transverse wave vectors respectively, ω is the angular frequency, μ_0 is the permeability and ε is the permittivity. This equation is fundamental to describe the dispersion in a cavity. For a DFB QCL, while k_z, $k_\perp$ and μ_0 are fixed, ε can be changed as it's a function of temperature and carrier densities.

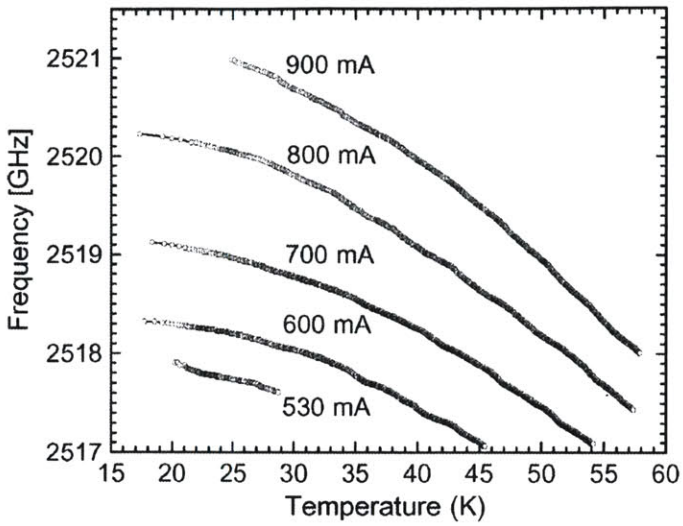

Figure 3.1.2 Temperature and current dependence of emission frequency of a 2.5-THz DFB QCL [105].

Currently, single mode operation has been demonstrated in different configurations of THz DFB QCLs, such as surface emitting [106] and edge emitting [107] in both linear and circular cavities [108][109]. But the tunability is small and in the order of a few GHz. The maximum operation temperature of THz DFB QCLs is often lower than the Fabry-Perot ones due to the additional loss from the grating. The tuning rate are typically from ~34 MHz/K to ~100MHz/K [105], depending on such factors as the device and waveguide structure, operation conditions (current and temperature) and the actual lasing mode. Another way to change device temperature is the Joule heating from injecting current, which can result in ~5.0 MHz /mA [110][111][112], 10-20 less than mid-infrared QCLs. The opposite tuning direction, due to a mode-pulling effect [105][113], was observed at a rate up to ~8MHz/mA. This mode-pulling effect is resulted from the blue-shift of the underlying gain spectrum with increased bias, and can be enhanced by a larger gain and a more diagonal design. Using a DFB QCL, up to ~30GHz tuning has been demonstrated in a microdisk laser whose small optical volume can provide a large mode spacing to avoid the mode hopping.

Although the tuning range of a single DFB QCL is limited, a clever design of DFB arrays can achieve broad band tuning. In mid-IR range, 200 cm^{-1} continuous tuning range has been achieved [114] by monolithically integrating an array of individually controlled

DFB lasers, whose lasing frequencies are slightly different. Recently, in THz frequency, this array concept has been realized to improve the beam pattern and radiation power [115]. Meanwhile this THz DFB array can be used to accomplish a broad tuning range [116].

It is worth pointing out a method to precisely design the lasing frequency (~1GHz) of DFB THz QCLs since it can be critical to realize tunable THz DFB arrays. It is difficult to control the lasing frequency by precisely defining the DFB periodicity because an accuracy of ~1GHz requires the periodicity precision of several nanometers, which is fairly difficult for contact lithography. Recently, a novel solution has been proposed to solve this problem by varying the DFB duty cycle in a scale of micron [117]. Precise control of the frequency shift in an order of 1GHz has been achieved with this method.

3.1.3 THz external cavity QCLs

For a broad-band tunable semiconductor laser, external cavity (EC) configuration with selective frequency feedback is widely used. Although mid-IR EC-QCLs have successfully demonstrated a tuning range over 400cm^{-1}, several initial efforts in THz region only achieved very limited success. Similar with conventional EC semiconductor lasers, the feedback of these THz EC-QCLs was provided by a diffraction grating or a simple movable mirror. The other crucial component of THz EC-QCLs is an anti-reflection (AR) coating applied to the gain medium/air interface to prevent/reduce reflections.

There are several difficulties to design THz EC-QCLs. First, the deep subwavelength cavity makes it challenging to couple the feedback radiation back into the cavity due to the strong mode mismatch between the free space and the cavity modes. Secondly, AR coating in THz region poses a crucial challenge to suppress lasing oscillation formed by the original semiconductor resonator. Due to the long wavelength (~100μm) of THz radiation, AR coating has to be as thick as ~25μm which is a quarter of the wavelength. It is too demanding for the current fabrication technique to achieve this thickness.

Additionally, the adhesion between the AR coating and laser fact causes troubles during the thermal cycles of cryogenic operation. Furthermore, the strong absorption of the coating material remains as an important concern.

Due to these difficulties, the first attempt to make THz EC-QCLs has achieved very limited success [118]. The device was designed to lase at ~4.7THz which is associated with the detection of atomic oxygen. The lasing oscillation was supposed to be suppressed by a tilted facet which was polished at an angle, θ_F, of 13° (Figure 3.1.3) which is slightly smaller than the Brewster angle, 15.1° ($n_{GaAs} \approx 3.7$). As illustrated in part b, an off-axis parabolic mirror is used to collimate the emitted light, and frequency selective feedback for angle tuning was enabled by a diffraction grating. But the tilted facet failed to suppress the lasing oscillation, and its reflection can compete with the feedback from the external feedback. This multiple feedbacks resulted in a multimodal operation shown in part c of Figure 3.1.3. This conclusion is proven by the match of mode spacing between the observed result and the calculated free spectral range, i.e. $\Delta f = c/n2L$. Here c is the speed of light, n and L are the effective index and the gain medium length respectively.

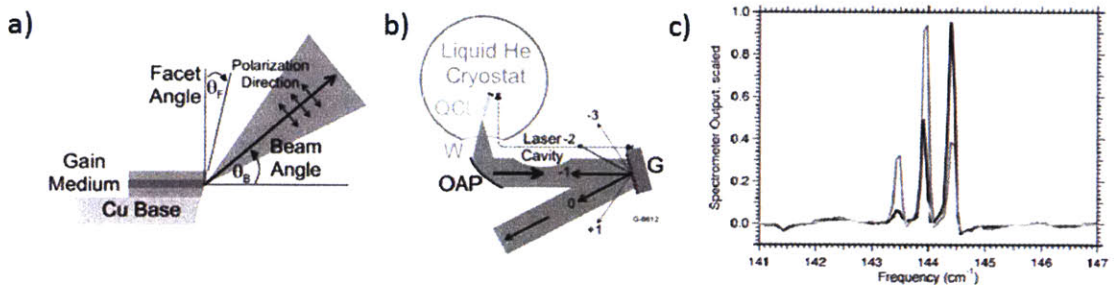

Figure 3.1.3 (from [118]) (a) The geometry used to eliminate lasing oscillation in an EC THz QCL. The function of an anti-reflection coating was achieved by a polished facet at Brewster angle. (b) The frequency selective feedback was achieved by an external grating. Optical configuration uses off-axis paraboloid (OAP) to collimate light from the polished facet. (c) Multimodal operation is due to a residual reflection from the polished facet combined with the reflection from grating.

Improved AR coatings led to new designs of tunable THz EC-QCLs [119][120][121]. An AR coating was formed by depositing a single layer of SiO_2 with an index of refraction, $n_{SiO_2} \approx 1.8 - 1.9$, on one of the laser facets. The ideal index of a $\lambda/4n$ impedance

matching layer for plane wave should be $n = \sqrt{n_{GaAs}} \approx 1.89$, slightly smaller than the experimental result which are 1.98 to 2.1 [122][123]. Thus SiO_2 is almost ideal, in THz region, as the material of a $\lambda/4n$ impedance matching layer between the gain medium ($GaAs/Al_{0.15}Ga_{0.85}As$) and atmosphere.

Figure 3.1.4 illustrates the setup of a demonstrated tunable EC THz QCL [120]. In the cryostat, a square gold mirror, used to provide the selective feedback, was mounted on a linear mechanical feed-through, termed "plunger", located close to the facet coated by a SiO_2 layer with targeting thickness for $\lambda \approx 41$ μm. With this AR coating on a cleaved facet in a control experiment, it was found that this coated facet has less than 0.12% reflectivity over a 1-μm bandwidth at a 41.9 μm center wavelength. Based on the light-current characteristic of the real device, a reflectance of up to 4% was estimated. Because there was no collimation lens between the mirror and the coated facet, the maximum change of cavity length was limited to ~160 μm due to the laser beam divergence. The other end of the laser was terminated by a cleaved facet that was not coated and used to out-couple the power.

In this cavity formed by the laser ridge and the external mirror, a laser operation was recovered. Single mode operation was only achieved when the current was slightly above the lasing threshold, while the multiple longitudinal modes appeared under high current. Continuous frequency tuning by effectively adjusting the cavity length was realized by moving the metallic mirror inside the liquid helium cryostat. However the continuous tuning was only obtained within a free spectral range of the cavity (~15 GHz) due to a lack of further frequency selective feedback among different longitudinal modes (part b). Nevertheless, single tunable mode could be selected, in a stepped manner, over a range of ~90 GHz, corresponding to ~ 2% of the lasing frequency.

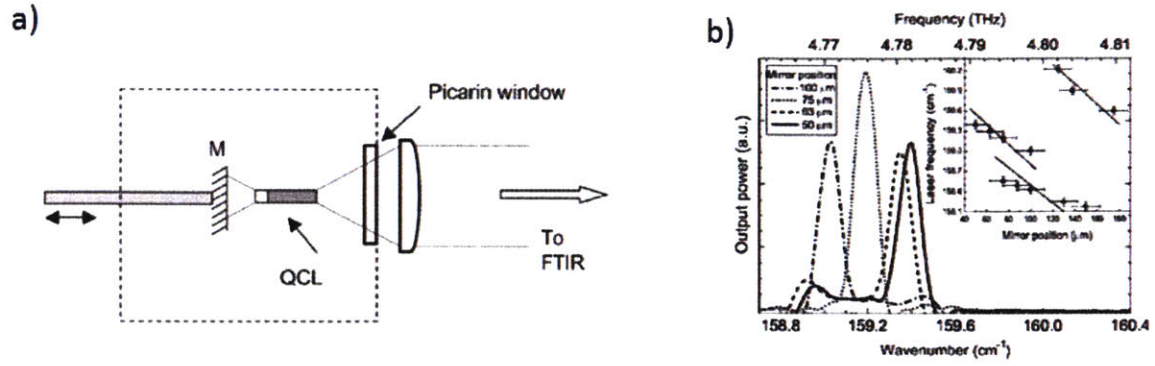

Figure 3.1.4 (a) Configuration o fthe EC QCL. It used a plunger to actuate a square gold external mirror (M) which reflected light back to the anti-reflection coated facet of the gain medium. The output is collected by the uncoated opposed facet. This design uses an improved λ/4n-thick layer of SiO_2 as an anti-reflection coating. (b) Discontinuous tuning was demonstrated in a broad range while continuous tuning within the free spectral range of the QCL chip was achieved.

More recently, a broader tuning range of 165GHz [124] has been achieved with an alternative EC configuration of THz QCL (Figure 3.1.5). In this design, a silicon hyper hemispherical lens was attached using a high-resistivity silicon (>10 KOhm-cm, $n_{Si} \approx$ 3.41) spacer. The good index match between silicon to the gain medium ($n_{GaAs} \approx 3.6$) leads to a low reflectivity at this interface. The thickness of the spacer was carefully chosen to reduce the beam divergence, and eliminate spherical and coma aberrations. Additionally, this spacer functions as a mechanical buffer to avoid the damage of the laser facet during the assembling. The hyper hemispherical lens can couple an external grating, which provides a frequency selective optical feedback, to the laser waveguide. This silicon lens not only reduces facet reflection and but also acts as a beam-forming element. Reflection at the lens/air interface is also reduced by an anti-reflection layer made of low-density polyethylene.

To optimize collimation of the THz beam, two EC designs were proposed: a large 10-mm diameter lens used to directly collimate the emitted beam (part b in Figure 3.1.5), and a smaller 3-mm diameter lens with the help of an off-axis parabolic mirror for beam collimation (part c). A larger lens enables the direct collimation which reduces the number of optical components, due to the smaller beam divergence yielded from larger beam waist which is proportional to lens size. On the other hand, smaller lens benefits

because its position is less sensitive to thermal contraction which can undesirably move the lens. Furthermore, long distance (~10 cm) collimation between the lens and the grating is practical only with the large diameter lens because it leads to a large beam waist. By contrast, the smaller lens should be placed closer to the aplanatic point to reduce optical aberrations because of the smaller collimated distances.

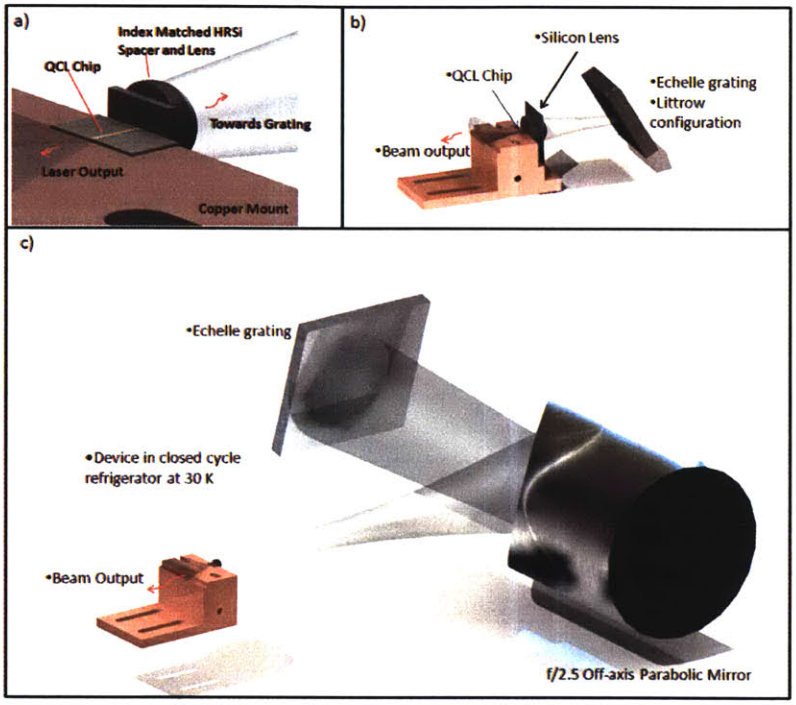

Figure 3.1.5 (courtesy by Alan Lee) External cavity QCL setup. Part (a) illustrates the configuration in which a QCL chip abutted to high-resisitivity silicon (HRSi) lens with a spacer inserted. (b) The setup with a larger lens (10-mm diameter HRSi lens) for direct beam collimation. (c) The setup with a larger lens (3-mm diameter HRSi lens) attached with optical glue. It resulted in a divergent beam which must be collimated with an off-axis parabolic mirror.

The tuning results were illustrated in Figure 3.1.6. For the 1.5-mm long device (configuration a), although a tuning of 165 GHz centered at 4.4 THz, equivalent to 3.8% of the central frequency, was obtained, frequency hopping was observed among the Fabry-Perot longitudinal modes spaced by 24 GHz which corresponded to an effective index n_{eff}=4.24. This frequency hopping is due to the residual reflection from the lens in additional to the external feedback and the lasing occurs preferentially on the longitudinal modes. Thus even though a single longitudinal mode operation was achieved by tuning the grating angle, the continuous tuning around these longitudinal modes was still limited

below 9 GHz. So although a relatively broad tuning has been demonstrated in this configuration, further development to achieve a continuous tuning should be carried out for practical spectroscopic applications.

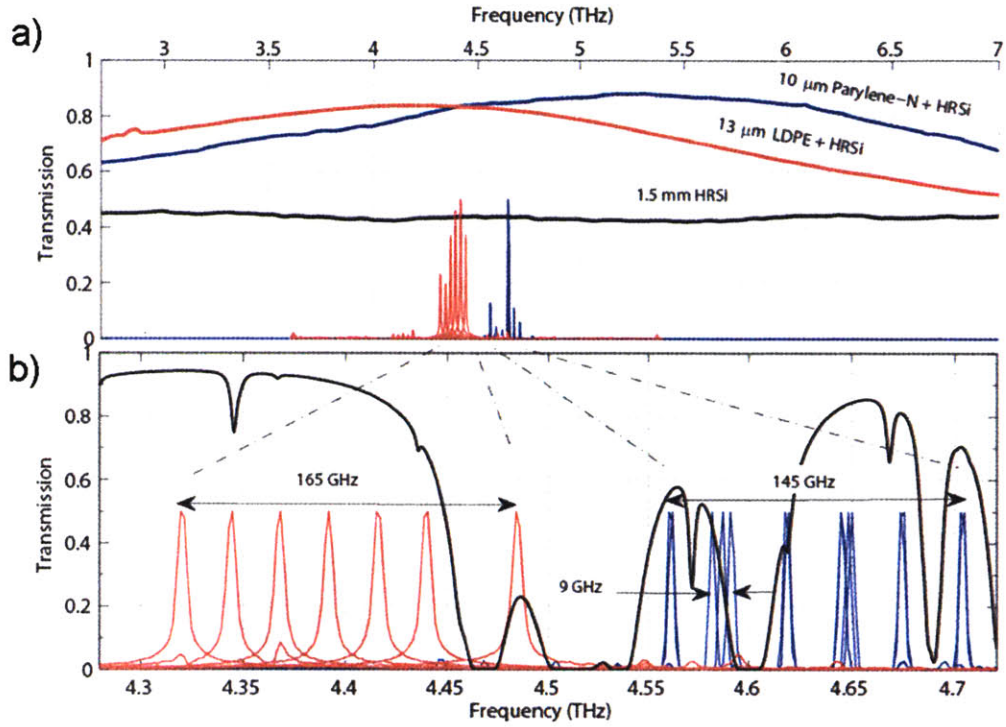

Figure 3.1.6 (from [124]) (a) Transmission spectra of a 1.5-mm thick HRSi window without or with different anti-reflection coatings. Unnormalized QCL spectra of the devices with 100-μm width and 1.5-mm length (red), and 150-μm width and 1.25-mm length (blue). (b), blow-up of the spectra from (b) after normalization and calculated atmospheric transmission through external cavity (HITRAN 2008).

3.1.4 Tunable THz QCLs with a coupled microcavity

Analogous with electronic systems, the resonance of the two photonics systems can lead to a splitting of their eigenfrequency. The magnitude of this splitting is determined by the coupling strength [125]. This resonance condition can be satisfied by coupling the second-order surface emitting cavity with the external cavity formed between the grating metal and piezo-actuated metallic surface at wavelength distance above the DFB grating (Figure 1.5.9). The control of the frequency detuning is achieved by varying the height of the external cavity which is comparable to the radiation wavelength. The metallic second-order gratings not only enable vertical coupling but also function as a coupler between

the laser cavity and the external cavity. The lower band edge mode of the DFB strongly couples with the external metallic cavity and therefore, an anti-crossing exists when the external cavity mode is in resonance with the lasing DFB mode. The coupled mode is a combination of the DFB and the external-cavity modes. As an important factor to determine the threshold, the confinement factor is high (low) when the modes are more DFB-like (external-cavity-like or mostly confined in the external cavity). The tuning range of this mechanism can be up to twice the anti-crossing, which does not depend on lasing frequency, before hopping takes place. In a laser with low lasing frequency, the percentage tuning range of the center frequency is larger than higher frequency design. This tuning mechanism is illustrated in Figure 3.1.7.

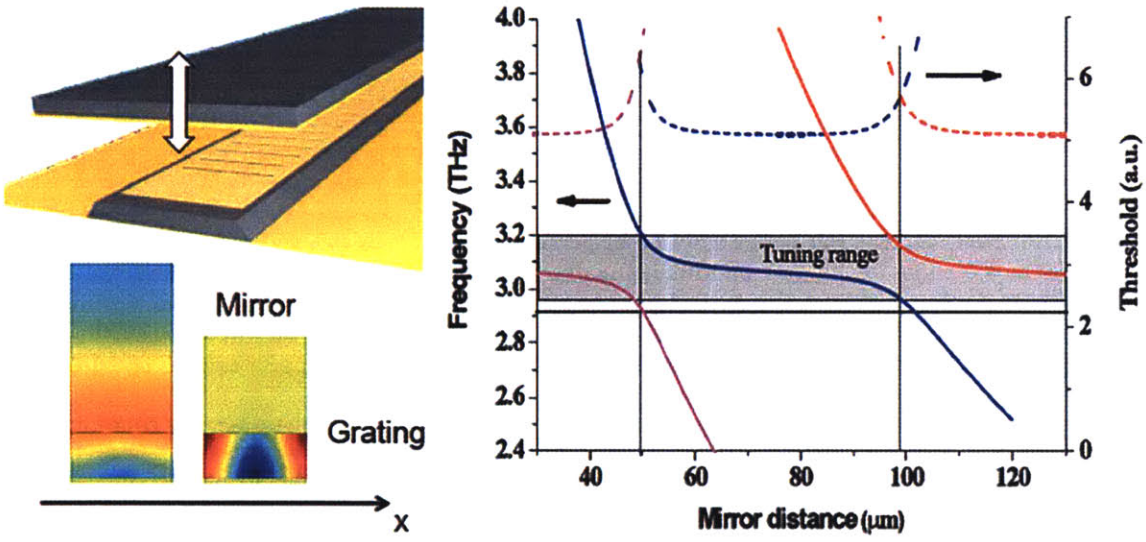

Figure 3.1.7 (from [126]) Top left: Schematics of the coupled cavities. The two coupled resonators are the metal-metal waveguide with DFB grating embedded, and the one comprised between the top grating metal and the movable metallic mirror above. Bottom left: Intensity of the electric field on a longitudinal cross-section of one period of grating (x is the propagation direction). The left plot corresponds to the anti-crossing point and the right figure refers to the middle of the tuning range which is indicated by the gray area on the right. Right panel: Simulated eigenfrequencies of the modes V.S. the mirror position. Plotted with dotted line is the respective threshold gain.

The spectrum of a typical laser of this kind without a top mirror is shown in Figure 1.5.10. Both upper and lower band-edge-modes, separated by 150 GHz, lased simultaneously. The different tuning behavior of the two modes with a metallic mirror unambiguously proved the proposed tuning mechanism. Illustrated in the figure below,

when the metallic mirror located at different positions above the gratings, the lower band-edge mode (with strong vertical emission) was clearly tuned and the upper-band-edge mode (non vertically radiating) instead, showed no tuning, as expected. However only 20 GHz tuning was achieved in this preliminary experiment. The theoretical tunability of a few hundreds of gigahertz might be obtained with device optimization[125].

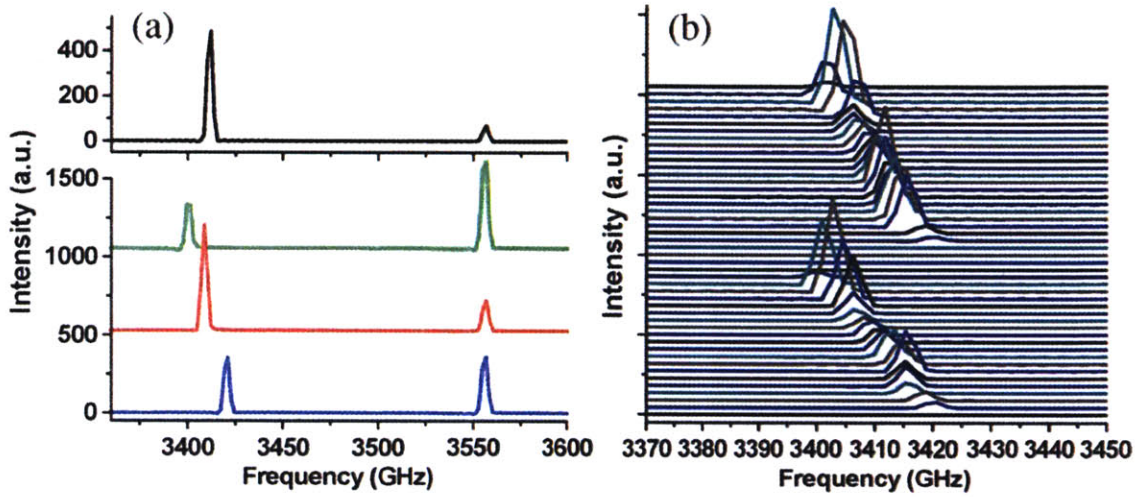

Figure 3.1.8 Part (a): The top figure shows the spectrum of a DFB device without a top mirror. The two peaks correspond to the two band-edge-modes. The bottom spectra demonstrated the tuning with different mirror positions. While the lower-band-edge clearly tunes with the mirror position, the upper-band-edge mode is not affected by the top-mirror, which matches the theory well. Part (b): When the mirror is in a wavelength comparable distance from the grating, a tuning of 20 GHz is observed without hopping.

3.2 Tuning mechanism of tunable THz QC wire lasers

From the review of the previous work of EC THz QCLs, it can be seen that conventional laser tuning methods are difficult to implement at terahertz frequency because of the relatively long wavelength λ compared to the cross-section w of semiconductor lasers. Continuous frequency tuning using an external-cavity grating has yet to be achieved [124], and electrical tuning by changing the refractive index due to temperature [106] or due to a cavity-pulling effect [127][128]produces a relatively small fractional tuning (~1%). In this section, a novel tuning mechanism that qualitatively differs from all other methods [129] is introduced. This mechanism is based on the manipulation of the evanescent propagating mode of an unusual device termed a 'wire laser'[88], which is

defined as a laser for which the dimension in the transverse direction w is much smaller than λ. To appreciate the difficulty in developing tunable terahertz QCLs and the novelty of the tuning mechanism in this work, it is instructive to revisit at a fundamental level how lasers are tuned in the previous work without introducing any intermediate variables such as effective mode index. In a uniform gain medium, the lasing frequency for a particular resonant mode is determined by its $\omega - k$ dispersion relation

$$k_z{}^2 + k_\perp{}^2 = \omega^2 \mu_0 \varepsilon \tag{3.2.1}$$

and the specific operation conditions.

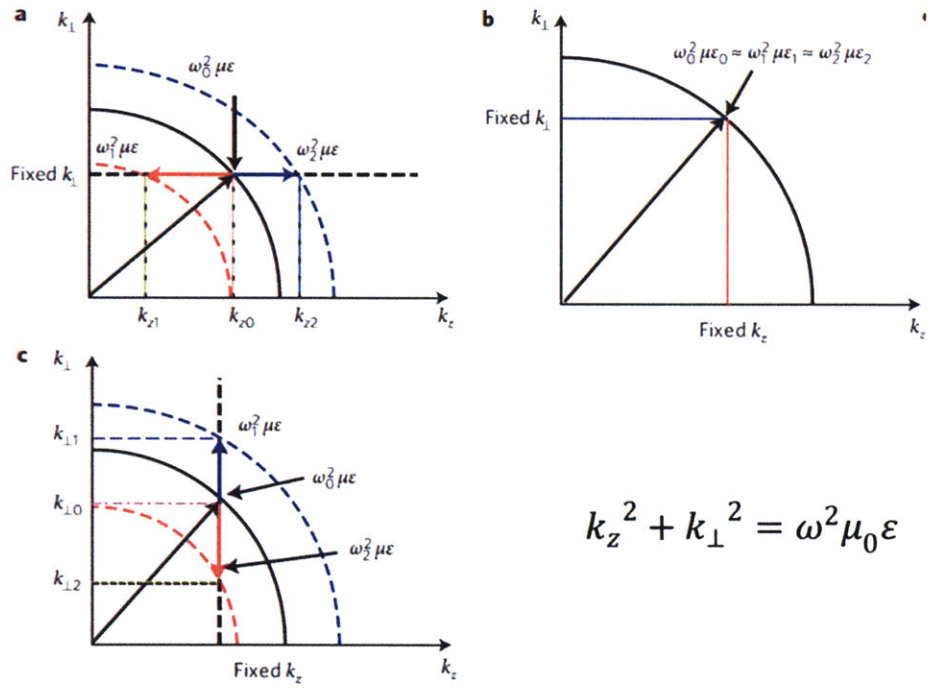

Figure 3.2.1 Illustration of different tuning mechanisms. The curves relating the transverse wave vector ($k_\perp$) and longitudinal wave vector (k_z) are based on equation 3.2.1, which is the dispersion relation in a uniform gain medium. The lasing frequency v is determined by the radius of a particular curve that intersects a specific value of $k_\perp$ and k_z, which are determined by operating conditions. The black curves represent the condition that determines the original frequency v_0 of a laser without tuning. The blue and red dashed curves represent the conditions for which the laser tuning is either blue- or red-shifted. a, The most commonly used tuning mechanism, in which both ε and $k_\perp$ are fixed and the lasing frequency is tuned by changing k_z. This can be accomplished by changing the cavity length of a Fabry–Perot laser, or changing the center wavelength of distributed Bragg reflectors (DBRs), or changing the angle of an external-cavity grating. b, Arrangement with both $k_\perp$ and k_z fixed. The tuning is achieved by changing the dielectric constant 1, which can be accomplished with temperature tuning or electrical bias. c, The tuning scheme of the present work, in which the frequency of a wire laser is tuned by directly changing the transverse wave vector $k_\perp$.

Equation 3.2.1 is same with 3.1.1. The lasing frequency ω of an already fabricated device can be tuned by changing the values of k_z (Figure 3.2.1a), $k_\perp$ (Figure 3.2.1c) or ε (Figure 3.2.1b). The dielectric constant ε can be tuned with temperature or electrically by carrier injection or a cavity-pulling effect, as discussed in section 3.1. However, this tuning has a limited range (~30 GHz for suitably designed terahertz QCLs). Most of the tunable lasers are tuned by changing k_z. Examples include changing the length of a Fabry–Perot cavity formed with either a ridge [130] or a surface-emitting structure [131], changing the center frequencies of distributed Bragg reflectors (DBR) [129], and changing the angle of an external-cavity grating [132]. Interestingly, these two mechanisms are the same as that used to tune a stringed musical instrument such as the violin, in which varying the length of a string corresponds to changing k_z , and varying the tension corresponds to changing ε . For sensing applications, mode-hop free continuous tuning is required, which is usually achieved using an external-cavity grating. A broad range of tuning of ~24% has been demonstrated with mid-infrared QCLs [132]. At terahertz frequencies, because of the long wavelengths (λ=100μm) compared to the subwavelength dimension w of the laser facet, it is difficult to focus a large fraction of the beam diffracted from the grating back to the gain medium. This difficulty is further exacerbated by the cryogenic conditions that are necessary for operation. As a result, continuous tuning based on this well-developed technique has not been achieved at terahertz frequencies, as discussed in the previous section. In contrast, instead of fighting the battle with brute force, the new tuning mechanism demonstrated here actually takes advantage of the small cross-section relative to the wavelength, and is achieved in the wire laser which has an extreme limit $w/\lambda \ll 1$.

Of the three parameters that determine the lasing frequency (k_z, $k_\perp$, and ε), very little effort has been made to change $k_\perp$ [133]. This is because in most solid-state and semiconductor lasers, λ is comparable with, or often smaller than, the transverse dimension of the cavity w. Consequently, little mode leaks out in the transverse directions and very little change can be made to $k_\perp$. For terahertz QC wire lasers based

on metal–metal waveguides, as described in chapter two, laser ridges can be made with deep subwavelength size in the transverse dimensions while maintaining a reasonable mode confinement. Such lasers showed unexpected radiation patterns with strong interference structures which are attributed to the mode attached to a wire laser. The unusual feature of THz wire QC lasers allows tuning of the lasing frequency by changing $k_{\perp}$, as demonstrated in this thesis. Such a tuning mechanism has no analogue with the aforementioned example of a stringed musical instrument, because changing the diameter of a string also modifies the sound velocity, in a similar manner to changing the refractive index in a laser. It should be clarified that the term 'wire laser' in this letter refers to w relative to the wavelength λ rather than the absolute size, with the implication $w/\lambda \ll 1$. The similar term 'nanowire laser' is typically used for lasers with a transverse dimension on the scale of nanometers, but they function with a relative dimension $w/\lambda \sim 1$ or greater.

A movable object, called a 'plunger' hereinafter, is placed along the side of a terahertz wire laser. The gap between the plunger and the laser can be adjusted mechanically. In the first design, which aims to demonstrate the principle of operation, the plunger can only be pushed towards the laser, irreversibly. The frequency tuning is achieved by the deformation of the transverse mode profile through the plunger movement. Two kinds of plungers, metal plunger and dielectric plunger, are used to tune frequency in different directions, which will be explained later.

3.3 Gain medium selection

3.3.1 Introduction

The design of THz QC wire laser should be based on the available gain mediums. This means that the characteristics of the gain medium should be factored into the design process. So, in order to achieve a successful tunable THz wire laser, the first step is to choose a best gain medium among our design portfolio from the perspectives of optimizing the continuous tunable range and robustness of single mode operation. To

achieve this goal, three aspects of the lasing performance should be evaluated: maximum operation temperature, gain bandwidth and voltage dynamic range.

General speaking, maximum operation temperature, indicates the absolute value of the gain. When temperature is increased, lasing performance degrades due to three reasons. First, electrons in the upper radiative state are excited to the higher energy and depopulated to the lower radiateive state by emitting phonons which are more populated in higher temperature. Secondly, electrons with high temperature can escape from the confinement of the quantum well, which is termed as 'thermal runaway'. Since most of the designs share these temperature degradation mechanisms, assuming a universal gain decreasing rate per degree, a higher maximum operation temperature denotes a larger gain. However, this rule should be used with caution because the universal gain decreasing rate is a crude approximation.

A larger gain bandwidth is critical to achieve a broader tuning range. A necessary condition of lasing is that gain should be larger than loss, which should be true across the whole tuning range. However, when this project started, it was not easy to measure the gain bandwidth of our gain medium directly due to a lack of experimental setup. So instead we use the lasing spectrum with short-pulsed operation to peek into this information. This is because of the different bias conditions during the rising and falling time of a pulse resulting in lasing on more modes. But again, since it is not a strict measurement of gain bandwidth, the pulsed spectrum should be used with caution.

It is not obvious that voltage dynamic range, defined as the difference between threshold and peak voltage, is important to achieve a broader tuning range. The reason lies in the fact that tunable THz wire QC lasers are physically connected with an area of unbiased gain medium on which bonding pad is seated. The direct connection between the unbiased gain medium with biased wire laser causes current speading in the lateral direction which can lead to non-uniform bias across different modules, and hence early negative differential resistance (NDR). A gain medium with larger voltage dynamic range

can sustain more bias non-uniformity. This early NDR introduced by the current spreading will be discussed in more detail later in this chapter.

3.3.2 Gain bandwidth

It is worth further discussing the gain bandwidth of THz QCLs in more detail. Theoretically, intersubband transition is like a delta function in an energy domain because the parabola of the subbands tracks each other in k space, illustrated in part (d) of Figure 1.3.1. In reality, the gain bandwidth is widened for three reasons. First, the gain is broadened by the lifetime of the subbands associated with THz radiation. Secondly, the dephasing scattering, seen by radiatitve transition, widens the gain bandwidth. Specifically, when electrons transit diagonally in real space, the interface scattering plays an important role in the gain bandwidth. Thirdly, optical gain spectrum can be a function of injector anticrossing. The FWHM linewidth due to scattering is given by

$$\Delta\nu_{scatt} \sim \frac{1}{\pi}\left[\frac{1}{2\tau_{4,eff}} + \frac{1}{2\tau_5} + \frac{1}{T_2^*}\right] \tag{3.3.1}$$

where phenomenological broadening term T_2^* is due to interface-roughness and impurity scattering, $\tau_{4,\mathrm{eff}}$ is the effective life time of the lower radiative state which is defined in [134], and τ_5 is the lifetime of upper radiative state. Intuitively, when injector anticrossing is increased to an extend in which the energy splitting is comparable with scattering linewidth, this anticrossing splitting essentially broadens the upper readiative state and increase the FWHM of the gain spectrum, which is illustrated in Figure 3.3.3. In this graph, state 4 and 3 are the upper and lower radiative states respectively due to a different notation. It is worth pointing out that, when injector anticrossings $2\hbar\Omega_{1-4'}$ reaches ~2.5 meV, the gain spectrum acquires a double-hump structure which can play an important role during the frequency tuning and will be discussed later.

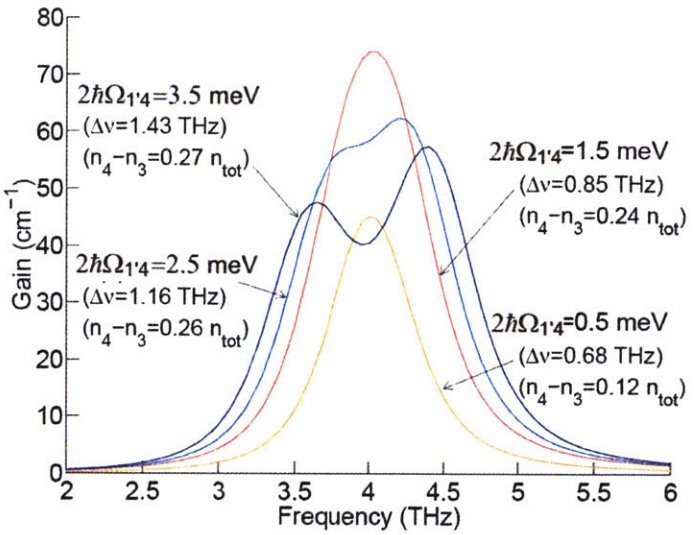

Figure 3.3.1 (from [134]) Computed gain spectra for the 4-level system designed to lase at 4THz with different injector anticrossings $2\hbar\Omega_{1-4'}$, assuming a perfect resonance between 1'–4 ($\Delta_{1-4'}$~0). The values of FWHM linewidth and population inversion are also listed beside each of the curves.

Additional to the upper radiative state, lower radiative state can also be broadened by a collector anticrossing splitting comparable with $\Delta\nu_{scatt}$ and the gain spectrum has a double-hump shape, which is demonstrated in Figure 3.3.2. More interestingly, different detuning configuration can cause the change of relative peak heights between the double humps (part b in Figure 3.3.2).

In order to achieve maximum tuning range, injector and collector antiacrossings need to be optimized. A smaller peak gain can happens along with the gain broadening. This smaller gain may reduce the lasing range because the lost is constant. Thus a tradeoff between FWHM and absolute gain should be carefully considered. Furthermore, the relative gain heights between the double humps can change and cause the frequency hopping from one hump to the other. This dynamics of the gain spectrum evolution should be factored into the mode selection strategy.

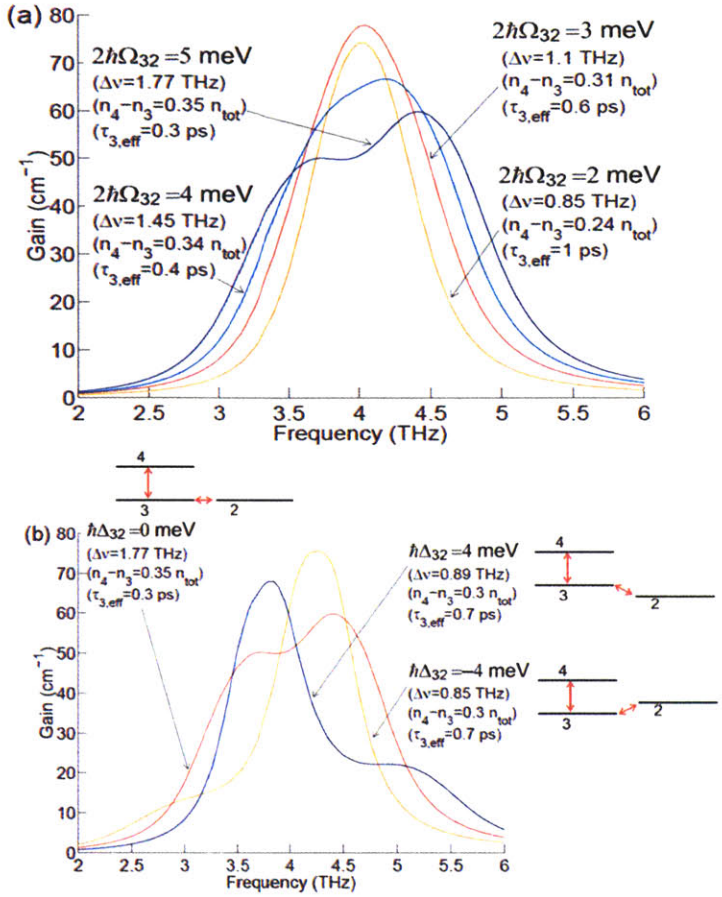

Figure 3.3.2 (from [134]) Simulated gain spectra for the 4-level QCL design described in ref [134]. (a) Illustration of the impact of different collector anticrossings $2\hbar\Omega_{32}$ assuming a perfect resonance between state 3 and 2(Δ_{32}~0); (b) Different gain spectra due to different detuning $\hbar\Delta_{32}$ at $2\hbar\Omega_{32}$ = 5 meV. The values of FWHM linewidth and population inversion are also listed.

3.3.3 The chosen gain medium

The design portfolio in our group mainly includes the FL series which have two well injectors and the OWI series which have one well injector. Both of them have achieved high temperature performance. The design of FL183S has the highest maximum lasing temperature (Tmax=172K) in FL series and design of OWI-222G has the best result (Tmax=186k) in OWI series. Regarding the temperature performance, OWI222G is marginally better than FL183S. The band diagrams and the power-current characteristics of FL183S and OWI222G are shown in Figure 3.3.3. The spectrum of FL183S spans ~0.6 THz, estimated from the frequency difference between the two lasing peaks (Figure 3.36), which is larger than OWI222G's ~0.5THz. The voltage dynamic range of FL183S (~3V)

is larger than OWI222G (2V), possibly because that two-well injector can provide enough electron injection even when it is slightly misaligned with the upper radiative state. The experimental result demonstrated that this had a huge advantage since a larger voltage dynamic range can abate the early NDR introduced by current non-uniformity.

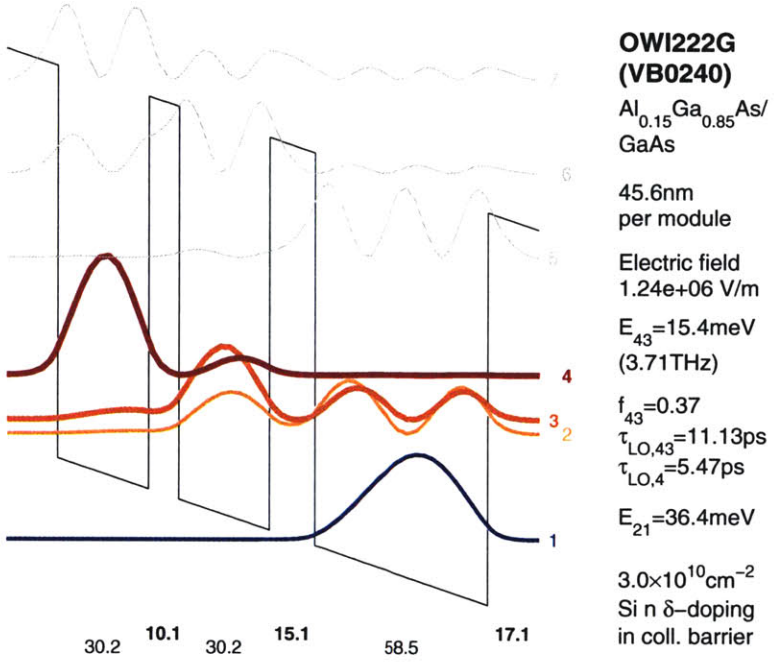

Figure 3.3.3 The conduction band diagram of OWI222G design. Electrons are injected from the injector (state 1) to the upper radiative state (state 4), and then transit to the lower radiative state (state 3). Next, they tunnel to state 3 which is eventually depopulated by emitting LO phonons.

Both FL183S and OWI222G have their gain peaks around a similar frequency, shown by the spectrum under the peak bias in the Figure 3.3.1. Besides, under several biases, FL183S lased around double frequencies at ~3.4THz and ~3.8THz, which indicates that the gain possibly has double humps near those two frequencies. Eventually, the competition between the two gain peaks favored the one at 3.8THz which has a larger gain. Thus the lasing frequency was ~3.8THz finally. This was proved by our experimental results which will be discussed later. The similar lasing frequencies are convenient for us to use same design of wire lasers for both wafers. Thus both wafers were chosen for the fabrication at the early stage.

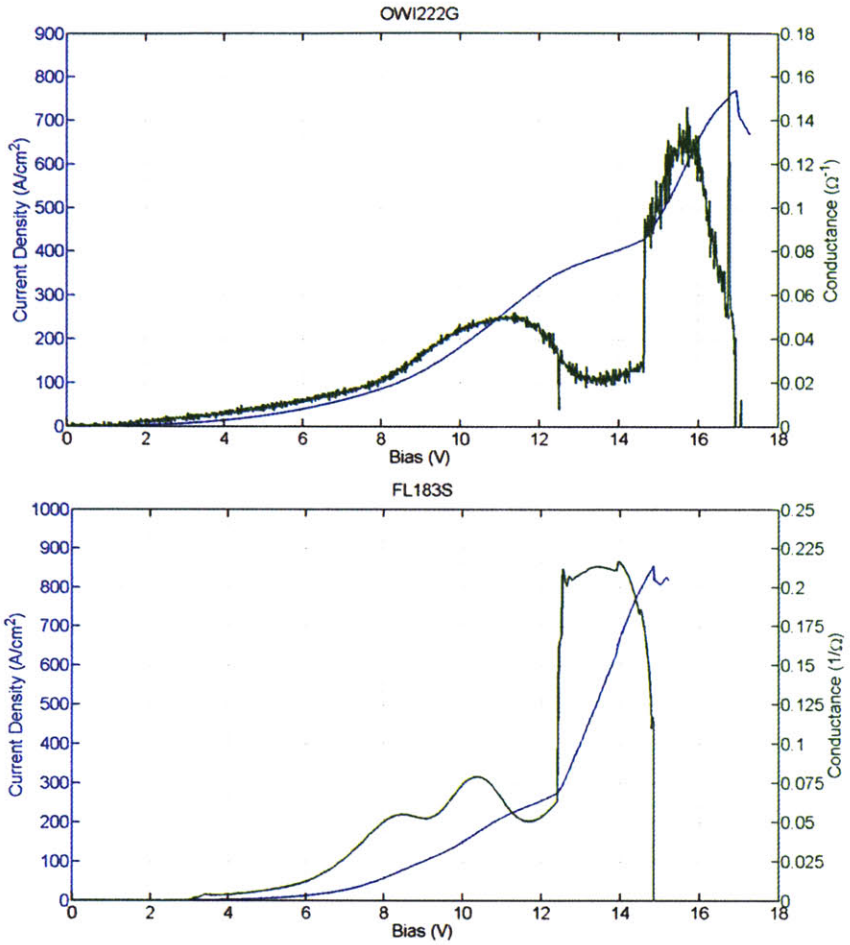

Figure 3.3.4 The current vs. bias (blue curve) and conductance vs. bias (green curve) of FL183S (lower figure) and OWI222G (upper figure). It clearly demonstrate that the dynamic voltage range of FL183S (~2.5V) is 25% larger than OWI222G (~2V).

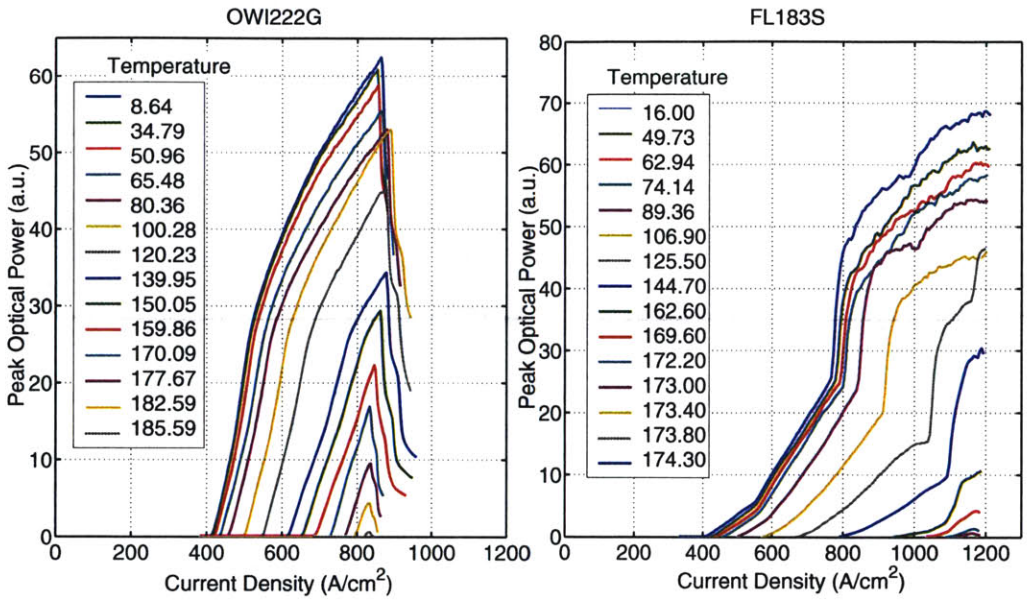

Figure 3.3.5 The power vs. current for different temperatures. The maximum operation temperature of OWI222G is ~186K, compared to ~175K of FL183S. The dynamic current range of FL183S (~800A/cm^2) is much large than OWI222G (~450A/cm^2).

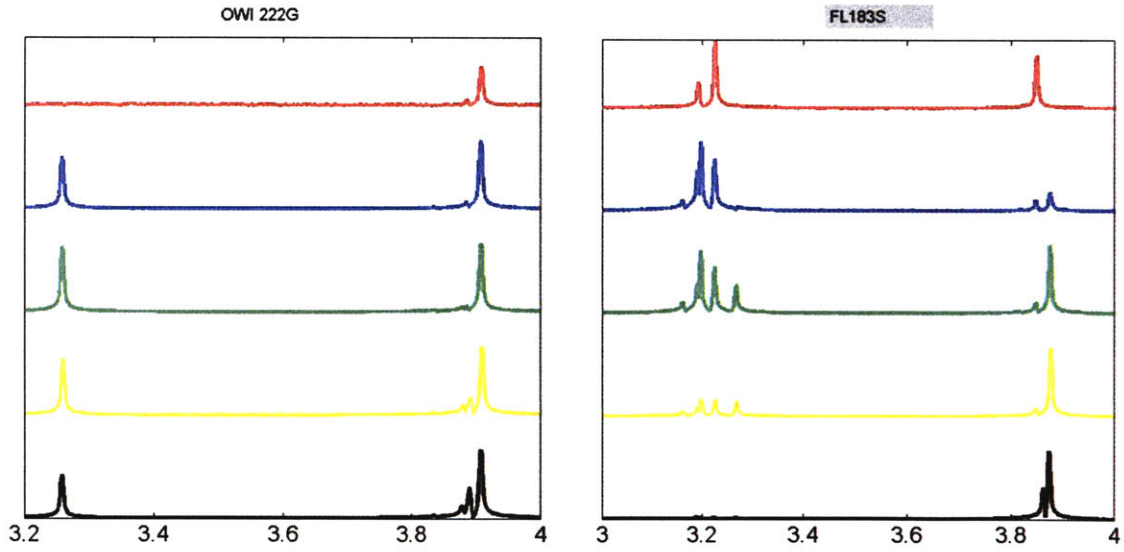

Figure 3.3.6 The spectra of the FP lasers based on OWI22G (left part) and FL183S (right part). Double frequencies lased simultaneously in both designs. From upper to bottom, the bias increases and the lasing at the higher frequency became stronger. The two designs had similar spectral space between two peaks.

3.4 Waveguide design with first order distributed feedback

In terahertz wire lasers, first order DFB is chosen to accomplish this single frequency emission. DFB structure can be conveniently integrated into THz wire lasers. In contrast, external gratings and moving mirrors only achieved very limited success because it is difficult to feedback the divergent THz beam back to the deep subwavelength waveguide.

This DFB structure has an asymmetric unilateral grating, illustrated in Figure 3.4.1. The laser ridge width is on the order of ~10um. The flat side of the waveguide is open and faces the plunger. The other side is corrugated and enables single mode operation. As a periodic photonic structure, DFB waveguide can be considered analogous to a solid state electronic system. Similar to the formation of electron band structure by introducing periodic energy potential, a photonic band structure stems from a periodic modulation of the effective index. This modulation can be achieved by the gratings of a DFB structure. Along the longitudinal direction, under the resonance condition $k_z = \pi/\Lambda$, where Λ is the grating period, two standing-wave solutions exist and each at a different frequency, forming a bandgap. These two modes are on the two edge of the bandgap and have unique properties, such as energy distribution and waveguide loss. More importantly, the relative loss value between the two modes can be controlled by using the design rule derived from the transmission line theory, which will be discussed later.

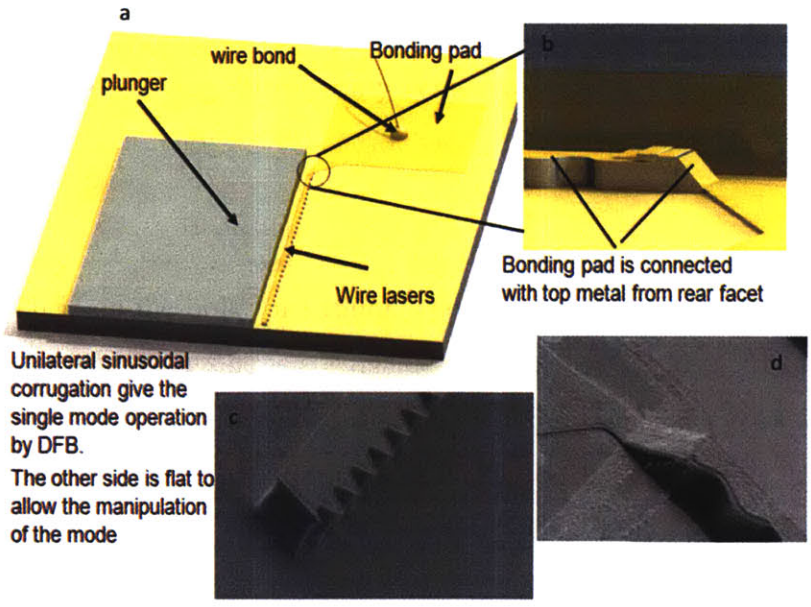

Figure 3.4.1 The waveguide design of the first tunable THz wire QC laser. (a) Overview of the tunable THz wire QC laser. A plunger is beside the flat side of the waveguide which has a DFB

structure on the opposite side. The bonding pad is connected with the top metal through a tilted rear facet, illustrated in part (b). (c) SEM image of the waveguide front facet. The DFB gratings are only on one side of the waveguide. (d) SEM graph of the tilted rear facet, on which the metal layer is insulated from the gain medium by a thin SiO_2.

In a tunable THz wire QC laser, DFB not only ensures single mode operation but also plays an important role to tune lasing frequency. Two standing waves on the two sides of the Bragg frequency stem from the resonance between the optical mode and grating, which require the longitudinal wavelength to be equal to the grating periodicity. Thus the longitudinal wavevector of the two bandedge mode is fixed by this DFB structure, leaving transverse wave vector to be changed. This corresponds to the part (c) of Figure 3.2.1.

3.4.1 Grating shape

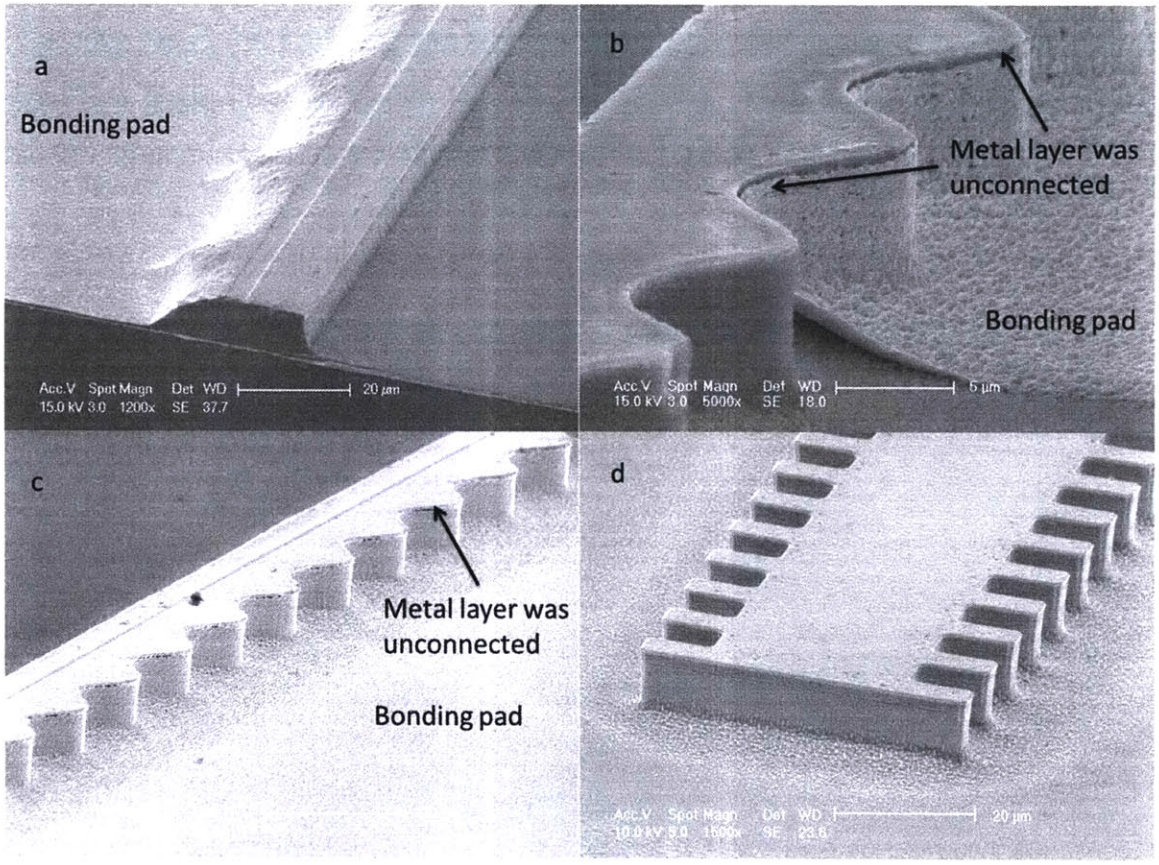

Figure 3.4.2 The different DFB grating designs. (a) A wet-etched grating was on the opposite side of a dry etched side wall. (b)(c) A grating design with sinusoidal shape coved by a gold layer. (d) A device with square shape gratings on both sides.

To enable robust single mode operation, different grating shapes and fabrication techniques have been tried and are shown in Figure 3.4.2. Two parameters should be determined by design: the grating periodicity and the coupling coefficient κ. The grating periodicity is approximately half the longitudinal wavelength of the band edge modes, since the stop band is centered at the Bragg frequency. The band edge modes for an infinitely long waveguide are perfectly in resonance with the grating. The upper band edge mode has its maximum electrical field at the narrow section of the grating, which has a smaller effective index (demonstrated in Figure 3.4.3). The opposite is true for the lower band edge mode, which has its maximum intensity localized in the section with larger effective index. For a device with finite length, translational symmetry is broken and the distribution of the mode is no longer uniform. This broken symmetry results in an envelope function of mode distribution whose shape depends on the boundary conditions of two facets and will be further discussed later.

Secondly, the coupling coefficient κ, which represents the strength of the coupling between modes and gratings, should be carefully considered to avoid spatial hole burning that can cause multimode operation. Mathematically, the coupling coefficient is defined as

$$\kappa = \frac{\pi \Delta n}{\lambda} + j\frac{\Delta \alpha}{2} \tag{3.4.1}$$

where Δn is the modulation of the index, λ is the wavelength, and $\Delta \alpha$ is the gain modulation. The band gap width is proportional to ~2κL, where L is the length of the laser. We can estimate this coupling coefficient from the calculated mode spectrum from on finite element simulation. Usually, large value of κL should be avoided because it can cause spatial hole burning, which further leads to multimode operation. On the other hand, very small κL indicates weak feedback that cannot provide enough mode selectivity. However, this parameter of κL should be applied very carefully in the case of THz QCLs with MM waveguides. The coupling coefficient is based on the standard coupling theory which assumes a weak coupling. In THz MM waveguide, modes are highly bounded by

the metal/semiconductor interface and have stronger interaction with metal grating compared to traditional index modulation. Thus κL should be used with caution.

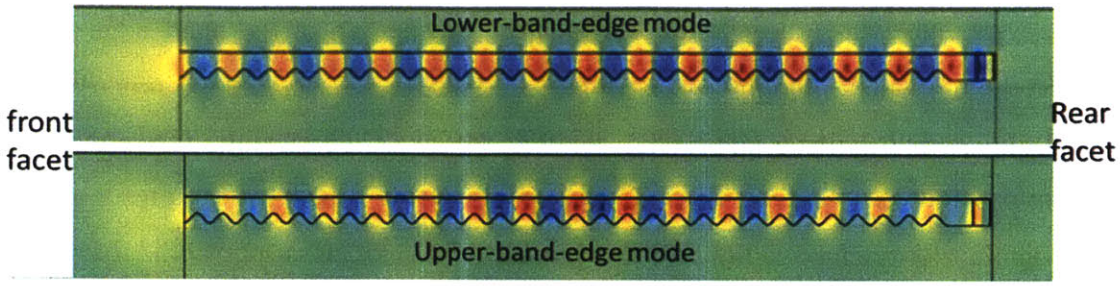

Figure 3.4.3 The mode distribution of upper-band-edge and lower-band-edge modes. Only the electrical field along the growth direction has been plotted.

Indeed, the different grating designs result in different coupling coefficient. For an index-coupled DFB structure, the coupling coefficient is

$$\kappa = \frac{k_0^2}{2\beta} \frac{\int_{corrugation} A_{q\neq 0} E_y^2(x)dx}{\int E_y^2(x)dx} \tag{3.4.2}$$

where β is the propagation constant, E_y is the electrical field in the growth direction of QCLs, and A is the grating area. The evaluation of this value requires numerical calculation based on precise measurement of the grating features, which is relatively difficult for early designs due to the unavailability of a precise shape.

The early grating designs (Figure 3.4.2) were not successful mainly due to the fabrication challenge and the metal coating on the gratings. The metal coating was mainly used to connect the top metal and a side bonding pad. To achieve this sidewall coating with directional e-beam evaporation, a tilted sidewall was attained by wet-etching whose reproducibility was usually poor. Even after significant effort was invested to imporve this connection, only limited success has been achieved. Either the connection was broken due to the metal discontinuities at the corner of laser ridge or the device was shorted due to bad coverage of the buried insulation layer. Success was achieved with the sinusoidal corrugation with bonding pad connected from the tilted rear facet. This

sinusoidal grating has only one frequency component to be added into the modulated optical modes. In this thesis, the amplitude of the sinusoidal features is always 3 μm, unless I specifically pointed out otherwise. The bonding pad design will be discussed later.

3.4.2 Using facet phase conditions to achieve lasing on the desired mode

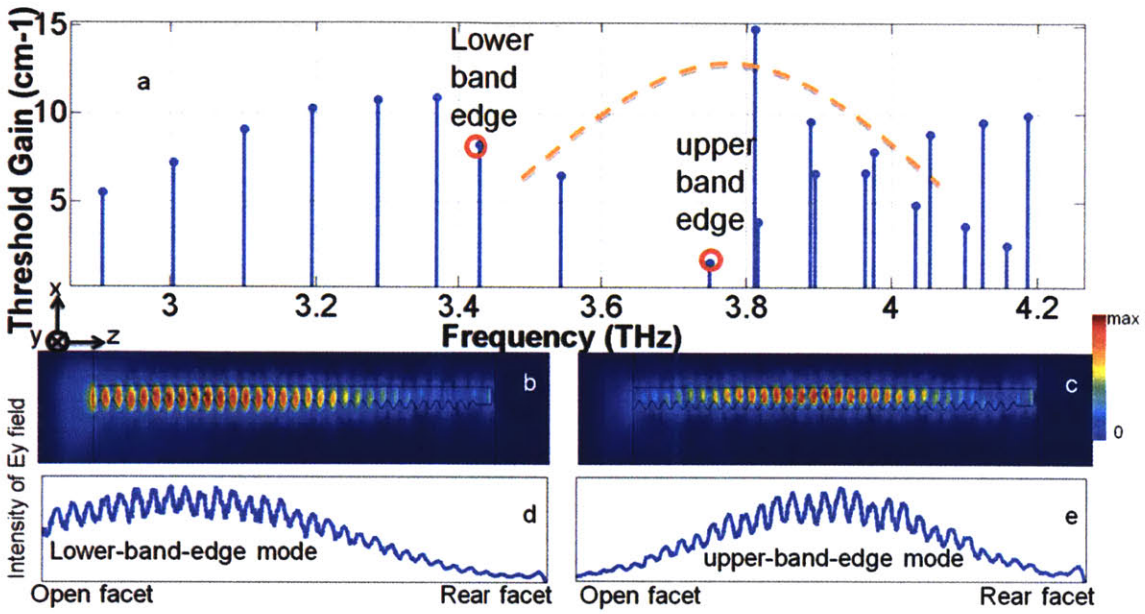

Figure 3.4.4 Band-edge-mode properties with the open front facet chosen to be at the widest location of the DFB ridge to select the upper-band-edge mode as the lasing mode. (a) Grating mode spectra of a typical DFB THz wire laser. Plotted is the radiation loss from the open facet. The dotted line is a schematic gain spectrum with a Lorentzian linewidth of ~0.5 THz. (b), (c) Intensity map (top view) of E_y of the lower- and upper-band-edge modes. (d), (e) Intensity plot of E_y of the lower- and upper-band-edge modes along the longitudinal direction of the device.

By carefully designing the position of the front facet relative to the DFB grating, either the lower band-edge or the upper band-edge mode can have lower radiation loss, and become the lasing mode, assuming single-mode operation. The upper band-edge mode has a maximum intensity localized at the narrow part of the grating, which results in a larger $k_{\perp}$. Similarly, the maximum intensity of the lower band-edge mode is located at the wider sector of the grating. The front facet, from which the radiation is coupled out, is open and can be defined by dry etching.

Both the facet phase condition and the DFB contribute to the mode discrimination. Asymmetric DFB corrugation in a metal–metal waveguide is used, enabling single-mode operation while facilitating access to the optical mode on the flat side. In a QCL wire laser, the lasing mode has the lowest threshold gain g_{th}. Mode discrimination refers to the g_{th} difference between the lasing mode and other modes. In general, larger mode discrimination results in a more robust single mode operation. In a THz wire laser whose width is ~10μm, higher order lateral modes have much smaller mode confinement Γ than the fundamental mode, and so they can be safely ignored. In the longitudinal direction, there are two standing-wave solutions on the two sides of the grating stop band centered at the resonance condition $k_z = \pi/\Lambda$, where Λ is the grating period. The upper-band- edge (lower-band-edge) mode has the maximum intensity located at the narrow (wide) part of the grating (Figure 3.4.4 (b) and (c)). These two modes have different frequencies but similar waveguide losses. It is desirable to select the upper-band-edge mode [135] as the lasing mode for its larger tuning range. When metal plunger were pushed towards wire lasers, both band edge modes were pushed toward grating and interacted more with it, which resulted in a wider stop band as discussed in the previous sessions. The broadening of the stop band pushes the upper (lower) band edge further to higher (lower) frequency and added up to (undercut) the tuning from the plunger. When a silicon plunger was used, the mode was sucked further from grating resulting in a weaker interaction, reducing the stopband width. This pulled the upper (lower) band edge to lower (higher) frequency and added up to (undercut) the tuning from the plunger. Therefore, the tuning range of upper band edge mode is always larger than the lower-band-edge mode with either metal or silicon plungers, which justifies our choice of upper band edge mode as the lasing one.

This goal can be realized by choosing the front facet of the wire laser to be at the widest section of the grating, which has been assumed for the discussion below. Because the fundamental modes of wire lasers are TEM like, the metal–metal waveguide of the THz QCLs can be modeled with a transmission-line theory. Because the reflection of the facet is high [75], the facet is essentially an open-circuit load, which requires that the maximum electric field intensity of the mode located exactly on the facet. However, the upper-band-edge mode requires minimum electrical-field intensity at the open facet if it

is at the widest part of the waveguide, which conflicts with the result from the transmission-line model. This conflicting requirement results in an envelope function that is localized in the center and vanishes at the facet, as illustrated in Figure 3.4.4 (e). On the other hand, the boundary condition for the lower-band-edge mode is consistent with both the transmission-line and DFB requirements, resulting in an envelope function with large amplitude at the facet. As a result, the upper-band-edge one has a lower radiation loss and thus becomes the lasing mode. In comparison, for the same reason, if the open facet is chosen at the narrow position of the waveguide, the envelope function will have maximum (minimum) close to the open facet, resulting in a higher (lower) loss for the upper (lower) band-edge mode. In addition, as described in [135], the rear facet is tilted and covered by gold, which causes the asymmetry of the mode.

3.4.3 Numerical analysis of the waveguide

For this thesis, the numerical analysis was mostly performed with COMSOL 3.2 and HFSS. Eigenmode solver was used to analyze the mode properties of the wire QC lasers. In these simulations, laser cavity was assumed as a cold cavity, which meant that the material loss and gain were not included, due to their unavailable precise information. Perfectly matched layer were used to ensure zero reflection at the boundary. The eigenvalue of the simulation result is the propagation constant, of which the imaginary part represents the loss of the waveguide. Due to the cold cavity assumption, only mirror loss was included by this imaginary part of the propagation constant. Mathematically, it can be written as:

$$\alpha_m = imag(\beta^2) \times 2 \times N_{bulk}/100 \qquad \textbf{(3.4.3)}$$

where β is the propagation constant and N_{bulk} is the refractive index of the bulk material. To achieve lasing, the model threshold gain g_{th} has to reach α_m/Γ in which mode confinement factor has been factored into. A typical mode spectrum is illustrated in Figure 3.4.5. The lasing mode is the upper band edge mode (3.75 THz) whose loss is ~2cm^{-1}. It is worth studying more about the upper bands which have two categories of

modes: The fundamental modes, indicated by a red dotted line, and the second order lateral modes, represented by green dotted line. The loss of fundamental mode increased from the band edge mode to higher order longitudinal modes because the mode energy was localized more close to the facet. The loss of the second order lateral mode decreased along frequency increasing because the modes became more localized in the center. In fact, sometimes both the upper band edge mode and mode B (4.15THz) could lase simultaneously in the experiment because of the broad gain band width. To achieve a robust single mode operation, other methods to further discriminate modes need to be deployed.

The simulation also proves the advantage in choosing the upper-band-edge mode as the lasing mode. For a specific device described below in Figure 3.4.5, upper-band-edge modes have a simulated tuning range of ~340 GHz by pushing the metal plunger from 20 μm distance to 1 μm, compared to ~190 GHz of the lower-band-edge mode.

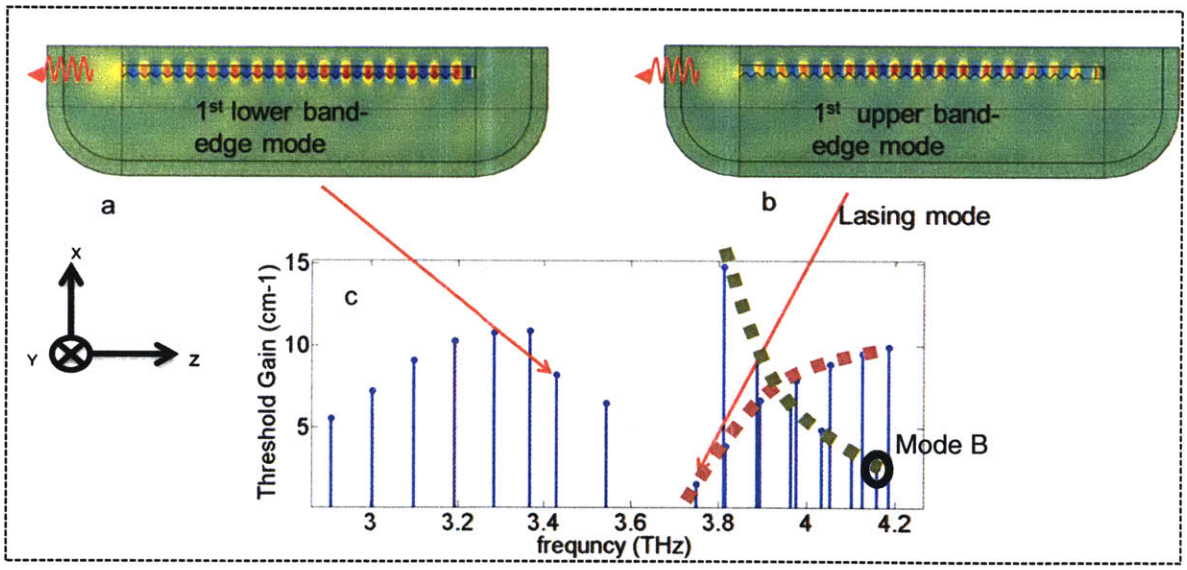

Figure 3.4.5 A typical mode spectrum of a device with 12.5 μm width and 13.7 μm periodicity. (a) The mode profile of a lower band edge mode. The mode maximum of Ey field was aligned with the wider section of the grating. (b) The mode profile of a lower band edge mode. The mode maximum of Ey field was aligned with the narrow section of the grating. (c) The mode spectrum of this device. Both upper and lower band edge modes are identified. The mode between the two band edges was a defect mode because the translational symmetry was broken by both front and rear fact.

3.4.4 Bonding pad design

The THz wire laser is a device with deep subwavelength dimentions. A typical width of this kind of laser is in the order of ~10 μm, which is much narrower than the typical wire-bond size of 60-80um. Due to this size mismatch, it is impossible to make wire bonds directly on top of the device to electrically bias QCLs. Thus, a bonding pad is a necessity, and should not interfere with the plunger movement.

As demonstrated in the previous section, the original effort tried to put the bonding pad beside the grating and connect it with the wire laser through a tilted corrugated side wall. The difficulties of this design came from the broken connection at the corner of laser ridges and the bad insulation under the metal layer on tilted side wall. Additionally, the metal layer on side wall introduced large extra losses which degraded the laser performance significantly. Thus an improved design proposed to place the bonding pad behind rear facet and connect it with the top metal through coating the tilted rear facet (Figure 3.4.1). The bonding pad and the metal layer on the rear facet were insulated from the gain medium by a thin layer of SiO_2. However, the mode can be guided into the thin SiO_2 layer by the gradually thinned rear facet, which is similar to a horn antenna. The SiO_2 thickness is only 300nm and the mode is extremely loss in this thin layer covered by a metal sheet. This is not only because SiO_2 is lossy but also because the mode is pushed into the metal due to the extremely tight confinement. The simulation showed that the reflection from the rear facet can be only ~60% with 300nm thick SiO_2.

The other drawback of this rear facet design is the fabrication difficulty. Wet etching by $NH_4OH:H_2O_2$ was used to select the plane 45 degrees relative to the vertical direction. But it is difficult to control wet etch speed to get the rear facet at a precise position. Moreover, the fabrication of this rear facet requires lithography on a tilted plane which is very challenging due to the piled up photoresist at the corner. This difficulty will be discussed in detail later.

3.5 Plunger design

As discussed in section 3.2, the novel tuning mechanism, developed in this thesis work, requires a plunger which is placed beside the flat edge of the wire lasers. This plunger

can change $k_\perp$ while the first order DFB can fix k_z. To extend the tunability of the plunger, two kinds of plungers have been designed: metal plungers which can increase $k_\perp$, and dielectric plungers which can decrease $k_\perp$. These two plungers manipulate the transverse mode in a very different way and have to be carefully thought separately. In this section, the design detail of these two plungers will be discussed in detail.

3.5.1 Metal plunger

Metal plunger and dietetic plunger manipulate the mode in different ways, which will be explained in this section.

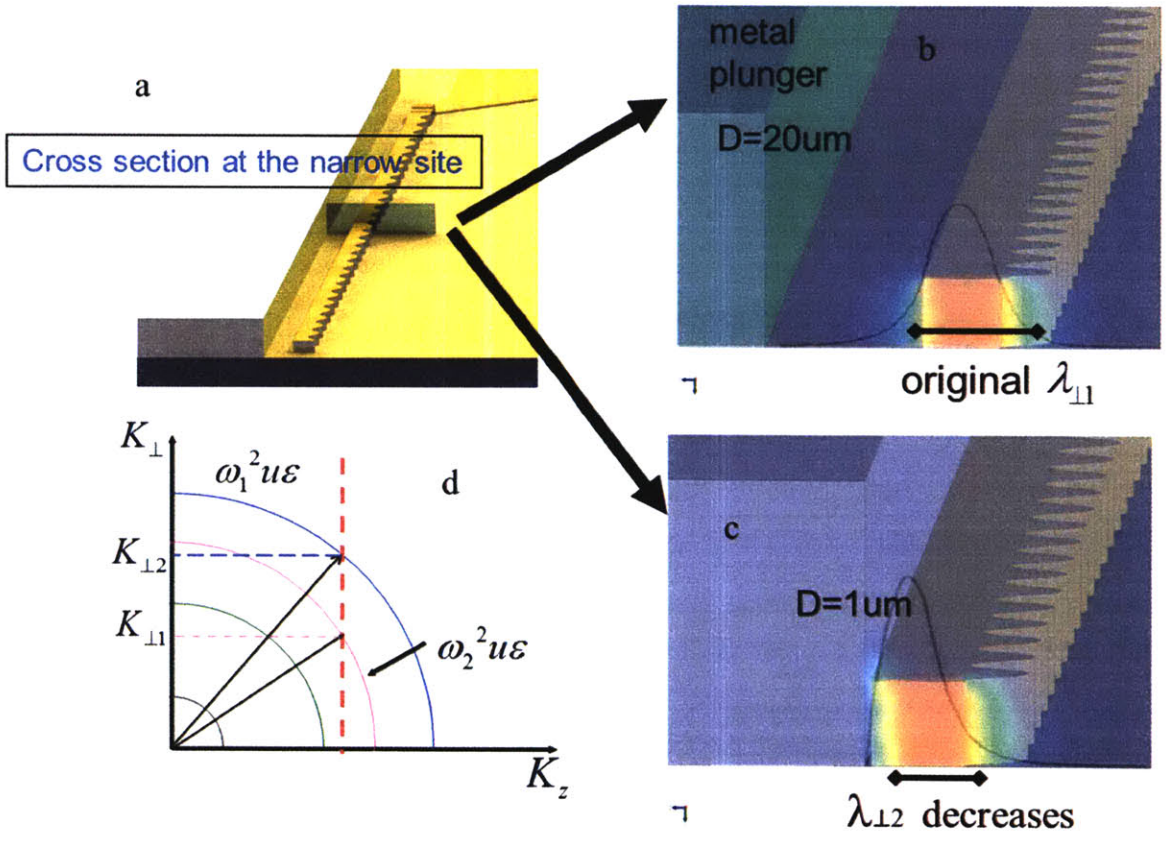

Figure 3.5.1 Illustration of the tuning mechanism with a metal plunger. a, Schematics of a wire laser and a assembled plunger. b, The mode profile of the cross section at a narrow section of the grating. Only Ey field is plot, and the plunger is ~20 μm away from the wire laser. c. Theoretical illustration of the tuning mechanism. d. A deformed mode profile when plunger is only 1μm away from the wire laser.

The basic setup is illustrated in Figure 3.5.1. The metal plunger is beside the flat side of the wire laser. In this thesis work, the metal plunger is made of gold because of its high

conductivity, chemical stability and mature coating technology. On the other side is the sinusoidal corrugation without a metallic cover which allows the mode to extend out of the MM waveguide substantially. The upper-band-edge mode is used to demonstrate the tuning mechanism because it is the preferred mode for tuning purposes which will be explained later. The double plasmon mode originally is symmetrical when the metal plunger is far away from the waveguide. When the plunger moves toward wire lasers, the electrical field is shorted on the surface of the metal and mode is terminated there. On the other side, the mode is bounded by both metal/GaAs interface and index mismatch. Thus effectively, the mode is squeezed in the lateral direction. So $k_\perp$ increases as the metal plunger is pushed towards the laser as the mode approaches cutoff in the lateral dimension, resulting in a blueshift tuning. A more theoretical understanding is illustrated in Figure 3.2.1(c) which starts from Maxwell equation mentioned in the introduction. In this Figure, each circle represents a value of $\omega^2\mu\varepsilon$. This figure essentially illustrated the tuning scheme in which k_z and ε are fixed while $k_\perp$ is changed.

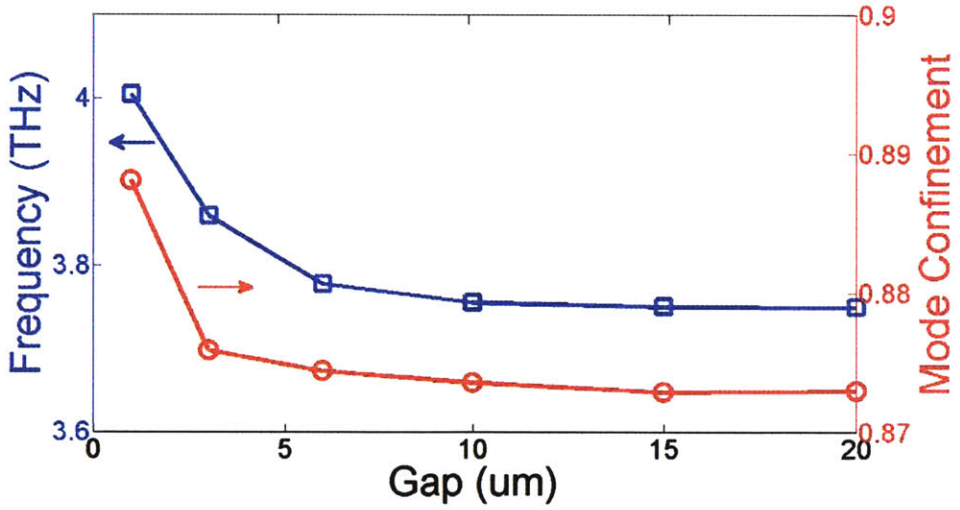

Figure 3.5.2 Illustration of the change of mode confinement during the tuning process. The x axis is the distance between plunger and wire laser. The blue curve represents the frequency tuning. The red curve demonstrates that the mode confinement increases when the plunger is pushed towards wire lasers. Both processes are very nonlinear.

A side product of this frequency tuning scheme is the changed mode confinement, illustrated in Figure 3.2.2. The mode confinement factor increases when the plunger is pushed towards to the wire laser. This confirms our conclusion that the mode is squeezed in the transverse direction. In a dielectric waveguide, squeezed mode should result in a

greater 'effective mode index' n_{eff} since more fraction of the mode is pushed into the solid core where the refractive index n is larger than vacuum n_0. However, the definition $k_z = n_{eff}(\omega/c)$ suggests that the parameter n_{eff} actually decreases due to the blueshift of ω (note that k_z is kept fixed by the grating periodicity), which is counterintuitive to conventional understanding. Hence, to avoid confusion, this tuning mechanism is best described by considering the variation of the parameter $k_\perp$ instead of the parameter n_{eff}. Figure 3.5.2 also illustrates the nonlinearity of the tuning process. Most of the tuning is from the last ~5μm of the plunger movement. This fact makes the design of mechanics more challenging since the high spectroscopic resolution can be translated into high precision of the movement in this case.

A drawback of the metal plunger is the associated extra loss. In general, the loss introduced by metal plunger can be categorized into two kinds: the scattering loss related to surface roughness and the metal loss. The scattering due to surface roughness is expressed as [136]:

$$\eta = 1 - \exp[-(\frac{4\pi\sigma cos\theta_i}{\lambda})^2] \quad \textbf{(3.5.1)}$$

where η is the percentage of scattering loss, σ is the root-mean-square (RMS) roughness of the mirror surface, θ_i is the incident angle, and λ is the light wavelength. In general, the RMS of plunger surface is less than 1um, which give a value of η <2% at 3THz.

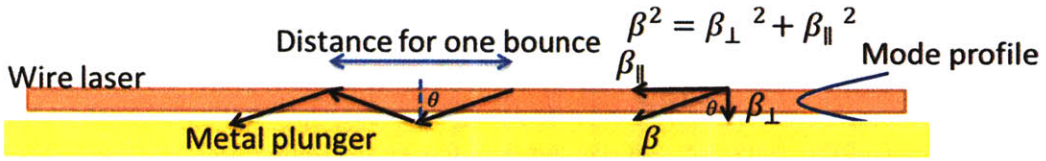

Figure 3.5.3 Illustration of the calculation of losses due to the surface roughness. Here, a geometric optical method is used to estimate the loss. The beam path is indicated in the middle of the figure. The incident angle is estimated by calculating the angle of the wave vector. The distance the light travel for one bounce is indicated in the figure and calculated in the next paragraph.

The loss due to this roughness scattering can be estimated. For the upper band edge mode, $\beta_\parallel$, which is the longitudinal wave vector and defined as π/Λ, is fixed by the DFB

grating. β, the total wave vector, is defined as $n_{GaAs} \times 2\pi/\lambda$, where λ is the free space wavelength. $\beta_\perp$, the transverse wave vector, can be calculated by the equation $\beta^2 = \beta_\perp{}^2 + \beta_\parallel{}^2$. The calculated incident angle θ ($\tan(\theta) = \beta_\parallel/\beta_\perp$) can be applied to the calculation of optical length per bounce by L=W(wire laser width)×tanθ. Here we assume the lasing frequency is 3.85 THz and the wire laser width is 10.5μm. The optical beam path is ~35 μm per bounce. Then the loss due to this surface roughness scattering is calculated by equation 1- η=exp(-αz), where α is the loss. Finally, this loss is estimated as $<5cm^{-1}$.

The other source of loss is free carrier absorption from the metal material of the plunger. Essentially, the radiation penetrates into the metal surface and accelerates the free electrons which dissipate the accumulated energy by heat. The skin depth *d*, defined as the distance where the energy density falls to 1/*e* of its value, is:

$$d = \frac{\lambda_0}{4\pi n\kappa} \approx \frac{1}{4\pi}\sqrt{\frac{c\lambda_0}{\mu\sigma}} \quad (for\ metal) \tag{3.5.1}$$

where λ_0 denotes the wavelength in vacuum, κ is called the attenuation index and σ is the conductivity of metal. For a frequency of ~3.8THz, the skin depth in gold layer is ~40nm which is much smaller than the metal thickness of real plunger. According to ref [137], the reflectance of the gold mirror is ~ 99% which indicates a small metal loss. However, this number should be used in a caution since the quality of the gold on plunger is unknown.

3.5.2 Dielectric plunger

In contrast, when dielectric plungers (silicon in this work) are pushed towards the laser, the mode is sucked out of the gain medium into the plunger because the index mismatch between the plunger and the gain medium is small. Effectively, this dielectric plunger expands the mode profile in the transverse direction, as shown in Figure 3.5.4d.

Consequently, $k_{\perp}$ decreases, and redshift tuning is achieved. Again, a graphical illustration of this tuning mechanism is illustrated in Figure 3.2.1 (b).

There are many dielectric materials we can choose to make a plunger. The main concerns include index mismatch and material loss in the THz range. The redshift tuning stems from a small index mismatch between this material and gain medium. Material loss should be small in the THz range to minimize the extra loss from plungers. Moreover, it should be easy to fabricate the plunger based on the chosen material. Given all these concerns, silicon is the best choice. Its refractive index is close to GaAs's, and the high resistivity silicon (~5000Ω/cm^{-2}) is used to minimize free carrier loss. The mature silicon technology facilitates the fabrication of this silicon plunger.

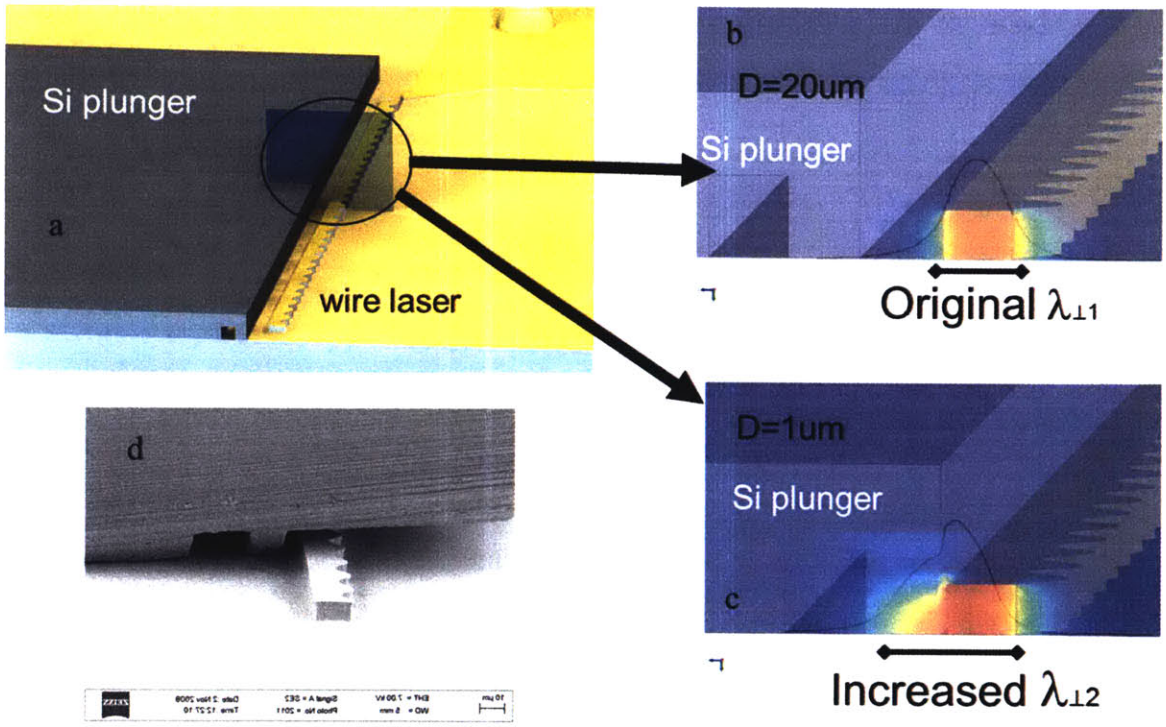

Figure 3.5.4 Illustration of the tuning mechanism with silicon plunger. a, Schematics of a wire laser and a assembled plunger. b, The mode profile of the cross section at a narrow site of grating. Only Ey field is plot. The plunger is ~20 μm away. c. A deformed mode profile when the plunger is only 1μm away from the wire laser. d. SEM image of an assembled device.

A major drawback of this silicon plunger is that it can cause a worse mode confinement. If bulk silicon is placed in a distance of ~1 μm from wire laser core, the mode will be significantly sucked into silicon due to the small index mismatch. The mode confinement

may drop to a level in which lasing cannot sustain. Thus we need an optimized design to limit the amount of mode the silicon plunger can suck out while maintaining its tunability. A trench in the silicon plunger (Figure 3.5.4 d) was used to achieve this goal. In this design, only a thin slab of silicon (~15μm wide) could manipulate the mode. However, a too slim silicon piece may result in a small tuning range due to its limited capability to suck mode out. Thus a width of 15μm is a result of the tradeoff between tunability and loss of mode confinement.

3.6 Mechanical design

It is challenging to design a mechanical system to demonstrate THz tunable wire lasers for two reasons. First, it is required to align plungers and wire lasers in a precision better than ~1μm. Furthermore, this system should be able function properly after a cooling from 300K to 5K. Secondly, continuous tuning requires a displacement resolution of better than 100nm. Thirdly, cryogenic mechanics is generally much more challenging than their counterpart in room temperature. This is further complicated by the difficulty to in-situ monitor the operation situation of the system at cryogenic temperature (~5K).

In spite of the difference, both metal and silicon plungers require a strictly parallel alignment between the flat edge of the wire laser and plunger. As will be discussed in section 4.4, a tiny tilt can result in a significant loss of tunability. This requires a guiding system to ensure that the plunger is always parallel with the wire laser along the entire displacement range.

The first design of this guiding system, illustrated in Figure 3.6.1, is a proof-of-concept design to quickly demonstrate the tuning concept. But this 'quick and dirty' mechanical design became a major obstacle to achieve continuous tunable THz wire QC lasers, which will be explained later. This guiding system, illustrated in Figure 3.6.1, was composed by an array of 10μm-high rails extruded on wire laser wafer and corresponding slots in the plunger wafer. Like male and female connectors, the shape and number of both extrusions and slots matched with each other, except that the slots were designed

longer than the rails to allow the plunger to move. The rails, made by 10μm high gain medium, were fabricated simultaneously with the DFB laser ridge in a same process. The length difference of the guiding rails and slots was also precisely designed to prevent the plunger from hitting into the DFB ridges. To achieve the size accuracy required by these strict alignments, a dry etching process, which could be well controlled, was used to fabricate both extrusions and slots. An actual plunger used in the experiment had an overhang which is ~7 μm above the laser ridge. Our simulation showed that this overhang has little effect on the tuning result because the evanescent mode was negligible at ~7μm height above the wire laser. To tune the frequency, the plunger could only be pushed towards the laser ridge and this movement was not reversible due to the lack of a restoring mechanism.

Although a guiding system was carefully designed, it was still challenging to align the plunger and the wire laser due to the small rail height (~10μm). The way of aligning was to nudge the plunger by micromanipulator until a click between the plunger and laser die was seen under microscope. In this procedure, it was easy to get the plunger onto the wire laser and caused a scratch in the top metal, which should be carefully avoided. After the alignment, a home-made clamp was used to fix the plunger, demonstrated in Figure 3.6.2 b. Then it was assembled on a device holder made by oxygen free copper as a heat sink.

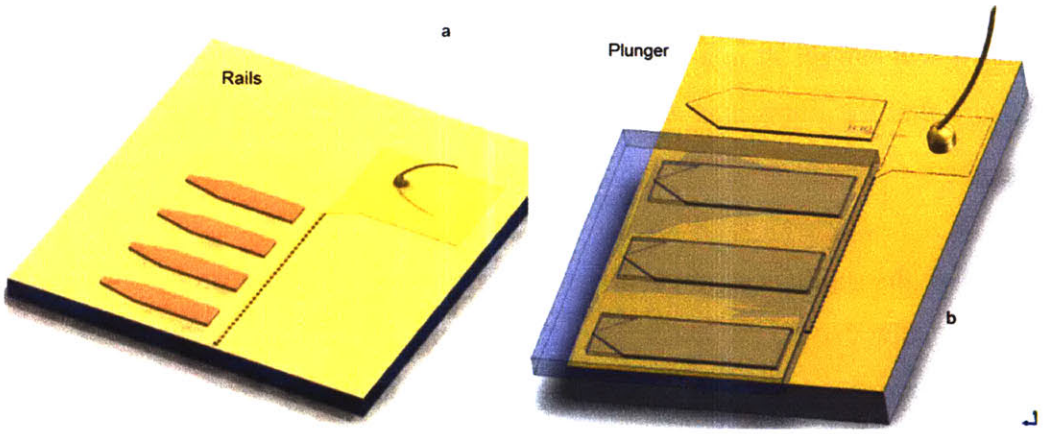

Figure 3.6.1 The guiding system of THz wire lasers. a. An array of taper-shape rails are made of 10μm high gain medium. b. Assembling scheme between plunger and device wafer. The slots in the plunger wafer match the rails on the laser die to guide the movement of the plunger toward the wire laser. The bonding pad is also shown in this figure.

The plunger is actuated by a piezoelectric-transducer (PZT) bender (P-871.140 Piezo Bender Actuator, http://www.physikinstrumente.com/en/products/prspecs.php?sortnr=101780). This bender has a continuous displacement range of 800 μm in either direction at room temperature, although data for cryogenic temperatures are not available. However, with this set-up, continuous tuning was difficult to achieve. This problem was identified as a known stick–slip effect **[138][139]**resulting from the difference between the static and dynamic friction when the plunger moves on the rails, which often causes an abrupt and discontinuous movement of the plunger. This effect is more severe when metal plungers are used because the frictional force between two gold surfaces increases when temperature drops to 5K**[140]**.

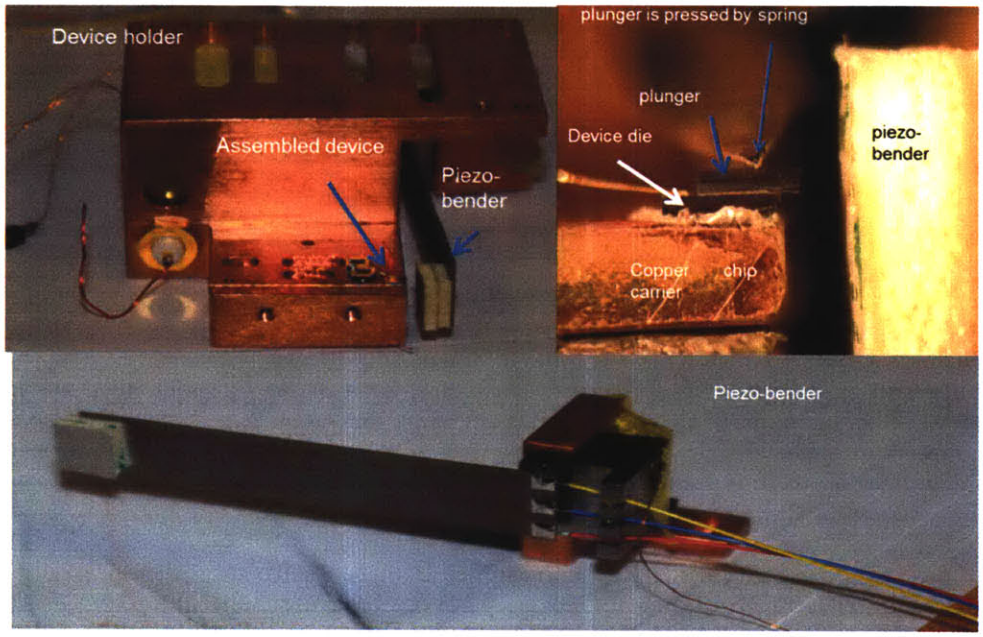

Figure 3.6.2 Initial design of device holder and actuator. a. Overview of the device holder with piezo-bender assembled. b. Detailed illustration of the assembling scheme between plunger and laser die. Only the tip of the clamp can be seen clearly because of the focal depth of the microscope. The piezo-bender is ~0.5 mm away from the plunger. c. The device of the piezo bender. It has three electrodes which connects the three layers of the piezo material.

Much effort was devoted to eliminating or reducing this stick-slip effect, such as using lubricant particles or making plunger suspending. But success was not achieved, using traditional methods to fight the force of friction, which was known several hundred years ago and is still not well understood. The failure could be attributed to the cryogenic

temperature operation and the microscopic size of the guiding system, which make these traditional methods difficult to implement.

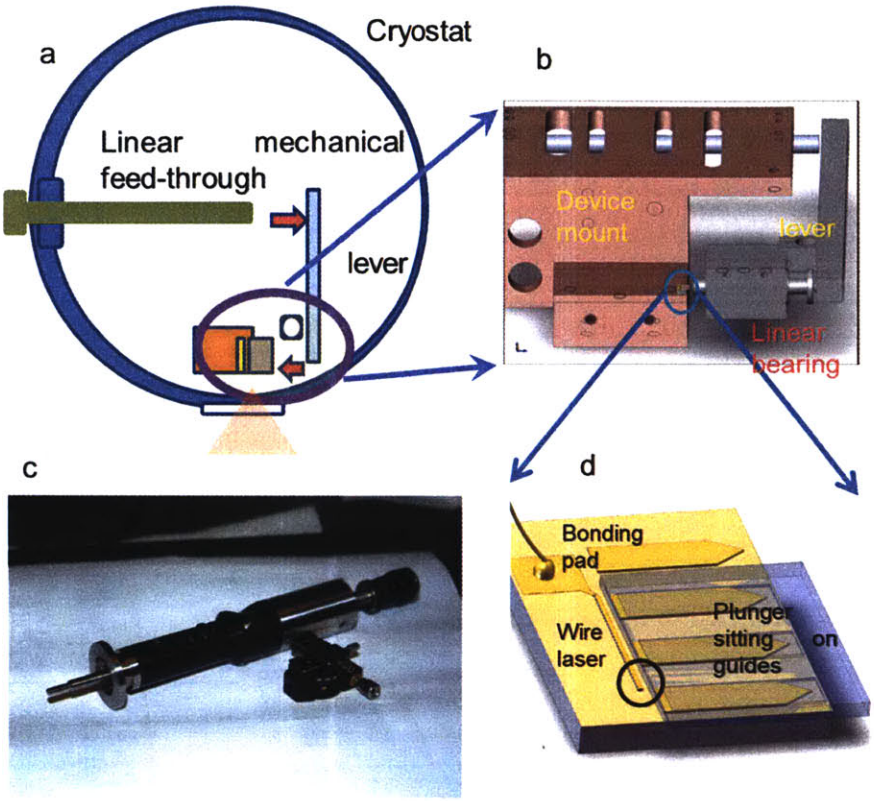

Figure 3.6.3 Design of the rigid mechanical system to overcome the friction problem. a, Schematic of the experimental setup, in which a differential micrometer is used to push the end of the lever's long arm, and the end of short am in turn pushes a plunger. b, Three-dimensional structure of device mount (copper color) and mechanical module (silver color). The device is mounted in the lower-right corner. c, Picture of the mechanical feed-through with a differential micrometer. d, Enlarged view of the highlighted region in b. It shows the plunger (transparent blue), lying on top of guide rails, is ready to be actuated by the shaft of a linear bearing.

Eventually, this friction problem was partially solved by a mechanical system comprising a lever actuated by a differential micrometer, which had a displacement resolution of 0.5 mm. This resolution was further improved by using this lever with a length ratio of ~4:1 between the two arms, shown in Fig. 3.6.3, resulting in a ~140-nm step resolution. This mechanical system was mostly made by rigid steel with except the thermal isolator, which was made of fiber glass. So the whole system was much stiffer than the PZT bender, allowing a much smaller deformation to overcome the static friction, resulting in a relatively smooth displacement of the plunger.

3.7 Fabrication of tunable THz QC wire lasers

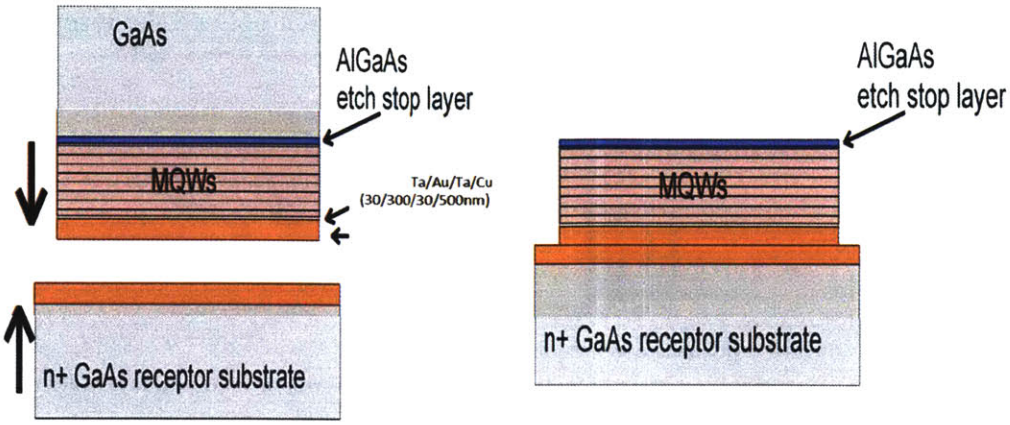

Figure 3.7.1 The key steps to prepare a gain medium for later lithography procedures. The left graph illustrates the thermal compression bonding, performed with 1500N force under 300 C° for a piece whose size is ~18mm by 18mm. Then the backside GaAs wafer was removed by a combination of mechanic lapping and wet-etching with $NH_4OH:H_2O_2$. The etching was stopped by an $Al_{0.50}Ga_{0.50}As$ etch stop layer, which would be removed by HF in next step.

The fabrication procedure of THz wire QC lasers can be divided into two stages. The first stage follows the same steps to make normal THz FP QCLs, shown in Fig 3.7.1. It started with depositing a metal multilayer on both a highly doped GaAs wafer and the QCL gain medium prepared by BOE dip. The metal stacks were Ta/Au/Ta/Cu (30/300/30/500nm). The first thin Ta layer was used to wet the GaAs surface and increase the adhesion of Au layer. Additionally, Ta has a very high conductivity and less loss in THz range than Titanium. The Au layer functioned as a dry etch stop layer in the later dry etching process. The second Ta layer was used to prevent Au and Cu forming alloy. The finishing Cu layer was employed to form a good thermal compression bonding between the receptor and gain medium wafers. After that, the backside GaAs wafer was removed by a combination of mechanic lapping and wet-etching with $NH_4OH:H_2O_2$. The etching was stopped by an $Al_{0.50}Ga_{0.50}As$ etch stop layer, which would be removed by HF in next step. Now the wafer was ready to be processed to define the tilted rear facet.

In the second phase of the fabrication, a layer of Ti/Au (30/300nm) was first deposited on GaAs wafer and eventually became the top metal of the wire QC lasers. Then, a wet etch by $H_2SO_4:H_2O_2$ followed a standard photolithography to define a tilted facet with ~45° angle, which is demonstrated in Figure 3.7.2. After that, a SiO_2 layer was deposited, and

then was defined by wet etch to cover the tilted side wall and the bottom ground as an insulation layer. After that, a bonding pad was deposited on top of the SiO_2 and connected with the top layer of wire lasers. Finally, a dry-etch defined the laser structure with the gold layer as a hard mask.

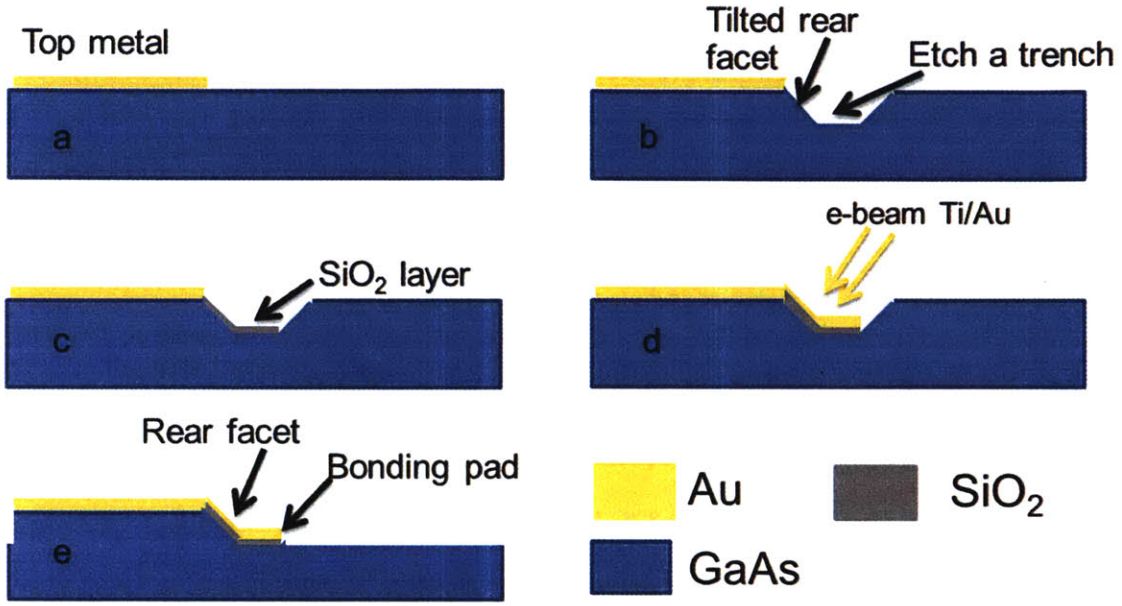

Figure 3.7.2 Fabrication process after the wafer bonding shown in Figure 3.7.1. (a) Top metal layer was deposited by e-bean evaporation. (b) A tilted sidewall formed by etching a trench. (c) A SiO_2 insulation layer was deposited in the trench. (d) A Ti/Au layer was deposited on top of SiO_2 and formed the bonding pad. (e) A dry etch was performed with the gold layer as the hard mask.

The challenge is to further improve the design from the perspective of the processing. First, the tilted facet and 10μm step pushed our fabrication capabilities to their limit. The large gap between the photomask and the tilted side wall resulted in a poor resolution during the contact lithography. Moreover the photo resist (PR) was piled up in the bottom corner and thinned down in the upper corner of the tilted sidewall. This non-uniform PR was a problem because this requires different exposure time in different areas. A balanced lithography recipe was required to universally fit to all the thickness, which was very challenging. Additionally, it was very hard to develop thick photoresist because of the abnormal heat transfer process in the corner during the baking time. Secondly, it was very difficult to connect bonding pad and top metal by using a directional e-beam deposition to achieve a thin layer of Ti/Au on tilted facets, illustrated by Figure 3.7.d (d). The reasons were threefold. First, there was a small overhang due to the wet etching,

shown in Figure 3.7.3. This could shadow the directional e-beam deposition and caused a disconnection at the upper corner. Secondly, there was a gap in the bottom corner also due to wet etching. This is illustrated by the SEM picture in Figure 3.7.3, although it did not happen to every device because of the nonuniform etching across the whole wafer. In this case, a disconnection resulted in an open circuit of the device. Thirdly, there was a weak connection at the upper corner of the tilted sidewall. Frequently, the metal layer was not even connected. This problem stems from the thin photoresist (~0.5um) at this upper corner in the lift-off process. The rule of thumb is that the thickness of the deposited metal is less than half the thickness of the PR. Thus, the maximum thickness of the Au layer at this upper corner is ~250nm, which may not survive the long dry etching step due to the bombardment, as illustrated in Figure 3.7.3. After many failures, we managed to develop a relatively successful recipe to fabricate this tilted rear facet. However, the low yield rate from this process motivated us to further improve the design and lead to the development of the comb-finger design, which will be explained in chapter five.

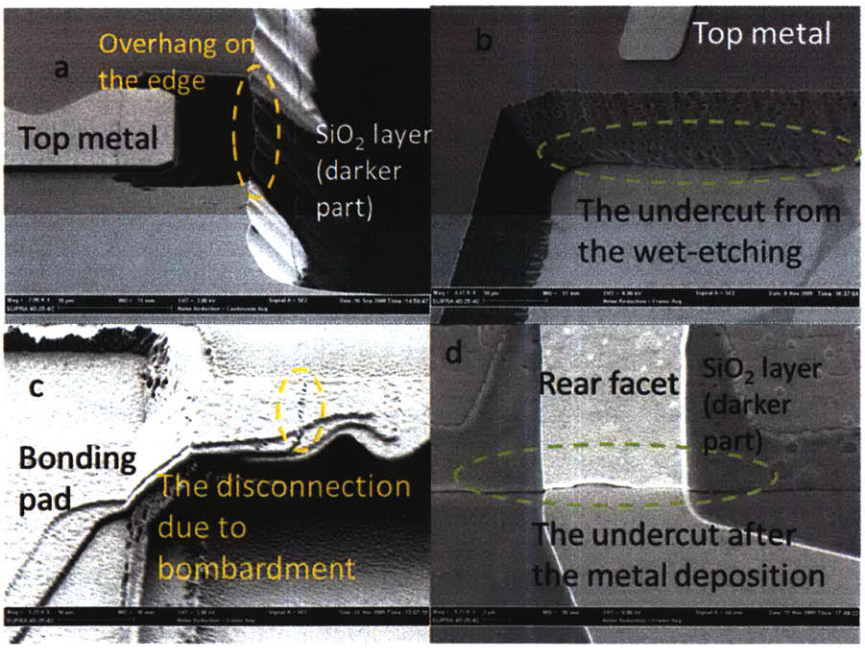

Figure 3.7.3 (a) SEM image of the overhang at the upper corner of the rear facet which can shadow the e-beam evaporation. (b) (d) SEM image of the gap caused by the over wet-etching. This gap is between the bonding metal layer and the gain medium (c) SEM image which shows the bombardment of metal layer which can cause disconnection.

The other important component of tunable THz wire QC lasers, the plunger, was relatively easy to fabricate. The fabrication of the metal plunger (Figure 3.7.4) started with GaAs wafers that could avoid any mismatch of thermal expansion with laser die. After standard contact lithography, Ti/Au (30nm/300nm) layer was deposited on the surface, and lift-off was performed to define the pattern. Then, a dry-etch by ECR-RIE with BCl_3 gas was used to etch away ~16μm thick GaAs, using Au as a hard mask. Finally, a second layer of Ti/Au (30nm/300nm) was sputtered on the sidewall of the plunger.

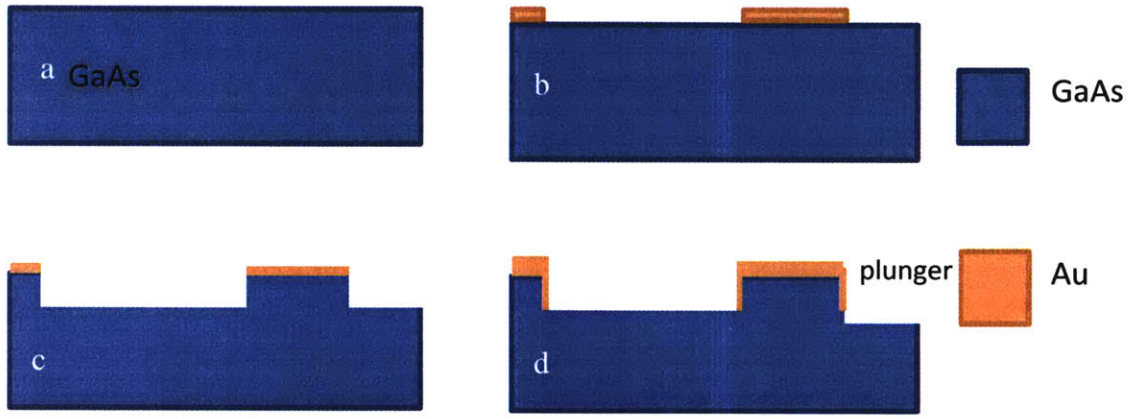

Figure 3.7.4 Fabrication process of the metal plunger. (a) The process started with a bare GaAs wafer. (b) Through a standard lift-off lithography and e-beam evaporation, a gold layer was formed on surface. (c) Dry etch was performed and the trench depth was about ~17μm. (d) A layer of Ti/Au was sputtered on side wall. The metal surface used to manipulate the mode is indicated in (d).

The fabrication of the silicon plunger started with a high resistivity (~5000Ω/cm^{-2}) silicon wafer. First, a 300nm-thick SiO_2 layer was deposited on the lapped surface. After standard contact lithography, buffered oxide etchant (BOE) was used to define the SiO_2 hard mask. Following that, a dry-etch by ICP-RIE with BCl_3 gas was applied to etch away ~17μm silicon, using the SiO_2 layer as a hard mask. Finally, the wafer was cleaned by piranha etching.

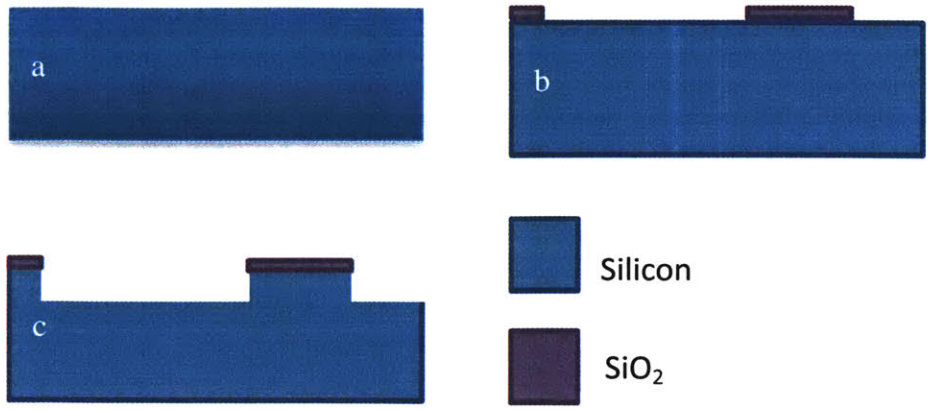

Figure 3.7.5 Fabrication process of the silicon plunger. (a) The process starts with a bare Silicon wafer. (b) SiO_2 was deposited on silicon wafer. After that a standard lithography and BOE etching were employed to define a SiO_2 hard mask. (c) Dry etch was performed and the trench depth was about ~17μm.

3.8 Tuning results

Before the measurement, the THz wire QC laser was first assembled on a heat sink made of oxygen free copper, and then was placed into a cryostat. The emitted laser light was collected without any optical components inside the cryostat due to the limited available space. Using a Nicolet 850 spectrometer (purged with N2 gas) and a Gallium-doped Germanium photodetector, all the spectra were measured at 5 K when devices were biased by a square wave with 90 KHz frequency and 200 ns duration.

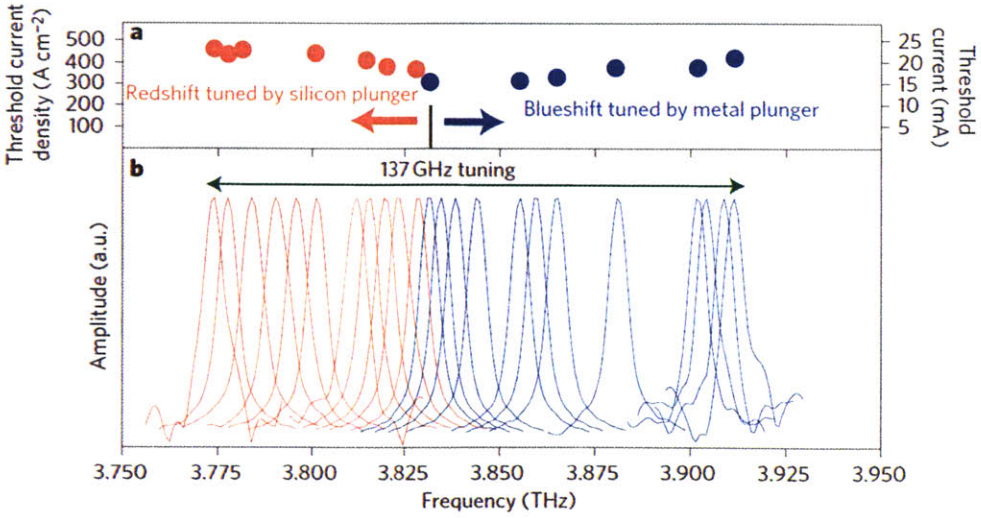

Figure 3.8.1 Tuning results from device T114. The device has an average width of 12.5 mm, a sinusoidal grating amplitude of 3 mm, periodicity of 13.7 mm and 30 periods. The blue and red

colours indicate the blueshift of frequency as tuned by a gold plunger and redshift by a silicon plunger. When operated without the plunger assembly, the device lased at the same frequency (~3.83 THz) as it did when the plunger was placed far away (25 mm in this case). (a) Threshold current densities of the device at different frequencies, showing a moderate increase as the plunger is pushed towards the laser ridge. (b) Broadband tuning of the device over a range of 137 GHz. All the spectra were recorded under the same drive current and temperature conditions. The small discontinuity is due to the stick–slip effect.

Frequency tuning was achieved using either the differential micrometer or the PZT bender. The results with the broadest tuning range, including both redshift and blueshift, from a single device are shown in Figure 3.8.1. With plungers, a redshift tuning of 57 GHz and a blueshift of 80 GHz were achieved. In combination, a total tuning of 137 GHz, or ~3.6% fractional tuning, was achieved. During the spectral measurements, both the device bias and the temperature were kept constant, so tuning due to Stark shift and/or temperature was negligible. In fact, the frequency shift of the DFB device with bias, with the plunger in a fixed position, was not measurable within the resolution (3.75 GHz) of the spectrometer. Hence, the frequency shift of the single lasing mode, shown in Figure 3.8.1, can be unambiguously attributed to the change of $k_{\perp}$ by changing the plunger position. The redshift tuning with the silicon plunger and blueshift tuning with the metal plunger are also consistent with our predictions.

Together, these results have firmly demonstrated the novel tuning mechanism explained in section 3.5. The total tuning range of ~137 GHz, although impressive and far greater than the previous results achieved with terahertz QCLs, is far less than the calculated result of ~430 GHz. This discrepancy can be explained by several possible scenarios. First, the theoretical calculation assumes a perfect parallel alignment between the plunger and the flat side of the DFB laser ridge. If the alignment is slightly off, even by half degree, the tuning range will be reduced by more than a factor of two. Such a misalignment could certainly not be ruled out in this proof-of-concept demonstration. This misalignment issue will be discussed in detail in chapter five. Secondly, as discussed earlier, most of the tuning is achieved when the plunger is very close (<~5 μm) to the laser ridge. Well-controlled movement of the plunger in such a close range was difficult to achieve with the present setup. The measured power changed along with the plunger position in a complicated way, due to the changing beam pattern and the changing

atmospheric attenuation with frequency. Also, the absolute power was too low in this experiment to be measurable using a power meter for two reasons. First, the measurement setup required the device to be placed far from the Dewar window, and secondly, a collecting optic, such as a metallic cone, was not allowed to collect the highly divergent beam emitted from the laser facet due to the spatial limitation. Thus, a more meaningful parameter for characterizing the laser performance is the threshold current at different plunger positions. This result is shown in the upper panel in Figure 3.8.1, which exhibited a moderate increase as either a silicon or a metal plunger was pushed towards the laser ridge. For the silicon plunger, this increase is due to a reduction of the mode confinement factor. For the metal plunger, the increase of the lasing threshold is likely due to the extra loss from the metal and a thin SiN insulation layer preventing shorting the plunger with the device.

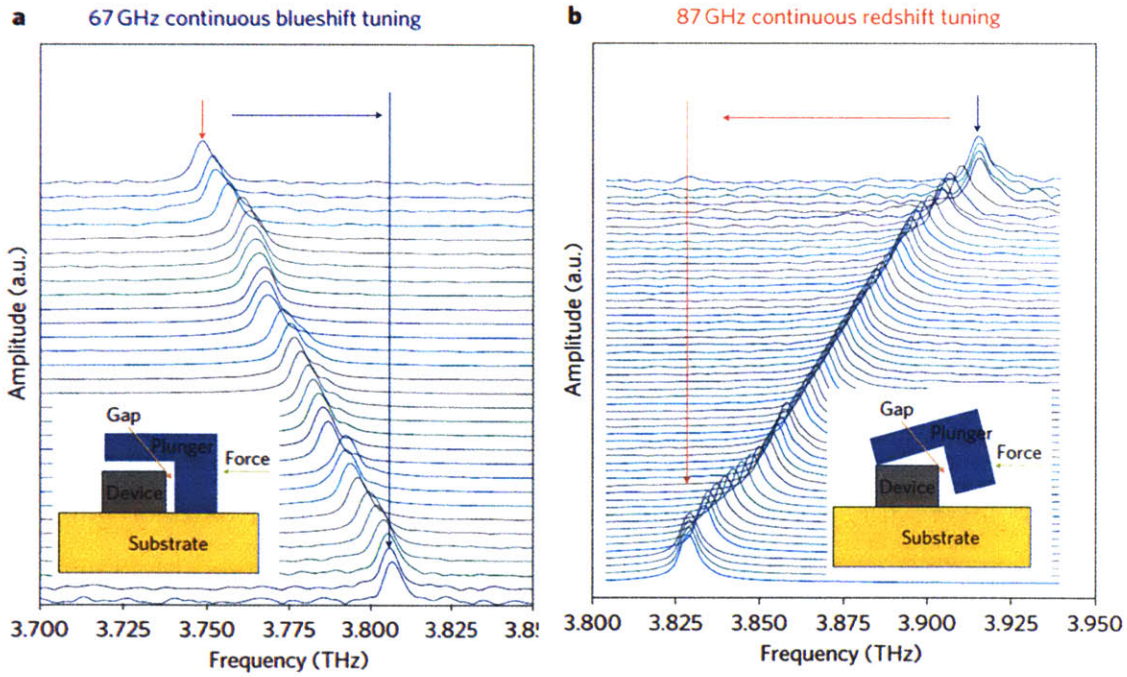

Figure 3.8.2 Continuous tuning spectra. (a) Continuous tuning of a device with a gold plunger over a range of 67 GHz. The device has an average width of 14.5 mm, sinusoidal grating amplitude of 3 mm, periodicity of 17.1 mm and 30 periods. All the spectra were recorded under the same drive current and temperature conditions. (b) Abnormal but continuous redshift tuning result for device T13, with a gold plunger, over a range of 87 GHz. The device has an average width of 12.5 mm, sinusoidal grating amplitude of 3 mm, periodicity of 13.7 mm and 30 periods. The tuning was redshifted when the plunger was pushed due to the roll-over movement, and is reversible for this particular case. The increased gap between the plunger and device during this process causes the abnormal redshift, as illustrated in the inset.

The tuning spectra in Figure 3.8.1 show some discontinuities, likely due to the stick–slip effect mentioned earlier. Additionally, the experimental results were not consistent because of the issue of friction. Figure 3.8.2 shows clear evidence of continuous tuning, although with smaller tuning ranges, from two measurements on different DFB devices. Figure 3.8.2a shows a continuous blue-shift tuning using a metal plunger, as expected. The result of a redshift tuning, shown in Figure 3.8.2b, was also attained by using a metal plunger. This puzzling result was understood when the set-up was inspected under a microscope at room temperature. It became clear that the plunger had been tilted inadvertently, and its overhang was hinged on the edge of the laser ridge, as illustrated in the inset in Figure 3.8.2b. As the upper edge of the metal plunger was pushed forward, the plunger was further tilted and the effective gap between the plunger and the laser ridge increased, resulting in the redshift tuning. Interestingly, free from the friction problem, this scheme allowed a reversible tuning, as a retreat of the piezo-bender relaxed the tilt of the plunger, yielding a blueshift.

3.9 Coating on sinusoidal side wall

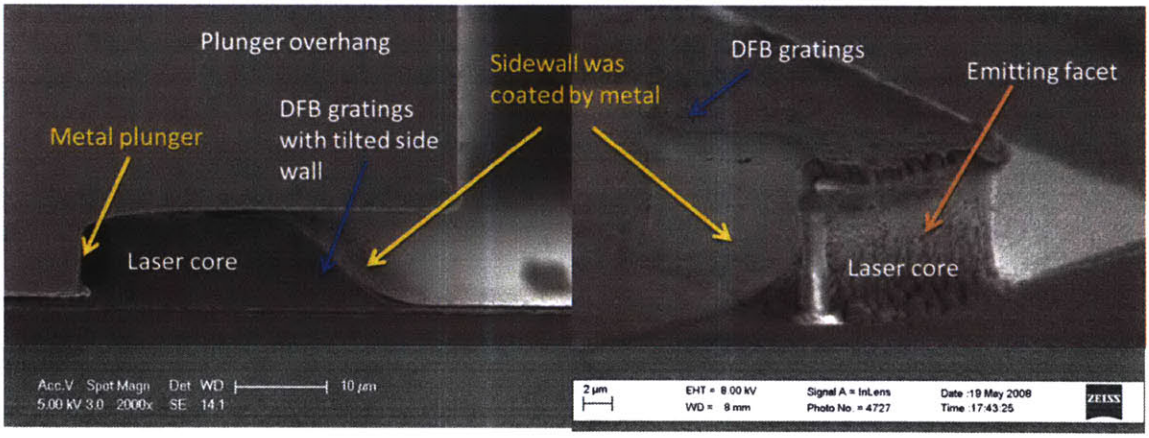

Figure 3.9.1 SEM images of the THz wire QC lasers with metal coverage on corrugated sidewall. The left figure shows a laser core assembled with a metal plunger, which had an overhang structure above the top metal. The DFB gratings were made in a tilted sidewall which was covered by a gold layer, insulated with a thin SiO_2 layer. The right figure shows a different design which had a vertical sidewall on the grating side which was also covered by Ti/Au layer. The rough sidewall was clearly demonstrated on the surface of the emitting facet.

The design with open sidewalls successfully demonstrated the novel concept of tunable THz wire QC laser. It is also worth discussing an attempt to increase the tuning range by

covering one sidewall with metal. The configuration of the two designs is illustrated in Figure 3.9.1. Both of them have a flat side wall open to facilitate the frequency tuning by plungers. In contrast, the sidewall on the grating side is covered by a Ti/Au layer insulated by a thin SiO_2. This design has two advantages. First, theoretically it can increase the tuning range by squeezing the transverse mode more tightly. As shown in Figure 3.9.2, the mode is totally confined in the laser core on the grating side (part b), compared to the other one which extends out of the open sidewall (part a). When the sidewall is covered by metal, the mode is sandwiched by two metal boundaries simultaneously. Simulation shows that, by covering the corrugated sidewall with metal, the tuning range of a device with 12.5μm width, is increased to ~600GHz using a metal plunger, compared to ~340GHz without a metal coating. Secondly, the metal layer on the side wall can connect the top metal with a bonding pad beside the laser core. This design can avoid the complicated rear facet, and so lead to a longitudinally symmetrical laser core.

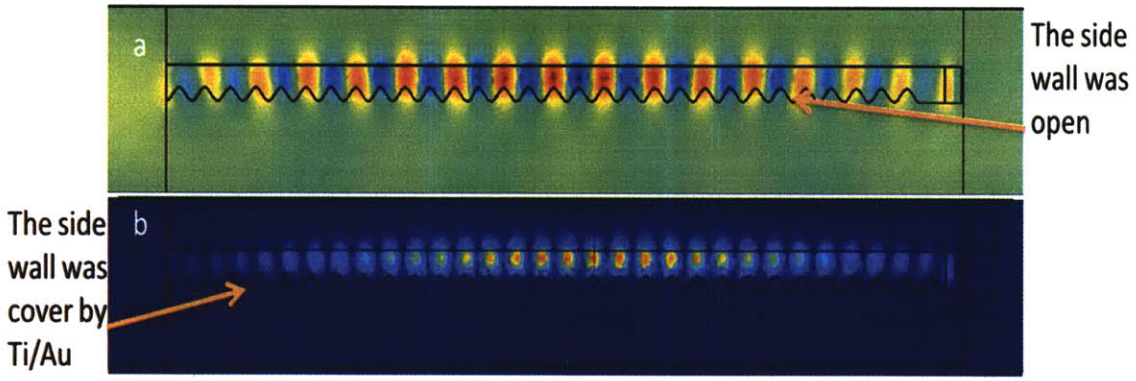

Figure 3.9.2 The modes of the QC wire laser with (b) and without (a) metal on the corrugated sidewall. In part a, the sidewall is open and the mode extends out from the grating side, while the mode was confined in the laser core by the metal on the grating sidewall in part b.

The biggest challenge to this design is how to coat the sidewall on the grating side. An isotropic sputter technique is not an option because it will coat everywhere unselectively. So we chose anisotropic e-beam evaporation. But it cannot coat vertical sidewalls. So wire-laser wafers were always tilted in the e-beam chamber to facilitate the metal coating since this sidewall cannot be "seen" effectively by the directional e-beam evaporator. To

avoid the device short circuit, the metal layer on sidewall was insulated from gain medium by a 300nm-thick buried SiO_2 layer.

In the first design, the gratings were embedded in a tilted side wall (Figure 3.9.1) to facilitate the sidewall coating. However, the yield rate was very low because either the coating was discontinuous at the corner or the device was shorted. The short circuit was due to the failure to attain full coverage of SiO_2 on the rough sidewall resulting from a dry etch. There are many SiO_2 balls forming on the rough sidewall, as illustrated in Figure 3.9.4. The intervals between these balls are not covered by SiO_2 and will be shorted if metal is deposited on them. Moreover, this tilted side wall can guide the mode into the lossy thin SiO_2 under the bonding pad, similar to the tilted rear facet. Thus, most devices based on this design did not lase at all or lased very poorly.

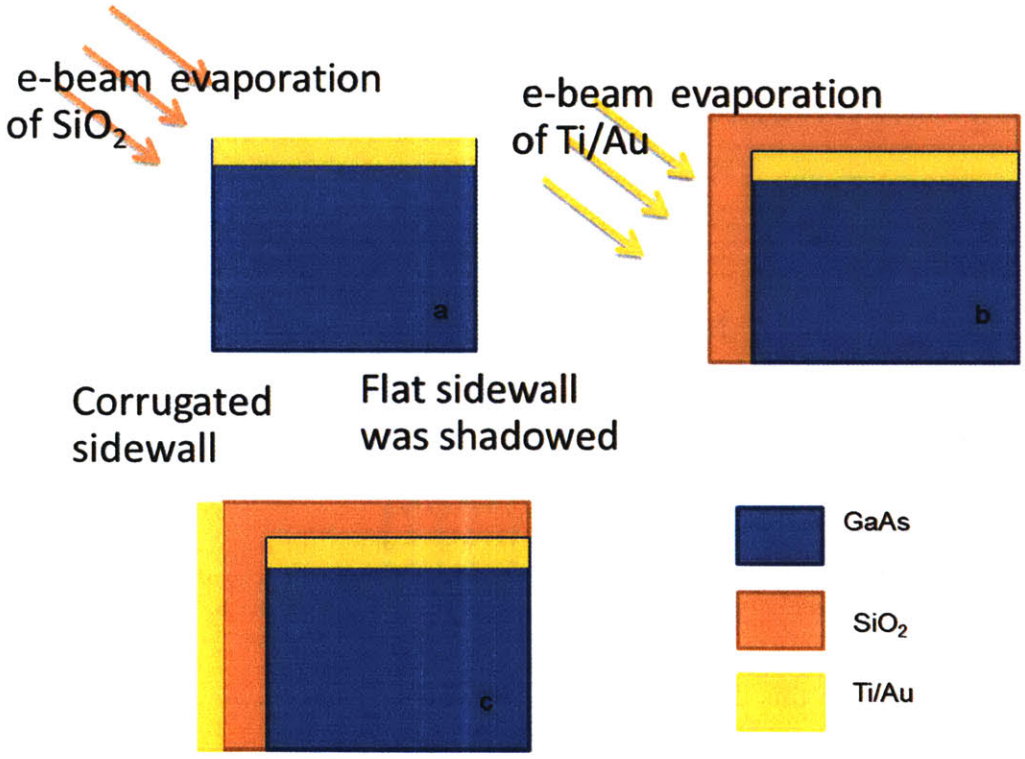

Figure 3.9.3 Schematics of process to coat corrugated sidewall. a, The process starts with a bare wire laser. ~ 1 μm SiO_2 was deposited with tilted angle and flat sidewall was shadowed. b, Ti/Au was deposited on SiO_2 with tilted angle in order to increase the coverage. c, The cross section of the completed device.

A second design kept the sidewall on the grating side vertical. However, this design still failed due to the rough side wall and the large material loss from the SiO_2 layer deposited by e-beam evaporation. Again the sidewall roughness resulted in a short circuit of the device. A thicker SiO_2 layer (1μm) was deposited to ensure a complete coverage, and perfect insulation between the metal layer and the gain medium. But for a ~15μm wide device, the lasing was stopped after the corrugated sidewall was coated with SiO_2/Ti/Au. Indeed, the thick SiO_2 layer introduced an extra scattering loss due to the sidewall roughness and an additional absorption loss due to the poor material quality of the SiO_2 from the e-beam evaporation. Annealing could not be applied because the high temperature (>500C°) may cause the metal stacks (Ta/Au/Ta/Cu) to form lossy alloys. Another possible reason is the extra loss and the smaller mode confinement introduced by the metal coverage on the corrugated sidewall. This result echoed the fact that lasing stopped when the metal plunger (Ti/Au) was very close (~1μm away) to the laser core with both sidewalls open.

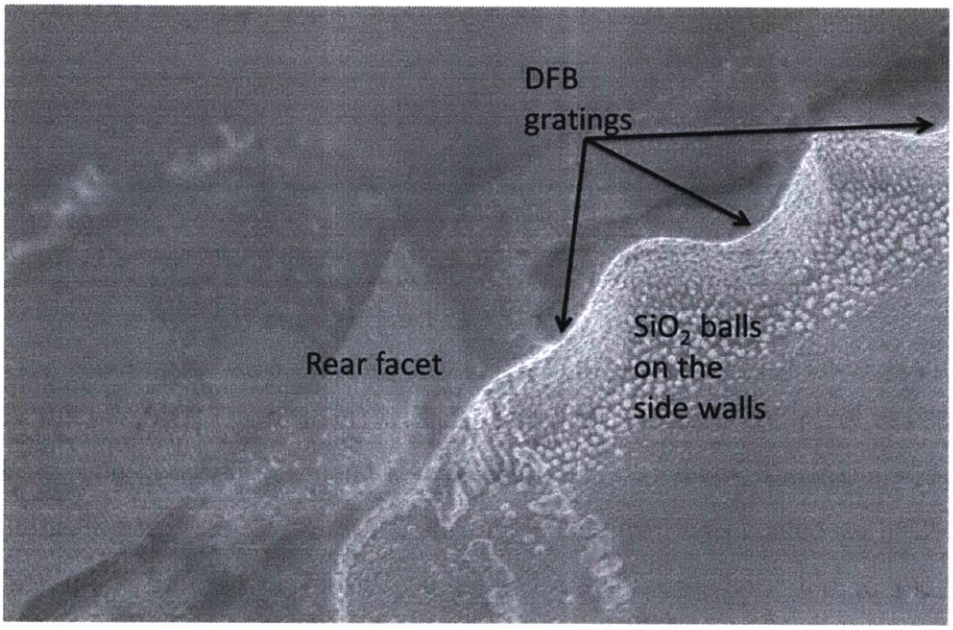

Figure 3.9.4 SEM image of a THz wire laser after a SiO_2 deposition which resulted in many SiO_2 balls formed on the rough side wall. The intervals of the SiO_2 balls were not covered and could short the device if a layer of metal was deposited on the sidewall.

3.10 Summary

In this chapter, following the discussion of the tuning mechanisms, the design principles of THz wire QC lasers and plungers were discussed in detail. The novel frequency tuning mechanism, by changing $k_{\perp}$, applies to wire lasers at any frequencies. For another wire laser technology at visible frequencies [141] developed at a same time, one could envision using a scanning probe to manipulate the transverse mode profile to tune the frequency for sensing and spectroscopy at nanometer scales. For terahertz wire lasers, further development based on MEMS (micro-electro-mechanical systems) technology will allow a better control of the plunger, which will result in a finer tuning over a broader frequency range in a reversible way, as discussed in next chapter. Such a controlled tuning will also offer a mechanism for frequency stabilization using feedback control. Finally, the generated tunable single-mode signal from a wire laser can be fed into an integrated terahertz amplifier to produce high-power radiation with good beam patterns, which will be discussed in chapter six.

4 Development of MEMS plungers

4.1 Introduction

Based on the THz wire laser, whose transverse dimension w is much less than the wavelength ($w \sim \lambda_0/6$), a record tuning range was demonstrated in the previous chapter. This tuning range was achieved by manipulating the transverse wave vector with a plunger, which is a moveable side object made of a metal or dielectric material. The practical applications require the plunger to move controllably and strictly translationally with a ~ 10 nm displacement resolution. However, due to the stick-slip effect [142] and the lack of a restoring mechanism in the guiding system, the plunger moved discontinuously and irreversibly [135], limiting its practical applications. These problems stem from the initial objective to make a 'quick and dirty design', in which the plunger slides on the laser substrate and is guided by a rail system, as illustrated in chapter three. Another problem is the plunger tilting which significantly reduces the tuning range. Moreover, the cryogenic operation of THz QCLs, which takes long to prepare the measurement, slowed the development progress. In the early development, although tuning was observed, the discontinuous frequency change puzzled us for a long time. Due to the jumpy lasing frequency, the mode hopping, which originates from unstable optical design, cannot be excluded. Another desired property of tunable wire QC lasers is a fast tuning speed which enables fast scan in spectroscopic applications. This needs a mechanical system which responses fast. These challenges call for a new design to increase the alignment precision and displacement resolution. In this chapter, a solution using plungers based on micro-electromechanical systems (MEMS), is presented.

4.2 Friction issue

Friction is a force resisting the relative motion of solid surfaces, fluid layers, and material elements sliding against each other. It may be one of the most ancient topics in physics. The classical rule of sliding friction was discovered by Leonardo Da Vinci more than five hundred years ago. But even till today, it is still not an antique topic. This is evidenced by

the research of the stick-slip effect which causes the jittering movement [142]. Essentially, this effect is from the atomic force between the two surfaces which contact with each other. The attraction force has to be overcome in order to move a mass and then accelerate too much before this mass eventually slows down by dynamic friction. This process is called stick-slip effect, an intensive research topic in the field.

As sketched in Figure 4.2.1, the apparatus to demonstrate stick-slip effect includes a surface made of Bristol board which has a nominal contact area of $8\times9cm^2$. A spring with stiffness k and constant speed v pulled a slider of mass m. A clear discontinuous displacement was observed. The slider was in a "stick" state associated with the elastic loading of the system and experienced a sudden "slip" corresponding to stress relaxation. This is directly related with the discontinuous tuning observed in the early development of tunable wire lasers. In our case, the actuator could deform and functioned as a spring. The plunger, sliding on device wafer, experienced stick-slip effect when it started to move. The resulted jittering displacement caused the discontinuous tuning. This effect was more severe when the plunger was in the distance range of ~5um from the laser ridge because the lasing frequency is very sensitive to the plunger position. However, this discontinuous displacement is hard to be directly observed due to the difficulty to install a monitoring equipment in the cryostat where the tunable wire laser was seated. On the contrast, this effect is indirectly proved by the continuous tuning result when a stiffer mechanical design was used.

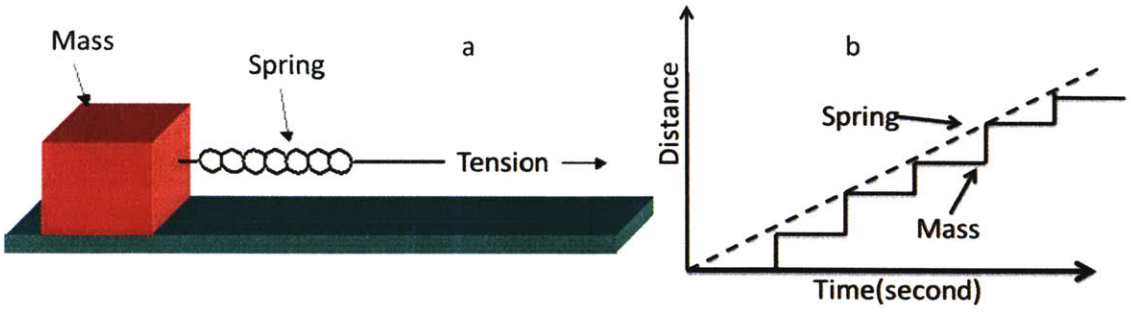

Figure 4.2.1 (a) The mass and spring being pulled by a tension force. (b) Time evolution of the slider displacement with respect to the bench, in the stick-slip phase. The jittering movement of the mass shows the creep precursor to the actual slip.

4.3 MEMS flexure

Flexure is a traditional mechanical design, broadly used in equipment which requires precise linear or rotary motion or a combination of both. It can eliminate frication which is a roadblock in many precision engineering works. Figure 4.3.1 illustrates two typical flexure designs. The key element in flexure structures is bending components which allow a precise linear or rotational movement. In part (a) of Figure 4.3.1, a curved hinge can bend and leads to motion. In part (b) and (c), the both beams can bend, resulting in a relative motion between the upper and lower stages. The flexure design can conveniently satisfy the requirement of different stiffness in different directions, using different bending designs. On the other hand, MEMS design is attractive to the field of photonics for its fast response and smaller features compared to traditional designs. As a combination of both, a MEMS flexure inherits the merits of its both ancestors. It has been applied broadly in photonic devices [143][144].

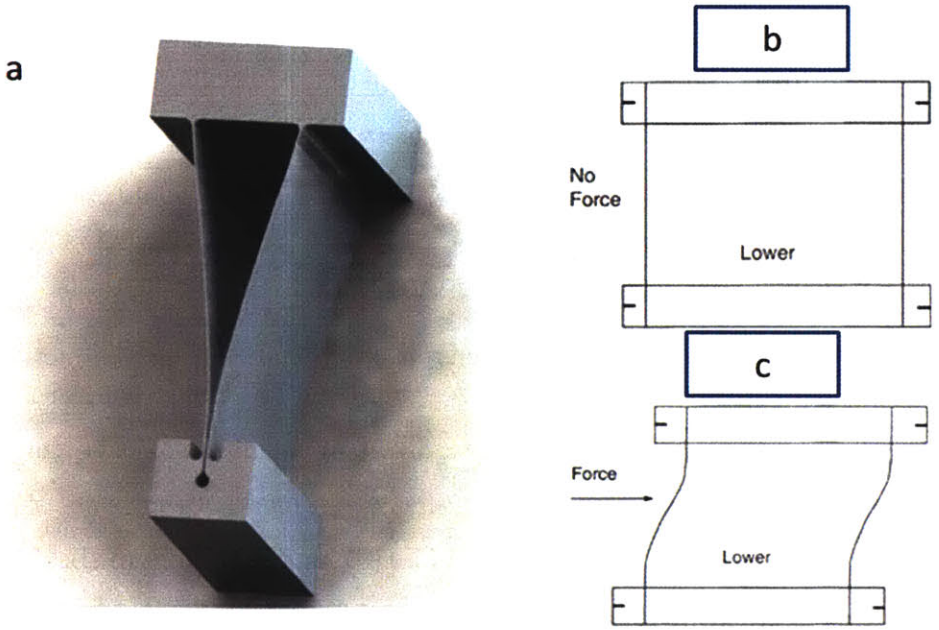

Figure 4.3.1 from [145] (a) a curved flexure design. (b) and (c) show a flexure that allows linear motion. As illustrated, pushing on the top stage can move it linearly with respect to the bottom stage.

There is little reported work about the MEMS technology operating at liquid helium temperature. In this thesis work, in a ~5 K environment, using a MEMS plunger

actuated by a differential micrometer, the distance between the plunger and THz wire laser is continuous changed which lead to a reversible frequency tuning. The assembling scheme of a MEMS plunger and a wire laser is illustrated in figure 4.3.2.

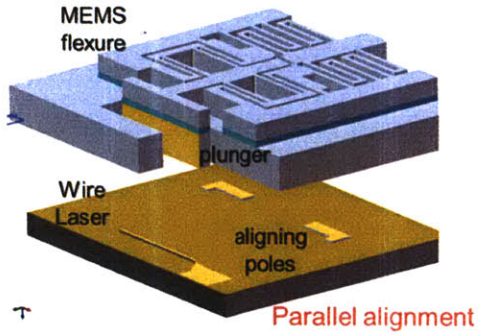

4.3.2 The assembling scheme of a MEMS plunger and a wire laser. The detail will be explained later.

Due to the small size of both the wire laser die (2 mm × 2 mm) and the MEMS plunger (2.3 mm × 2.3 mm), it is difficult to implement a traditional aligned bonding technique here. In this work, a female–male aligned scheme is used in the assembly between the plunger wafer and the wire laser die, resulting in a better than 10 μm alignment precision. Using a clamp to fix the assembled structure, instead of bonding, avoids the mismatch between the thermal expansion coefficients of the silicon (MEMS plunger) and GaAs (material system for THz QCLs) wafers. A two-stage flexure design is used to isolate the misalignment from the external actuator. The appeal of the MEMS system is its frictionless, controllable, and reversible movement of the plunger. In addition, the compactness and potential fast tuning speed make this technique very attractive.

4.4 Sensitivity to the alignment quality

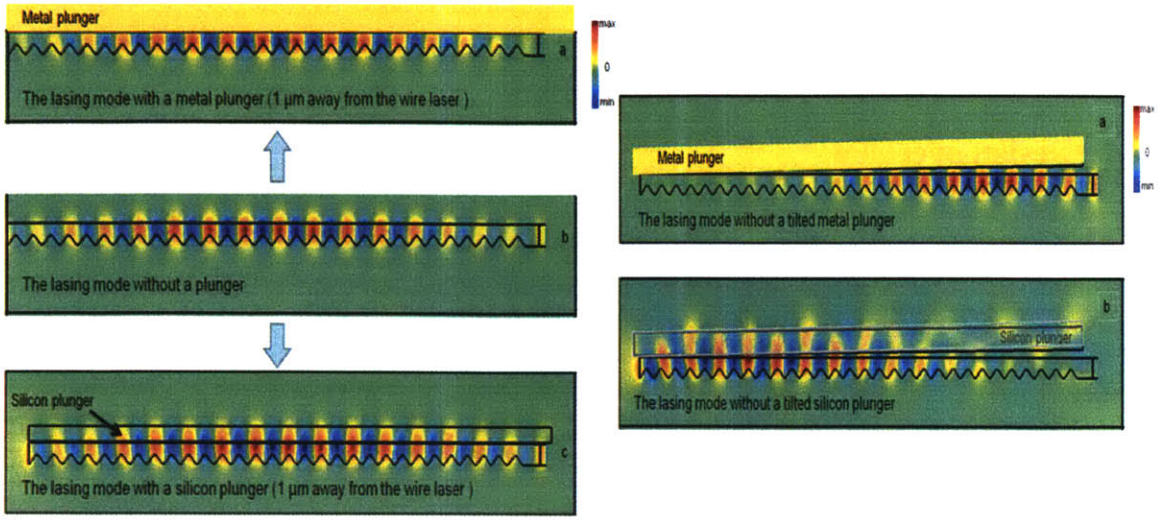

Figure 4.4.1 The left column: a. Lasing mode with the metal plunger 1 μm away from the wire laser. b. Lasing mode without the plunger. c. Lasing mode with Silicon plunger 1 μm away from the wire laser. The right column: a. Lasing mode with the metal plunger tilted by ~0.5 degree. b. Lasing mode with the silicon plunger tilted by ~0.5 degree.

One important characteristic of the tuning mechanism of a THz wire laser is the large sensitivity to both distance and relative direction of the plunger. As described in previous chapter, the frequency tuning is achieved by changing $k_{\perp}$, the transverse wave vector. This tuning mechanism is enabled by a substantial fraction of the mode traveling outside the waveguide core, which is a trademark of wire lasers. Most of the tuning is from the last few microns' movement of the plunger before it hits the wire laser. This highly nonlinear process requires the plunger to move as close as possible to the wire laser, in order to achieve the largest tuning range. Furthermore, it is necessary to keep the plunger parallel to the flat side of the wire laser throughout the tuning range. When the metal (dielectric) plunger is tilted relative to the flat edge of the wire laser, the mode will be pushed (extracted) longitudinally to the end where the plunger is further from (closer to) the wire laser, as illustrated in the right column of figure 4.4.1, compared to the ideal cases. Thus the tuning range is reduced dramatically with a metal plunger because the plunger cannot effectively move close to the mode. The simulation shows that even when the tilt angle of the metal plunger is as small as ~0.5°, the tuning range is reduced to 157 GHz, compared to the 370 GHz without tilting, that is, a reduction by more than a factor of 2. Additionally, the plunger can tilt about the Y-axis, resulting in an abnormal and undesired tuning behavior [135].

4.5 Design rule

4.5.1 Design overview

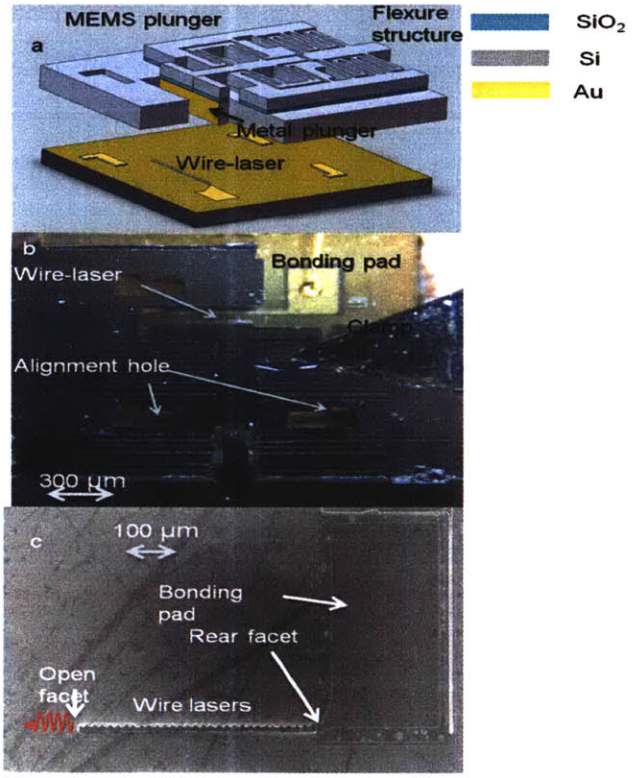

Figure 4.5.1 a. Illustration of the MEMS plunger and the wire-laser before assembling. b. Image of an assembled device. c. SEM picture of a bare wire laser. Different structures are indicated in the every image.

The design of the wire-laser and the MEMS plunger needs to take into account of several critical constrains that interleave with each other. First, due to the preciousness of the MBE-grown QCL wafer, the size of the wire-laser die should be limited in the range of a few millimeters. This also limits the size of the MEMS plunger because it has to reside on the wire-laser die. Secondly, to minimize the tilt about X and Y-axis, the spring design of the MEMS should have larger torsional stiffness about X and Y-axis (Figure 4.5.3). Thirdly, the alignment error should be minimized between the MEMS wafer and the wire-laser die. Fourthly, at liquid helium temperature (~5 K) the maximum displacement of the plunger should be larger than 20 μm to enable a full tuning range, which was discussed earlier. The assembling scheme between the MEMS wafer and wire-laser

should avoid the possible problems caused by the thermal expansion coefficient mismatch during the cooling process.

Combining all these considerations, we have come up with a design that is illustrated in Figure4.5.1 a and b. A complete device is assembled from two components, a wire-laser and a MEMS plunger, which were fabricated separately. The wire laser followed the same fabrication steps and used the same MBE-grown wafer as in ref. [135] (wafer VA0094, design FL183S, which is a resonant phonon design). This design has a gain peak around 3.8 THz. The device has an average width of 10.5 μm, 3-μm corrugation amplitude, 30 periods and 14.5-μm periodicity. The bonding pad is in the corrugation side of the wire-laser to avoid the interference with the plunger movement. Three alignment extrusions on the wire-laser die are 10-μm high, same with the height of the wire-laser. These extrusions are used to align the MEMS plunger and the wire-laser, which will be illustrated in detail later. One important feature of a real wire-laser is the tail structure (Figure 4.5.2), from non-uniform dry etching, in the bottom corner of the flat side wall. Thus, the bottom of the plunger is 1.5 μm higher than the substrate surface of the wire-laser die in order not to be blocked when it approaches the wire-laser.

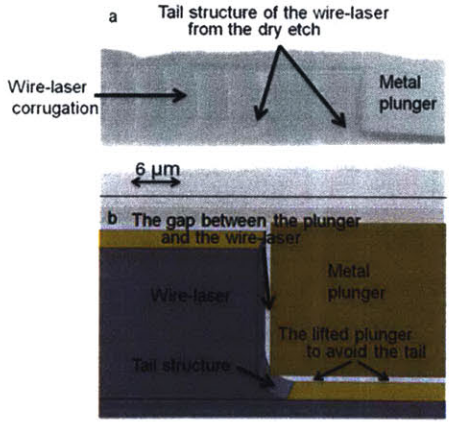

Figure 4.5.2 a. SEM image which illustrates the tail structure in the bottom corner of the wire-laser. b. Schematics of the lifted plunger to avoid the tail structure.

4.5.2 Two stage design to reduce tilting

The design was carried out, from three aspects to minimize the tilting possibilities about both X and Y-axis (Figure 4.5.3). First, a two-stage flexure design is used to enable a restorable and non-tilting MEMS plunger, as illustrated in Figure 4.5.3. The first stage in this design can isolate the second stage, which is attached with the plunger, from the external misalignment of the actuator. The shape of front of the first stage has a circular-arc edge, which could avoid the torque about Y-axis to be transferred to the second stage. Even when the first stage is actuated slantways, because of the front arc shape, the tilting of the second stage is minimized as long as the friction between the first-stage front and the second-stage tail is not too large. The stiffer design of double compound rectilinear spring is used in the second-stage design to minimize the tilt of the plunger at the expense of a smaller movement range compared to that of the first stage, in order to assure a greater precision.

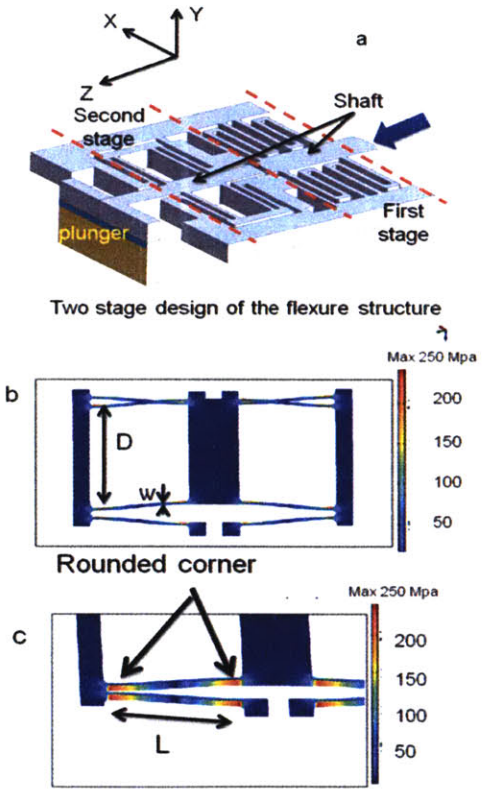

Figure 4.5.3 a. Illustration of flexure structure. b and c. Simulated results of the stress in the flexure structure with ~ 20-μm displacement. The maximum stress has been indicated in the color bar.

Secondly, since the alignment quality between the MEMS plunger and the wire-laser is crucial to the performance of the tunable wire-lasers, three L shape alignment

elements (Figure 4.5.5) are used to minimize the initial tilting about Y-axis. These three L-shape extrusions on the wire-laser wafer can click with the three L-shape holes in the MEMS plunger wafer. The size of the holes is only 10 microns larger than the extrusion structure to optimize the precision. The distances between the three alignment elements are 1200 μm, which has been maximized under the constraints of the die size. In this configuration, the worst case will give a ~0.5 degree (~180/120π) tilting. In addition, the alignment hole in the MEMS wafer is through the whole SOI wafer to facilitate the alignment when the extrusion can be seen through the holes. During the assembling, the MEMS wafer is first roughly aligned with the wire-laser die visually. Then the MEMS wafer is nudged by a micrometer until the alignment holes click with the extrusions and the laser die is forced to move with the MEMS wafer together. The difficulty of this alignment lies in the 10-μm thickness of the alignment structure. This small thickness could be easily shadowed by dusts which are larger than 10 μm size. Or if the edge of the extrusion or the holes is not sharp, the clicking effect will not function well because it is very easy to slide the MEMS structure (~500-μm thick) onto the 10-μm high structure. Thus a clean surface and sharp edge of the alignment structure are crucial for a good alignment. Therefore, solvent cleaning and nitrogen gas blowing were performed before the aligning to remove dirt or dust.

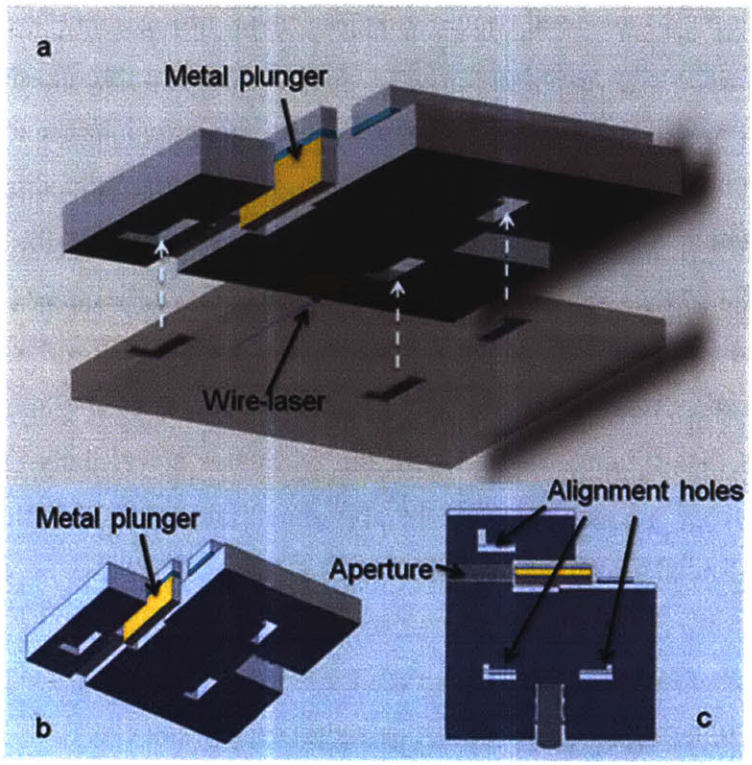

Figure 4.5.4 a. Illustration of the alignment scheme between the wire-laser and MEMS plunger. b and c. Detail of the backside of the MEMS plunger wafer from tilted (b) and bottom (c) view.

Thirdly, the plunger design needs to take into account of the tilting possibility about X-axis (Figure 4.5.3). The plunger mass and device layer thickness should be designed carefully to ensure no severe tilt of the second stage about X-axis. The torsional stiffness of simple leaf design about X-axis, which is proportional to the torsional stiffness of double compound rectangular design, is $Eh^3wD^2/2L^3$, where L, w, h, W, D and E are the length, width, height of the beam, the distance between the two beams, and Young's modulus, respectively. On one hand, the larger height is preferred to increase the torsional stiffness about X-axis. On the other hand, if the height is too large it can cause dry-etching difficulties due to a large aspect ratio. Therefore, 50-μm thickness of the device layer is chosen and the size of the plunger is ~ 700×50 ×550 μm^3. Additionally, as indicated by the torsional stiffness equation, to optimize this value, D should be maximized under the size constraint. Here, D was chosen as 250 μm for the second stage. A mechanical FEM simulation was performed, with commercial software COMSOL 3.5, to confirm that the design requirement is satisfied. It showed a negligible tilt about X-axis resulting from the plunger mass.

4.5.3 The mechanical strength of the MEMS plunger under cryogenic temperature

The possibility of catastrophic failure with the maximum displacement of the plunger should be considered after minimizing the tilting. The yield stress of Silicon is 5-7 GPa at room temperature and the data at 5 K are not known. In addition, because any defect from fabrication in the beam can cause failure as the stress is accumulated, the structure strength is not easily predicted before actual implementation. Thus a large safety factor is necessary to ensure non-failure displacement of the flexure. The largest stress in a cantilever beam is $3EwS/2L^2$ where S is the maximum displacement. As discussed in the introduction part, at least 20-μm displacement is required to cover the full tuning range. In the actual design, 40-μm maximum displacement of the second stage was used to yield a large safety margin. The non-actuated gap between the second-stage tail and the front-stage front is ~9 μm. Thus the required displacement range of the first stage is ~9 μm larger than the second stage. Therefore, a softer three-fold spring is used in the compound spring design of the first stage to ensure a larger displacement range. Indicated by the equation above, to achieve the 40-μm displacement range at ~5 K, thin and long beams should be used to avoid material failure. On the other hand, to avoid buckling of the second stage, thick beams should be used to increase the stiffness. This tradeoff between the two underlying factors results in the 20-μm thick and 650-μm long beam design in the first stage and 25-μm and 700-μm in the second stage. In addition, all the corners of the flexure structure were rounded by 25-μm radius halo (Figure 4.5.3 c) to avoid the stress concentration in the corner. A FEM simulation was performed to evaluate the maximum stress under the largest displacement. This simulation (Figure 4.5.3 b and c) shows that the maximum stress is 250 MPa with ~20 μm displacement. This gives a safety factor of ~20 at room temperature, which should yield a sufficient margin to compensate for the property change of silicon at cryogenic temperature.

4.5.4 Other considerations

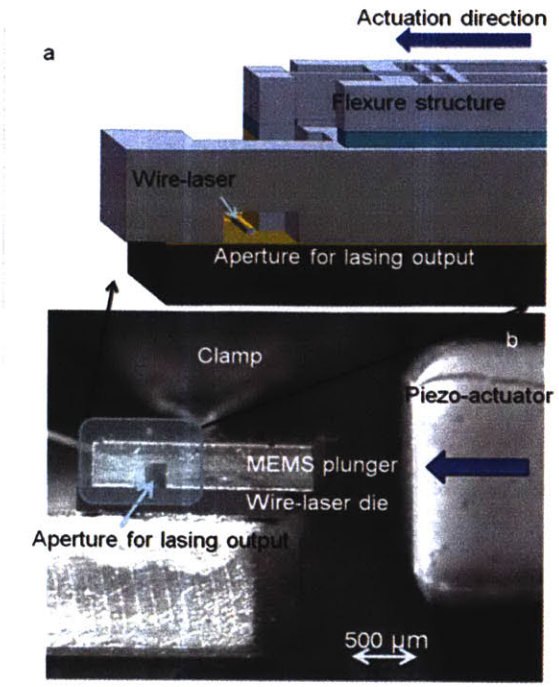

Figure 4.5.5 a. Illustration of relative position of the wire-laser and the output aperture. b. Photograph of the side view of an assembled device.

Besides the non-tilting and non-failure displacement at liquid helium temperature, several other factors need to be addressed. First, the bottom surface of the plunger is ~1.5 μm elevated from the bottom of the supporting structure, to avoid interference of the tail structure of the wire-laser (Figure 4.5.5). Second, beside the plunger head, as illustrated in Figure 4.5.5a, there is a ~ 250-μm deep and 200-μm wide trench, which is used as an aperture to output the laser emission. The depth of 250 μm was chosen so that the light can come out and the left ~250-μm handle wafer is still strong enough to survive during the later alignment step.

4.6 Fabrication

The MEMS plunger fabrication process is outlined in Figure 4.6.1. The process began with lithography on the handle side and dry etching for ~ 1.5 μm depth. Thus, the bottom of the plunger was lifted by 1.5 μm to avoid the interference from the tail structure of the wire-laser, which is discussed earlier. Then 3-μm thick SiO_2 was deposited on both sides

of wafer by PECVD, followed by an annealing at 1000 C^o for ~ 1 hour to increase the oxide strength during the later long dry etching. Both sides of the SiO_2 were patterned by standard lithography and BOE etching, and were used as hard masks. After this, a 10-μm thick photoresist was spun on the handle side of the wafer and patterned in such a way that all the through holes were open and the output aperture mentioned earlier was covered by photoresist. Then silicon etching was performed for ~250 μm depth by deep reactive ion etching (DRIE) using equipment from Surface Technology Systems. After this etching, the photoresist was stripped by piranha and the handle side of silicon was etched again until the through holes reached the embedded SiO_2. Thus the different depth etching in one side was achieved by this double mask technique. After the etching on handle side, two DRIE steps were performed on the device side, even though all the holes are through all the way to the SiO_2 layer. This two-step process is adapted so that a narrow gap (~9 μm) between the first and second stage can be etched uniformly all the way through. First, only the gap between the first and second stages was exposed to DRIE for ~35-min (~30-μm depth) etching with a thick photoresist mask. Then the photoresist was stripped and the whole device side was etched with annealed SiO_2 as the mask. This DRIE with double mask is necessary to achieve vertical sidewall of the beams of the flexure structure, which is necessary to avoid structure failure when the beams are deflected. It is desired to have DRIE reach the stop layer (SiO_2 in this case) simultaneously across the whole area because any further etching will drill a notch in the bottom corner, which can result in a weakened mechanic structure. However, the gap size between the two stages is only ~6 μm on mask (Figure 4.6.1), which is much smaller than other places and will result in a much slower etching rate. Thus only this gap was

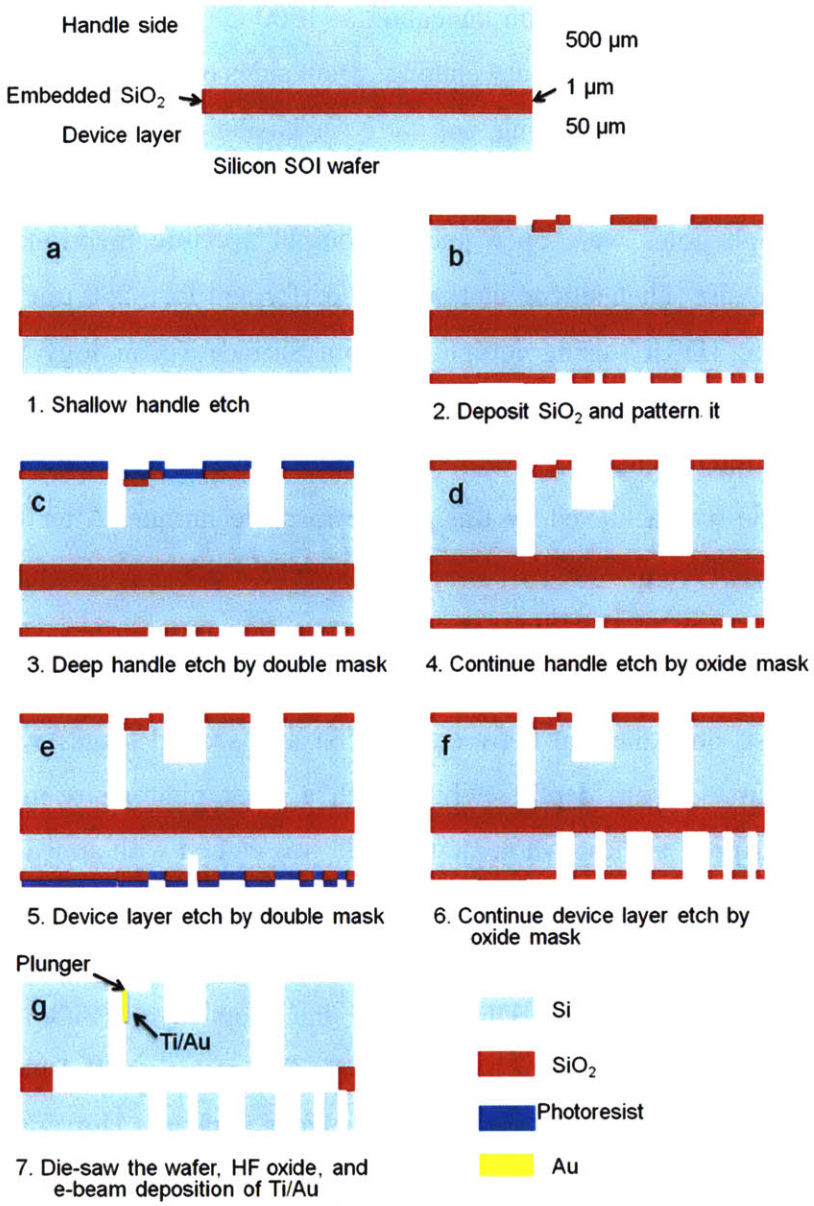

Figure 4.6.1 Illustration of the fabrication process.

etched for ~35 min first and then it reached the embedded SiO_2 simultaneously with other area during the second DRIE etching. Then the wafer was divided into separated MEMS chip by die saw. To release the flexure structure, a diluted (49% HF: water=1:5) HF etchant was used to etch away embedded SiO_2. Because of a much larger area, the SiO_2 layer under the plunger is only partially removed from the perimeter (~20 μm), leaving the plunger still mechanically attached to the device side that can be pushed by an external actuator. Finally, the side wall of the plunger was coated with Ti:Au by directional e-beam deposition.

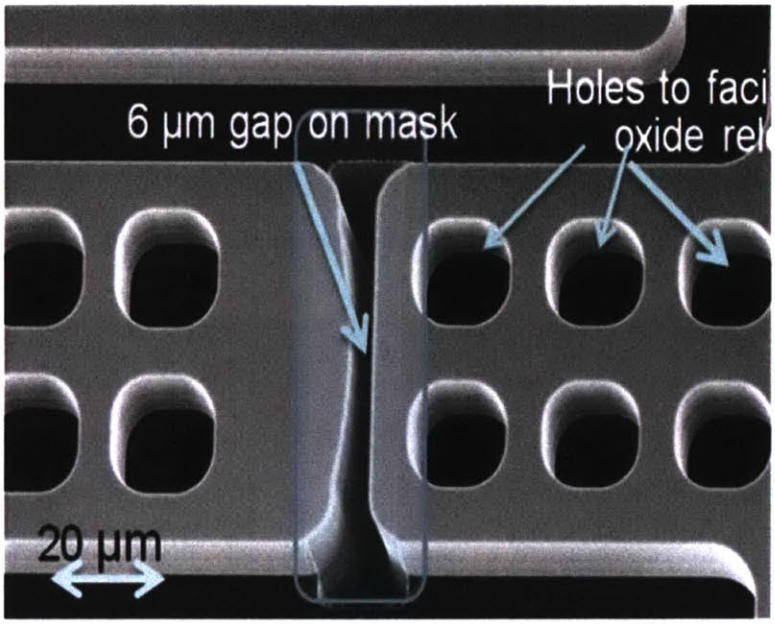

Figure 4.6.2 SEM picture of the small gap between the front of the first stage and the tail of the second stage.

Another important concern about the fabrication is profile of folded beam. The dry etching process can shape a sloped side wall of folded beam (Figure 4.6.3), which can change the characteristics of the folded beam. For instance, the stiffness of longitudinal and transvers direction can be changed due to this imperfect vertical sidewall [146]. Depending on the different slope angle, this imperfection can increase the stiffness in specific directions. The fabrication of MEMS plunger resulted in relatively vertical sidewall for most devices. However, we did observe the sloped side wall when the opening is very narrow, indicated in Figure 4.6.4. When the opening size is smaller than

5μm, the dry etched sidewall has a negative slope while others have relatively vertical shape. So this sloped sidewall is not an issue for the current flexure design while it will be a problem in the design of comb-drive which will be discussed later.

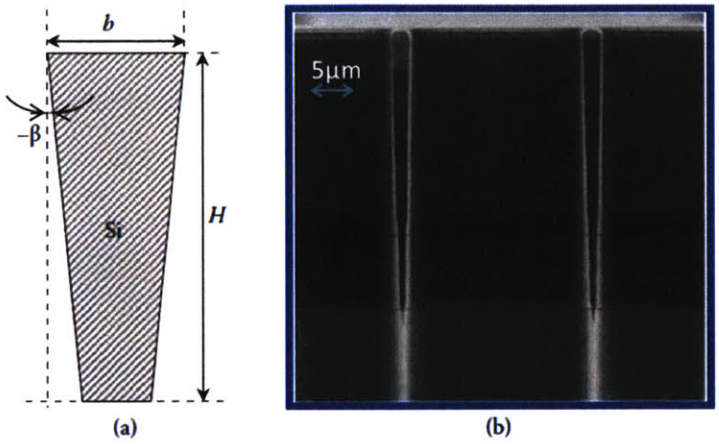

Figure 4.6.3 from [146] (a) schematics of sloped folded beam. (b) SEM picture of the sloped profile.

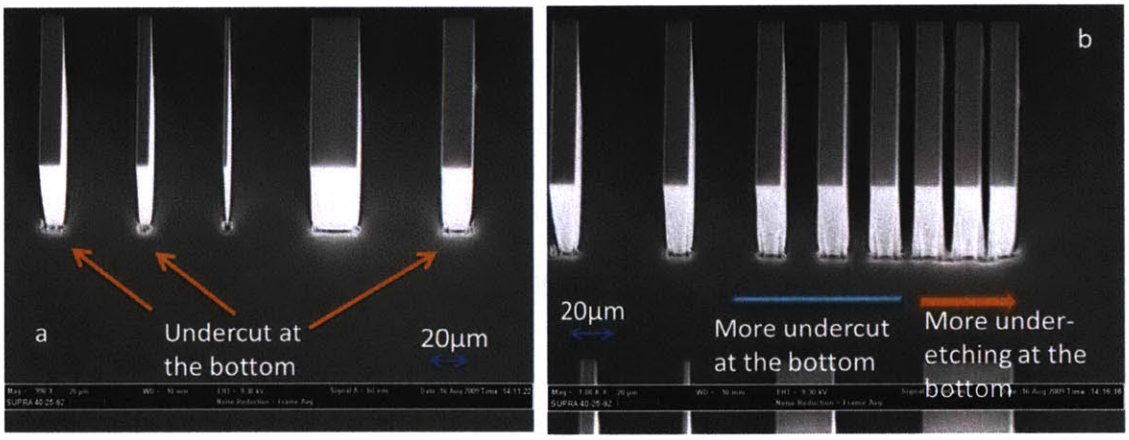

Figure 4.6.4 the dry etching result of different size of openings or slabs. In general, with smaller opening (<5μm), the dry etch resulted in an inner sloped sidewall (under-etching in the bottom). For relatively larger openings, the undercut was observed in the bottom.

4.7 Actuator

In the current design, a comb-driver actuator is not integrated with the MEMS chip yet. Instead, compared to the actuation system in ref [135], between the lever end and the MEMS plunger a piezo-actuator (Thorlab AE0505D08F), which has a maximum displacement of 9.1 μm and a resonance frequency of 138 kHz at room temperature, is added to achieve fine and fast tuning (Figure 4.7.1 b). This piezo-actuator is chosen

because it has the largest displacement among the available ones, given the space limitation of the cryostat. However, at cryogenic temperature, the maximum displacement is estimated to be reduced to ~1-2 μm, which cannot cover the whole tuning range. In an actual operation, sequentially, the lever is pushed by the micrometer to realize coarse tuning and the piezo-actuator is then used to realize fast fine tuning by pushing MEMS plunger. In this fine tuning system, the MEMS plunger has a smaller resonance frequency (~15 kHz from FEM simulation) which determines the largest tuning speed.

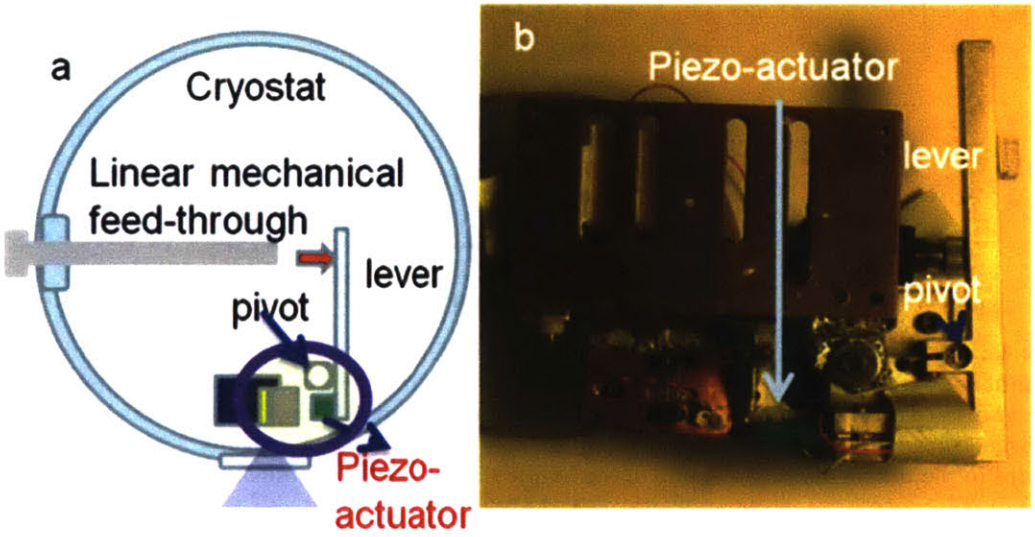

Figure 4.7.1 Schematics of the cryostat setup. b. Photograph of the actuator mechanical system. A piezo-actuator is installed between the lever and the MEMS plunger. In an actual operation, sequentially, the lever is pushed by the micrometer to realize coarse tuning and the piezo-actuator is then used to realize fast fine tuning by pushing MEMS plunger.

4.8 Measurement and result

After the wire laser and plunger were fabricated separately, they were aligned and assembled according to the pre-defined alignment holes and extrusions on the plunger and laser wafers. The gap between the plunger and the flat side of the DFB laser is ~20 μm in a nonactuated position. The external differential micrometer can push the plunger all the way towards the laser. When the micrometer is reversed, the meandering MEMS springs retract the plunger reversibly. The assembled device was mounted in a cryostat (Figure 4.7.1 a and b) for measurement. All spectra were measured at 5 K using a Nicolet

850 spectrometer (purged with N_2 gas) and a Ge:Ga photodetector in pulse mode with 90-kHz frequency and 200-ns duration.

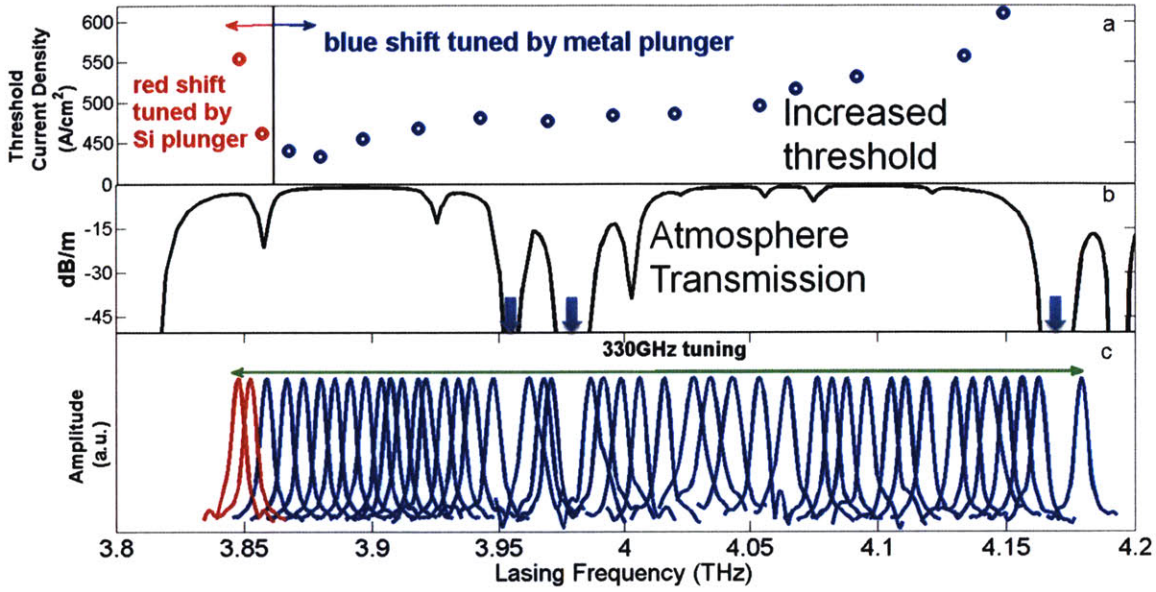

Figure 4.8.1 Tuning results from device A, which has 10.5-μm average width, 3-μm sinusoidal grating modulation, 30 periods, and a grating period of Λ = 14.5 μm. (a) Threshold current densities of the device at different frequencies. (b) Atmospheric attenuation at different frequencies (HITRAN 2008). The three arrows indicate strong absorption lines. (c) Tuning over a range of 330 GHz in device A. The gaps in the tuning spectra are due to the highly absorption lines indicated in part b.

At ~5 K, the MEMS plunger functioned as expected without structure failure. A continuous tuning of 330 GHz, or 8.6% fractional tuning, was achieved with MEMS plungers and a device with 10.5-μm average width, 3-μm sinusoidal grating modulation, 30 periods, and a grating period of Λ = 14.5 μm. As illustrated in Figure 4.8.1, a Si plunger enables ~30 GHz tuning, compared to ~300 GHz achieved using a metal plunger. The range of blue-shift tuning (with the metal plunger) is impressive and slightly less than the predicted tuning range (340 GHz), possibly due to a small misalignment. However, the tuning range of the red-shift (with the Si plunger) is underwhelming, even compared to that achieved (~57 GHz) from a rudimentary system which demonstrated a ~1:2 red:blue tuning range. This is due mostly to the use of a doped Si plunger. When Si plunger was close to the wire laser, the mode was extracted out of the gain media into the silicon plunger. The mode effectively saw less gain media and this resulted in an increased threshold current. Additionally, the lasing frequency (~4 THz) coincides with

the absorption spectra of the impurities, which causes a significant lasing modal loss when Si plunger was close to the wire laser. The much larger tuning range from the metal plunger (compared to ~80 GHz in Ref. [135]) was achieved mostly because the MEMS plunger enables controllable and reversible tuning with a more precise alignment, enabling full exploration of the available tuning range. Furthermore, it is obtained from a slightly narrower laser ridge (10.5 μm as opposed to 12.5 μm in the previous work [135]) which has a larger fraction of the mode propagates outside of the waveguide and is accessible for manipulation. The threshold current density, which is an important indicator of the laser performance, increased when the lasing frequency was tuned away from the original frequency without a plunger. This is due both to additional loss introduced by the plungers and more likely to a decreased gain when the frequency is further away from the gain peak.

4.9 Summary

Operation of MEMS-based systems at liquid helium temperature is a great challenge. The successful operation of this tunable THz wire-laser presented some demanding requirements, including precise alignment between two different material systems and strict translational movement of the plunger without tilt. The mismatch of thermal expansion coefficient in the two material systems causes additional complexity. These requirements have been met and record tuning range of the THz wire laser operated at ~5 K temperature has been demonstrated.

The work, introduced in this chapter, is the first demonstration to apply silicon MEMS technology to tune THz QCLs. The device, whose size is ~2×2 mm^2, is very compact compared to other existing THz tuning techniques. Additionally, the MEMS plunger enables fast electrical tuning, which is highly desirable for many spectroscopy applications. Furthermore, actuators using comb-drives can be integrated with the flexure design, enabling an all MEMS-based tunable THz wire laser whose frequency can be "dialed" electronically.

Benefiting from this MEMS plunger, a record tuning range of ~330 GHz with single-mode operation was achieved using a narrower laser ridge compared to our previous work. This broad tuning range could be extended further in the red-shift with the present gain medium if a high-resistivity Si plunger was used. It can be extended even further by using heterogeneous gain media with broader gain bandwidths in future development. The gaps in the broad tuning range (Figure 4.8.1) from atmospheric water absorption prove the utility for spectroscopy applications.

5 Development of tunable THz wire lasers with robust single mode operation over a larger tuning range

A continuous and restorable tuning over 330GHz has been demonstrated, using MEMS plungers to eliminate the jittering movement due to the stick-slip effect. What will be the next step of this technology after the first demonstration? Spectroscopy, the major application of tunable THz sources, prefers more stable single mode operation, larger tuning range and faster tuning speed, which define the new design objects.

To achieve a better tuning performance, we focused on the unique features of THz wire QC lasers: deep subwavelength double surface plasmon waveguide. Special electrical connection was designed to suppress the un-preferred modes and enable electrical bias of wire lasers. This solution kills the two birds with one stone: both optical and electrical designs are optimized simultaneously. Moreover, a fast tuning (>15KHz) was enabled by a design composed with a piezostack actuator for fine tuning and a mechanical lever for rough tuning. This prototype can be applied for fast scan in spectroscopic applications. These improvements are introduced in this chapter.

5.1 The bottleneck of the tuning range

Tuning range is an important design target of tunable THz laser especially for practical applications. By scanning over a larger frequency range, more spectroscopic information can be collected. Although the tunable THz QC wire laser has demonstrated tuning over 330GHz, several factors limit the further improvement of the tuning range.

First, the tunability from changing $k_{\perp}$ is limited. As discussed in early chapters, the tuning is achieved by changing $k_{\perp}$ when the plunger moves toward to a wire laser. So the tuning range is determined by the closest distance the plunger can move to. The plunger cannot touch the sidewall of the wire laser because it can cause short circuit or permanent physical damage. On the other hand, due to the ununiformed dry etching, there is always a tail structure (Figure 5.1.1) at the bottom corner of the wire laser. So the distance

between the plunger and the wire laser sidewall cannot be smaller than ~ 1μm. Thus all the simulations in this thesis always assume that that the closest distance is 1μm. In these simulations, the tuning range is ~370 GHz using only metal plungers, compared with experimental result of 310GHz achieved in the device with 14.3μm periodicity and 10.5μm width. So it looks like that the experimental tuning range is not limited by the tuning mechanism. But, this conclusion should be drawn with a caution due to the significantly simplified model.

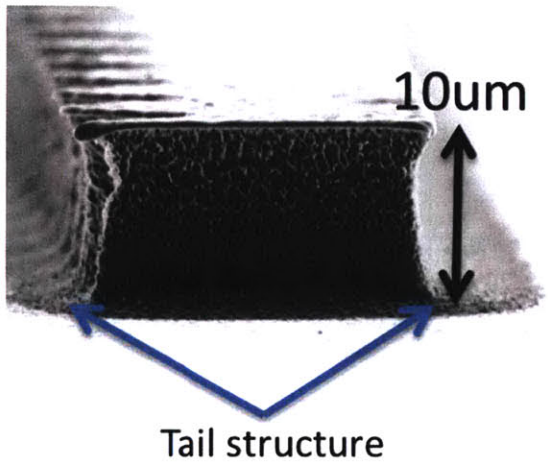

Figure 5.1.1 Illustration of the tail structure at the bottom corners of the THz wire laser due to the ununiformed etching. This can block the plunger from moving further toward the wire lasers. When the plunger touches this tail, the wire laser is either shorted or physically damaged.

Secondly, the tuning range can be limited by gain bandwidth, illustrated in Figure 5.1.2. When the metal or silicon plunger moves toward the laser ridge, the lasing frequency will either shift to blue or red side of the spectrum respectively, until the gain is smaller than the modal loss when the lasing stops. In the previous designs, the lasing mode, which had the smallest modal loss, was designed slightly lower than the gain peak when the plunger did not present. This design was based on the concern that more potential tuning range, which was equal to the net gain bandwidth, should be allocated to metal plungers which had a larger tunability than silicon.

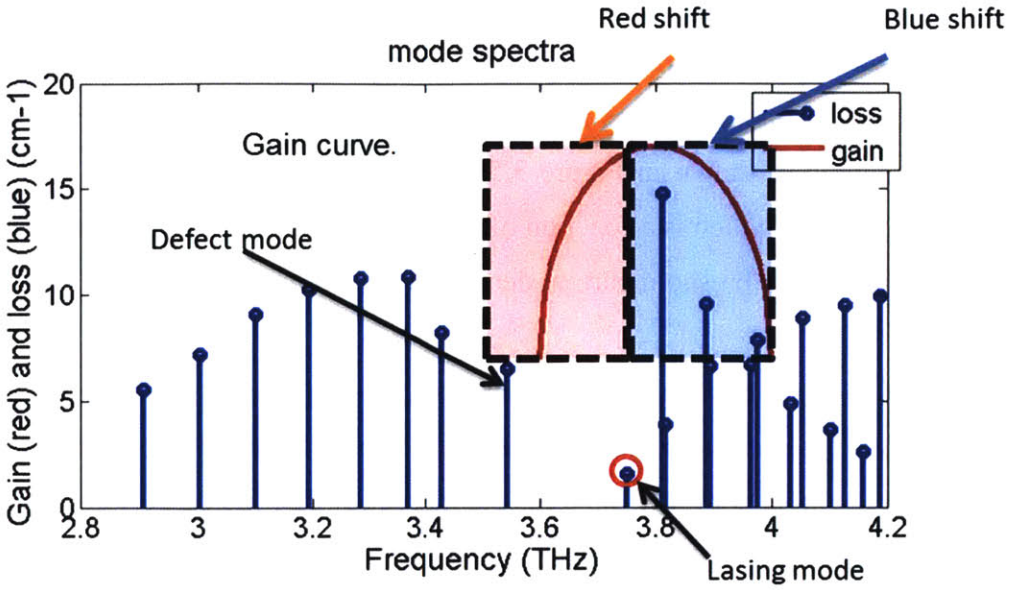

Figure 5.1.2 Illustration of the gain availability for different modes. The gain curve is overplayed with the absorption spectrum of a THz wire laser (12.5 μm wide, 13.7um periodicity). The gain curve is qualitatively shown and is not scaled precisely in the figure. In addition, this gain curve is shifted up for better visualization. The lasing mode without tuning is indicated in the figure. The possible blue and red shift tuning ranges are also indicated, assuming no mode hopping. Additionally, indicated in the stop band, a defect mode was observed at ~3.55THz.

How large is the net gain bandwidth. This net gain can be calculated as:

$$g_{net} = g_{matieral} - \frac{\alpha}{\Gamma}$$

where $g_{material}$ is the material gain whose value is set by the gain medium design, α is the material cavity loss and the Γ is the mode confinement. FL183S, with the phonon depopulation scheme and the two-well injector configuration, has a relatively large gain bandwidth while the precise value is not available. A typical Fabry-Parot device of this design can lase at two frequencies separated by ~0.7THz space (Figure 3.3.6) which can be estimated as the lower boundary of the gain bandwidth. Additional to the gains seen by different modes, the loss and mode confinement are important factors to determine the lasing frequency. Indeed, these two parameters can dynamically change during the tuning process, resulting in mode hopping.

When the metal plunger approaches the wire laser, as described in the previous chapter, the mode is 'pushed' into the wire laser by the plunger. On the opposite side, the mode is

pushed out but still bounded by the metal-metal waveguide. So qualitatively, the mode confinement is increased. Furthermore, the mode overlaps more with the grating which can cause scattering, so the mode loss is increased. This increased mode confinement is proved by the simulation shown in Figure 3.5.2. On the other hand, the metal plunger also introduces extra loss which is a function of surface roughness and metal quality. This is proven by the increased threshold current density in the tuning process.

In contrast, when a silicon plunger is used, the mode is sucked into the plunger and the mode confinement decreases significantly. Due to the free electrons absorptions and other scattering impurities in silicon, the mode loss is increased. The increased loss is further amplified by the relatively small mode confinement which appears in the denominator in the equation 1.8.1. At some point, the increased modal loss is large enough to eliminate the net gain and the lasing stops. This qualitative analysis matches the experimental observation well, illustrated in Figure 4.8.1.

During the tuning, the dynamically changed gain 'seen' by each mode determines the lasing frequency. As described in section 3.4, the upper-band-edge mode is designed as the lasing mode which has the smallest threshold gain. By engineering the grating parameters, the frequency of this mode is close to the gain peak when the plunger is not presented. When the plunger moves toward the wire laser, the frequencies of all the modes will shift. Take the metal plunger as an example -- the upper-band mode blue-shifts to higher frequencies and 'sees' less and less gain. In contrast, the lower-band-edge mode 'sees' more and more gain since it locates at the other half of the gain spectrum, demonstrated in Figure 5.1.2. At some point, the lower-band-edge mode 'sees' larger gain than the upper-band-edge mode and becomes the lasing mode. If the standing wave in the waveguide becomes too strong, the spatial hole burning kicks in and causes a multimode lasing. If a silicon plunger is used, the mode spectrum shifts to the lower frequency while the gain spectrum keeps same. So the upper-band-edge mode again sees less and less gain and some other higher order longitudinal modes see larger gain, resulting in a changed lasing mode. This process is difficult to be quantified because

many parameters of the THz wire laser cavity are experimentally unavailable, but it can limit the continuous tuning range due to the possible mode hopping described above.

Identifying the dominant one, out of two possible causes of the limited tuning range, is crucial to further expand the tuning range. To achieve this, based on the same gain medium (FL183S), two devices which have the same width (12.5μm) but different periodicities (device A: 13.7μm; device B: 13.5μm) were fabricated. The tuning by a metal plunger was measured in a pulsed mode (80KHz, 200ns pulse width) and the result is illustrated in Figure 5.1.3. Device A lased at a lower frequency (~80GHz) than device B when a plunger is not used. However, the tuning range of both devices, using a metal plunger, terminated at similar frequencies (~4.15 THz). This inferred that the tuning range was limited by the gain bandwidth. Several other possibilities can be excluded by this experimental observation. First, the same width of both devices assured the same waveguide loss due to the sidewall roughness. Secondly, the same gain medium and plunger excluded the possibilities caused by different material gains or plungers. If the tuning range was dominantly limited by the plunger's tunability, it should be independent of the starting frequency. In contrast, the tuning ended at similar frequencies. These indicated that the tuning was actually limited by the gain bandwidth.

Because the upper bound of the tuning range is determined by the gain bandwidth, which cannot be changed much, the tuning range can only be expanded by starting from a lower frequency where the gain is still larger than the loss. However, as we have discussed, the gain seen by different modes can change dynamically during the tuning process and mode hopping can happen. To solve this problem, a comb-shape connector was proposed to ensure a single mode operation to further increase the tuning range.

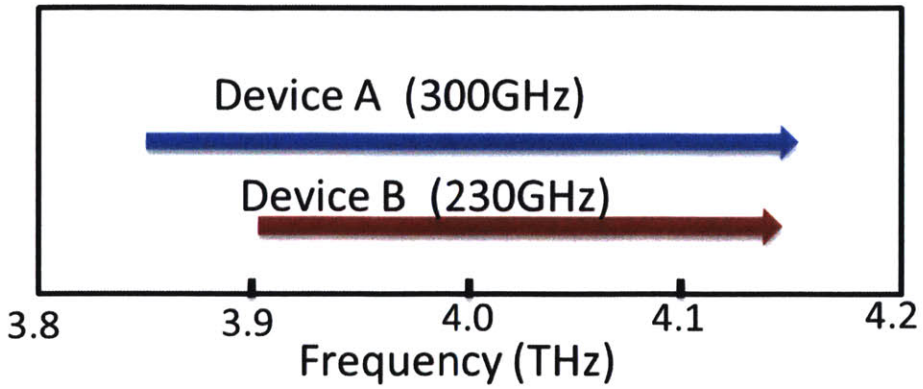

Figure 5.1.3 Tuning range of the devices from the same wafer but with different initial lasing frequencies by using different periodicities. The width (10.5 μm) of the device A and B is same to assure the similar overlap between the mode and the sidewall roughness. The frequency tuning started at different frequencies and ended at similar frequencies.

5.2 Design to increase the tuning range

As discussed earlier, the tuning range was limited by the bandwidth of the net gain. To augment the tuning range, our focus is placed on the characteristics of the gain spectrum. Due to the reduced mode confinement and the extra loss, the tuning range of silicon plunger is much smaller than the metal plunger. In the previous design, when the plunger was not used, the initial lasing frequency was close to the gain peak. So only the upper half of the gain spectrum, indicated by the blue box in Figure 5.1.2, was utilized. Naturally, we asked ourselves if the lower half of the gain, indicated by red box in Figure 5.2.1, can be used to increase the tuning range of the metal plunger. Indeed, as long as enough mode discrimination is provided by the DFB, the upper-band-edge mode can be designed at a much lower frequency than the gain peak while maintaining a single mode operation. Then the tuning range can be significantly increased because more gain bandwidth can be utilized. In summary, larger mode discrimination, a lower starting lasing frequency and a larger tunability from the metal plunger are needed to achieve this challenging goal. I will start the discussion about how to achieve a lower initial lasing frequency, then the method to enable a larger tunability will be addressed. After that, we will explore how to improve the mode discrimination using comb-shape connectors in the next section.

Usually, the initial lasing can be designed at a lower frequency by using a larger periodicity of the DFB grating. In the first implementation of this design, mode hopping was observed instead of continuous tuning, because the mode discrimination originated from DFB cannot dominate the gain curve. In other words, the loss difference seen by different modes is less than the gain difference. We can take the first and second order mode as an example, demonstrated in Figure 5.2.1. In A, if the loss difference ΔL, is smaller than the gain difference Δg, the second mode will lase first. In B, after the metal plunger tunes the two modes into the upper half of the gain curve, the first order mode lases and mode hopping happens.

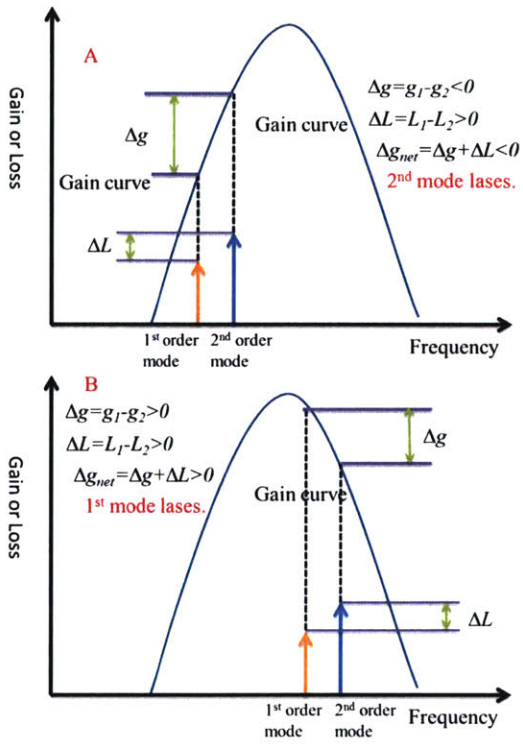

Figure 5.2.1 Schematics of the lasing dynamics. After the metal plunger tune the modes from lower half of the gain curve (part A) to higher half (part B), the lasing mode jumps from second order mode to the first order one. In this scenario, the gain difference is larger than the loss difference.

A larger fraction of mode outside of the waveguide can lead to an increased tuning range. Intuitively, the metal (silicon) plunger can squeeze (suck) more mode into (out) of a narrower wire lasers. In the simulation, when the average width of wire laser is narrowed down to 6.5 μm from 12.5 μm, the tuning range can be as high as ~650GHz which is very impressive. But, we should be aware that the drawback of this method is an even smaller

mode confinement, which increases the laser threshold and reduces the tuning range. So there should be an optimized width to maximize the tuning range. In the experiment, several width, including 12.5um, 10.5um and 8.5um, have been tried. The result will be discussed later.

5.3 Mode selector and robust single mode operation

5.3.1 First design of mode selector

The first generation of THz wire lasers had a tapered rear facet which was covered by Ti/Au/SiO_2 multiplayer. As discussed in the previous chapter, it introduced additional loss due to the mode leaking into the bonding pad. Moreover, this design requires complicated fabrication processes, illustrated in chapter 3, which led to a low yield. Additionally, due to the breaking symmetry between the front and rear facet, undesired defect mode (Figure 5.1.2) can bring more uncertainty to the lasing dynamics. To solve these problems and improve the robustness of the single mode operation, a novel design of comb-shape connectors, illustrated in Figure 5.3.1, is developed.

In the new design, the bonding pad is placed beside the wire laser and connected with the wire laser by comb-shape connectors while both the bonding pad and connector metals are insulated from the underneath gain medium by a thin layer of SiO_2. Thus in the area of the connectors and the bonding pad, the material layers from top to bottom is Au/Ti/SiO_2/gain medium.

It is just as important to realize that this comb-shape connector design actually functions as a mode selector by selectively increasing losses of undesired modes. In the first design, there are five fingers connected with the wider part of the DFB grating. This preliminary design replaced the old bonding pad (chapter 3) and partially proved its function as a mode selector. These connectors were connected to the waveguide at the widest section to minimize their interference with the desired lasing mode which is the upper band edge mode in this case, and it has the maximum intensity at narrow sections. As illustrated in Figure 5.3.1, the electrical field is attached to and confined by the top and bottom metal

layers and tends to propagate in the material with larger permittivity. In the case of THz wire laser, the connectors' top layer can guide the surface plasmon mode and the underneath GaAs has larger permittivity (~13.1) compared to vacuum. So qualitatively, when modes see the connectors, they are guided into bonding pad by the connectors. On the other hand, the magnetic field does not see the difference between GaAs and vacuum because both of them have same permeability. So we don't need to consider magnetic field in this design. The electrical field of the upper-band-edge mode localizes in the narrow section of the waveguide. At the wider section, electrical field almost diminishes. So when the connectors centered at the widest part of DFB, they see little upper-band-edge mode and do not perturb the mode. However, higher order longitudinal modes are sucked into the connectors and bonding pad. Demonstrated in Figure 5.3.1f and g, the maximum electrical field of the fundamental mode is almost aligned well with the narrow sections in the gratings. In contrast, the higher order modes misalign with narrow sections more. So these higher order modes are more perturbed by the connectors at the wider sections. In the bonding pad and the connectors, the gain medium is not biased due to the insulation of the thin SiO_2 layer beneath the metal layer. So the leaked mode sees a cold laser cavity with loss. Additionally, these modes have larger radiation loss because they can emit from the bonding pad. Therefore, the undesired modes yield a larger loss and the mode discrimination is increased. But because the periodic symmetry of the first order DFB is broken, there is still some overlap between the upper-band-edge mode and the widest section. So the loss of this lasing mode can increase slightly. To keep the additional loss of lasing mode relatively low, only five connectors are used. These five connectors are arranged every six periods of the DFB structure to minimize the symmetry breaking.

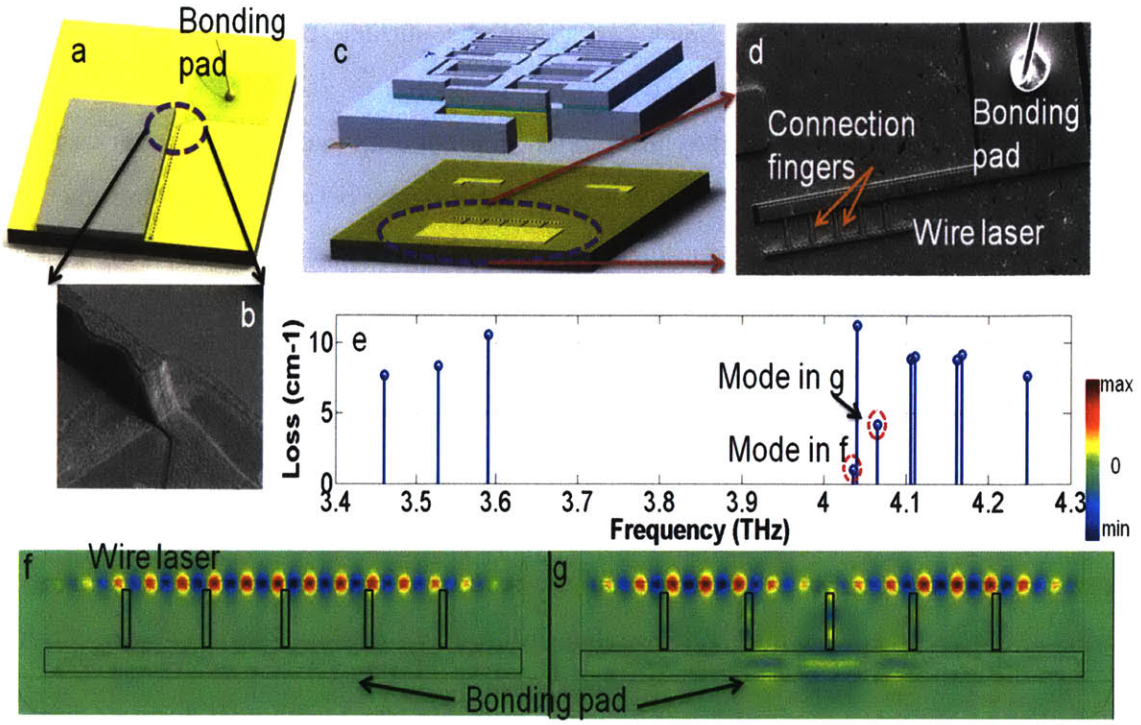

Figure 5.3.1 Schematics of the first comb-shape connection design. Comb-shape connection bridge the laser ridge and bonding pad which is electrically insulated from the gain medium by SiO_2 layer underneath. In the graph, only five fingers design is illustrated. a, Schematics of the previous design of wire lasers. b. SEM picture of the rear facet. c, Schematic illustration of the new wire-laser design and the MEMS plunger. d, SEM picture of the new wire-laser design. e. A typical mode spectrum of wire laser with comb-shape connectors. f and g, The mode intensity of first and second upper-band-edge modes, respectively. A clear leakage of the mode from the wire laser to the bonding pad is shown in g.

In the design of comb-shape connectors, the key parameters are the width and length of the connectors. Wider connectors can guide more fraction of mode into bonding pad which will undesirably increase the loss of the lasing mode. Moreover, these connectors have to be strong (wide) enough to survive in the later fabrication steps. So a width of ~4μm was chosen to optimize the tradeoff. Besides, the connector cannot be too short because the current can spread into the unbiased connectors and even bonding pad from the wire laser. On the other hand, the connectors should not be too long due to the limitation of the wafer area. Given all these constraints, the connector length was designed as ~80μm.

The first, second and third upper-band-edge modes are illustrated in Figure 5.3.1. The simulation was simplified by assuming a cold cavity and lossless materials. So the model only included the radiation loss. After the tilted rear facet was avoided, the modes are symmetric longitudinally. The higher order longitudinal modes leak into the bonding pad through the connectors. For the first mode, the loss is increased to ~1cm^{-1} from ~0.5cm^{-1}. As a comparison, the loss of second order mode is increased to ~4 cm^{-1} from ~1.3cm^{-1}, the loss of third order mode increased to ~8cm^{-1} from ~3cm^{-1}. Clearly the mode discrimination is increased substantially.

5.3.2 Fabrication and the results of wire lasers with comb-shape connectors

The fabrication process of the wire lasers is illustrated in Figure 5.3.2. First, wafer bonding and substrate removal were performed and the procedures were the same as the process of normal THz QCLs described previously. After that, a 300nm thick SiO_2 layer was deposited by PECVD at 300C^{o} followed by a standard contact lithography and wet etching. Then a layer of Ti/Au (30nm/300nm) was deposited by e-beam evaporation and defined by a standard lift-off process. Finally, with this metal layer as a hard mask, a dry-etch by ECR-RIE was performed to etch 10μm gain medium. Compared with the fabrication process with tilted rear fact, the process is much simpler because it eliminated the lithography over a 10μm step and improved the yield rate.

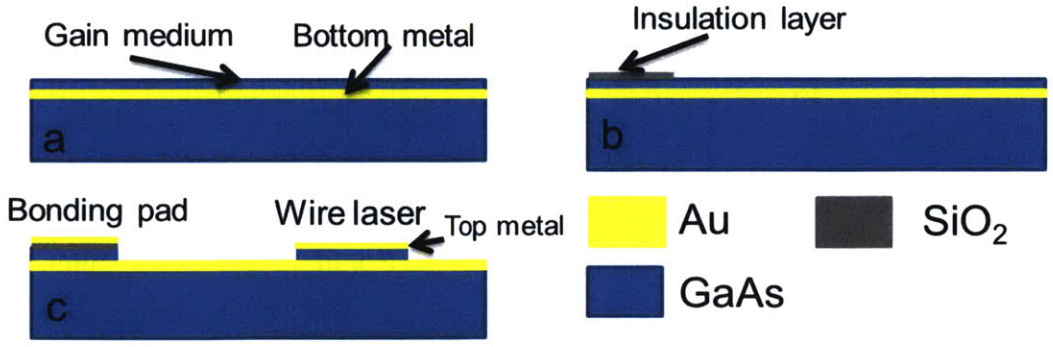

Figure 5.3.2 The processes to fabricate wire lasers with comb-shape connectors. Similar with the normal THz QCL fabrication, the wafer bonding and the substrate removal resulted in a bonded wafer shown in part (a). (b) Deposition of a thin SiO_2. (c) After a deposition of Ti/Au layer as a hard mask, the 10μm thick gain medium was etched away.

The fabrication result is shown in Figure 5.3.1 (d). In general, good fabrication quality was demonstrated although the dry-etching causes non-uniform sidewall feature which

was explained in chapter four. In addition, the metal piece between the connectors sometimes could not been removed in lift-off process because the metal layer is thick (~330nm) compared to the thin photoresist (~450nm). As a rule of thumb, in a liftoff process, the metal thickness should not be more than half of the photoresist. However, in the fabrication of the THz wire laser, the metal has to be thick enough to survive the ion bombardment in the dry-etching step and the photoresist cannot be too thick due to the high resolution requirement of the DFB gratings.

The device was measured according to similar procedures with the previous experiments. At 5K, the device was biased by a short square pulse train with 200ns duration and 80 KHz repetition rate. The THz signal was detected by a photo detector with a face to face configuration. The maximum operation temperature of ~109K was achieved in a ~10.5μm wide device which lased at ~3.9THz. This temperature was higher than previous devices with a tilted rear facet due to the associated additional loss described in the previous chapter. This higher temperature also indicated that the additional loss from the connectors was not significant for the lasing mode.

A typical IV curve of a device with the comb-shape connectors is shown in the latter section (Figure 5.6.2 (b)) and is compared with a typical Febry-Perot device. This IV curve deviated from the FP device's significantly and has a larger current density in the lower biases. This was not surprising because the current spreading was expected and explained in section 5.5. Here, the current spreading length is different from the diffusion length L_D due to the existence of the vertical field. The electrons are dragged down to the bottom contact before they reach the diffusion length. Thus the current spreading length, depending on the geometry, is smaller than the diffusion length. A significant amount of current spread to the bonding pad and caused a softer and earlier NDR compared to FP devices, due to the different actual bias across the different modules. This current spreading effect will be discussed in detail later.

Using the devices with the comb-shape connectors, tuning was observed although it did not break the record. This was because the tuning range was limited by the same factors

which were described in section 5.1. But the key information from this batch of devices was that comb-shape connectors actually worked and needed to be improved, as discussed in the next paragraph.

It is interesting to discuss the devices whose initial lasing frequency was designed below the gain peak. For instance, 8.5μm wide devices were fabricated based on both FL183S and OWI222G wafers which both had gain peak at ~3.8THz. The facets were chosen at the widest part of the sinusoidal modulation. Thus the upper-band-edge mode was chosen as the lasing mode. The lasing frequencies of bare wire lasers were designed at ~3.75 THz (device A), ~3.6 THz (device B) and ~3.4THz (device C) by using different DFB periodicities. The amplitude of the sinusoidal modulation was 3um. The sidewall of DFB side was open without any metal coating. Five connectors were on the DFB side and were distributed every six periods. The length of the connectors was 80μm and the width was ~4μm.

The spectra of all the three kinds of devices (A, B and C) are shown in Figure 5.3.3. The lasing frequency did not scale with the DFB periodicities as expected. The actual lasing frequency of the device A was ~100GHz higher than the designed 3.75THz because the fabricated device turned out to be narrower than 8.5μm. The rule of the thumb is that if the average width is reduced by 0.1 μm, the lasing frequency is increased by ~20 GHz. Thus this ~100GHz difference can be attributed to 0.5-0.6 μm width difference between the designed and the actual laser which is possibly due to the lithography and liftoff step during the fabrication. Either over-exposure or loose contact in the lithography step could cause this size difference.

But the lasing frequencies of device B and C deviated from the designed 3.6THz and 3.4THz significantly. This mismatch was because the loss difference could not dominate over the gain difference seen by the cavity modes, illustrated in Figure 5.2.1. When the designed lasing mode is far below the gain peak, other modes close to the gain peak can see larger gain although they are lossier. The gain difference was larger than loss and the lasing happened on the modes other than the upper-band-edge mode. Thus device B

lased at ~3.81THz in spite of the designed 3.6THz. Device C lased at an unpredictable 3.97THz which was much higher than the designed 3.4THz. Moreover, when the plunger was used to tune the frequency, mode hopping was observed frequently due to the complicated mode selection dynamics. In other words, this deviation of the lasing frequency from the initial design was because the comb-shape connectors cannot provide enough mode discrimination. This indicated that a stronger mode selector was needed and more comb-shape connectors can be an option to ensure a robust single mode lasing.

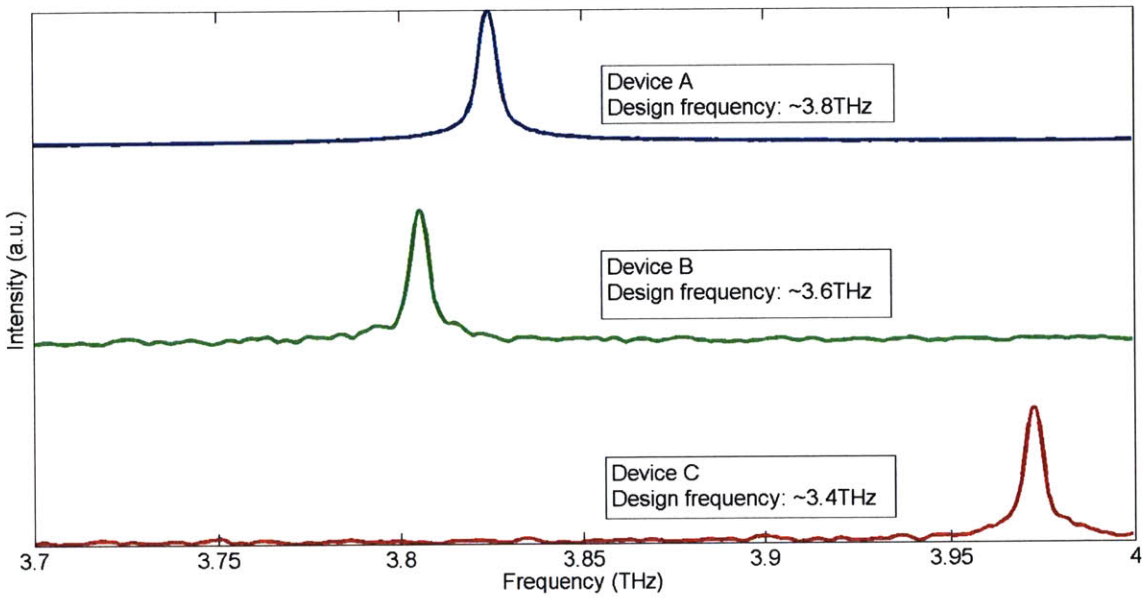

Figure 5.3.3 The spectra of the devices with different periodicities. The gain peak is ~3.85THz, and all the devices have ~8.5um width. The design frequencies of device A, B and C are ~3.75THz, ~3.6THz and ~3.4THz corresponding to the periodicities of 16μm, 17.05μm and 18.3μm respectively. But the actual lasing frequencies deviated from the design values significantly. Especially device C lased at ~3.98THz compared to ~3.4THz in the original design.

In addition to different periodicities, different average widths have been tried for five-connector design. These includes 10.5 μm (device D), 8.5 μm (device E) and 6.5um (device F) width. To compare them apple to apple, the lasing frequency of all of device D, E and F were designed close the gain peak (~ 3.9THz). The maximum operation temperature of device D was the highest (108K) compared to ~97K of device E and ~57K of device F. The power-current curve of device D is shown in Figure 5.3.4. In this curve the changing differential slope efficiency resonates with our guess of the gain's double-hump structure (Figure 3.3.1). The maximum operation temperature of the 12.5μm wide

device is ~115 K which is similar to 10.5μm and 8.5μm devices. So it indicates that below 8.5μm, the device width will play an important role either due to the reduced mode confinement or larger overlap between the mode and the sidewall roughness. Thus the optimized average width should be between 10.5μm and 8.5μm. With an 8.5μm width, the tuning capability from a metal plunger is limited to ~500GHz according to the simulation.

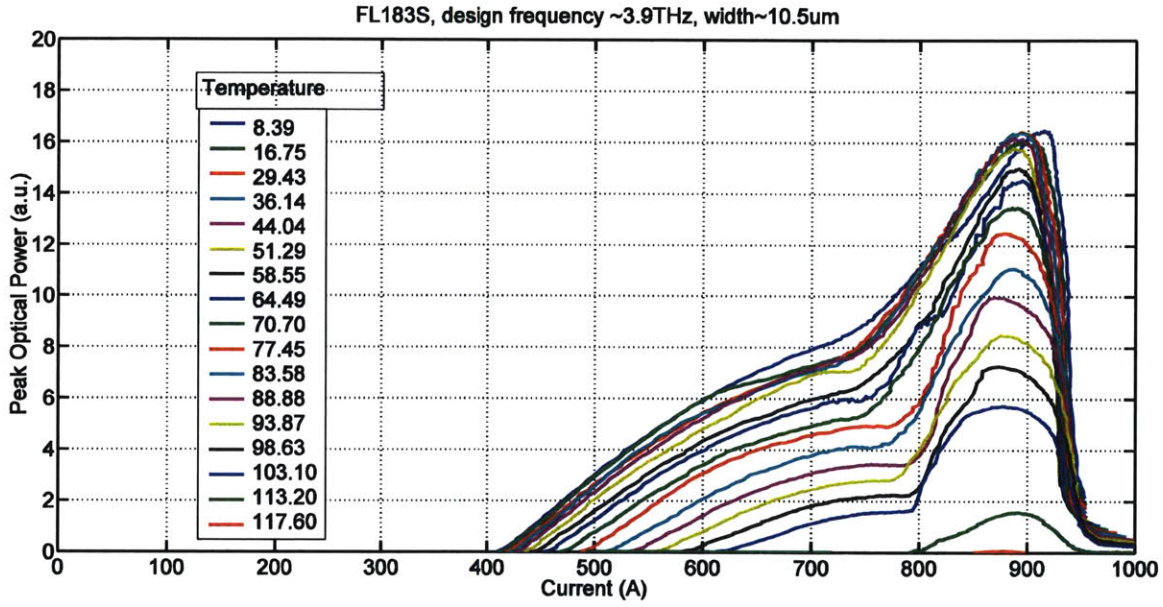

Figure 5.3.4 The curve of power Vs current density for device D (part I) at different temperatures. The maximum operation temperature is ~118K and the inlet lists the measurement temperatures.

It is worth to discuss the results of the devices based on OWI222G wafer. It performed much worse than FL183S again. The maximum operation temperature was 68K with a 10.5μm wide device whose designed lasing frequency was 3.75 THz. This further confirmed our concern about its smaller dynamic voltage range (section 3.3). The current spreading in the comb-shape connectors introduced non-uniform electrical field in the different modules, which caused some modules to enter NDR earlier than others. So a resulted early NDR led to a degraded lasing performance and a smaller tuning range. As a conclusion, although a preliminary design of comb-shape connectors was demonstrated, a significant improvement is needed for practical applications.

5.3.3 Second design

To improve the design of the comb-shape connectors, the number and the geometry of the connectors were optimized and the second design with comb-shape connectors were fabricated based on FL183S wafer (VA0094).

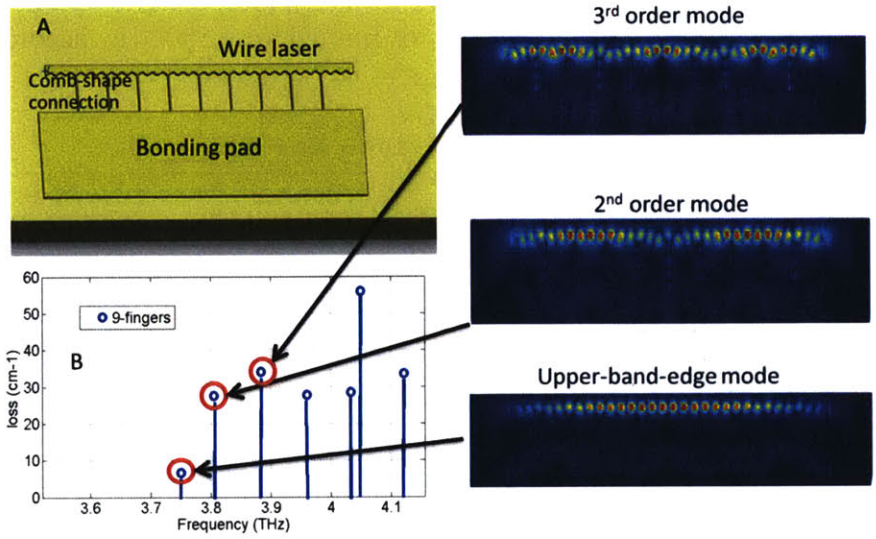

Figure 5.3.5 Schematics of the wire laser with nine connectors and its mode spectrum. (A) The device configuration with nine connectors. (B) The mode spectrum. The right half graph illustrates the electrical field intensity of the first three modes in the upper band. In this simulation, the length of the connectors was only 40um compared to 100um in actual device due to the limited computer memories.

To further increase the mode discrimination, more comb-shape connectors were used in a new design. First, a design with nine connectors was proposed and illustrated in Figure 5.3.5, in which the simulation results are shown in the lower part. This wire laser had a width of ~10.5μm and a periodicity of ~14.3μm, and the connector width was ~4μm. Compared to the five-connector design, the mode discrimination was increased significantly. The modal loss difference between the first and second longitudinal modes was larger than $20cm^{-1}$. To understand the mode spectrum, reader should be careful with the definition of the loss, which is the modal loss and defined as α/Γ, where Γ is the mode confinement factor. The right graph of Figure 5.3.5 plots the electrical field intensity of the first three upper-band modes in the growth direction. As illustrated, the upper-band-edge mode was barely perturbed. But for the second and third order modes, a larger fraction of mode was sucked into the connectors and the bonding pad.

Although the mode discrimination between the upper-band-edge and second order modes was increased significantly, the loss of the third mode was still not much higher than the second mode. Because the third order mode has a much higher frequency than the upper-band-edge mode, the possible gain difference may be larger than the loss difference, resulting in an undesired frequency. So two more connectors were added to further increase the mode loss difference, illustrated in Figure 5.3.6. These two connectors were two grating periods away from the center of the DFB waveguide.

The positions of these two extra connectors were chosen carefully to maximize the loss increase of the undesired modes, while minimizing the loss increase of the upper-band-edge mode. As discussed earlier and illustrated in Figure 5.3.5, the upper-band-edge mode maximum was aligned with the narrowest section of the waveguide. Moreover, this alignment is perfect near the center of DFB grating and worse near the two ends of the waveguide. It infers that if we want to minimize the perturbation of the upper-band-edge mode, the two extra connectors should be placed at the widest sections not far away from the center of the DFB structure. Furthermore, the envelope of the third order mode had a maximum intensity at the center. At this position, similar to the upper-band-edge mode, the maximum of the electrical field intensity for the third mode aligned well with the narrow section of the waveguide, and the alignment gets worse at the position further away from the center. So the two extra connectors should be placed far away from the waveguide center. In the real design, given the concerns of leaving upper-band-edge mode unperturbed and increasing the loss of third order mode, the extra two connectors were placed two periods from the center, indicated in part A of Figure 5.3.6.

To prove the design concerns, a simulation based on finite element method was performed and the result was shown in Figure 5.3.6. The loss of the desired upper-band-edge mode was almost unchanged. In contrast, the third order mode had a loss of $53cm^{-1}$ compared to $34cm^{-1}$ with only five connectors. Even the loss of the second order mode was further increased to $34cm^{-1}$ from $27cm^{-1}$. Illustrated in right graph of Figure 5.3.6, the upper-band-edge mode was almost not interfered. But the second and third order mode had a significant amount of mode leaked into the lossy bonding pad. The electrical field

distribution of the third order mode even deformed significantly due to the perturbation of the two extra connectors.

Can we further boost the mode discrimination by adding more connectors? The answer is difficult. This is because adding more connectors on other locations will also increase the loss of the upper-band-edge mode. So even more additional loss can be introduced for the higher order modes, the mode discrimination is increased only marginally. Given that the loss difference between the upper-band-edge mode and higher order modes was already high, no additional connectors were added.

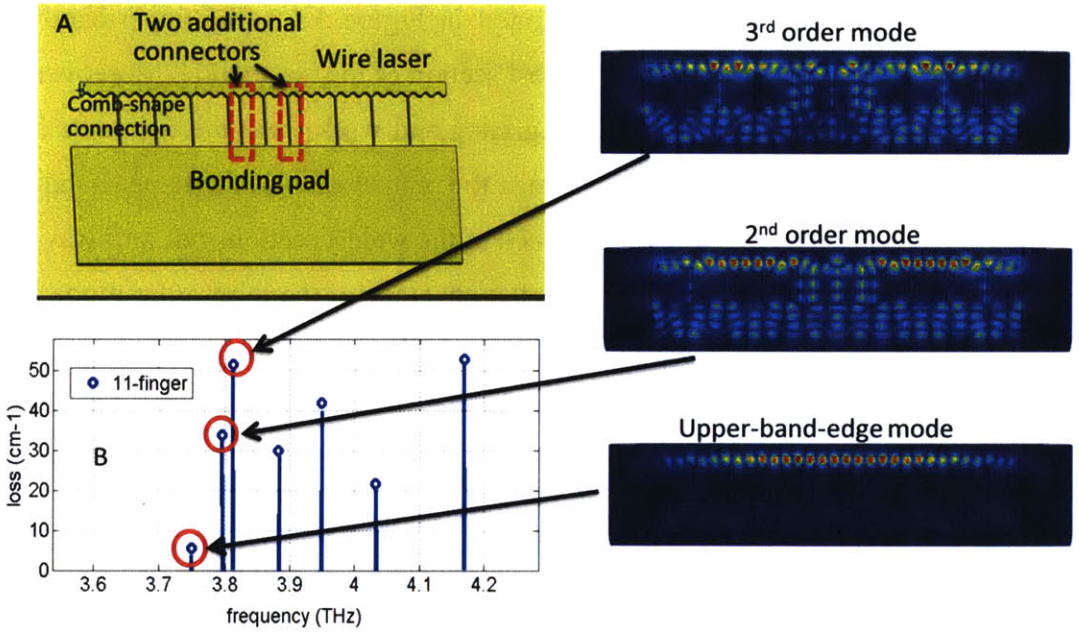

Figure 5.3.6 Schematics of the wire laser with eleven connectors and its mode spectrum. A is the device configuration. The additional connectors are highlighted in the graph. B illustrates the mode spectrum. The right half graph plots the electrical field intensity of the first three modes in the upper band. As illustrated, the second and third order modes were sucked into the waveguide.

5.4 Fast tuning by using a Piezo-Stack actuator

For the spectroscopic applications using amplitude or wavelength modulation techniques, a fast-tuning capability (1K-100KHz) is desired for the tunable laser system. Since the differential micrometer was used for tuning, the capability of MEMS plunger for fast

modulation had not been explored. Here we present a tuning configuration by a piezo-actuator based on the improved wire laser which was discussed in the previous section. This system is capable of tuning in a speed up to ~15 KHz.

As described in the previous chapters, the displacement resolution of the lever was about ~140nm. But this is still not enough for the practical application. This problem could be potentially solved by using piezostack. The expansion ratio of typical piezo material is 1000:1. That is, a piezostack with 10mm length can expand ~10um. At 5K, this expansion can be only ~10-20% of the range in room temperature. In our experimental setup, a piezo-actuator (Thorlab AE0505D08F) was added between the lever end and MEMS plunger. It has a maximum displacement of 9.1 μm and a resonance frequency of 138 kHz at room temperature. This piezo-actuator is chosen because it has the largest displacement among the available ones, given the space limitation of the cryostat. However, at cryogenic temperature, the maximum displacement is estimated to be reduced to ~1-2 μm, which cannot cover the whole tuning range which requires ~10 μm displacement range. In an actual operation, sequentially, the lever is pushed by the micrometer to realize the rough tuning and piezo-actuator is used to realize the fast fine tuning by pushing MEMS plunger. In this fine tuning system, the MEMS plunger has a smaller resonance frequency (~15 kHz) which determines the largest tuning speed.

Eventually, the cryostat was setup to face a fast responded photo-detector (>>100KHz), as illustrated in Figure 5.4.2. After the plunger was actuated by the lever to a desired position, the fine tuning was turned on by piezo-stack which was modulated by a sinusoidal signal. This signal was also used as a reference of lock-in amplifier to filter the signal detected by the photo-detector. Finally, the filtered signal was displaced on oscilloscope.

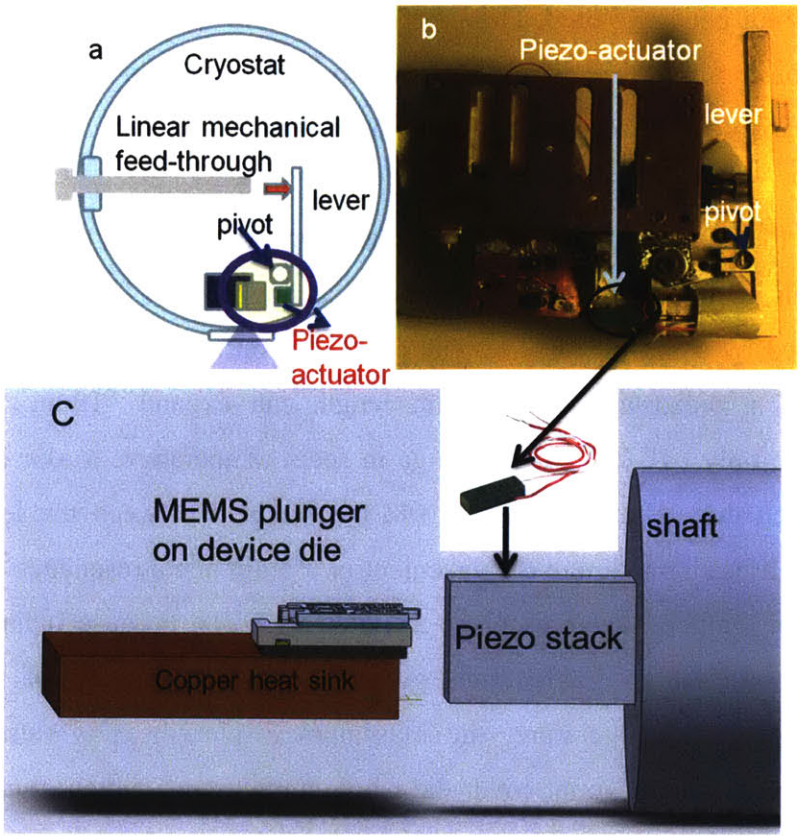

Figure 5.4.1 a. schematics of the setup inside the cryostat. b. the heat-sink module including mechanical lever. c. Blowup of the mounted device with the piezostack beside it. The inset figure is the picture of the piezostack.

If the fast tuning was enabled, a signal, with oscillation at the same frequency with the modulation signal of piezo-stack, should be observed. When the plunger approached the wire laser, the frequency moved further away from the gain peak and additional loss was introduced by the plunger, both mechanisms resulted in a lower emission power. Additionally, the beam pattern changed when the plunger moved, resulting in a changed collected power. Thirdly, different frequencies saw different atmospheric absorption. All these factors contribute to the intensity modulation, which can be used as the indirect evidence of the fast frequency modulation.

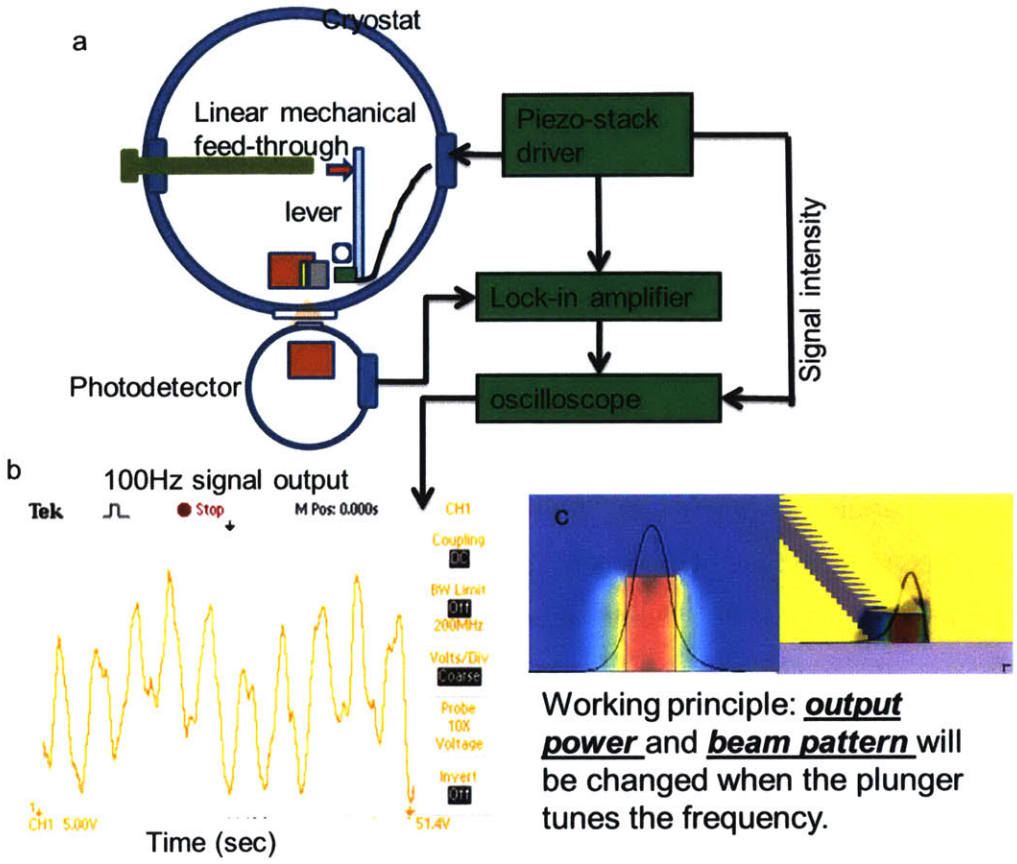

Figure 5.4.2 Illustration of fast tuning with the tunable THz wire laser. a. the schematics of the setup. b. the output signal shown on oscilloscope. c. illustration of the working principle.

The wire laser used to demonstrate the fast tuning is a device described in section 5.3. It has 10.5-μm average width, 3-μm sinusoidal grating modulation, 30 periods, a grating period of Λ = 14.1 μm and ~4-μm wide connection fingers. A MEMS metal plunger is used in this work, and the preparation and assembling of MEMS plunger is described in chapter 4. All the measurements were performed at 5 K temperature using a Ge:Ga photodetector in a pulse mode with 90-kHz frequency and 200-ns pulse duration. The signal from photodetector was amplified by a lock-in amplifier before the read-out. Due to a narrower laser core than the designed value, the lasing frequency of the wire laser without the plunger was at 3.93 THz despite the gain peak at ~3.8 THz. Its maximum operation temperature is 115 K, higher than 105 K of the previous design due to the improved bonding-pad design. The achieved tuning range using this metal plunger is ~220 GHz. The fine tuning range increased when the plunger was closer to the wire laser.

The achieved tuning range is smaller than the record of 330 GHz because of the higher initial lasing frequency (3.93 THz) and limited gain bandwidth in the higher frequency end. Figure 5.4.2 plots the output of photodetector, placed ~10 cm away from the wire laser facet (the beam path in atmosphere is ~5cm.), when the piezo-actuator was modulated with a 200-Hz saw-tooth signal. The slow response of lock-in amplifier (1ms), which is necessary to measure the signal from the photodetector, limits the time resolution of the signal and only 200-Hz modulation was used to demonstrate the concept. Clearly demonstrated in Figure 5.4.2c, the intensity of the output signal was modulated in the same frequency with piezostack's. However, the precise calibration of lasing frequencies during this modulation is difficult to achieve due to the instability of the mechanical system and the hysteresis of the piezo-actuator. The introduction of feedback mechanism in the future work should address these problems.

In summary, we demonstrated a fast frequency tuning of a terahertz wire-laser. Using a piezo-actuator and a MEMS-plunger enables a tuning speed up to ~15 KHz. Although the whole tuning range was not covered by only piezo-actuator, fast tuning should be able to be extended to the full scope by using better piezo-actuator in a larger cryostat.

5.5 Current spreading effect

5.5.1 Origin of current non-uniformity in THz wire lasers

It is meaningful to discuss the current non-uniformity in a separated section since it plays a crucial role to design DFB THz QCLs. The necessity of this section is further reckoned since the comb-shape connector, an important origin of current non-uniformity, was applied in the design of surface emitting and third order THz DFB QCLs [115][147].

In the design of a THz wire laser, there are two origins of the current non-uniformity. First, due to the imperfect anisotropic dry etching, the sidewalls of the wire laser were curved, as discussed in chapter three and shown in part a of Figure 5.5.1. The undercut of the sidewalls can be as big as 1.5 μm contributed from both sides. When the width of the laser ridge is ~10μm, this problem can be significant enough to kill lasing as what

happened with the wire lasers based on OWI222. The other origin is the comb-shape connector. Using a thin SiO_2 layer, these connectors are electrically insulated from the underneath gain medium. However, these gain mediums are physically connected with the biased wire laser. The relatively high conductivity in the growth planes of the quantum well structure causes current to spread to the connectors, illustrated in Figure 5.5.1.

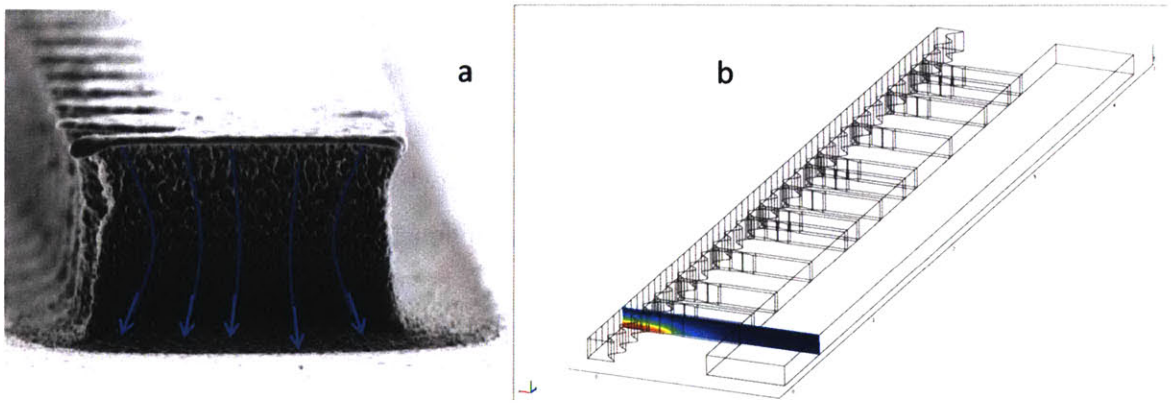

Figure 5.5.1 Illustration of two kinds of current non-uniformity in THz wire laser design. (a) The current non-uniformity from the curved sidewall. The undercut from the two sides totaled to 1.5μm. (b) The current spreading due to the unbiased connectors and bonding pad connected with the biased wire laser. The colored graph plots the potential distribution in a cross-section within the laser core, connector and bonding pad. The non-zero potential in the unbiased connector is due to the current spreading.

When the current flows through the narrower (undercut) section, the electrical field increases due to the larger current density. This can be explained by ohm's law $j = \sigma E$, which indicates a larger (smaller) electrical field given a constant resistivity, a smaller (larger) cross-section and a conserved current. This is illustrated in the simulation result shown Figure 5.5.1. When there are eleven ~ 4 μm comb-shape connectors, the spread current can be as high as ~20% of the total current. The difference of the electrical field in different modules causes non-uniform bias condition. That is, when some modules are in lasing bias, some are not. So the threshold voltage or current density is increased. When the modules with the higher electrical field enter NDR, some other modules have less electrical field and are still in the lasing region. So the device enters NDR earlier. The maximum operation temperature can decrease since less gain is available. Actually, these effects were all observed in the experiment.

5.5.2 Improvement

To address the current spreading problem, several solutions were proposed. First let's focus on the curved sidewall which was etched by Electron Cyclotron Resonance Reactive Ion Etcher (ECR/RIE). This system uses a low-pressure, high-density plasma source with a manually tuned driven source and electromagnetic coils. The wafer sits on the electrode which applied a RF bias. This RF power controls the ion bombarding energy. Microwaves (power~600W) are injected axially through a dielectric window into the source plasma. The source plasma controls the ion/radical flux streams in a vacuum chamber where the wafer is etched. One important drawback of ECR tools is the wafer etching non-uniformity that is translated from the magnetic field induced plasma non-uniformities.

The curved sidewall profile was more likely due to aging and contaminated chamber of the ECR/RIE which was shared by many different users. Although significant amount of effort had been committed to optimize the process, the result was still not a satisfactory, as illustrated in Figure 5.5.2 (d). The possible undesired chemical etching and ion-enhanced inhibitor etching shaped the curved sidewall profile.

A new Inductively Coupled Plasma Reactive Ion Etcher (ICP RIE) (SAMCO Model 200iP), purchased by MIT, was used to achieve a better etching profile. This system uses a low-pressure, high-density plasma source. Similar with ECR-RIE system, the powered electrode, on which the wafer sits, controls the ion bombarding energy. The ion/radical fluxes are controlled by a powered RF coil. ICP tools provide better line width control, higher throughput, and less plasma damage, versus ECR tools, by having higher ion fluxes and lower ion bombarding energies.

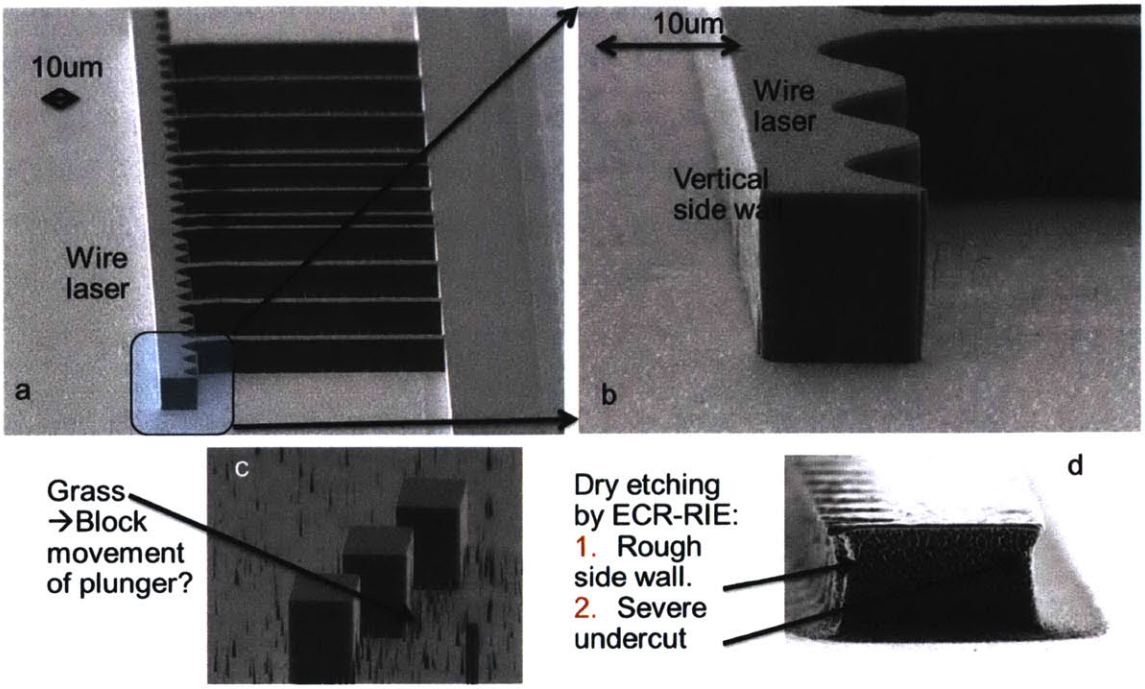

Figure 5.5.2 SEM images of the fabrication result with the ICP and ECR tools. (a) Overview of the THz wire laser with the comb-shape connectors and the side bonding pad. (b) The blowups of the front facet. A vertical sidewall is demonstrated. (c) The grass structure from the micromask effect. (d) The dry etching result by ECR-RIE as a comparison. The rough sidewalls and severe undercut are demonstrated.

The Figure 5.5.2 shows the fabrication result which demonstrated very nice vertical sidewalls from the ICP etcher. Compared with the result from ECR-RIE (part d of Figure 5.5.2), the ICP tool gave a very smooth and almost perfectly vertical sidewall. The sidewall roughness featured with many vertical lines and was from the hard mask roughness. Part c showed many grass structures after the ICP etching due to a micromask effect which was a result of the undesired deposition during the dry etching process. The size of the grass was in the order of ~100nm. So these grass should not be able to block the movement of the plunger.

The other current spreading source is the comb-shape connector and the side bonding pad. A longer and narrower connector design was proposed to reduce this current spreading effect, and illustrated in Figure 5.5.3. Using a longer connector, less current is able to spread into the bonding pad area. In the improved design, ~100μm long connectors were used. Additionally, a small section of these connectors were gradually narrowed and

functioned as a bottleneck of the current spreading. This adiabatic design also ensured that the narrow section did not block the mode being guided out. An abrupt change of the connectors can result in a large mode impedance mismatch and lead to a large reflection. Thus an abrupt change can prevent the undesired mode to be efficiently guided into the bonding pad. The calculated result, from a 10.5μm wide laser core with eleven 3μm-wide connectors, showed that only ~13% current transported through connectors and bonding pad while the mode description was in a similar lever with the uniform connector design.

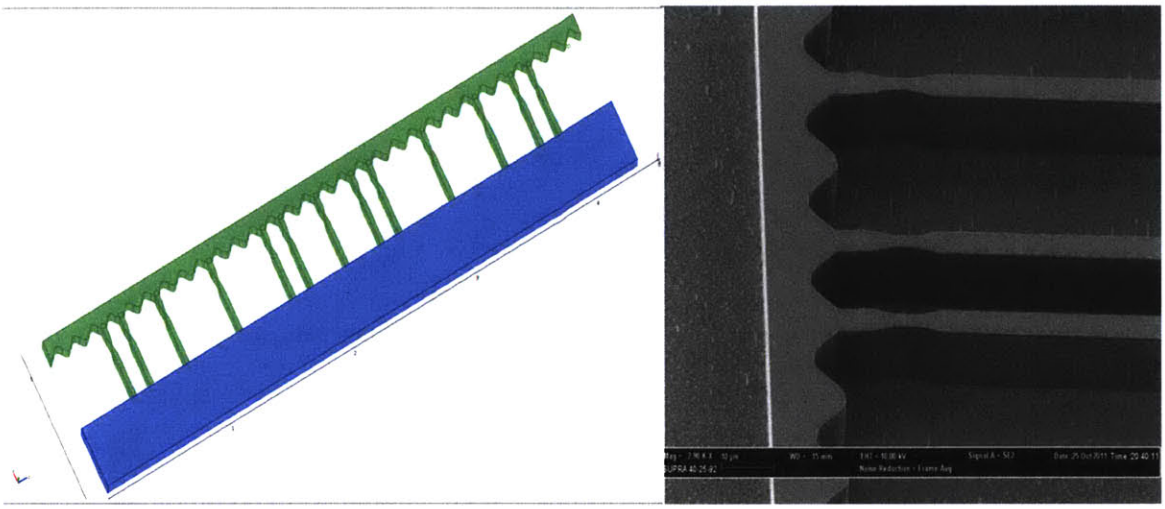

Figure 5.5.3 The improved design of the comb-shape connectors. The left graph shows the overview of the whole device in which the section in blue color represents the bonding pad and the green part includes the wire laser and connectors. On the right, the SEM image shows the fabrication result of this design.

5.6 Experimental result

The measurement procedure was similar to the previous experiments. The device was measured at liquid helium temperature. A pulsed operation with 0.1% duty cycle was used to minimize the current heating. Spectra were taken by a Nicolet Fourier transform infrared spectroscopy by using an external Ge:Ga detector. A metal MEMS plunger, actuated by the external lever system, was used to tune the lasing frequency.

The design of the first order DFB follows the discussion in section 5.3 and 5.4. Thirty periods of grating with sinusoidal shape, whose modulation amplitude is 3μm, was only

placed at one side of the waveguide. As described in the previous section, eleven-comb-connector design was used to increase the mode discrimination. Both dry-etched facets located at the maximum width of the waveguide to ensure the upper-band-edge mode to lase. To compare the eleven comb-connector design with the previous five connector design, both designs were fabricated.

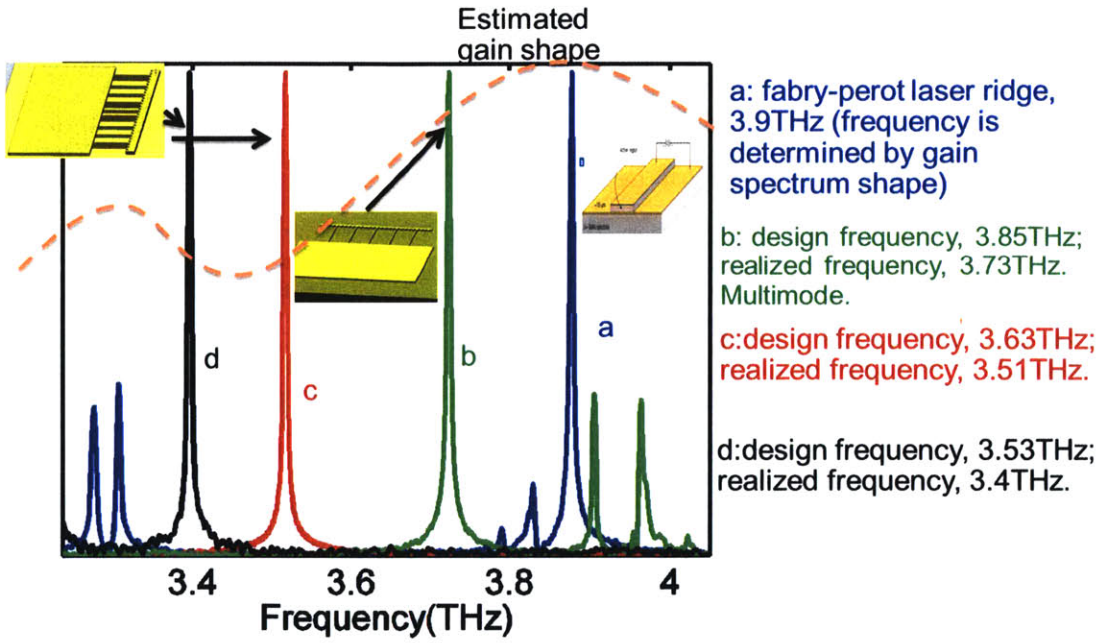

Figure 5.6.1 The normalized spectra of the different designs implemented in FL183S wafer. Schematics of the gain spectrum are plot along the spectra. The corresponding device type for each spectrum is indicated beside it. Spectrum (a) was from a Fabry-Perot device. Spectrum (b) was from a device with five connectors. Spectra (c) and (d) were from devices with eleven connectors. The designed frequency and actual frequency of each spectrum are listed beside the graph. The color of the texts matches the spectra plot. As illustrated, the realized frequencies are systematically 120GHz smaller than designed frequencies. The eleven connector design provided enough mode discrimination for single mode operation, compared with the five connector design which resulted in a multimode operation due to the limited mode discrimination.

Most devices have a width of ~10.5μm, and different periodicities were also used for two reasons. The first reason is to ensure that at least one of the designs can hit the designed frequency in the lower half of the gain spectrum. Usually, due to the fabrication uncertainty, the actual size can be off by 0.5-1μm compared with the original design. This can lead to a frequency change of ~100-200GHz. The other reason is to test the grating functionality since the lasing frequencies should scale with the periodicities.

The spectra of different designs, implemented in the wafer VA0094 (FL183S), are plot in Figure 5.6.1. Spectrum (a) shows that a Fabry-Perot device lased at ~3.9THz and ~3.3THz simultaneously. This agrees with the theoretical predication of double-hump gain shape in reference [134]. A schematic gain spectrum is plot along the actual measured spectra. Spectrum b, c and d were from the DFB wire QCLs with 10.5μm width. Among them, device b (Λ=14.3μm) has five connectors while device c (Λ=15.3μm) and d (Λ=15.8μm) have eleven connectors. The single mode operation of device c and d, compared with the multimode operation of device b, clearly demonstrated that the eleven-connector design is more capable to achieve a robust single mode operation than the five-connector design. Additionally, the realized frequencies were systematically ~120GHz lower than the designed frequencies. This consistent result proved that the DFB gratings functioned properly to choose the correct mode.

Because the lasing frequency is much lower than the gain peak, the device performance is also highly correlated with the lasing frequencies. Compared to FP device (Tmax~170K), the maximum operation temperatures of device b (Tmax~118K), c (Tmax~103K) and d (Tmax~82K) are significantly lower due to the worse mode confinement and more scattering loss from sidewall roughness. Additionally, device c and d had even lower Tmax because their lasing frequencies were further from gain peak and they saw less gain, compared to device b.

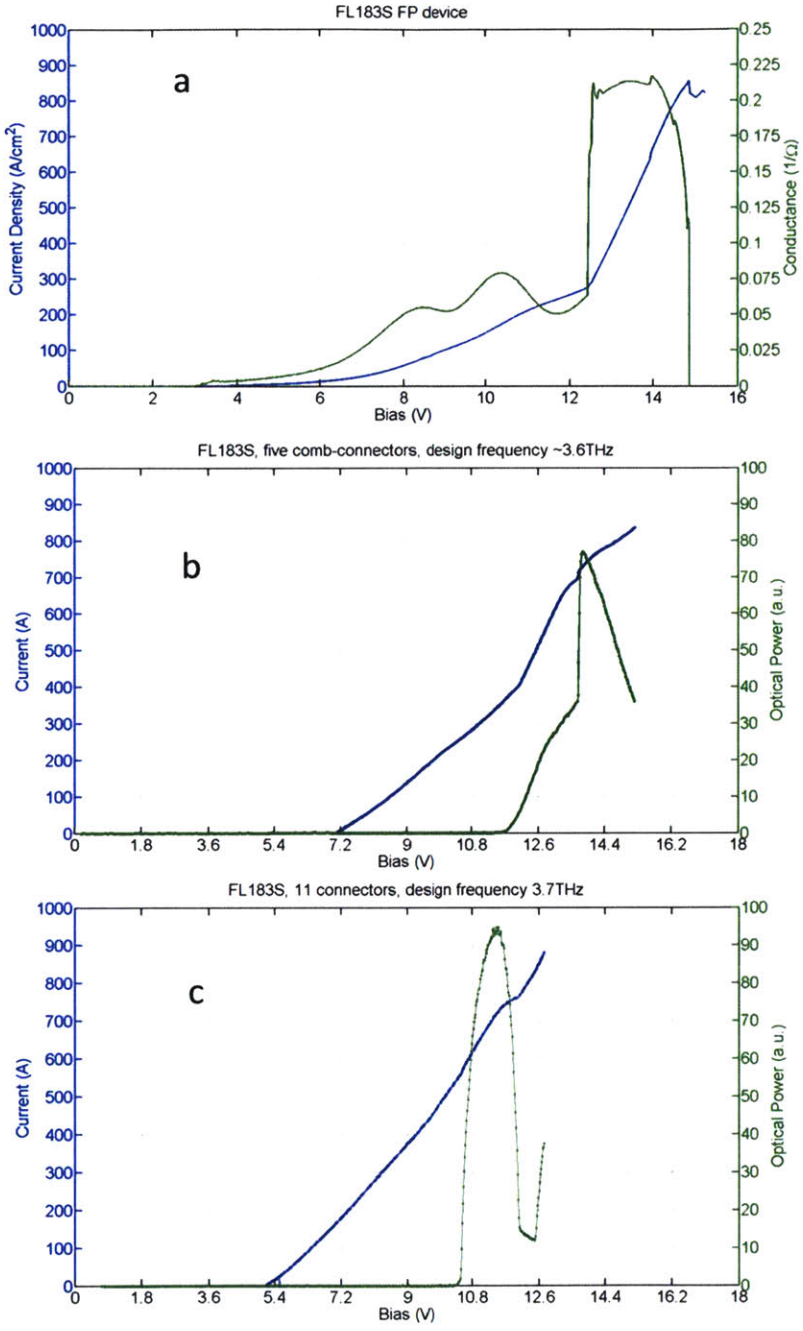

Figure 5.6.2 (a) Current density (blue) and conductance (green) vs. voltage of a typical FL183 Fabry-Perot device (~1mm long, 100μm wide). (b) Current density (blue) and optical power (green) vs. voltage of a device with five comb-connectors whose design frequency is ~3.6THz. (c) Current density (blue) and optical power (green) vs. voltage of a device with eleven comb-connectors whose design frequency is ~3.7THz. From up to bottom, the IV curves have less obvious kinks and are more like a diode. This clearly demonstrated the current spreading in part b and c.

It is worth noticing that the single mode operation was achieved first time in a THz QC wire laser at a frequency much lower than the gain peak. In this case, device d lased at

~3.4 THz, half THz lower than the gain peak (~3.9THz). This is a direct prove that the eleven-connector design achieves a robust single mode operation. This sets the foundation to further increase the tuning range by utilizing the lower half of the gain spectrum.

The pulsed current density-voltage (J-V) curve of an eleven-connector device is shown in Figure 5.6.2 (c) along with the light-voltage curve. As a comparison, J-V curve of a FP device (part a) and a five-connector device (part b) is also included. As illustrated, the increase of the connector number from five to eleven does not significantly increase the current density at the peak bias because of the use of the improved connector design described in the section 5.5.2. But the J-V curve of an eleven-connector device has less obvious kink and more like a diode's linear I-V curve compared to the five-connector device. This is a strong indication of a larger current spreading. On the other hand, due to the improved dry etching and the special connector design, the maximum operation temperature of the new design (~118K) was actually higher than the previous five-connector devices (~110K).

Although the better results had been achieved with design of FL183S, the performance of OWI222G design were not that good. The maximum operation temperature of a 10.5 μm device (f~3.8THz) based on OWI222G was only ~50K, which was much worse than FL183S. The devices with 8μm on OWI222G wafer even didn't lase at all. This might be due to the possible low peak gain at cryogenic temperature although it degrades slowly at higher temperature compared to traditional design [77]. Moreover, the small dynamic voltage range of OWI222G can play an important role due to the early NDR induced by the current spreading effect, as discussed in section 5.5.

The measurement of frequency tuning was carried out after assembling a metal MEMS plunger with a laser chip. The maximum observed continuous tuning, using only a metal plunger, was ~300GHz, which was below our expectation since more tuning range should have been achieved due to a lower starting frequency. This tuning range is slightly smaller than our previously best result which is ~310GHz. It is possibly due to a

misalignment between the plunger and the wire laser. This 300GHz tuning range is not far from the theoretical limitation which is ~380 GHz. Getting the full possible tuning range relies critically on a perfect alignment which is very difficult in the current design. For instance, sometimes realigning the plunger on a same device could lead to a ~100GHz increase of the tuning range. Thus a further optimization of the alignment design is necessary to achieve a larger tuning range in the future.

5.7 Summary

In this chapter, we analyze the bottlenecks which can hold off the future practical application of the tunable THz QC wire laser. Tuning range, robust single mode operation and tuning speed are supposed to be improved for the practical applications. A narrower QC wire laser as well as an improved fabrication technique was proposed to increase the tuning range. This new design forced more fraction of mode propagating outside of the wire laser core, and the new fabrication technique eliminated the current non-uniformity due to the curved sidewall. Moreover, its starting lasing frequency without a plunger was adjusted to a frequency much lower than the gain peak to increase the tuning range from a single metal plunger. Moreover, the robust single mode operation was achieved by a comb-connector design, which selectively guided the undesired modes into the lossy connectors and bonding pad. Furthermore, using a piezostack actuator, the tuning speed was increased to ~2 KHz while the full tuning range was not covered due to the spatial constraint. The final tuning range with the latest setup did not break the previous record possibly due to an imperfect alignment between the plunger and the wire laser. However, more importantly, our experiments have demonstrated every component needed to achieve practical applications except a power amplification section which will be discussed in the next chapter.

6 Summary and future work

6.1 Key contributions

In this thesis I have described a novel tunable QCL which enables a broad and continuous frequency tuning in THz range. To achieve this, not only a THz wire QCL was designed, but also a frictionless and restorable plunger based on MEMS technology was developed.

The first broad-band continuous tunable THz QC wire laser demonstrated a tuning range of ~137GHz centered at 3.83THz. This result was based on two novel designs. First, an unsymmetrical first order DFB structure was implemented in a THz wire QC laser, which had deep subwavelength lateral dimensions (~10μm). The first order DFB resulted in an envelope function over the periodic oscillation of electromagnetic wave, which led to different mirror losses for different longitudinal modes. Using a wire laser, this design was able to kill higher order lateral modes which had larger overlap with sidewall roughness and a lower mode confinement compared to the fundamental lateral mode. On the other hand, corresponding to the smaller mode confinement, a significant amount of laser mode propagated outside of the laser core and could be manipulated by an external subject, termed "plunger". This plunger was made from either gold (metal plunger) or high-resistivity silicon (silicon plunger). Pushed close toward the flat side of THz wire laser (<10 μm distance), the metal (silicon) plunger can tune the lasing to a higher (lower) frequency. This tuning mechanism is described by equation 3.2.1. Fixing longitudinal wavevector k_z and refractive index, only transverse wavevector $k_\perp$ is changed by the plunger and the lasing frequency was tuned. The novelty of this tuning method lies in the fact that traditional tuning mechanisms only change k_z (EC lasers) or refractive index (temperature tuning and bias tuning) which have been proven difficult for THz QCLs [75-90]. In a preliminary experiment, the plunger slid on a THz wire QC laser finished with a gold layer. A combined continuous tuning over 137GHz was demonstrated with a metal plunger (80GHz) and a silicon plunger (57GHz). This was a record of continuous tuning range up to the time when the paper was published [135]. Although this result was a milestone in the development of tunable THz QCLs, a significantly technical difficulty,

originating from the friction between the plunger and the QC laser chip, was observed. This technical challenge delayed the development of this work by two years.

To overcome this friction problem, a MEMS-based plunger was developed. Either a metal or silicon plunger was attached with a flexure, which suspended above a handling wafer to avoid contact and eliminate friction. The gap between the flexure and the handling wafer was ~1.5 μm after a sacrificial SiO_2 layer was etched away. This suspended flexure was actuated by an actuator composed by a frictionless lever and hermetic push-pull feedthrough assembled in a cryostat. The tuning range was very sensitive to the alignment condition between the plunger and the wire QC laser which ideally should be parallel with each other. To satisfy this alignment requirement, the flexure design had two stages to isolate the possible misalignment from the external actuation. The flexure design complied with the rule of SOI technology and was tailored to the cryogenic operation. Among these concerns, it is worth emphasizing that the mechanical structure was designed soft enough to avoid the material failure at ~5K. This is actually the lowest operation temperature of a MEMS based on SOI, as far as we know. The MEMS plunger was assembled with a THz wire QC laser through a male-female alignment scheme. The alignment should have a tilting less than ~0.5 degree. A homemade clamp was used to fix the plunger wafer on the laser substrate for the operation at ~5K.

To further increase the tuning range, several designs with narrower DFB ridges were implemented. A narrower ridge was used to force more fraction of mode propagating outside of the laser core and resulted in a larger tunability. Additionally, the initial lasing frequency without a plunger was designed at a frequency much lower than the gain peak to fully utilize the lower half of the gain spectrum. But this theoretical result was complicated by the smaller gain the mode could see at a lower frequency, which led to mode hopping, and poor temperature performance. To solve these problems, finally 10.5 μm wide DFB ridge was used and an optimized comb-shape connectors were designed to achieve a robust single mode operation by increasing the mode discrimination.

The best tuning result achieved is ~330 GHz with a THz wire QC laser which originally lased at ~3.8THz without a plunger. In this impressive 8.6% tuning range, 310GHz was achieved using a metal plunger and 27 GHz from a doped silicon material. The tuning range from a silicon plunger was smaller than the theoretical value due to a large absorption from the doped silicon material. To adapt this prototype for practical applications, a fast tuning was enabled by using a piezostack actuator. A fast tuning up to 2 KHz with a limited tuning range was demonstrated.

6.2 Ongoing and future work

Although significant progresses has been achieved, the performance of this tunable THz wire QC laser can still be further improved from several aspects, such as its output power, beam pattern, and integrated electrically-driven actuator. Several research efforts, which will be discussed below, have been already carried out or planned to address these issues.

6.2.1 Integrated comb-drive actuator

As a preliminary design, the current mechanical system has demonstrated a world record of continuous tuning range of THz QC lasers. However, from an engineering perspective, it still has several technical problems to be addressed. First, the current design has a bulky and complicated mechanical system which is not ready for practical applications. Secondly, the actuation from a differential micrometer does not have a robust resolution due to the fundamental limitation of these macroscopic mechanics, such as backslash et.al. Additionally this mechanical actuator is assembled with a cryostat which couple the external vibration into the actuation. This coupling can make the tuning very unstable if these vibration is in a resonance with the MEMS resonant frequencies.

An integrated comb-driver is ideal to solve the problems associated with the mechanical system. The concept was demonstrated in Figure 6.2.1. An integrated comb-driver is connected to the flexure on the opposite side of plunger. When the stator and rotor of the comb-drive are electrically biased, the electrostatic force between the comb-fingers can actuate the flexure and pull the plunger on the other side. It is worth pointing out that the

actuation force tends to pull the rotor to the stator. So in the design illustrated in Figure 6.2.1, the plunger has to be very close to the wire laser when comb-drive is not biased. On the other hand, by switching the relatively position of the rotor and stator, the plunger can be pushed toward the wire laser, which is not plot.

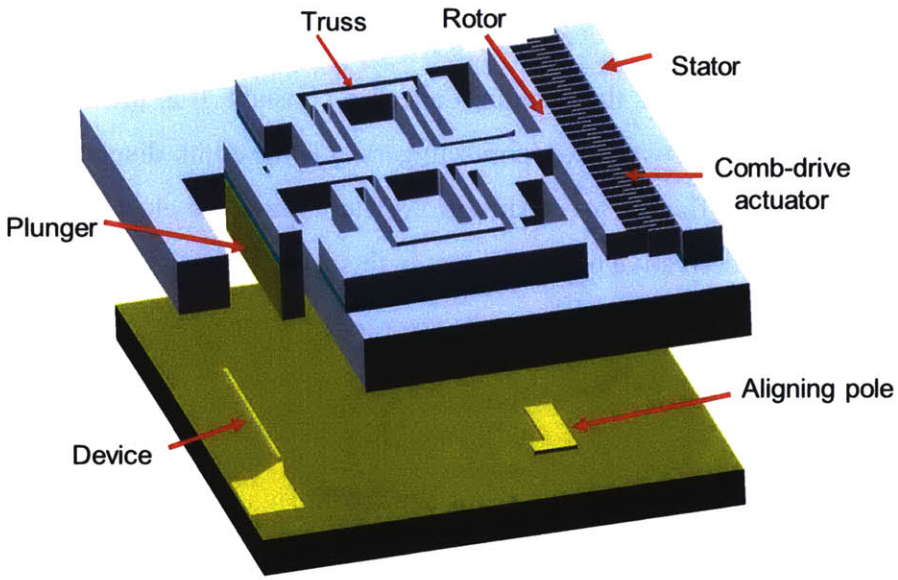

Figure 6.2.1 Schematics of MEMS plunger with an integrated comb-driver. The rotor can be pulled by the stator when they are electrically biased. The alignment method is still similar to the original MEMS plunger design.

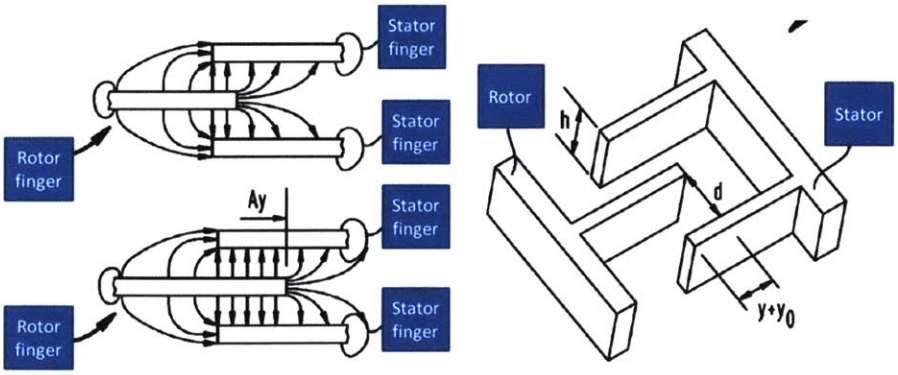

Figure 6.2.2 Illustration of the working mechanism of comb-driver. The electrical fringe field pulls the rotor fingers and stator fingers close to each other when they are electrically biased. The upper-left (lower-left) part is the position of rotor and stator fingers before (after) actuation. The fight subfigure illustrates the 3-D configuration between rotor and stator fingers.

The electrostatic force coming from the comb-drive is from the fringing field between the rotor and stator fingers, illustrated in Figure 6.2.2. This fringe field applies forces on the

surface charge of the fingers and pulls them together. Quantitatively, this can be understood by calculating the energy stored in the system. The capacitance between the stator and the rotor can be expressed as:

$$C = \frac{2n\epsilon_0 b(y + y_0)}{d} \tag{6.2.1}$$

where n is the finger number, ϵ_0 is the vacuum dielectric constant, b is the comb-finger width, y_0 is the initial overlap between two comb fingers, y is the comb displacement and d is the gap size between the fingers. According to Newton's law, the electrostatic force, F_{el}, is equal to the negative derivative of the energy, in this case, with respect to y:

$$F_{el} = \frac{1}{2}\frac{\partial C}{\partial y}V^2 = \frac{n\epsilon_0 b}{d}V^2 \tag{6.2.2}$$

where V is the applied voltage between the stator and rotor. This force actuates the rotor which is connected with the plunger.

Although comb-drive has been existing for a long time, it is still challenging to design this comb-drive MEMS plunger. First, in order to cover the whole tuning range, at least ~15 μm displacement has to be achieved which can be difficult due to the unavailable material parameters in liquid helium temperature. For this large displacement, several hundreds of finger pairs are needed depending on the gap size of the finger pairs. Additionally, the system stability can be a potential problem. In the direction vertical to the desired movement, the comb-drive is not stable because the fingers between stator and rotor attract each other. When the restoring force provided by the flexure is not enough to compensate the instability of comb-drive, the fingers will move out of the balanced position and touch each other, resulting in a short circuit. Furthermore, it is very challenging to make wire bonds, which are required to bias comb-drive, on MEMS plunger because it is only loosely fixed on the laser chip by a clamp in this demonstration stage. The potential solution can be the silver glue used to stick the wire onto a bonding

pad on MEMS wafer. Or a stronger bonding between the MEMS chip and the laser chip can be used.

6.2.2 Optimization of THz wire lasers

The design of THz wire lasers can be optimized in three aspects. First of all, the length of the wire laser can be further increases in order to reduce the lasing threshold. Originally, the length of wire lasers is always kept as 30 periods of DFB grating. The concerns are two folds. By fixing the length, all the designs are comparable. Besides, in the previous design, the mirror loss, which is inverse proportional to ln(1/L), was the only mechanism to discriminate different longitudinal modes. So a longer laser can reduce the mode discrimination and possibly cause mode hopping. Since the comb-shape connectors are a much effective mode selector, the mirror loss is not a dominate factor anymore and can be reduced by elongating the DFB laser. So a larger gain bandwidth can be achieved, resulting in a wider tuning range.

Till now, the grating of first order DFB structure always has a sinusoidal shape with 3 μm amplitude. Originally, this DFB design includes a concern to tradeoff between the feedback intensity and the possibility of spatial hole burning. If the coupling is too weak, it is not enough to discriminate the different longitudinal modes. On the other hand, if the coupling is too strong, a spatial hole burning occurs and results in a multimode operation. Traditionally, this coupling is quantified according to a coupling coefficient $|\kappa|=\pi n_{eff}\Delta f/c$ where n_{eff} is the effective refractive index, Δf is the size of stop band and c is light speed. However, this perturbation calculation fails because the surface-plasmon modes are strongly coupled to the metallic corrugation, and a large discontinuity in the dielectric constant is seen at each grating step [148]. Thus the optimization of the grating parameters can only be done empirically. The goal is to get a larger mode discrimination. The parameters which can be played include grating shape and grating amplitude. In addition, a defect can be implemented into the periodic grating to test the tunability of the defect mode.

Width optimization has been partially done and currently 10.5μm is chosen in the final design for this thesis. However, the performance of 8 μm wide devices is not much worse than 10.5 μm wide devices. So the optimized device width is very possibly between 8 μm and 10.5 μm. A larger tuning range can be achieved based on a device with the optimized width.

6.2.3 Master oscillator power amplifier (MOPA)

Currently, the biggest problem, preventing this preliminary design from practical applications, is the limited emission power and divergent beam pattern. The reasons are three folds. First, the facet reflectivity of such a narrow laser ridge is very high (>80%) [75], as described in the previous chapter. Secondly, the first order DFB structure further confines mode into the cavity center and further limits the output coupling. Thirdly, due to the deep subwavelength size of the output aperture, the beam is very divergent and the power collected per solid angle is very low. For these reasons, the output power hasn't been precisely measured yet.

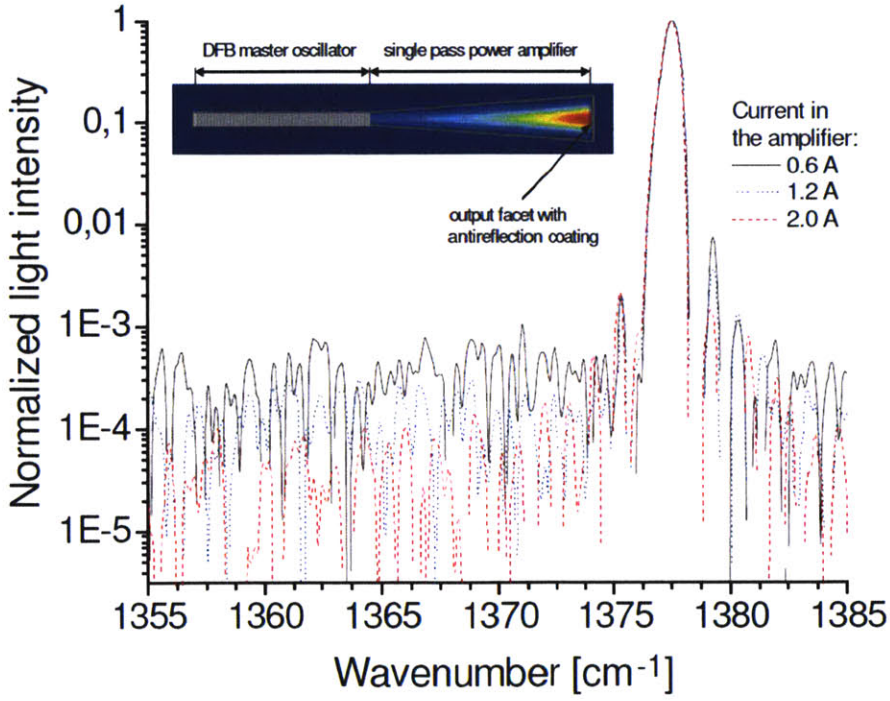

Figure 6.2.3 from [149]. Device configuration (inset) and spectra of a MOPA with 1° tapered structure. The DFB laser acts as the seed laser and the tapered section is a single-pass traveling wave

amplifier. Using a finite-difference time-domain method, the calculated light intensity is demonstrated. The device geometry is indicated by grey lines.

One possible solution is using master oscillator power amplifier (MOPA), which has been successfully implemented in mid-IR QCLs [149]. The device configuration and experimental result are shown in Figure 6.2.4. Essentially, the relative weak power from the seed laser, which in this case is a DFB QC laser, was fed into an optical amplifier which was coated with anti-reflection layer son both facets to kill lasing. In the electrically biased amplifier, the lasing cannot occur due to the larger mirror loss. The fed light was amplified by the gain medium in a single pass and reemitted out of MOPA. In the work in mid-IR range, an amplification of factor ~2 was observed. Additionally, the beam divergence was reduced by this amplifier.

However, it can be challenging to design a MOPA device for a THz QC laser because the difficulties to efficiently couple the emission from the seed laser to the amplifier while preventing amplifier from lasing. Due to divergent beam emitted out of wire laser, it is hard to recouple most of the power back to an aperture with deep subwavelength dimensions. Moreover, it is very challenging to kill lasing in a metal-metal waveguide because the mode is strongly attached with metal-semiconductor interface and see a large mode reflection at any discontinuities of this interface.

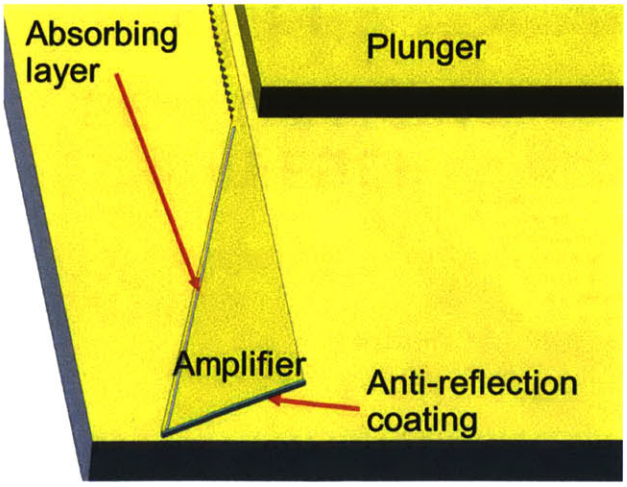

Figure 6.2.4 A possible design of MOPA for THz QC lasers. The amplification section is connected with a DFB laser seamlessly to avoid the coupling difficulty. An absorption layer was deposited on

the tilted edge in order to kill the lasing of amplifier. An anti-reflection coating is deposited on the tilted out-coupling facet. This facet is tilted to scramble its feedback.

The possible solution is shown in Figure 6.2.5. The amplification section was connected with DFB laser seamlessly to avoid the coupling difficulty. An absorption layer was deposited on the tilted edge in order to kill the lasing of amplifier. An anti-reflection coating is deposited on the tilted out-coupling facet. Both edges are designed tilted to scramble their reflection. In this amplifier, the lasing can possibly be eliminated and the amplification amplitude depends on the length of the amplifier.

6.2.4 Integration of a silicon plunger and a metal plunger

The current design of tunable THz wire QC lasers is still only a proof of concept. Although both silicon and metal plunger are used to tune a single cavity, they are not in-situ switchable. To further extend the tuning range by a single plunger, a possible design is illustrated in Figure 6.2.6.

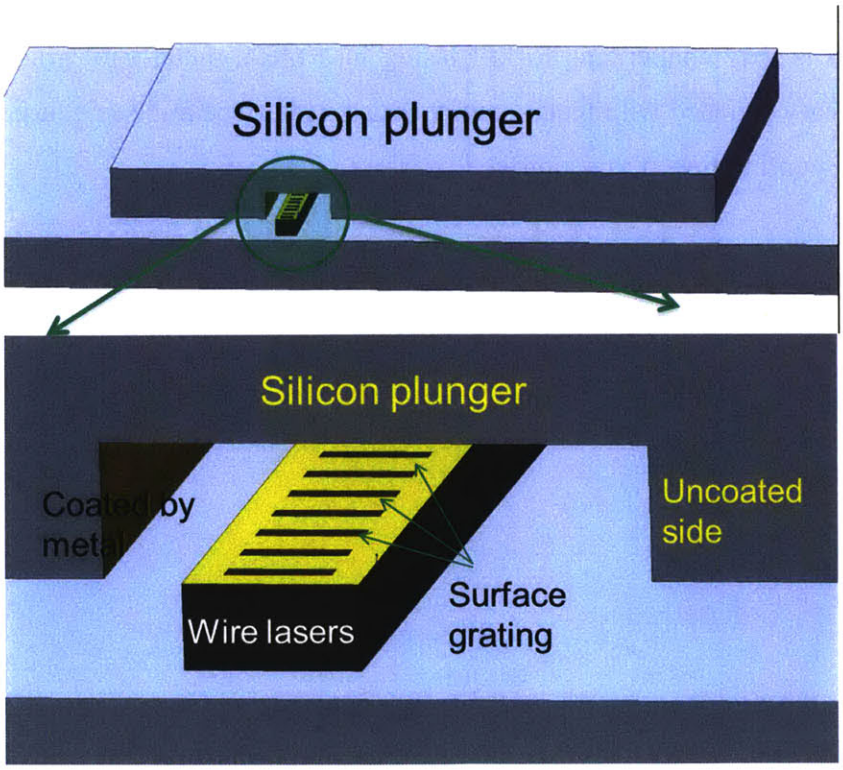

Figure 6.2.5 The configuration of a device which can be tuned to both higher and lower frequencies with a single plunger. The lower part is a blowup of the upper figure. The first order grating is

formed in the metal layer on top of the device. One of the two sidewalls of the plunger is coated by metal. By pushing and pulling the plunger, the metal and silicon plunger can function on the device alternately without delay.

In our design, the continuous switching is realized by designing the grating on top of the ridge. The first order grating is formed in the metal layer on top of the device. Then the two side walls are open to be accessed by a plunger, which is made by high-resistivity silicon. One of the two sidewalls of the plunger is coated by metal. By pushing and pulling the plunger, metal and silicon plunger can function on the device alternately without delay. The to/from mechanical motion could be made reversible using a MEMS based actuator with comb-driver on both sides of the laser ridge.

Appendix A: Fabrication recipe of MEMS plunger

SOI Wafer: double side polished,

The thickness of handling side is 500μm; the thickness of device side is 50μm.

Step 1: Standard lithography with Shipley 1813 photoresist

resist/spread/spin 6/8/30 sec .5/.75/4 krpm

Prebake 95deg C 30 min in oven

Expose (5mW/cm^2 ks2 aligner) 170sec

MF319 develop 30-40sec

Rinse in water for at least 1.5min

Postbake 30min 120 deg C in oven

Step2: Shallow etch the handling side by ~2 μm

The pattern: (a) alignment mark for the double side alignment

(b) Etch the plunger bottom avoid the contact with laser die

Recipe:

Etch	12.5
- Overlap	0
Passivation	11
- Overlap	0
Pressure	
- Fixed APC	75
- Pressure Control	
RF	
Coil (Etch/Pass)	600/600
- Match (Load/Tune)	50/50
Platen (Etch/Pass)	80/60
- Match (Load/Tune)	50/50
Gas	
SF6 (260sccm)	70
C4F8 (170sccm)	35

Step 3: Coat both side with ~3 μm SiO_2 by DCVD in MTL which will be used as hard mask later.

Step 4: Anneal (~1000^{0}C) at N_2 environment to strengthen the SiO_2 layer.

Step 5: Standard lithography with Shipley 1813 photoresist on both sides sequentially and pattern the SiO_2 layer.

Step 6: Standard lithography with AZ 4620 on the handling side.

Recipe:

resist/spread/spin 6/8/30 sec .5/.75/3 krpm

Prebake 95deg C 30 min in oven

Expose (5mW/cm^2 ks2 aligner) 300sec

MF319 develop 30-40sec

Rinse in water for at least 1.5min

Postbake 30min 120 deg C in oven

Step 7: Etch ~300 μm Si on the handling side, using photoresist as a hard mask

Recipe (JB etch):

Etch	15
- Overlap	0
Passivation	11
- Overlap	0
Pressure	
- Fixed APC	
- Pressure Control	28
RF	
Coil (Etch/Pass)	800/600
- Match (Load/Tune)	33/45
Platen (Etch/Pass)	120/60
- Match (Load/Tune)	50/50
Gas	
SF6 (260sccm)	105
C4F8 (170sccm)	50

Step 8: After striping the photoresist with piranha, the handling side was etched down to the embedded oxide layer with JB etch recipe, using SiO_2 layer as a hard mask.

Step 9: Standard lithography with AZ 4620 on the device side.

Step 10: Standard lithography with AZ 4620 on the device side.

Step 11: Etch Si for ~20min on the handling side, using JB etch recipe and photoresist as a hard mask. This step is necessary because there is a narrow trench (~4 μm) between the two stages which require a longer etching time than other region whose opening size is ~20 μm.

Step 12: After striping the photoresist with piranha, the device side was etched down to the embedded oxide layer with JB etch recipe, using SiO_2 layer as a hard mask.

Step 13: Die-saw the chip with wafer protected by thick photoresist (AZ4620).

Step 14: Release embedded SiO_2 sacrificial material under the movable parts with HF(49%):H_2O=1:4.

Step 15: Tilt the wafer with ~40^0 and coat the sidewall of the plunger with Ti/Au (30nm/300nm) by e-beam evaporation.

[1] A. W. M. Lee, "Terahertz Imaging and Quantum Cascade Laser Based Devices," MIT.

[2] Y. Y. Wang, T. Notake, M. Tang, K. Nawata, H. Ito, and H. Minamide, "Terahertz-wave water concentration and distribution measurement in thin biotissue based on a novel sample preparation," *Physics in Medicine and Biology*, vol. 56, no. 14, pp. 4517–4527, Jul. 2011.

[3] A. Rostami, H. Rasooli, and H. Baghban, *Terahertz Technology: Fundamentals and Applications*, 1st ed. Springer, 2011.

[4] D. T. Leisawitz, "Scientific motivation and technology requirements for the SPIRIT and SPECS far-infrared/submillimeter space interferometers," 2000, vol. 4013, pp. 36–46.

[5] D. Leisawitz, "NASA's Far-IR/Submillimeter Roadmap Missions SAFIR and SPECS," 2003.

[6] J. W. Waters, "Submillimeter-wavelength heterodyne spectroscopy and remote sensing of the upper atmosphere," *Proceedings of the IEEE*, vol. 80, no. 11, pp. 1679–1701, Nov. 1992.

[7] S. Kumar, "THz QC lasers: recent progress and future challenges," 2010.

[8] P. H. Siegel, "Terahertz technology," *IEEE Trans. Microwave Theory Tech.*, vol. 50, p. 910, 2002.

[9] C. Chyba, "Exploration of the solar system roadmap, science and mission strategy." NASA Office Space Sci. Solar Syst. Exploration Subcommittee, 1999.

[10] M. C. Gaidis, "Space-based applications of far infrared systems," presented at the 8th Int. TerahertzElectron. Conf., Darmstadt, Germany, 2000, pp. 125–128.

[11] "Biomedical Applications Revealed for Terahertz Spectroscopy," *Photonics.com*. [Online]. Available: http://www.photonics.com/WA46015. [Accessed: 10-Jun-2012].

[12] D. M. Mittleman, M. Gupta, R. Neelamani, R. G. Baraniuk, J. V. Rudd, and M. Koch, "Recent advances in terahertz imaging," *Applied Physics B: Lasers and Optics*, vol. 68, no. 6, pp. 1085–1094, Jun. 1999.

[13] D. D. Arnone, C. M. Ciesla, A. Corchia, S. Egusa, M. Pepper, J. M. Chamberlain, C. Bezant, E. H. Linfield, R. Clothier, and N. Khammo, "Applications of terahertz (THz) technology to medical imaging," *Proceedings of SPIE*, vol. 3828, no. 1, pp. 209–219, Sep. 1999.

[14] S. L. Dexheimer, Ed., *Terahertz Spectroscopy: Principles and Applications*, 1st ed. CRC Press, 2007.

[15] G. Diamond, "A low cost alternative to terahertz imaging for security and defense applications," *SPIE Newsroom*, 2008.

[16] A. W. M. Lee, B. S. Wil, S. Kumar, Qing Hu, and J. L. Reno, "Real-time imaging using a 4.3-THz quantum cascade laser and a 320 /spl times/ 240 microbolometer focal-plane array," *IEEE Photonics Technology Letters*, vol. 18, no. 13, pp. 1415–1417, Jul. 2006.

[17] Y. Chen, H. Zhao, and X.-C. Zhang, "Terahertz applications for detection of explosives," *I-PLUS Presentations*, Apr. 2007.

[18] J. F. Federici, B. Schulkin, F. Huang, D. Gary, R. Barat, F. Oliveira, and D. Zimdars, "THz imaging and sensing for security applications—explosives,

weapons and drugs," *Semiconductor Science and Technology*, vol. 20, no. 7, pp. S266–S280, Jul. 2005.

[19] *Patent US4755678 - Simultaneous measurement of moisture content and basis weight of paper sheet with a submillimeter laser. .*

[20] A. Cantor, P. Cheo, M. Foster, and L. Newman, "Application of submillimeter wave lasers to high voltage cable inspection," *IEEE Journal of Quantum Electronics*, vol. 17, no. 4, pp. 477–489, Apr. 1981.

[21] A. E. Costley, R. J. Hastie, J. W. M. Paul, and J. Chamberlain, "Electron Cyclotron Emission from a Tokamak Plasma: Experiment and Theory," *Phys. Rev. Lett.*, vol. 33, no. 13, pp. 758–761, 1974.

[22] S. Sattler and H. J. Hartfuss, "Experimental evidence for electron temperature fluctuations in the core plasma of the W7-AS stellarator," *Phys. Rev. Lett.*, vol. 72, no. 5, pp. 653–656, Jan. 1994.

[23] D. Woolard, "Terahertz Electronics Research for Defense: Novel Technology and Science," in *Eleventh International Symposium on Space Terahertz Technology*, 2000, vol. -1, p. 22.

[24] E. R. Brown and M. A. Celis, "All Solid-State Photomixing THZ Transmitter," Jun. 2005.

[25] J. Waldman, H. R. Fetterman, W. D. Goodhue, T. G. Bryant, and D. H. Temme, "Submillimeter modeling of millimeter radar systems," in *Society of Photo-Optical Instrumentation Engineers (SPIE) Conference Series*, 1981, vol. 259, pp. 152–157.

[26] M. J. Coulombe, T. Horgan, J. Waldman, G. Szatkowski, and W. Nixon, "A 524 GHz Polarimetric Compact Range for Scale Model RCS Measurements," *ANTENNA MEASUREMENTS AND TECHNIQUES ASSOCIATION (AMTA) PROCEEDINGS*, 1996.

[27] P. C. Ashworth, E. Pickwell-MacPherson, and E. Provenzano, "Terahertz pulsed spectroscopy of freshly excised human breast cancer," *Optics Express*, vol. 17, no. 15, p. 12444, 2009.

[28] P. Taday and D. A. Newnham, "Technological advances in terahertz pulsed systems bring far-infrared spectroscopy into the spotlight," *Spectroscopy Europe*, vol. 16, pp. 20–24, 2004.

[29] P. A. George, "An overview of Terahertz Spectroscopy." 2008.

[30] D. Woolard, R. Kaul, R. Suenram, A. H. Walker, T. Globus, and A. gSamuels, "Terahertz electronics for chemical and biological warfare agent detection," vol. 3, pp. 925–928.

[31] D. Woolard, "The potential use of submillimeter-wave spectroscopy as a technique for biological warfare agent detection.," presented at the 22nd Army Sci. Conf., Baltimore, MD, 2000.

[32] B. B. Hu and M. C. Nuss, "Imaging with terahertz waves," *Opt. Lett.*, vol. 20, p. 1717, 1995.

[33] W. L. Chan, J. Deibel, and D. M. Mittleman, "Imaging with terahertz radiation," *Reports on Progress in Physics*, vol. 70, no. 8, pp. 1325–1379, Aug. 2007.

[34] P. F. Taday, "Applications of Terahertz Spectroscopy to Pharmaceutical Sciences," *Phil. Trans. R. Soc. Lond. A*, vol. 362, no. 1815, pp. 351–364, Feb. 2004.

[35] D. M. Mittleman, S. Hunsche, L. Boivin, and M. C. Nuss, "T-ray tomography," *Opt. Lett.*, vol. 22, no. 12, pp. 904–906, Jun. 1997.

[36] K. D. Kihm, H. S. Ko, and D. P. Lyons, "Tomographic identification of gas bubbles in two-phase flows with the combined use of the algebraic reconstruction technique and the genetic algorithm," *Opt. Lett.*, vol. 23, no. 9, pp. 658–660, May 1998.

[37] J. Pearce, H. Choi, D. M. Mittleman, J. White, and D. Zimdars, "Terahertz wide aperture reflection tomography," 2005.

[38] V. P. Wallace, E. MacPherson, J. A. Zeitler, and C. Reid, "Three-dimensional imaging of optically opaque materials using nonionizing terahertz radiation," *J. Opt. Soc. Am. A*, vol. 25, no. 12, pp. 3120–3133, Dec. 2008.

[39] R. F. Kazarinov and R. A. Suris, "Possibility of the amplification of electromagnetic waves in a semiconductor with a superlattice," *Sov. Phys. Semicond.*, vol. 5, p. 707, 1971.

[40] J. Faist, F. Capasso, C. Sirtori, D. L. Sivco, and A. Y. Cho, "Quantum Cascade Lasers," in *Intersubband Transitions in Quantum Wells: Physics and Device Applications II*, vol. 66, H. C. Liu and F. Capasso, Eds. San Diego: Academic Press, 2000, pp. 1–83.

[41] F. Capasso, R. Paiella, R. Martini, R. Colombelli, C. Gmachl, T. L. Myers, M. S. Taubman, R. M. Williams, C. G. Bethea, K. Unterrainer, H. Y. Hwang, D. L. Sivco, A. Y. Cho, A. M. Sergent, H. C. Liu, and E. A. Whittaker, "Quantum cascade lasers: ultrahigh-speed operation, optical wireless communication, narrow linewidth, and far-infrared emission," *IEEE J. Quantum Electron.*, vol. 38, p. 511, 2002.

[42] K. Faist, D. Hofstetter, M. Beck, T. Aellen, M. Rochat, and S. Blaser, "Bound-to-continuum and two-phonon resonance, quantum-cascade lasers for high duty cycle, high-temperature operation," *Quantum Electronics, IEEE Journal of*, vol. 38, no. 6, pp. 533 –546, Jun. 2002.

[43] Y. Bai, S. R. Darvish, S. Slivken, W. Zhang, A. Evans, J. Nguyen, and M. Razeghi, "Room temperature continuous wave operation of quantum cascade lasers with watt-level optical power," *Applied Physics Letters*, vol. 92, no. 10, pp. 101105–101105–3, Mar. 2008.

[44] Y. Bai, S. Slivken, S. Kuboya, S. R. Darvish, and M. Razeghi, "Quantum cascade lasers that emit more light than heat," *Nature Photonics*, vol. 4, no. 2, pp. 99–102, 2010.

[45] P. Q. Liu, A. J. Hoffman, M. D. Escarra, K. J. Franz, J. B. Khurgin, Y. Dikmelik, X. Wang, J.-Y. Fan, and C. F. Gmachl, "Highly power-efficient quantum cascade lasers," *Nature Photonics*, vol. 4, no. 2, pp. 95–98, 2010.

[46] J. Faist, F. Capasso, D. L. Sivco, C. Sirtori, A. L. Hutchinson, and A. Y. Cho, "Quantum cascade laser," *Science*, vol. 264, p. 553, 1994.

[47] R. Kohler, "Terahertz semiconductor-heterostructure laser," *Nature*, vol. 417, pp. 156–159, 2002.

[48] M. Rochat, L. Ajili, H. Willenberg, J. Faist, H. Beere, G. Davies, E. Linfield, and D. Ritchie, "Low-threshold terahertz quantum-cascade lasers," *Appl. Phys. Lett.*, vol. 81, p. 1381, 2002.

[49] B. S. Williams, H. Callebaut, S. Kumar, Q. Hu, and J. L. Reno, "3.4-THz quantum cascade laser based on longitudinal-optical-phonon scattering for depopulation," *Appl. Phys. Lett.*, vol. 82, p. 1015, 2003.

[50] B. S. Williams, S. Kumar, Q. Hu, and J. L. Reno, "High-power terahertz quantum-cascade lasers," *Electron. Lett.*, vol. 42, p. 89, 2006.
[51] B. S. Williams, "Terahertz quantum cascade lasers," PhD Dissertation, Massachusetts Institute of Technology, Department of Electrical Engineering and Computer Science, 2003.
[52] C. Gmachl, "Tunable Terahertz Lasers: A wrench of wavelength," *Nature Photonics*, vol. 3, no. 12, pp. 683–684, 2009.
[53] A. A. Danylov, J. Waldman, T. M. Goyette, A. J. Gatesman, R. H. Giles, J. Li, W. D. Goodhue, K. J. Linden, and W. E. Nixon, "Terahertz sideband-tuned quantum cascade laser radiation," *Opt. Express*, vol. 16, no. 8, pp. 5171–5180, Apr. 2008.
[54] M. C. Gaidis, H. M. Pickett, P. H. Siegel, C. D. Smith, R. P. Smith, and S. C. Martin, "A 2.5 THz receiver front-end for spaceborne applications," in *Terahertz Electronics Proceedings, 1998. THz Ninety Eight. 1998 IEEE Sixth International Conference on*, 1998, pp. 13 –17.
[55] L. S. Rothman, D. Jacquemart, A. Barbe, D. Chris Benner, M. Birk, L. R. Brown, M. R. Carleer, C. Chackerian, K. Chance, L. H. Coudert, V. Dana, V. M. Devi, J.-M. Flaud, R. R. Gamache, A. Goldman, J.-M. Hartmann, K. W. Jucks, A. G. Maki, J.-Y. Mandin, S. T. Massie, J. Orphal, A. Perrin, C. P. Rinsland, M. A. H. Smith, J. Tennyson, R. N. Tolchenov, R. A. Toth, J. Vander Auwera, P. Varanasi, and G. Wagner, "The HITRAN 2004 molecular spectroscopic database," *Journal of Quantitative Spectroscopy and Radiative Transfer*, vol. 96, no. 2, pp. 139–204, Dec. 2005.
[56] E. J. Heilweil and M. Campbell, "THz Spectral Database." NIST, 2005.
[57] R. S. Tera, "RIKEN THz Spectral Database." photonics Laboratory, 2005.
[58] H.-B. Liu, H. Zhong, N. Karpowicz, Y. Chen, and X.-C. Zhang, "Terahertz Spectroscopy and Imaging for Defense and Security Applications," *Proceedings of the IEEE*, vol. 95, no. 8, pp. 1514 –1527, Aug. 2007.
[59] A. F. Fercher, C. K. Hitzenberger, G. Kamp, and S. Y. El-Zaiat, "Measurement of intraocular distances by backscattering spectral interferometry," *Optics Communications*, vol. 117, no. 1–2, pp. 43–48, May 1995.
[60] M. Choma, M. Sarunic, C. Yang, and J. Izatt, "Sensitivity advantage of swept source and Fourier domain optical coherence tomography," *Opt. Express*, vol. 11, no. 18, pp. 2183–2189, Sep. 2003.
[61] E. R. Brown, J. R. Söderström, C. D. Parker, L. J. Mahoney, K. M. Molvar, and T. C. McGill, "Oscillations up to 712 GHz in InAs/AlSb resonant-tunneling diodes," *Applied Physics Letters*, vol. 58, no. 20, pp. 2291–2293, May 1991.
[62] M. Tachiki, M. Iizuka, K. Minami, S. Tejima, and H. Nakamura, "Emission of continuous coherent terahertz waves with tunable frequency by intrinsic Josephson junctions," *Phys. Rev. B*, vol. 71, no. 13, p. 134515, Apr. 2005.
[63] F. Zernike and P. R. Berman, "Generation of Far Infrared as a Difference Frequency," *Phys. Rev. Lett.*, vol. 15, no. 26, pp. 999–1001, Dec. 1965.
[64] J. R. Morris and Y. R. Shen, "Theory of far-infrared generation by optical mixing," *Phys. Rev. A*, vol. 15, no. 3, pp. 1143–1156, Mar. 1977.
[65] M. A. Piestrup, R. N. Fleming, and R. H. Pantell, "Continuously tunable submillimeter wave source," *Applied Physics Letters*, vol. 26, no. 8, pp. 418–421, Apr. 1975.

[66] B. C. Johnson, H. E. Puthoff, J. SooHoo, and S. S. Sussman, "POWER AND LINEWIDTH OF TUNABLE STIMULATED FAR-INFRARED EMISSION IN LiNbO3," *Applied Physics Letters*, vol. 18, no. 5, pp. 181–183, Mar. 1971.

[67] J. M. Yarborough, S. S. Sussman, H. E. Purhoff, R. H. Pantell, and B. C. Johnson, "EFFICIENT, TUNABLE OPTICAL EMISSION FROM LiNbO3 WITHOUT A RESONATOR," *Applied Physics Letters*, vol. 15, no. 3, pp. 102–105, Aug. 1969.

[68] K. Kawase, J. Shikata, and H. Ito, "Terahertz wave parametric source," *Journal of Physics D: Applied Physics*, vol. 35, no. 3, pp. R1–R14, Feb. 2002.

[69] S. Preu, G. H. Döhler, S. Malzer, L. J. Wang, and A. C. Gossard, "Tunable, continuous-wave Terahertz photomixer sources and applications," *Journal of Applied Physics*, vol. 109, no. 6, pp. 061301–061301–56, Mar. 2011.

[70] B. Ferguson and X.-C. Zhang, "Materials for terahertz science and technology," *Nature Materials*, vol. 1, no. 1, pp. 26–33, 2002.

[71] J. Dyson, "The equiangular spiral antenna," *Antennas and Propagation, IRE Transactions on*, vol. 7, no. 2, pp. 181 –187, Apr. 1959.

[72] E. Brown, "THz generation by Photomixing in Ultrafast Photoconductors," *International Journal of High Speed Electronics and Systems*, vol. 13, pp. 497–545, 2003.

[73] A. Maestrini, J. Ward, J. Gill, H. Javadi, E. Schlecht, G. Chattopadhyay, F. Maiwald, N. R. Erickson, and I. Mehdi, "A 1.7-1.9 THz local oscillator source," *Microwave and Wireless Components Letters, IEEE*, vol. 14, no. 6, pp. 253 – 255, Jun. 2004.

[74] S. Preu, S. Malzer, G. H. Döhler, Q. Z. Zhao, M. Hanson, J. D. Zimmerman, A. C. Gossard, and L. J. Wang, "Interference between two coherently driven monochromatic terahertz sources," *Applied Physics Letters*, vol. 92, no. 22, pp. 221107–221107–3, Jun. 2008.

[75] S. Kohen, B. S. Williams, and Q. Hu, "Electromagnetic modeling of terahertz quantum cascade laser waveguides and resonators," *J. Appl. Phys.*, vol. 97, p. 053106, 2005.

[76] A. W. M. Lee, B. S. Williams, S. Kumar, Q. Hu, and J. L. Reno, "Real-Time Imaging Using a 4.3-THz Quantum Cascade Laser and a 320 x 240 Microbolometer Focal-Plane Array," *IEEE Photon. Technol. Lett.*, vol. 18, p. 1415, 2006.

[77] S. Kumar, Q. Hu, and J. L. Reno, "186 K operation of terahertz quantum-cascade lasers based on a diagonal design," *Applied Physics Letters*, vol. 94, no. 13, pp. 131105–131105–3, Apr. 2009.

[78] A. J. L. Adam, I. Kašalynas, J. N. Hovenier, T. O. Klaassen, J. R. Gao, E. E. Orlova, B. S. Williams, S. Kumar, Q. Hu, and J. L. Reno, "Beam patterns of terahertz quantum cascade lasers with subwavelength cavity dimensions," *Applied Physics Letters*, vol. 88, no. 15, pp. 151105–151105–3, Apr. 2006.

[79] D. Burghoff, T.-Y. Kao, D. Ban, A. W. M. Lee, Q. Hu, and J. Reno, "A terahertz pulse emitter monolithically integrated with a quantum cascade laser," *Applied Physics Letters*, vol. 98, no. 6, pp. 061112–061112–3, Feb. 2011.

[80] "MODULE 4-6 DIODE LASER POWER SUPPLIES," *The Center for Occupational Research and Development*. [Online]. Available: http://agamemnon.cord.org.

[81] "Laser diode," *Wikipedia*. [Online]. Available: http://en.wikipedia.org/wiki/Laser_diode.
[82] J. P. Zhang, D. Y. Chu, S. L. Wu, S. T. Ho, W. G. Bi, C. W. Tu, and R. C. Tiberio, "Photonic-Wire Laser," *Phys. Rev. Lett.*, vol. 75, no. 14, pp. 2678–2681, Oct. 1995.
[83] C. Z. Ning, "Semiconductor nanolasers," *physica status solidi (b)*, vol. 247, no. 4, pp. 774–788, 2010.
[84] K. Ding, Z. C. Liu, L. J. Yin, M. T. Hill, M. J. H. Marell, P. J. van Veldhoven, R. Nöetzel, and C. Z. Ning, "Room-temperature continuous wave lasing in deep-subwavelength metallic cavities under electrical injection," *Phys. Rev. B*, vol. 85, no. 4, p. 041301, Jan. 2012.
[85] M. Munsch, J. Claudon, J. Bleuse, N. S. Malik, E. Dupuy, J.-M. Gérard, Y. Chen, N. Gregersen, and J. Mørk, "Linearly Polarized, Single-Mode Spontaneous Emission in a Photonic Nanowire," *Phys. Rev. Lett.*, vol. 108, no. 7, p. 077405, Feb. 2012.
[86] J. Claudon, J. Bleuse, N. S. Malik, M. Bazin, P. Jaffrennou, N. Gregersen, C. Sauvan, P. Lalanne, and J.-M. Gérard, "A highly efficient single-photon source based on a quantum dot in a photonic nanowire," *Nature Photonics*, vol. 4, no. 3, pp. 174–177, 2010.
[87] M. I. Amanti, G. Scalari, F. Castellano, M. Beck, and J. Faist, "Low divergence Terahertz photonic-wire laser," *Opt. Express*, vol. 18, no. 6, pp. 6390–6395, Mar. 2010.
[88] E. E. Orlova, J. N. Hovenier, T. O. Klaassen, I. Kašalynas, A. J. L. Adam, J. R. Gao, T. M. Klapwijk, B. S. Williams, S. Kumar, Q. Hu, and J. L. Reno, "Antenna Model for Wire Lasers," *Phys. Rev. Lett.*, vol. 96, no. 17, p. 173904, May 2006.
[89] F. Toor, D. L. Sivco, H. E. Liu, and C. F. Gmachl, "Effect of waveguide sidewall roughness on the threshold current density and slope efficiency of quantum cascade lasers," *Applied Physics Letters*, vol. 93, no. 3, pp. 031104–031104–3, Jul. 2008.
[90] MARCUSE and D. Marcuse, "MODE CONVERSION CAUSED BY SURFACE IMPERFECTIONS OF A DIELECTRIC SLAB WAVEGUIDE," *BELL SYSTEM TECHNICAL JOURNAL*, vol. 48, no. 10, p. 3187–, 1969.
[91] P. K. Tien, "Light Waves in Thin Films and Integrated Optics," *Appl. Opt.*, vol. 10, no. 11, pp. 2395–2413, Nov. 1971.
[92] T. D. Visser, H. Blok, B. Demeulenaere, and D. Lenstra, "Confinement factors and gain in optical amplifiers," *Quantum Electronics, IEEE Journal of*, vol. 33, no. 10, pp. 1763 –1766, Oct. 1997.
[93] A. V. Maslov and C. Z. Ning, "Modal gain in a semiconductor nanowire laser with anisotropic bandstructure," *Quantum Electronics, IEEE Journal of*, vol. 40, no. 10, pp. 1389 – 1397, Oct. 2004.
[94] S. Kumar, "Development of terahertz quantum-cascade lasers," MIT, 2007.
[95] S. Kohen, "Electromagnetic modeling of terahertz quantum cascade laser waveguides and resonators," MS Dissertation, Massachusetts Institute of Technology, Department of Electrical Engineering and Computer Science, 2004.
[96] A. J. L. Adam, I. K. salynas, J. N. Hovenier, T. O. Klaassen, J. R. Gao, E. E. Orlova, B. S. Williams, S. Kumar, Q. Hu, and J. L. Reno, "Beam patterns of

terahertz quantum cascade lasers with subwavelength cavity dimensions," *Appl. Phys. Lett.*, vol. 88, p. 151105, 2006.

[97] S. P. Khanna, M. Salih, P. Dean, A. G. Davies, and E. H. Linfield, "Electrically tunable terahertz quantum-cascade laser with a heterogeneous active region," *Applied Physics Letters*, vol. 95, no. 18, pp. 181101–181101–3, Nov. 2009.

[98] G. Scalari, M. I. Amanti, C. Walther, R. Terazzi, M. Beck, and J. Faist, "Broadband THz lasing from a photon-phonon quantum cascade structure," *Opt. Express*, vol. 18, no. 8, pp. 8043–8052, Apr. 2010.

[99] L. Lever, N. M. Hinchcliffe, S. P. Khanna, P. Dean, Z. Ikonic, C. A. Evans, A. G. Davies, P. Harrison, E. H. Linfield, and R. W. Kelsall, "Terahertz ambipolar dual-wavelength quantum cascade laser," *Opt. Express*, vol. 17, no. 22, pp. 19926–19932, Oct. 2009.

[100] S. Kumar, C. W. I. Chan, Q. Hu, and J. L. Reno, "A 1.8-THz quantum cascade laser operating significantly above the temperature of [planck][omega]/kB," *Nature Physics*, vol. 7, no. 2, pp. 166–171, 2011.

[101] G. Scalari, C. Walther, J. Faist, H. Beere, and D. Ritchie, "Electrically switchable, two-color quantum cascade laser emitting at 1.39 and 2.3 THz," *Appl. Phys. Lett.*, vol. 88, p. 141102, 2006.

[102] J. R. Freeman, O. P. Marshall, H. E. Beere, and D. A. Ritchie, "Electrically switchable emission in terahertz quantum cascade lasers," *Opt. Express*, vol. 16, no. 24, pp. 19830–19835, Nov. 2008.

[103] C. Gmachl, D. L. Sivco, R. Colombelli, F. Capasso, and A. Y. Cho, "Ultra-broadband semiconductor laser," *Nature*, vol. 415, no. 6874, pp. 883–887, Feb. 2002.

[104] C. Walther, M. Fischer, G. Scalari, R. Terazzi, N. Hoyler, and J. Faist, "Quantum cascade lasers operating from 1.2 to 1.6 THz," *Applied Physics Letters*, vol. 91, no. 13, pp. 131122–131122–3, Sep. 2007.

[105] H. W. Hübers, S. G. Pavlov, H. Richter, A. D. Semenov, L. Mahler, A. Tredicucci, H. E. Beere, and D. A. Ritchie, "Molecular Spectroscopy with TeraHertz Quantum Cascade Lasers," *Journal of Nanoelectronics and Optoelectronics*, vol. 2, no. 1, pp. 101–107, 2007.

[106] S. Kumar, B. S. Williams, Q. Qin, A. W. Lee, Q. Hu, and J. L. Reno, "Surface-emitting distributed feedback terahertz quantum-cascade lasers in metal-metal waveguides," *Opt. Express*, vol. 15, no. 1, pp. 113–128, Jan. 2007.

[107] T.-Y. Kao, Q. Hu, and J. L. Reno, "True phase-matched third-order DFB terahertz quantum-cascade lasers using weakly-coupled cavities," in *Lasers and Electro-Optics (CLEO), 2011 Conference on*, 2011, pp. 1 –2.

[108] L. Mahler, A. Tredicucci, F. Beltram, C. Walther, J. Faist, B. Witzigmann, H. E. Beere, and D. A. Ritchie, "Vertically emitting microdisk lasers," *Nature Photonics*, vol. 3, no. 1, pp. 46–49, 2009.

[109] L. Mahler, M. I. Amanti, C. Walther, A. Tredicucci, F. Beltram, J. Faist, H. E. Beere, and D. A. Ritchie, "Distributed feedback ring resonators for vertically emitting terahertz quantum cascade lasers," *Opt. Express*, vol. 17, no. 15, pp. 13031–13039, Jul. 2009.

[110] G. Scamarcio, M. S. Vitiello, V. Spagnolo, S. Kumar, B. Williams, and Q. Hu, "Nanoscale heat transfer in quantum cascade lasers," *Physica E: Low-dimensional Systems and Nanostructures*, vol. 40, no. 6, pp. 1780–1784, Apr. 2008.

[111] M. S. Vitiello, G. Scamarcio, and V. Spagnolo, "Time-resolved measurement of the local lattice temperature in terahertz quantum cascade lasers," *Applied Physics Letters*, vol. 92, no. 10, pp. 101116–101116–3, Mar. 2008.

[112] N. Beverini, G. Carelli, A. De Michele, A. Moretti, L. Mahler, A. Tredicucci, H. E. Beere, and D. A. Ritchie, "Frequency Characterization of a Terahertz Quantum-Cascade Laser," *Instrumentation and Measurement, IEEE Transactions on*, vol. 56, no. 2, pp. 262 –265, Apr. 2007.

[113] J. M. Hensley, J. Montoya, M. G. Allen, J. Xu, L. Mahler, A. Tredicucci, H. E. Beere, and D. A. Ritchie, "Spectral behavior of a terahertz quantum-cascade laser," *Opt. Express*, vol. 17, no. 22, pp. 20476–20483, Oct. 2009.

[114] B. G. Lee, H. A. Zhang, C. Pflugl, L. Diehl, M. A. Belkin, M. Fischer, A. Wittmann, J. Faist, and F. Capasso, "Broadband Distributed-Feedback Quantum Cascade Laser Array Operating From 8.0 to 9.8 um," *IEEE Photonics Technology Letters*, vol. 21, no. 13, pp. 914–916, Jul. 2009.

[115] T.-Y. Kao, Q. Hu, and J. L. Reno, "Phase-locked arrays of surface-emitting terahertz quantum-cascade lasers," *Applied Physics Letters*, vol. 96, no. 10, pp. 101106 –101106–3, Mar. 2010.

[116] A. Wei Min Lee, T.-Y. Kao, D. Burghoff, Q. Hu, and J. L. Reno, "Terahertz tomography using quantum-cascade lasers," *Opt. Lett.*, vol. 37, no. 2, pp. 217–219, Jan. 2012.

[117] D. G. Allen, T. Hargett, J. L. Reno, A. A. Zinn, and M. C. Wanke, "Index Tuning for Precise Frequency Selection of Terahertz Quantum Cascade Lasers," *Photonics Technology Letters, IEEE*, vol. 23, no. 1, pp. 30 –32, Jan. 2011.

[118] J. M. Hensley, D. J. Bamford, M. G. Allen, J. Xu, A. Tredicucci, H. E. Beere, and D. A. Ritchie, "Demonstration of an External Cavity Terahertz Quantum Cascade Laser," in *Optical Terahertz Science and Technology*, 2005, p. TuA3.

[119] D. B. Fenner, J. M. Hensley, M. G. Allen, J. Xu, and A. Tredicucci, "Antireflection Coating for External-Cavity Quantum Cascade Laser Near 5 THz," *MRS Online Proceedings Library*, vol. 1016, p. null, 2007.

[120] J. Xu, J. M. Hensley, D. B. Fenner, R. P. Green, L. Mahler, A. Tredicucci, M. G. Allen, F. Beltram, H. E. Beere, and D. A. Ritchie, "Tunable terahertz quantum cascade lasers with an external cavity," *Applied Physics Letters*, vol. 91, no. 12, pp. 121104–121104–3, Sep. 2007.

[121] J. M. Hensley, D. B. Fenner, M. G. Allen, J. Xu, R. P. Green, L. Mahler, A. Tredicucci, F. Beltram, H. E. Beere, and D. A. Ritchie, "An External Cavity 4.7 Terahertz Quantum Cascade Laser," in *Optical Terahertz Science and Technology*, 2007, p. WB4.

[122] K.-S. Lee, T.-M. Lu, and X. Zhang, "Tera Tool [terahertz time-domain spectroscopy]," *IEEE Circuits and Devices Magazine*, vol. 18, no. 6, pp. 23–28, Nov. 2002.

[123] K. Kawase and N. Hiromoto, "Terahertz-Wave Antireflection Coating on Ge and GaAs with Fused Quartz," *Appl. Opt.*, vol. 37, no. 10, pp. 1862–1866, Apr. 1998.

[124] A. W. M. Lee, B. S. Williams, S. Kumar, Q. Hu, and J. L. Reno, "Tunable terahertz quantum cascade lasers with external gratings," *Opt. Lett.*, vol. 35, no. 7, pp. 910–912, Apr. 2010.
[125] L. Mahler, A. Tredicucci, F. Beltram, H. E. Beere, and D. A. Ritchie, "Tuning a distributed feedback laser with a coupled microcavity," *Opt. Express*, vol. 18, no. 18, pp. 19185–19191, 2010.
[126] H.-W. Hübers, S. G. Pavlov, H. Richter, A. D. Semenov, L. Mahler, A. Tredicucci, H. E. Beere, and D. A. Ritchie, "High-resolution gas phase spectroscopy with a distributed feedback terahertz quantum cascade laser," *Applied Physics Letters*, vol. 89, no. 6, pp. 061115–061115–3, Aug. 2006.
[127] L. A. Dunbar, R. Houdré, G. Scalari, L. Sirigu, M. Giovannini, and J. Faist, "Small optical volume terahertz emitting microdisk quantum cascade lasers," *Applied Physics Letters*, vol. 90, no. 14, pp. 141114–141114–3, Apr. 2007.
[128] H. Zhang, L. A. Dunbar, G. Scalari, R. Houdr, and J. Faist, "Terahertz photonic crystal quantum cascade lasers," *Opt. Express*, vol. 15, no. 25, pp. 16818–16827, Dec. 2007.
[129] J. Buus, M.-C. Amann, and D. J. Blumenthal, "Tunable Laser Diodes and Related Optical Sources." Nature Publishing Group, 2005.
[130] J. Xu, "Tunable THz quantum cascade lasers with an external cavity," *Appl. Phys. Lett.*, vol. 91, p. 121104, 2007.
[131] M. C. Y. Huang, Y. Zhou, and C. J. Chang-Hasnain, "A nanoelectromechanical tunable laser," *Nature Photon.*, vol. 2, pp. 180–184, 2008.
[132] R. Maulini, "External cavity quantum-cascade laser tunable from 8.2 to 10.4 [mu]m using a gain element with a heterogeneous cascade," *Appl. Phys. Lett.*, vol. 88, p. 201113, 2006.
[133] M.-C. Amann, S. Illek, C. Schanen, and W. Thulke, "Tunable twin-guide laser: A novel laser diode with improved tuning performance," *Applied Physics Letters*, vol. 54, no. 25, p. 2532, 1989.
[134] S. Kumar and Q. Hu, "Coherence of resonant-tunneling transport in terahertz quantum-cascade lasers," *Phys. Rev. B*, vol. 80, no. 24, p. 245316, Dec. 2009.
[135] Q. Qin, B. S. Williams, S. Kumar, J. L. Reno, and Q. Hu, "Tuning a terahertz wire laser," *Nat Photon*, vol. 3, no. 12, pp. 732–737, Dec. 2009.
[136] P. Beckmann and A. Spizzichino, *The Scattering of Electromagnetic Waves from Rough Surfaces*. Artech Print on Demand, 1987.
[137] M. Naftaly and R. Dudley, "Terahertz reflectivities of metal-coated mirrors," *Appl. Opt.*, vol. 50, no. 19, pp. 3201–3204, Jul. 2011.
[138] O. M. Braun and A. G. Naumovets, "Nanotribology: microscopic mechanisms of friction," *Surf. Sci. Rep.*, vol. 60, pp. 79–158, 2006.
[139] T. Baumberger, F. Heslot, and B. Perrin, "Crossover from creep to inertial motion in friction dynamics," *Nature*, vol. 367, pp. 544–546, 1994.
[140] N. N. Gosvami, M. Feldmann, J. Peguiron, M. Moseler, A. Schirmeisen, and R. Bennewitz, "Ageing of a Microscopic Sliding Gold Contact at Low Temperatures," *Phys. Rev. Lett.*, vol. 107, no. 14, p. 144303, Sep. 2011.
[141] F. O. Rupert, "Plasmon lasers at deep subwavelength scale," *Nature*, vol. 461, pp. 629–632, 2009.

[142] T. Baumberger, F. Heslot, and B. Perrin, "Crossover from creep to inertial motion in friction dynamics," *Nature*, vol. 367, no. 6463, pp. 544–546, Feb. 1994.

[143] J. Li, Q. X. Zhang, and A. Q. Liu, "Advanced fiber optical switches using deep RIE (DRIE) fabrication," *Sensors and Actuators A: Physical*, vol. 102, no. 3, pp. 286–295, Jan. 2003.

[144] P. Dainesi, A. Kung, M. Chabloz, A. Lagos, P. Fluckiger, A. Ionescu, P. Fazan, M. Declerq, P. Renaud, and P. Robert, "CMOS compatible fully integrated Mach-Zehnder interferometer in SOI technology," *IEEE Photonics Technology Letters*, vol. 12, no. 6, pp. 660 –662, Jun. 2000.

[145] "Curved Hinge Flexure." [Online]. Available: http://www.wa.ctw.utwente.nl/staff/d.m._brouwer.

[146] A.-Q. Liu, *Photonic MEMS devices: design, fabrication and control*. CRC Press, 2009.

[147] T.-Y. Kao, Q. Hu, and J. Reno, "True Phase-Matched Third-order DFB Terahertz Quantum-Cascade Lasers usingWeakly-coupled Cavities," in *CLEO:2011 - Laser Applications to Photonic Applications*, 2011, p. CThE4.

[148] B. S. Williams, S. Kumar, Q. Hu, and J. L. Reno, "Distributed-feedback terahertz quantum-cascade lasers with laterally corrugated metal waveguides," *Opt. Lett.*, vol. 30, pp. 2909–2911, 2005.

[149] S. Menzel, L. Diehl, C. Pflügl, A. Goyal, C. Wang, A. Sanchez, G. Turner, and F. Capasso, "Quantum cascade laser master-oscillator power-amplifier with 1.5 W output power at 300 K," *Opt Express*, vol. 19, no. 17, pp. 16229–16235, Aug. 2011.